Rapid Prototyping Technologies for Processing of Nanomaterials with Applications to Microfluidics and Nanoelectronics

by

Collin Tittle

A thesis
presented to the University of Waterloo
in fulfilment of the
thesis requirement for the degree of
Master of Applied Science
in
Electrical and Computer Engineering

Waterloo, Ontario, Canada, 2017

Author's Declaration

I hereby declare that I am the sole author of this thesis. This is a true copy of the thesis, including any required final revisions, as accepted by my examiners.

I understand that my thesis may be made electronically available to the public.

Abstract

The focus of this thesis is on the processing of nanomaterials using rapid prototyping technologies. To develop the necessary skills in fabrication and electronics, a thin film microheater was developed and applied to genetic amplification using the polymerase chain reaction in a manner compatible with point-of-care settings. Subsequently these skills were applied to the processing and characterization of molybdenum disulfide for next generation electronics. After preliminary protocol and infrastructure development was achieved, the unexpected discovery of superhydrophobic behaviour present in laser processed Kapton films necessitated a change in focus. These films were investigated and discovered to be some of the most superhydrophobic surfaces ever reported while also addressing the long standing issues of durability and manufacturability. These films were then applied to membrane distillation for the desalination of water. For the energy efficient technique of air gapped membrane distillation, mass fluxes approach the state-of-the-art were achieved and no membrane failure was observed, indicating long lifetimes.

Acknowledgements

First and foremost I would like to thank Professor Christopher J. Backhouse for his guidance and mentorship. I would also like to thank the many people who helped me along the way. To name just a few: Gordon Hall, Raphaele Camasta, Alicia Dubinski, Nicholas Lanigan, Dilara Yilman, Chanele Polenz, Dr. Michael Pope, and Dr. Moira Glerum.

Dedication

I would like to dedicate this thesis to my family. To my mother who always believed in and support me. To my father who taught me hard work and tenacity. To my brother who reminds me to always enjoy life to the fullest. Thank you.

Table of Contents

List of Figures

List of Tables

You can know the name of a bird in all languages of the world, but when you're finished, you'll know absolutely nothing whatever about the bird... So let's look at the bird and see what it's doing– that's what counts. I learned very early the difference between knowing the name of something and knowing something.

–Richard Feynman

Chapter 1

Introduction

Nanotechnology offers the promise of the miniaturization of vast numbers of technologies with innumerable benefits. With the advent of microscopy techniques such as scanning-tunnelling microscopy, atomic force microscopy and transmission electron microscopy it is now possible to observe nature on the atomic level. When such techniques are combined with modern nanofabrication methods such as electron beam, focused ion beam, and nanoimprint lithography it is possible to fabricate and characterize nanometer-scale structures.

While truly amazing advances have been made using the above-mentioned traditional nanofabrication techniques they have been limited by high costs and an inflexibility to design alterations. The development of rapid prototyping technologies allows for designs to be easily altered in a higher throughput, low-cost manner; however, its application to nanotechnology has been limited by a lack of resolution. It was the objective of this thesis to demonstrate such techniques could be applied to the processing of nanomaterials for a diverse set of applications.

As an initial project to develop fabrication and electronics skills, as well as to learn biological handling procedures, rapid prototyping techniques were used to fabricate thin film microheaters for nanobiotechnology applications. These microheaters were used to perform quantitative polymerase chain reaction (qPCR), a standard molecular biology technique for the amplification and quantification of genetic material. The results of this project were that a standard medical diagnostic was performed in an affordable manner potentially suitable for point of care applications while developing skills in thermal design, control systems, fabrication, and molecular biology.

The next progression was to demonstrate the application of rapid prototyping technologies for the characterization of molybdenum disulfide (MoS_2), a two-dimensional material similar to graphene and of experimental interest for next generation electronics. The majority of existing literature relies upon the use of low throughput, high-cost techniques for both fabrication and characterization. The objective was to apply the approach used for fabricating the microheaters to the processing, device fabrication, and characterization of MoS_2. Preliminary infrastructure development was performed including the development of processing and optical characterization protocols, and assembly of an electrical characterization system capable of providing preliminary results; methods which are still being used and developed by others. While developing these new fabrication techniques it was observed that our processing was producing surfaces with remarkable superhydrophobic properties; a discovery which required further investigation and yielded important results.

Superhydrophobic surfaces traditionally suffer from two challenges. The first being complicated and expensive fabrication processes and the second being the fragility of the resulting surfaces. A technique for the rapid prototyping of controllably wettable surfaces was developed. Mechanically durable, chemically inert, and temporally stable surfaces with properties ranging from hydrophilic to superhydrophobic could be produced, addressing many of the long-standing challenges in the field. Applications of these surfaces to evaporative desalination, self-cleaning coatings, and electrical conductivity measurements were demonstrated.

A promising technology for water desalination, membrane distillation, utilizes a porous superhydrophobic membrane to separate a hot, saline feed solution from a cold permeate solution of pure water. Utilizing the Laplace pressure difference between these two solutions, water vapour is driven through the pores from hot to cold. This technology has the advantage of operating at much lower temperatures and pressures than traditional desalination techniques; however, development has been hindered by a lack of durable, porous, superhydrophobic membranes. After a review of the field and long-standing issues, application of the novel superhydrophobic films as long lasting membranes capable of state-of-the-art distilled water production was demonstrated.

The following structure will be followed. In Chapter 2, the rapid fabrication of microheaters for qPCR and the resulting trials will be discussed. Chapter 3 will detail the infrastructure development for the processing and characterization of MoS_2. The superhydrophobic films will be discussed in two parts. Chapter 4 will discuss the surface fabrication and characterization with Chapter 5 focusing on their application to desalination, specifically membrane distillation.

While the initial focus of this thesis was on the rapid processing of MoS_2 for nanoelectronic applications, the serendipitous discovery of a novel method of producing hydrophobic surfaces necessitated a change of focus. Using rapid prototyping techniques, controllable superhydrophobic surfaces could be patterned creating highly durable films with applications to water desalination.

Chapter 2

Rapidly Prototyped Microheaters for Lab-on-Chip Applications

2.1 Introduction

As discussed in Chapter 1, standard microfabrication technologies such as lithography and etching are incompatible with an iterative design process which necessitates the ability to rapidly adjust one's design. Standard technologies often require long lead times to produce new designs at the cost of thousands of dollars whereas rapid prototyping technologies such as laser ablation, CNC milling, and 3D printing utilize computer aided design (CAD) files to rapidly fabricate a design under computer control. These CAD files may be swiftly modified in a process compatible with an iterative design methodology. The fabrication of a microheater designed to perform low-cost medical diagnostics was used as a platform to improve skills in fabrication and control systems and learn fundamentals of molecular biology while developing appropriate biological handling procedures. These skills are essential for successful demonstration of the microfluidic processing of two-dimensional materials which will be discussed in Chapter 3.

Fabrication of systems capable of providing robust thermal control, particularly for the implementation of the polymerase chain reaction (PCR), has been identified as a crucial goal of microfabrication technologies [9]. While integrated isothermal and flow-through PCR systems have been demonstrated ([10], [11], [12]), these large, complex systems required substantial power budgets and sophisticated manufacturing methods. By miniaturizing the microheater, robust thermal control may be obtained through active heating and passive cooling thus allowing operation on a much smaller power budget. Thaitrong *et al.* demonstrated a complete system capable of operating on a low power budget; however, a highly complex, multiple material fabrication process was necessary [13].

Thin film microheaters are considered promising candidates for point-of-care applications as they excel in utilizing low power budgets; an important constraint for portable genetic analysis [14]. A recent review noted that although successful demonstrations exist ([15], [16], [17]), they are still limited by their inability to actively cool and the manufacturing complexity associated with the necessary sensor integration for thermal control [14]. Monolithic heating and sensing has been achieved by techniques such as lithographically patterned platinum films, however as noted by Almassian *et al.* a low cost solution with the capability of integration with additional functionalities such as capillary electrophoresis (CE), a necessity for complete genetic diagnostics, remains yet to be achieved [14] [18].

We chose a commercially prepared polymeric mirror comprised of a 1.5 mm thick PMMA substrate coated with a thin aluminum film as a platform for our microheater as it could be processed and integrated using rapid-prototyping manufacturing technologies in a manner compatible with potential complementary metal-oxide semiconductor (CMOS) production. After introducing several design and process modifications from previous versions, we demonstrated that a ring heater design using this platform provided thermal control with a completely integrated temperature sensor utilizing the thermal coefficient of resistivity of aluminum films. Although there were indications of temperature non-uniformities, a complete PCR was performed using only the PMMA microheater combined with an inexpensive current source and microcontroller.

2.2 Materials and Methods

2.2.1 Chip Manufacture

The bases for the microheaters were fabricated from 30 mm by 40 mm sections of 1.5 mm thick poly(methyl methacrylate) mirror (Acrylite Mirror 0A000, Evonik; hereby referred to as PMMA) using a Universal Laser Systems VLS 2.30 CO_2 laser ($10.6\mu m$) with settings of 30% power, 10% speed, 1000 pulses per inch, and 1.5 mm focus (at surface). The chips were then transferred to one of two CNC mills which milled two features into the PMMA side of the chip. The first was a 1 mm deep, 1.5 mm diameter well which was cut using a 1.509 mm diameter 2-flute carbide endmill using either a Tormach PCNC 770 (10 000 rpm, feed rate of 10 inches/min, 3 revolution dwell, and using coolant) or a Taig Micromill (10 400 rpm, feed rate of 60 mm/min in steps of 0.2 mm). The milling was performed by either Gordon Hall or Dr. Christopher Backhouse.

The second feature (called the moat) was a 1 mm deep circular trench which increased the radial thermal resistance; the resistance to thermal conduction away from the well in the plane of the chip assuming axial symmetry. From the center of the well, the moat had an inner radius of 2.5 mm and an outer radius of 6 mm which allowed for a 1 mm thick wall of PMMA between the well and moat features. The moat was cut to a depth of 1 mm using a 1.509 mm diameter 2-flute carbide endmill with either 2 passes of helical machining at 10 000 rpm, a feed rate of 20 inches/min, and no coolant with the Tormach PCNC 770, or 10 400 rpm with a feed rate of 60 mm/min in 0.2 mm steps using the Taig Micromill. These features may be seen clearly in Fig. 2.2c.

Chips were cleaned of milling debris using de-ionized (DI) water ($18M\Omega$ cm) and gentle agitation before being returned to the laser with the aluminized layer upwards.

In previous work heater traces were milled into the chip; however, to improve the work-flow a procedure for laser patterning of the heater traces was developed. An alignment jig, fabricated from 1.5 mm PMMA (Acrylite FF), consisting of a 30 mm by 40 mm rectangular cut out with a known offset was used to hold the chips in position for laser patterning. A resistive heater, of design to be discussed in § 2.2.3, was patterned through the aluminum film using 10% power, 30% speed, 1000 pulses per inch, and focused at 1.5 mm (surface). Asymptote code for complete chip manufacture and heater patterning may be found in Appendix B.

Cutting and patterning using CNC milling and especially laser ablation introduces built-in stress to the PMMA which if not released will frequently result in cracking upon exposure to solvents. A one hour anneal at $98°C$, between two glass plates was used to relieve the stress and prevent cracking. The pressure from the glass plates was necessary due to the anisotropic nature of the PMMA. Due to the extrusion process, the PMMA structure is different along its two axes and without pressure, the chips would bow during the annealing process as a consequence of the unequal contraction rates along both axes. Subsequently, 10 mm of the acrylic paint protecting the aluminum film was removed from the bottom of the chip using a Kimwipe soaked in acetone and pressed against the surface for 80 seconds before gently wiping downwards to remove the paint and expose the aluminum. Longer exposure or higher pressures were shown to damage the aluminum film. Using a 1.10 mm diameter drill bit, a hole was drilled through the chip to allow for pressure equalization. Finally, chips were cleaned with Sparkclean (concentration of approximately 5 g/L) to remove any debris or milling oil residue, then rinsed with DI water.

Figure 2.1: Image of a complete chip from PMMA side of the chip. The well and moat are visible in the center with heater traces protruding to the right. The sensor is located directly below the well and is obscured in this image. Electrical contact is made to the right edge of the chip using a zero insertion force (ZIF) socket (TE Connectivity 2-531020-8-ND, Digikey).

2.2.2 Holder and Optical Assembly

To hold the chip and provide a platform for optical interrogation a two-piece aluminum holder was fabricated. The bottom of the holder was a solid block of aluminum with a 30 mm by 30 mm by 1.25 mm recess cut in at one end. Identical

O-rings with a 12 mm inner diameter were placed on the top and bottom portions of the assembly. These hermetically sealed around the outside of the moat and the volume enclosed was pressured to 12 psi (lab pressure line regulated using Clippard Instrum. Lab Inc. type 1175-2 regulator). Additionally, the top part of the holder contained a LED and lens assembly for an Ocean Optics spectrometer allowing for the microheater to be optically interrogated. The well was illuminated by a 465 nm LED (Kingbright WP710A10QBC/G, Digikey) which was filtered by a short pass filter (Roscolux 338 Sapphire Blue short pass filter). The LED was aligned with the well at an angle of 15° from vertical. Fluorescence was collected using an aspheric lens (Philips, CAY 046) focused 400 μm inside the reaction volume and filtered using a 3 mm thick long pass filter (Evonik Acrylite 2CO4 GT long pass filter). The aspheric lens focused light onto an lens assembly (Ocean Optics 74AH) which was connected to a spectrometer (Ocean Optics USB4000) by a $600\mu m$ diameter optical fiber (Ocean Optics). The long pass filter, which has a cut-off wavelength of approximately 500 nm, attenuates light from the LED while allowing fluorescence from Rhodamine B (a fluorescent dye used for calibration) or Ssofast Evagreen (a fluorescent intercalator used to tag DNA) to be transmitted through. This lowers the baseline noise measurement in the system and improves the signal to noise ratio.

Electrical connection to the chip was made by contacting the exposed aluminum traces with a zero insertion force (ZIF) connector (TE Connectivity 2-531020-8-ND, Digikey). The appropriate leads were connected to a LabJack U6 microcontroller. The use of the LabJack allowed for the control of drive and sensor currents and voltages from Python scripts run off a PC as discussed in § 2.2.4.

2.2.3 Heater Design

The heater design (seen in Fig. 2.1) was developed and simulated by Professor Christopher J. Backhouse and consists of an approximately radially symmetric ring heater design with an integrated temperature sensing trace. This design varies from other reports in several ways and addresses several deficiencies noted by Almassian *et al.* such as replacing external temperature sensors with an integrated sensor directly below the reaction volume. Additionally, by varying the depth of the moat surrounding the well, the heating and cooling rates may be varied negating the need for active cooling.

When considered using a first principles model of thermal capacitances and resistors, the time constant associated with heating and cooling of the system may be estimated to be $\tau = RC$ [1]. The thermal behaviour of the system is dominated by three factors: the thermal capacitance of the well (C_w), the radial thermal resistance (R_r), and the vertical thermal resistance (R_v). All may be approximated in the following manners.

$$R_r = \frac{1}{2\pi kt} ln \frac{r_o}{r_i} \tag{2.1}$$

$$R_v = \frac{h}{k\pi r_o^2} \tag{2.2}$$

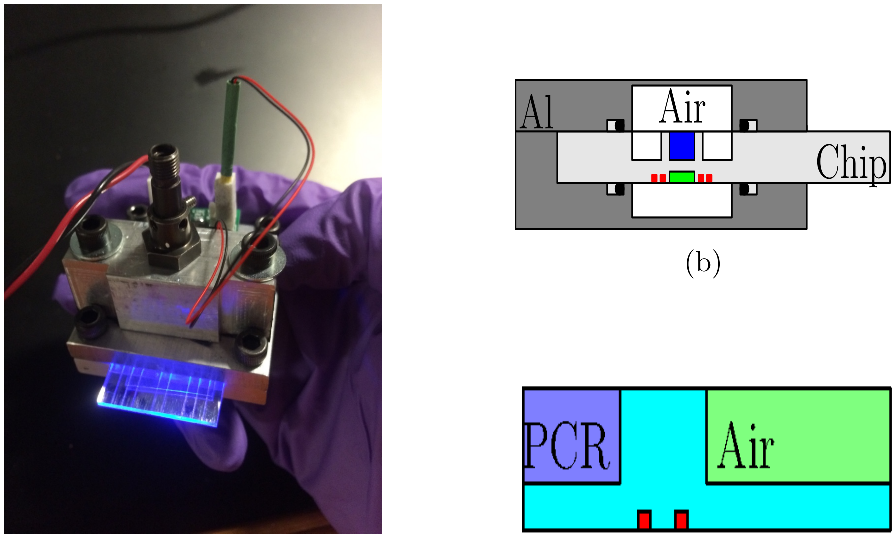

(a)

(b)

(c)

Figure 2.2: **(a)** Assembled experimental apparatus with microheater chip extending from the front and illuminated internally using LED with a connector for an optical fiber extending from the top. **(b)** Schematic (not to scale) of assembled experimental apparatus showing aluminum holder (grey) holding the microheater. The air gap and moat (white) are sealed by o-rings (black). In middle of chip heater traces (red) and sensor (green) are shown. The PCR well is shown in blue. Electrical connections are performed using ZIF socket to the right edge **(c)** Expanded side view focusing on main structures for thermal modelling. The PCR well is shown in blue and is separated from the air moat (green) by the PMMA wall. The heater traces are shown in red at the bottom.

$$C_w = \rho_d c_p \pi r_i^2 h \tag{2.3}$$

In this approximation, the filled well and PMMA walls are assumed to have the same thermal properties with a radius r_i of 2.5 mm and a height h of 1.5 mm. The PMMA thickness in the moat region has thickness t equal to 0.5 mm and radius of r_o equal to 6 mm with a thermal conductivity k. The PMMA is assumed to have a density of ρ_d and specific heat capacity of c_p. These values are summarized Table 2.1.

R_r	$1393.4K/W$	k_w	$0.6W/Km$
R_v	$66.3K/W$	k_p	$0.2W/Km$
C_w	$0.052J/K$	$\rho_{e,Al}$	$2.8 \times 10^{-8}\Omega m$
R_e	30Ω	ρ_w	$1000kg/m^3$
τ_h	$3.4s$	ρ_p	$1200kg/m^3$
τ_c	$72.2s$	c_w	$4180J/Kkg$
t_{tc}	$40s$	c_p	$1466J/Kkg$
α_{Al}	$0.0039K^{-1}$		

Table 2.1: Parameters for Thermal Modelling of Microheater. Based on table produced by Professor Christopher J. Backhouse.

To first order, the primary cooling pathway is radial conduction of heat from the well through the PMMA due to its thermal conductivity exceeding that of air by an order of magnitude. Based on these considerations, the time constant for cooling may be calculated to be $\tau_c = C_w R_r$ which equals approximately 70 s. The well will cool according to Newton's Law of Cooling: $T = T_0 + \Delta T e^{-t/\tau}$ with T_0 equal to 93° C. ΔT is equal to -28° C as the final temperature is 65° C rather than the boundary condition which is room temperature. Thus, the cooling time may be calculated to be approximately 40 s.

For heating, it is assumed that radially uniform Joule heating occurs in the heating traces beneath the PMMA well and that vertical conduction through PMMA dominates any conduction into air (based on difference in thermal conductivity). Thus, the time constant for heating is determined by the relation $\tau_h = C_w R_v$ which is approximately equal to 3.4 s. After 5 τ, the temperature will be within 1 % of its final value and assumed to be constant at the high set temperature after approximately 15 seconds. The capacitance is proportional to the volume of the well while the resistance is inversely proportional to the thickness. Thus both time constants are proportional to r_i^2. The power input from Joule heating is $P = I^2 R_e$ where I is the electrical current and R_e is the electrical resistance of the heater trace. Using Newton's Law of Heating, once at steady state, the set temperature as a function of room temperature (T_0) is given by $T - T_0 = PR_r = (I^2 R_e) R_r$. The resistance and capacitor models for heating and cooling are seen in Fig. 2.3.

To heat the well, current is passed through the two semi-circular heater segments highlighted with the red arrows in Fig. 2.5. Passing through the centre of the two hemispheres is a zig-zag trace which narrows substantially underneath the well. As

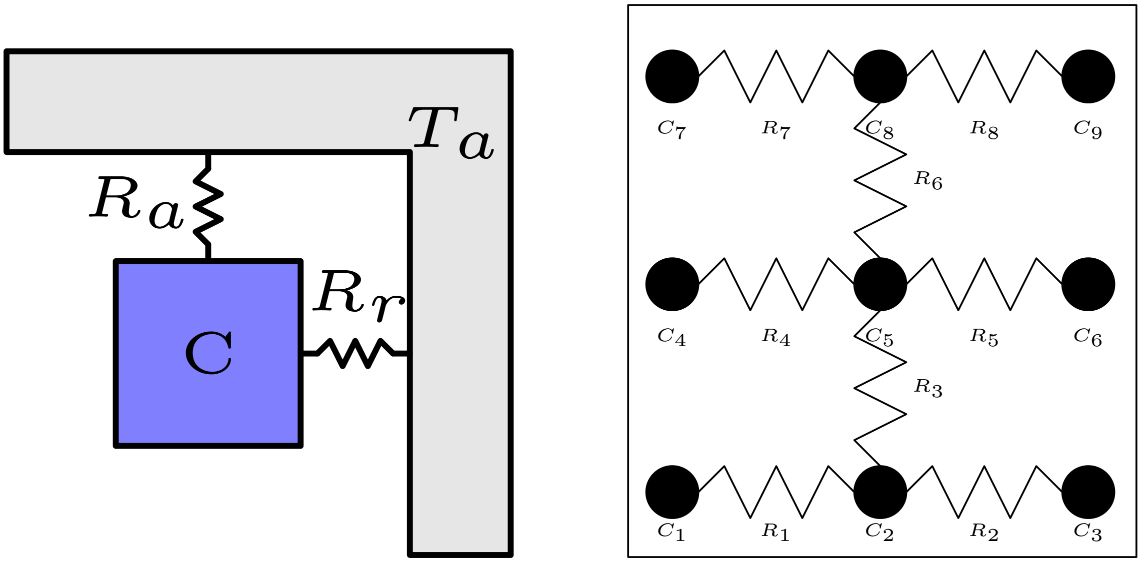

(a) (b)

Figure 2.3: **(a)** In cooling, the behaviour is modelled as a thermal capacitance C being dissipated by conduction through thermal resistance R_r (radial conduction through PMMA) and R_a (vertical conduction through the air). **(b)** In heating, the thermal behaviour of the PCR well is dominated by the heat introduced using Joule heating at point C_2. Thermal flow is depicted as a network of distributed capacitances and resistances in both the axial and radial directions. The PCR well is given by C_5.

the resistance of a film is inversely proportional to the width the narrowest region, located directly underneath the well, will dominate the trace resistance. This results in the temperature sensor returning data for the region of interest rather than an average of the temperature of the entire chip. The resistance of this trace was monitored using a 4-point resistance measurement in which $200\mu A$ of current was passed through the traces highlighted by the blue arrows in Fig. 2.5 and the voltage drop across the green arrows monitored using the LabJack. Four point resistance measurements were used to remove the effects of contact resistance and allow for accurate monitoring of the film resistance changes by separating the current source from the voltage measurement. A current of known magnitude is passed through the sensor using the $200\mu A$ source on the LabJack which induces a voltage drop across the sensor. Simultaneously, the voltage drop is monitored using the differential voltage measurement function between two of the analog inputs on the LabJack. Based on the measured resistance and thermal coefficient of resistivity (determined using the procedure described in § 2.3), the temperature could be determined using Eq. 2.4 where R_0 and T_0 are the resistance and temperature at room temperature respectively and α is the thermal coefficient of resistivity.

$$R_h = \alpha R_0 (T - T_0) \tag{2.4}$$

Based upon this measured temperature, the current through the heater trace

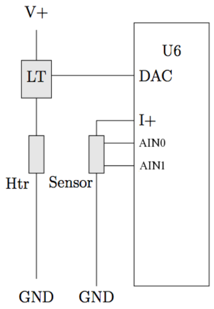

Figure 2.4: Electrical circuit for microheater control. The DAC is the analogue output of LabJack U6 (denoted U6 in figure) which is used to control the current through the microheater (Htr) by adjusting the output of the LT3092 current source (LT). The LT3092 was powered using a DC power supply. The 200 μA current source for the sensor is denoted by I+ and the two analogue inputs to the U6 for differential voltage resistance measurements are denoted AIN0 and AIN1. Figure modified from one prepared by Dr. Christopher Backhouse.

adjusted using a controller developed by Dr. Christopher Backhouse, which adjusted the current by an amount proportional to the error in the temperature. As may be seen in Fig. 2.4, the current through the heater was set by the analogue voltage output of the LabJack U6 connected to an LT3092 (Linear Technology) 2-terminal programmable current source. Although this preliminary controller satisfied the necessary criteria, a more complex proportional-integral-derivative (PID) controller might allow the set temperature to be achieved in a faster and more accurate manner. As many be seen in Fig. 2.4, the current through the sensor trace was provided by the LabJack 200 μA current source and the voltage drop across the sensor was measured by two analogue inputs on the LabJack.

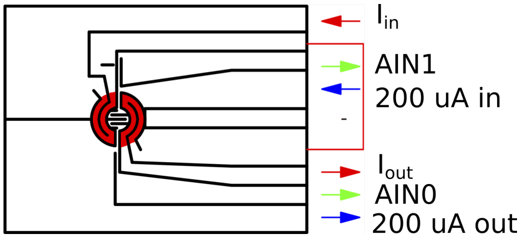

Figure 2.5: Microheater schematic where red arrows indicate heater electrical connections with the solid red line being the electrical jumper between the two components. Blue arrows indicate connections for the 200μA current source and green arrows indicate connections for the differential voltage measurements of the sensor trace. Black lines indicate path along which laser cut through the aluminum film separating the traces.

2.2.4 Control Code

A Python code was written to control the microcontroller and cycle the temperature. This code was initially written by Professor Christopher J. Backhouse and was modified and extended by Collin Tittle. Full code is presented in Appendix A; however, the main functionality will be discussed herein. To use this code the following packages must be installed on the system: Python 2.X, Libusb, PyUsb 1.0, Numpy, Pylab or Pyplot, and the LabJack U6 utility [19] [20] [21] [22] [23] [24].

The basic functionality of the code is as follows. As described in § 2.2.6, the PCR consists of holding the reagent volume at one of two temperatures for a specific time, then rapidly changing to the other. Within the code, two temperatures (THigh and TLow) are defined and the control code achieves both temperatures using independently tuned proportional-integral-derivative controller (PID). This feedback algorithm adjusts the current flowing through the heater traces based upon the magnitude (proportion), integral, and derivative of the error between the current and set temperatures. The weighting factors for each term may be independently adjusted for different applications to prevent events such as overshoot or oscillations. Each factor must be tuned independently and will change if heater design is changed.

The basic PID control algorithm is shown below which controls the current flowing through the heater traces based upon the temperature determined from the sensor trace resistance. This algorithm also calls the *FastRecord* function which collects spectra using the Ocean Optics spectrometer. Basic tuning of the PID was performed which achieved satisfactory performance of the heater; results are shown in § 2.4. This function also sends the current and temperature data to be stored using the *DVec.append* function.

```
def  PID(timehold=10,tempset=90.0,Ihold=10, TimConi=10, TimCond=10, Kp =
    2.0, Igain=1.0):
   """ PID control algorythm """
   global SpecNum;
   ESum = 0.0;
   CloseEnough = False;
   LastError = tempset - PresentTemp();
   DVec = [];
   #FastRecord();
   for i in range(int(timehold)):
      FastRecord();
      Error = tempset - PresentTemp();
      if (abs(Error) < 0.01):
         CloseEnough = True;
      if (CloseEnough==True):
         ESum = ESum + Error;
      if (TimConi > 0.001):
         Iset = Ihold +\
             Kp*( Error + ((ESum*Igain)/TimConi) +
                 (TimCond*(Error-LastError)));
      else:
```

```
            Itest = Ihold + Kp*( Error + (TimCond*(Error-LastError)));
            if Itest <= 220:
               Iset = Itest;
            else:
               Iset = 220;
            #Iset = Ihold + Kp*( Error + (TimCond*(Error-LastError)));
         x = (time.time(),Iset,tempset,tempset-Error,SpecNum);
         DVec.append(x);
         IactualCT = CTCurrentMeasure(); #returns current from previous set
         print("Time: %5.3f Step: %2d Iset: %2f TSet: %2f Temp: %5.3f Sum:
             %5.3f Der: %5.3f Spec: %d Imeasure: %f" %
            (x[0],i,x[1],x[2],x[3],ESum,Error-LastError,SpecNum,IactualCT));
         LastError = Error;
         SetCurrent(Iset);
   return(DVec);
```

The *TsetHigh* function passes the values for the high temperature to the PID control algorithm. A similar function called *TsetLow* is used to set the low temperature

```
def TsetHigh(initialcycle=False):
   global IScHigh;
   print("TSetHigh");
   if (initialcycle == True):
      tHigh = int(tHighinitialheat);
   else:
      tHigh = tHighPID;
#timehold=10,tempset=90.0,Ihold=10, TimConi=10, TimCond=10, Kp = 2.0)
   rv=PID(timehold=tHigh,tempset=THigh,Ihold=IHighhold,TimConi=0.0,
       TimCond=3.0, Kp = 4 );
   return(rv);
```

The *FastRecord* function records and saves an optical spectrum using the Ocean Optics spectrometer.

```
def FastRecord():
   global HomeDir, SpecNum;
   #d.getFeedback(u6.BitStateWrite(0,1));
   res_on = oo.getSpectrum();
   #d.getFeedback(u6.BitStateWrite(0,0));
   np.savetxt(("%s/Spectra/Spectrum%1d.txt" % (HomeDir,SpecNum)),res_on);
   SpecNum += 1;
```

The code below cycles the heat through 40 cycles of high and low temperatures.

```
for Ncycle in range(40):
   print("Now in cycle %d " % Ncycle);
   rv = TsetHigh(initialcycle=InitialHeating); FullDataVec.extend(rv);
```

```
        InitialHeating = False;
    rv = TsetLow(); FullDataVec.extend(rv);
```

2.2.5 Simulations

Two-dimensional simulations using a lumped thermal model implemented using the open source finite element program Fenics were performed by Professor Christopher J. Backhouse [25]. In the simulation, the boundary condition of the edge of the moat was held at room temperature, with Joule heating in the resistive traces. As the aluminum manifold is 3.66 mm above the PCR well, vertical heat conduction and convection are approximately equal, thus an effective heat transfer coefficient of 10.556 $\frac{W}{Km^2}$ was used. Although the distance to the bottom of the chip is smaller, the same heat transfer coefficient was used which results in a slight overestimation of the heat lost through the bottom of the chip. As can be seen in the simulations in Fig. 2.6, the dual ring heater design is expected to produce a radially uniform temperature distribution with only slight increases directly above the heater traces. The thermal isolation of the inner well can subsequently be tuned by changing the moat depth. With the 1 mm deep moat depth, thermal isolation was high enough that with a 30Ω heater resistance, only 60 to 70 mA of current was needed (0.1W) which is capable of being supplied from any USB port. This isolation was low enough though that the well temperature could be lowered on a time scale of approximately 30 seconds which is a relevant time scale for a rapid PCR.

2.2.6 Polymerase Chain Reaction

The polymerase chain reaction (PCR) is one of the most important tools for medical diagnostics as it allows for the rapid and targeted amplification of genetic material. A successful PCR is dependent on two components: an accurate understanding and implementation of the biochemistry, and precise thermal cycling of the reaction volume using accurate instrumentation. The development and optimization of a PCR reaction for the amplification of exon 2 of the human *HFE* gene, a sequence associated with hereditary human haemochromatosis, was done by Chanele K. Polenz using commercially available thermocyclers. To implement the PCR onto the microheater the following workflow was used. Microfabrication of heaters was performed in the Backhouse Lab and the PCR reaction was set up in the Glerum lab using the reagents in Table 2.2. The microheater wells were then filled and sealed using AB1170 PCR tape (Absolute qPCR plate seals, ThermoFisher Scientific). Chips were then transported back to Backhouse Lab, sealed into the chip holder, and thermal cycling was initialized. A hot start Taq polymerase was used to inhibit polymerase activity until after an inhibiting antibody was denatured from the polymerase in the initial long melting stage; however, as good practice, quickly moving from well filling to thermal cycling (less than five minutes) was targeted.

To set up the PCR reaction the following reagents (Table 2.2) were combined in a microfuge tube. Standard biological handling protocols such as ethanol sterilization

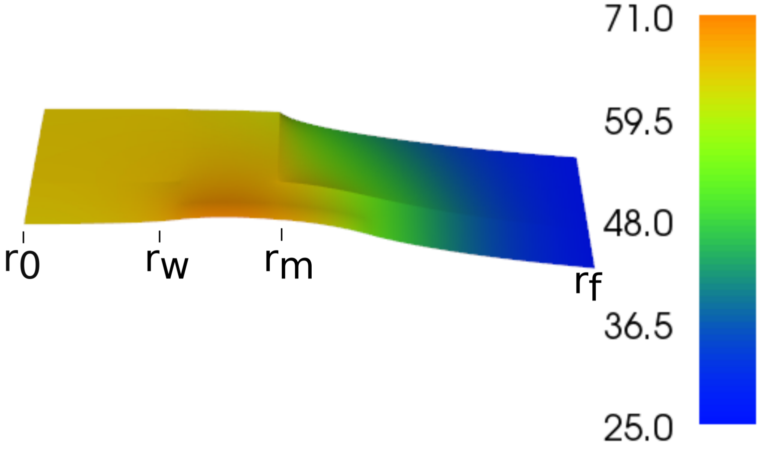

Figure 2.6: 2D simulation of microheater. The well is centered at r_0 in the bottom left corner of the simulation and extends outwards to r_w . Within that region it can be seen that the thermal uniformity is within ±0.5°C. In the heater region (r_w to r_m), a slight temperature increase may be seen due to the proximity to the heater traces. In the region of the well and remainder of the chip (r_m to r_f) cooling, as expected, to match the fixed boundary condition of 25°C at r_f may be seen. Simulation performed by Professor Christopher J. Backhouse.

of all surfaces prior to handling and proper pipette technique were followed in all circumstances. The microheater well was filled with $10\mu L$ of reagent.

Component	Final Conc. in 25 μL	Volume Added (μL)
PCR Grade Water	-	1.42
SsoFast EvaGreen Supermix (2X)	1X	12.50
BSA(100X)	2μg/μL	0.50
Primer F: HFE_a_H63D_F(20μM)	900nM	1.13
Primer R: HFE_a_H63D_R_2(20μM)	900nM	1.13
gDNA(15.0ng/μL)	5.0ng/μL	8.33

Table 2.2: Summary of PCR reagents and concentrations for genetic amplification

The microheater discussed in § 2.2 was used to thermally cycle the reaction volume using the protocol seen in Table 2.3.

At elevated temperatures, the double-stranded DNA melts apart forming single stranded DNA allowing for amplification in the subsequent step. When the temperature is lowered to the annealing temperature of 65°C, the DNA primers bind to their complementary, specific locations on the single-stranded DNA. Additionally at this temperature, since it is a two-step PCR, the Taq polymerase will attach at the primer location and begin adding new bases in the 5' to 3' direction creating

Step	Time (minutes)	Temperature (°C)
1	2:00	93
2	0:40	65
3	0:40	93
4	Go To 2	39X

Table 2.3: Thermal set points and hold times for optimized PCR reaction.

a new double-stranded segment of DNA. As the thermal cycling is repeated, the quantity of DNA increases exponentially. Accurate thermal control is necessary as if the annealing temperature is too high no binding between the primer and DNA will occur resulting in no amplification. Primer dimer formation (the attachment of primers to one another rather than the template DNA) is a possible by-product if the annealing temperature is too low. Another possible outcome of a low annealing temperature is simply insufficient Taq activity resulting in little amplification. If the melting temperature was not high enough, separation of the DNA will not occur, preventing the subsequent annealing and if the melting temperature overshoots, it is possible to boil the mixture causing irreversible damage to the reagents.

2.2.7 Modes of Failure

Before application to PCR was possible, several existing modes of microheater failure had to be addressed. To ensure that the AB1107 PCR tape remained sealed to the chip, the chamber above the well (see Fig. 2.2b for region labelled 'Air') was pressurized to 12 psi. However, this pressure was sufficient to crack the chips if a pressure gradient between the top and bottom existed. To address this challenge, a second O-ring was placed underneath the chip in a recess and a hole was drilled through the chip in the moat region. The pressure equalization hole described in § 2.2.1 through the moat region of the chip was sufficient to equalize the pressure on the top and bottom of the chip and following this implementation no failures of this type were observed.

Another cause of stress-induced cracking originated from the anisotropic grain structure of the extruded PMMA used to fabricate the mirror. The consequence of this is that during annealing, the chips would contract in differing amounts along the x-axis and y-axis, which resulted in bowing. When the bowed chips were clamped in the holder, the stress would induce cracking in the chips. This issue was successfully addressed by annealing between two glass plates with heavy steel weights resting on top to prevent any bowing of the chips.

Nominal aluminum film thickness was observed to vary from 50 nm to 200 nm based upon an assumed value for the resistivity of the film. Based upon known trace dimensions and four-point resistance measurements, the nominal thickness was approximated using the assumed value. In thinner films, cracks in the aluminum traces at constrictions were observed. This is likely due to the high current density gradient at these points. This caused cracking of the trace and the circuit to become open. This problem was addressed by selecting sheets of mirror with thicker aluminum films, annealing chips to remove any pre-existing stress, and flaring the trace designs to remove the constrictions and decrease the current density gradient at those points.

Above a threshold current, of approximately 120 mA, cracks in the aluminum traces at constrictions were observed. This is likely due to the high current density gradient at these points. This caused cracking of the trace and the circuit to become open. This problem was addressed by limiting the heater current, annealing chips to remove any pre-existing stress, and flaring the trace designs to remove the constrictions and decrease the current density gradient.

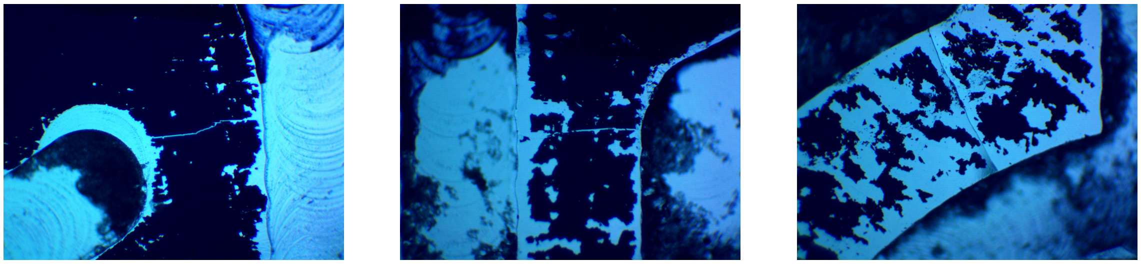
(a) Crack 1 (b) Crack 2 (c) Crack 3

Figure 2.7: Three examples of chip failures due to cracking. It can be seen that all occur laterally across the traces at constrictions in the trace where the current density gradient is high.

2.3 Calibration

The temperature sensor was calibrated by determining the temperature coefficient of resistivity (TCR, α). An improved process was developed for monitoring the chip in an oven as it cooled to determine the TCR. The chip was embedded within an aluminum block and held at 95° C for 2 hours using an oven (Fisher Scientific Isotemp Lab Oven, 13-247-737G). Subsequently, the oven was turned off and the chip was allowed to cool slowly over the course of 12 hours to room temperature. Due to the large thermal mass of the block, intimate thermal contact between the chip and the block, and slow cooling time (12 hours), it was assumed that the aluminum block and chip would be in thermal equilibrium. To record the temperature of this block, a temperature sensor (LM35, Texas Instruments) was placed within the aluminum block as well. The sensor was connected to a LabJack U6 which powered the unit and recorded the temperature output. As described in § 2.2.3, the sensor traces were contacted using a ZIF socket which was connected to the LabJack and differential resistance of the sensor was recorded in the same manner. A representative cooling curve may be seen in Fig. 2.8.

In prior work to calibrate the heater by Dr. Christopher J. Backhouse, the relationship between the decreasing fluorescence of Rhodamine B with increasing temperature was used, much as in [1]. The well was filled with $10\mu M$ Rhodamine B in 1X Tris-Borate-EDTA (TBE) buffer and illuminated with the LED. As in [1], the

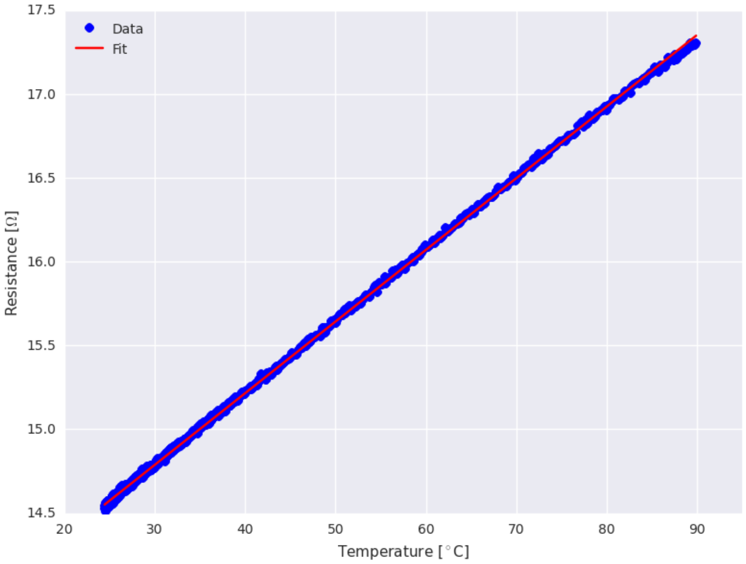

Figure 2.8: Cooling curve of microheater for TCR calibration. As expected, a linear relationship between temperature and resistance was observed with a TCR of $0.002944K^{-1}$

relationship between temperature and fluorescence was monitored using the Ocean Optics USB 4000 spectrometer. As seen in Fig. 2.9, the temperature determined from Rhodamine B fluorescence accurately tracked the sensor temperature throughout the thermal cycling.

2.4 Results

Prior to performing the PCR with the microheater, the PCR was validated using a BioRad CFX96 qPCR machine. This commercial machine performed the thermal cycling necessary for genetic analysis as well as melt curve analysis of the products. Melt curve analysis is a technique by which the fluorescence is monitored as a function of temperature. Based upon DNA length and which bases are present the temperature at which the double-helix melts apart and fluorescence decreases will vary. The melt peak is identified as the maximum of the derivative of the melt curve taken with respect to temperature. In Fig. 2.10, a single melt peak is visible indicating one product. As well the melt temperature agrees with the expected value for *HFE* exon 2. These findings were confirmed using gel electrophoresis much as in Fig. 2.11a. Obtaining consistent results using the BioRad CFX provided a solid benchmark against which subsequent trials may be compared.

After successful optimization and validation of the PCR on the BioRad CFX, with the materials used for microheater fabrication (done by Chanele K. Polenz), implementation on the microheater platform was performed. As the molecular biology of the reaction had been validated, and thermal simulation and calibration had

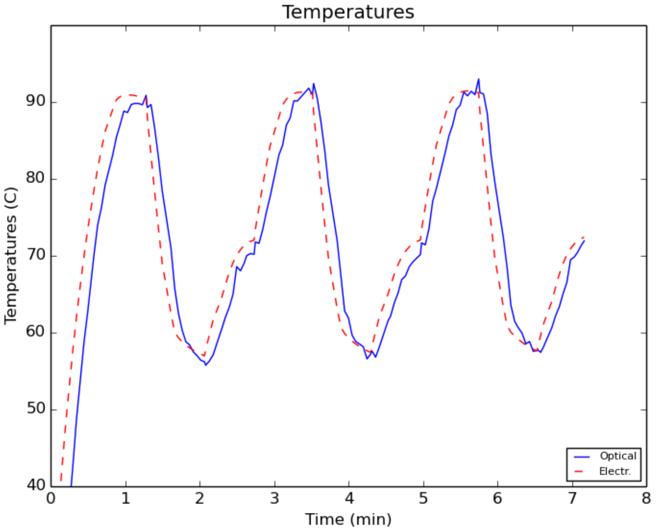

Figure 2.9: Utilizing the well-known relationship between the temperature of Rhodamine B and its fluorescence, the temperature of the well was tracked [1]. The electrical temperature was tracked using the TCR of the sensor. As expected the optical temperature may be seen to track the electrical temperature with a slight delay as the thermal mass of the well takes longer to change than that of the sensor. Data collected by Dr. Christopher J. Backhouse.

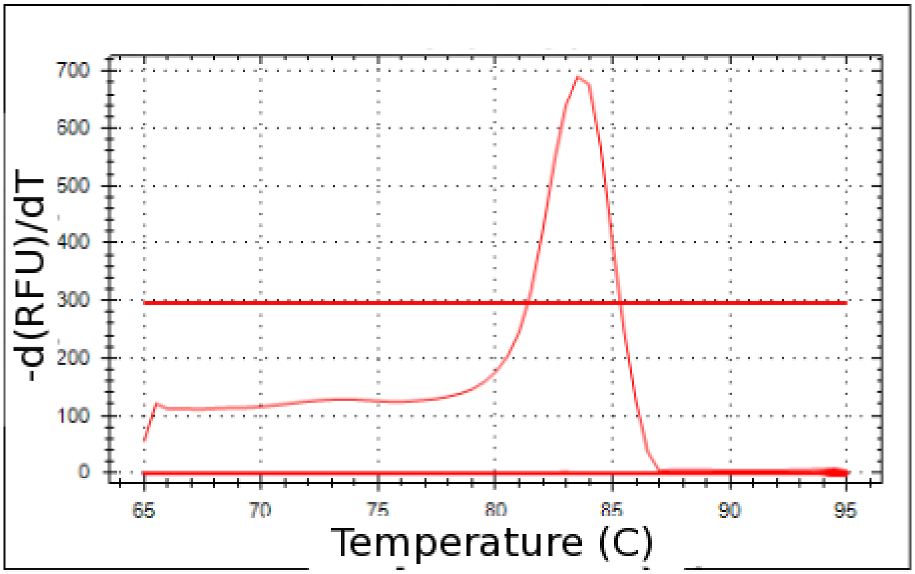

Figure 2.10: Derivative of melt curve from PCR performed on BioRad CFX. The melting temperature is seen to be 83.5° with only one product peak being observed. The melt temperature corresponds with the predicted temperature for the 112 bp long HFE exon 2 product. This demonstrates a successful PCR with targeted amplification being performed and the validity of the reaction conditions.

been performed (§ 2.2.5 and 2.3), similar experimental results might be expected.

After completion of the thermal cycling, the PCR products were analyzed using melt curve analysis and gel electrophoresis as was done for the PCR products from the BioRad in Fig. 2.10. In Fig. 2.11b, the melt curve analysis of the microheater product is shown in which two peaks can be seen. The larger peak with a melt temperature of 82.5°C agrees within 1°C to that of Fig. 2.10 indicating that these may be the same product. The second peak has a melt temperature of 75.5°C which suggests a second product. For further investigation, gel electrophoresis was performed as seen in Fig. 2.11a. The strong band at approximately 112 ± 10 bp agrees with the BioRad product (gels not shown) and the anticipated length of the PCR (based upon PCR design). The band in Fig. 2.11a at approximately 75 bp may be the result of primer-dimers and is the likely origin of the second melt curve analysis peak.

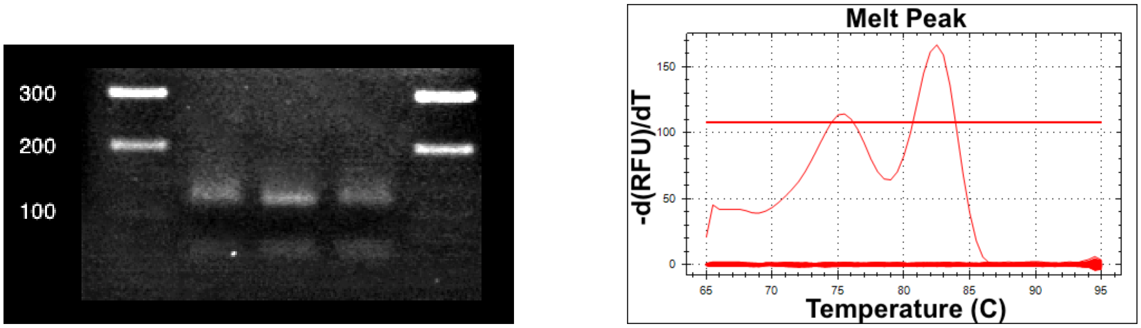

(a) (b)

Figure 2.11: **(a)** A five lane gel in 2% agarose with 0.5 X TBE buffer at a field of 5.6 V/cm. Outer lanes are size standards with bands at 100, 200 and 300 base pairs. The three central lanes containing samples from three runs with the microheater show a product at the anticipated length of 112 ± 12 bp and an unexpected second band at approximately 75 bp. This second band may be attributed to the presence of a primer dimer **(b)** Melt curve analysis of same product as in **(a)**. The presence of two peak in the melt curve analysis indicates two products. The higher peak at 82.5°C is within one degree of the CFX product seen in Fig. 2.10 which also had a product length of approximately 112 bp from gel electrophoresis. The second peak indicates a second shorter product which may be the second band at approximately 75 bp seen in **(a)**.

Spectra were collected for all trials performed using the microheater by the Ocean Optics spectrometer with the goal of demonstrating this application to qPCR. In many trials evidence suggested that this system was working, however consistent results between fluorescence increase during amplification and decreases during melt curve analysis were not able to be successfully demonstrated. The observation of bubble formation in the reaction chamber after thermal cycling in the microheater assembly may provide an explanation for the varying fluorescence intensity.

2.5 Discussion

After initial simulations indicated expected thermal uniformity with this microheater design, experimental results were used to validate the models and inform design modifications needed to address difficult to simulate materials deficiencies. After subsequent simulation of the finalized heater design, the system was demonstrated to follow the anticipated dynamic thermal behaviour and successfully perform genetic amplification. The broad functionality of the thermal design is demonstrated with the results of the electrical and optical calibration, and analysis of the PCR results. It is important to note that due to the low power consumption (0.1 W) the opportunity for integration with CMOS technologies exists. Additional modules such as fluid handling and capillary electrophoresis could be incorporated into this integration.

While this is a promising start, several further problems must be addressed for this microheater to be used in a modular manner. The first issue relates to the thermal uniformity of the system. The PCRs consistently showed the correct amplicon, but the presence of an artifact, likely a primer-dimer, seems to indicate that the temperature of some portion of the well is too low. As the temperature sensor at the bottom of the well indicates the temperature to be at or above the temperature used with the CFX, at which no primer dimers were observed, it is likely that a thermal non-uniformity vertically across the well may exist. Further trials with Rhodamine B should be performed to validate the temperature uniformity. The moat depth may be adjusted to decrease the thermal losses and improve thermal uniformity as well. The implementation of a three-dimensional simulation rather than a two-dimensional one could provide important guidance for any modifications in this regard. While LED excitation and fluorescence detection allowed for calibration with Rhodamine B and provided preliminary results of fluorescence increase during amplification, consistent qPCR and melt curve results were not able to be achieved. Efforts to minimize bubble formation in the reaction chamber should be investigated as well as validating the collection efficiency of the new optical module. Using flexible optical components such as the Ocean Optics spectrometer for real-time quantification of genetic amplification performed on a low-cost module would represent a significant advancement in the field.

In conclusion, it may be seen that a thin-film microheater was designed and fabricated using rapid prototyping technologies, and with the integrated sensor and low-cost materials addressed many of the issues discussed by Almassian *et al.* in the introduction. In addition to fabrication development, tuning of the PID controller was performed and microcontrollers were used to implement Python control codes. The application of this system to genetic amplification using the polymerase chain reaction allowed for the development of molecular biology skills while demonstrating an important point-of-care application for this technology. A similar design philosophy will be applied to the fabrication of next generation electronics using molybdenum disulfide in the following chapter.

Chapter 3

Molybdenum Disulfide: Processing, Fabrication, and Characterization Using Rapid Prototyping Technologies

3.1 Introduction

In the previous chapter, thermal control of microliter volumes of biological reagents was demonstrated using rapidly prototyped fabrication technologies. A similar design philosophy will be pursued in this chapter as the processing, fabrication, and characterization of electronic devices fabricated from two-dimensional materials are investigated.

The discovery of graphene by Novoselov and Geim in 2004 commenced an immense research push into the properties and applications of two-dimensional materials [26]. A specific family of two-dimensional materials are called transition metal dichalcogenides (TMDs). These materials are of the form MX_2 where M is a transition metal element (Groups 3 to 12 of the periodic table) and X_2 is a chalcogen (S, Se, or Te) with molybdenum disulfide (MoS_2) being one of particular interest due primarily to its thickness dependent direct bandgap [27]. MoS_2 has been identified by many as a promising candidate material for next generation electronics both because of its direct bandgap and the potential for metal-insulator transistors (MITs) to occur in this material [28]. MITs (also called Anderson transitions) are a transition between metallic and insulating properties; this transition is highly desired for switching applications such as transistors due to the extremely high on/off ratio. A demonstration using highly doped MoS_2 in a dual-gated transistor design by Radisavljevic and Kis showed the metal-insulator transition in monolayer MoS_2 and a metal to semiconductor transition in the liquid phase was demonstrated by Chou *et al* [29] [30]. Monolayer and few-layer MoS_2 has been applied to a variety of situations such as gas sensors, p-n junctions, inkjet printing, transistors, and as a catalyst in the hydrogen evolution reaction ([31] [32] [33] [34] [35]).

The pursuit of next-generation electronics to replace our highly developed silicon infrastructure is normally the realm of low throughput and expensive, but high precision, clean room fabrication technologies. However, as discussed in the previous chapters these technologies are generally incompatible with a rapid, low-cost design process. In this work, rapid prototyping technologies such as laser fabrication of electrodes and sonication were used for processing and characterization of MoS_2.

3.1.1 General Properties

MoS_2 can be found in one of several crystal structures, with the thermodynamically stable structure being the semiconducting 2H phase (unless otherwise specified it should be assumed that this is the form being referenced). In bulk, 2H MoS_2 possesses a 1.29 eV indirect bandgap, however when exfoliated the bandgap progressively shifts towards the 1.9 eV direct bandgap present in monolayer [36]. This direct bandgap makes MoS_2 a promising candidate for electronic applications such as transistors, where direct bandgap materials are preferential to indirect materials (such as Si). A phase of MoS_2 exhibiting metallic characteristics, called 1T, has also been characterized and many important applications have been shown and will be discussed later.

3.1.2 Sample Preparation

MoS_2 has been prepared by various techniques such as mechanical exfoliation ([37], [38], [39], [40], [41], [42]), chemical vapour deposition (CVD; [43], [44], [45]), lithium intercalation which produces the 1T phase of MoS_2([4], [46], [47]), and liquid phase exfoliation (discussed below). In a recent review, Zhang *et al.* identify five advantages of liquid-phase exfoliation. The first is that low-cost precursors such as molybdenite powder may be used rather than pristine technical grade crystals. Second, the techniques can be readily scaled to large-scale production and device manufacture. Thirdly, as will be discussed later, MoS_2 nanosheets can be separated based on size and thickness to have desired properties isolated. Fourth, as they are already in solution, functionalization and hybridization are easier. Finally, nanosheets in solution can be deposited on any substrate in contrast to the high substrate dependence of CVD techniques [27]. This idea was further supported by the following quote from a review on liquid exfoliation of layered materials by Nicolosi *et al.*, "Liquid exfoliation allows the formation of thin films and composites, is potentially scalable, and may facilitate processing by using standard technologies such as reel-to-reel manufacturing"[48]. Thus it may be seen that liquid phase exfoliation is a preparation technique compatible with rapid prototyped processing of MoS_2.

The local minimum of the potential energy distribution of a solid immersed in a liquid is minimized when the surface energies are equivalent [27]. According to Halim *et al.*, the surface energy of MoS_2 is approximately 35 mJ m^{-2} and thus 1-methyl-2-pyrrolidone (NMP) has proven to be an effective solvent due to its closely matching surface energy [49]. Coleman *et al.* have effectively demonstrated the use of NMP and probe sonication to produce mono and few layered MoS_2 nanosheets

[50]. Using an identical technique Lee *et al.* produced MoS_2 nanosheets with an average diameter of $1\mu m$ and thicknesses varying from 3 nm to 17 nm [51]. Resistivities of 214 Ω cm and mobilities of 6.2 and 6.3 cm^2 V^{-1} s^{-1} for positive and negative bias respectively were also measured [51]. Recently, the mechanism behind the success of NMP exfoliation has been explored in greater detail. Gupta *et al.* observed that the presence of trace amounts of water in a primarily NMP solvent plays a critical role. Water molecules were observed to passivate dangling bonds on Mo terminated edges which enhanced the stability of the dispersion and prevented chemical degradation of the sheets [52]. Jawaid *et al.* also identify the importance of water in NMP for exfoliation. When desiccated NMP in an inert atmosphere was used, exfoliation yield was observed to greatly decrease. They identified the presence of a reactive species formed through the reaction of NMP, H_2O, and O_2(g) which oxidized sheet edges creating Coulombic repulsion between sheets which disrupted bonding and enhanced stabilization [53]. Spontaneous exfoliation of MoS_2 in solutions of NMP and H_2O_2 was observed by Dong *et al.* and it is likely that this is related to the effects discussed by Gupta and Jawaid [54] [52] [53]. A variety of other additives and solvents have been used to exfoliate MoS_2 such as sodium cholate ([3], [5], [55]), HPLC grade isopropanol ([56]), combinations of an alcohol and water ([57], [58], [49]), and even pure water ([59]).Using sodium cholate as a additive, Backes *et al.* successfully related the absorption spectrum to the nanosheet size distribution for MoS_2 [3]. Seven settling fractions were observed with a correlation between the settling fraction and spectral features; this topic will be discussed further in § 3.4.1. Similar UV-Vis spectra were observed by Forsberg *et al.* for MoS_2 suspensions in pure water [59].

One common method of solvent selection has been to use the Hansen Solubility Parameters (HSP) to optimize the concentration of ethanol/water and IPA/water mixed solvents [58] [49]. Zhou *et al.* determined the optimal concentration of ethanol and water to be 40% ethanol and 60% water by volume which they subsequently confirmed experimentally [58]. Halim *et al.* used Young's equation (Eq. 4.1) to determine the surface energy of mixtures of IPA and water with the objective of finding a mixture with a surface energy matching that of MoS_2. They concluded that a concentration between 10 and 30% IPA would optimize the solvent-solution interactions [49]. It should be noted that neither of these reports observed any photoluminescence, which is widely regarded as an important benchmark for the presence of monolayered MoS_2. Recently Bernal *et al.* used a combination of 70% isopropanol (IPA), 30% water (by volume) as a solvent for probe sonication of MoS_2. Using this mixture, photoluminescent nanosheets were observed and were confirmed to be monolayer and few-layer sheets by AFM imaging [57].

3.1.3 Film Formation

Using clean room techniques, individual flakes of MoS_2 may be individually examined both optically and electrically. However, to examine electrical characteristics using rapid prototyping methods, the individual flakes must be assembled into films. Lee *et al.* formed MoS_2 films by vacuum filtration of nanosheets onto nitrocellulose membranes and subsequently dissolving the membrane using acetone [51]. They subsequently examined the electrical behaviour using interdigitated electrodes (IDE), which will be further discussed below. Cunningham *et al.* used the Langmuir-Blodgett technique to form films of MoS_2 on the surface of water (taking advantage of the hydrophobic nature of 2H MoS_2) and subsequently transferred the films to samples of indium tin oxide (ITO) coated glass using dip coating [56].

3.1.4 Characterization

Electrical connection to semiconducting MoS_2 films is commonly done in one of two ways. In a method pioneered by the Chhowalla Group at Rutgers, metallic 1T MoS_2 was used as an intermediate contact between semiconducting 2H MoS_2 and metal electrodes. When semiconducting MoS_2 is contacted with metal electrodes, such as the interdigitated electrodes used by [51], high resistance Schottky contacts are formed [46]. The use of metallic 1T MoS_2 contacts has been demonstrated to have Ohmic-like behaviour and contact resistance as low as $200\Omega\mu m$ [46]. Low resistance ($300\Omega\mu m$), ohmic contacts have also been observed using degenerately Nb doped MoS_2 with an undoped MoS_2 channel [60]. Liu et al. demonstrated the application of graphene as an ohmic contact to MoS_2 with minimal contact resistance [61]. It was hypothesized that with a finite density of states, the Fermi level of graphene is readily tunable by a gate potential for near-perfect band alignment. By combining this result with the demonstration by Lin *et al.* of laser-induced graphene in polyimide films, interdigitated graphene electrodes were fabricated and used to contact MoS_2 for what is believed to be the first time [62]. This will be discussed in greater detail in § 3.3.

Several standard techniques exist for the characterization of MoS_2 nanosheets. Optical characterization in the form of absorption and photoluminescence spectroscopy has led to many important observations. Backes *et al.* noted a relationship between the absorption spectrum and the thickness of liquid phase exfoliated MoS_2 nanosheets [3]. This empirical relationship is discussed further in the absorption section, however, it utilizes peak positions to determine the average nanosheet diameter and thickness. As it is an empirical relationship, it may be susceptible to any differences in experimental setup from their apparatus and should thus be used with additional validation. Photoluminescence is a commonly used technique for characterization of MoS_2 nanosheets as it is strongly quenched as they trend from monolayer to bulk [36]. Additionally, peak position may be used to directly extract the layer number [36]. Near unity photoluminescence quantum yield has been demonstrated by [63] and photoluminescence has been observed in mechanically exfoliated, chemically exfoliated, and ultrasonically exfoliated MoS_2, thus making it a useful metric for comparison between techniques [36][4][64].

Electrical characterization of MoS_2 provides important knowledge of the mobility and defects present in the lattice structure [56] [51]. Information on the traps present, which may be related directly to variations in processing, can also be obtained through electrical characterization. Zhu *et al.* observed two types of traps in CVD MoS_2, M-type (mid-gap) and B-type (band edge), however, the temperature at which the lifetimes were recorded could not be found, although the temperature ranges of the other experiments in the paper were reported to be between 4 K and 400 K[45]. Type B traps were observed to have a time constant of 10^{-4} to 10^{-5} s and a density of 10^{14} $eV^{-1}cm^{-2}$. Type M traps were observed to have a time constant of 10^{-7} s and a density of 10^{12} $eV^{-1}cm^{-2}$. The type B traps were observed to have an activation energy of approximately 0.15eV. According to Hong *et al.* in 2015, the formation energy of a sulfur vacancy was found to be 2.12 eV, two sulfur vacancies were 4.14 eV, and a molybdenum vacancy was 6.20 eV [65]. Using a technique called deep level domain spectroscopy (DLDS), Arrhenius plots may be formed which relate to the activation energy of traps present in MoS_2 much as was done for semi-insulating indium phosphide by [66].

3.2 Sample Processing

The technique for sample preparation described within falls under the class of liquid phase exfoliation, however, it differs in several key respects from the traditional implementation. The primary difference between the work done by the Coleman group ([51] [56] [5]) and our methodology was that they tended to use high powered probe sonication or mechanical shear exfoliation while gentle, short term sonication was used in this work with the hope of producing large, undamaged nanosheets, rather than small diameter sheets produced in the above mentioned works.

As detailed in the complete procedure in Appendix C, a ground molybdenite powder with an average grain size of approximately $3\mu m$ (MolySlip Moly Powder - Technical Grade Molybdenum Disulfide) was combined with a solvent in a microfuge tube and sonicated for between 360 and 1500 seconds depending on the solvent (see Table 3.1). All solvents used were technical grade and ordered from standard scientific chemical suppliers (details in Appendix C). While many solvents were tested, the primary solvent used was a mixture of 25% IPA, and 75% MilliQ water. For comparison with literature, NMP was additionally used as this is the primary solvent used by the Coleman group.

After sonication, settling of particulates into four distinct bands over varying time scales was observed. The current model used is that sonication creates a black MoS_2 suspension which is comprised of several fractions. These fractions settle at differing rates creating visually different regions which appear to also possess different physical properties which will be discussed below. The most important parameters for this process are the settling times of the different fractions (τ_1, τ_2, τ_3). It appears that the primary factor dictating the variation in these parameters is the solvent used as this determines both the degree of exfoliation and zeta potential effects which will electrostatically suspend particles in solution.

The times in Table 3.1 have been determined based on a combination of both quantitative and qualitative results. τ_0 denotes minimum sonication time and is determined by the time required for the sample to appear uniformly jet black and evenly suspended under qualitative observation. The first settling fraction to appear is a rapidly forming silver layer at the bottom of the microfuge tube which is

Sonication and Settling Parameters for Solvent Exfoliation of MoS_2					
Solvent	τ_0 (s)	τ_1 (mins)	τ_2 (mins)	τ_3 (hrs)	$V_{abs}(\mu L in mL)$
100% IPA	360*	5	30	8+*	200 in 2.8
75/25 IPA/Water	360*	5	30	8*	200 in 2.8
50/50 IPA/Water	360*	5	30	6*	200 in 2.8
25/75 IPA/Water	360	5	30	6.3 ± 0.4	200 in 2.8
100% Water	540*	2	10	2*	200 in 2.8
Chloroform	720*	1	2	0.3*	500 in 2.5
Heptane	1500*	1	2	0.3*	1000 in 2
Acetonitrile	360*	10	30	6*	200 in 2.8
NMP	360*	20	45	8+*	200 in 2.8

Table 3.1: τ_0 denotes sonication time. τ_1 corresponds to the settling time required for the silver layer to form. τ_2 refers to settling time required for black layer to form from micron or barely submicron visible particles settling out of solution. τ_3 refers to the settling half life defined by Eq. 3.1. τ_1, τ_2 and τ_3 all start at t = 0 (ie. sonication is completed). V_{abs} denotes the volume of sample in solvent required for absorption measurements. * denotes estimation rather than experimental determination.

likely attributed to unexfoliated, bulk MoS_2 with average particle sizes of several micrometers in diameter. This layer forms in the time up to τ_1 after sonication and after τ_1 has elapsed no further growth of the silver layer is observed. Subsequent settling is a black layer which is formed by a time τ_2 after sonication and is likely composed of large, perhaps partially exfoliated particles. Partially exfoliated particles may have sizes on the same scale as the wavelength of visible light. Due to this scatter dominates over reflection and the particles appear darker. Dynamic light scattering analysis of this fraction (discussed later), indicates a large particle size supporting this assertion. After this time no further growth of the black layer may be visually observed. τ_3 is defined in Eq. 3.1 as the settling half-life for the suspended nanosheets and has been determined experimentally for 25/75 IPA/Water using absorption spectroscopy; estimations have been provided for other solvents. Results from absorption spectroscopy measurements will be discussed in detail in § 3.4.1 however, for now, it will suffice to note that it can be used as a measure of the concentration of a species. Formally the term optical extinction spectroscopy should be used as both light absorption and light scattering are present in this system, however, simply absorption spectroscopy will be used. Fig. 3.1 shows the settling behaviour of 25/75 IPA/Water from which τ_3 was determined to be 6.3 ± 0.4 hours by using the Scipy curvefit package and fitting Eq. 3.1 to the data (code provided in Appendix A). A similar method was used by [59] to determine the settling constant however, the value reported herein is approximately one-quarter of that report [59]. This could attributed to differences in nanosheet size, solvents used, cuvette material, or handling procedures.

$$Abs_{\lambda=900nm} = C_1 e^{-t/\tau_3} \tag{3.1}$$

Between τ_2 and τ_3 no growth of the black layer is visible. Additionally, in this time period strong absorption and apparent photoluminescence (both to be discussed later) could be obtained. At any time between τ_2 and τ_3 it is possible to form a silver film from the supernatant using the procedure described in § 3.3. Films formed close to τ_3 were visually observed to be discontinuous and when formed on a graphene IDE (§ 3.3) no conductivity could be measured with a digital multimeter (DMM). However, multiple depositions could be performed to develop conductive films.

For optical measurements, a supernatant sample should be extracted between τ_2 and τ_3. While waiting longer for optical characterization will reduce the magnitude of noise from scattering off bulk particles, the standard extraction time used is $\tau_3/2$ hrs (3 hrs) for both 25/75 IPA/Water and NMP. This characterization time allowed for differences in solvent and sonication time to be observed. V_{abs} denotes the volume of sample in solvent required for absorption measurements and was determined based upon the volume of sample required to reach an absorbance value between 0.25 and 0.4 (depending on when extracted) at $\lambda = 900nm$, which is within the range recommended by the manufacturer. As an example with 25/75 IPA/Water, τ_0 produces a suspension, which when diluted with 200μL of the sample in 2.8mL of solvent, has an absorbance at 900 nm of 0.4 ± 0.1 Absorbance units. In such a suspension produced at τ_0, slight turbidity is visible with a faint yellow hue to the solution.

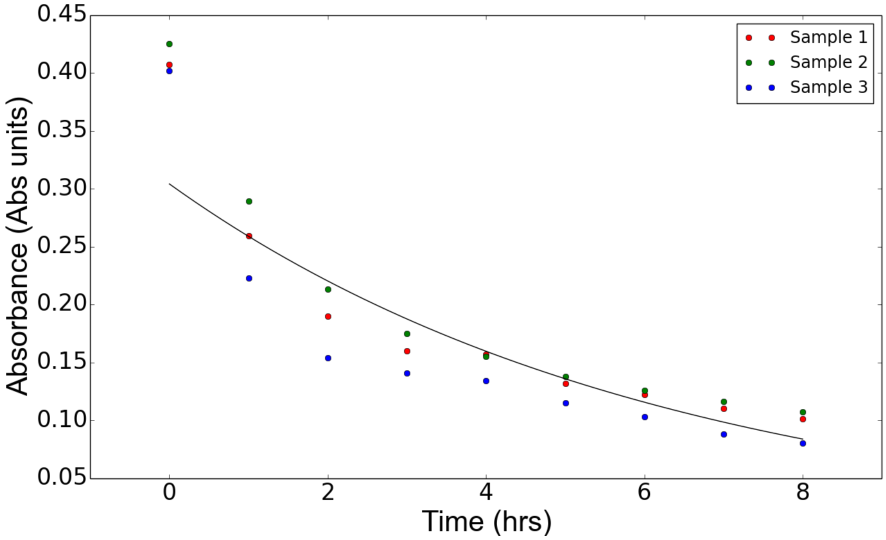

Figure 3.1: Absorption at 900 nm vs. Time for MoS_2 exfoliated in 25% IPA, 75% water. From this τ_3 was experimentally determined to be 6.3 ± 0.4 hours by fitting Eq. 3.1 to the data.

A complementary fabrication procedure using lithium intercalation and forced hydration separation to form MoS_2 nanosheets was used by our collaborator Dr. Michael Pope. This is a similar fabrication process to that used by Eda *et al.* which produces 1T metallic phase nanosheets [4]. Subsequent heat treatment has been shown to cause a phase change back to the 2H semiconducting phase which is

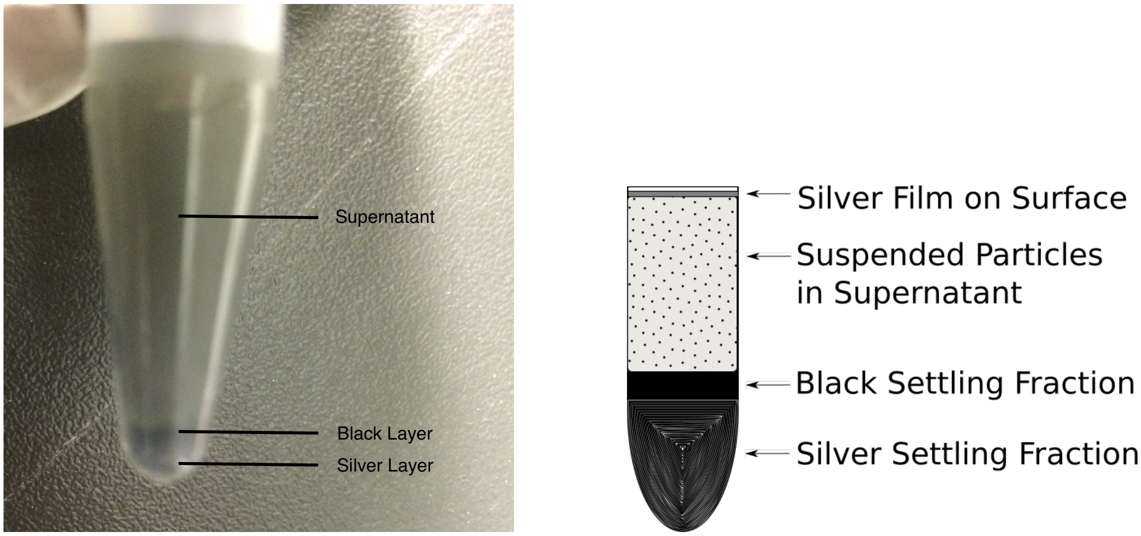

(a) (b)

Figure 3.2: Silver, black, and supernatant settling fractions of MoS_2 exfoliated in 25%IPA, 75% H_2O. A silver film is always present on the surface when the concentration of water is greater than or equal to 75%.

produced using liquid phase exfoliation [4]. Samples prepared by our collaborator will be referred to as Pope Lab samples for the remainder of this thesis.

3.3 Fabrication

3.3.1 Indium Tin Oxide/Carbon Electrodes

A standard challenge in electrical characterization is to contact samples without damaging or substantially changing their characteristics. In clean room fabrication electrodes are often lithographically deposited onto samples, however, such an approach is not conducive to rapid prototyping. To contact MoS_2 film samples on glass substrates, a fabrication procedure for conformal electrodes made from a heterostructure of carbon tape and indium tin oxide (ITO) coated plastic was developed. This allowed for electrodes to be adhered to samples prepared on glass substrates in a manner that minimized damage to the films.

The carbon tape, ITO electrode structures were fabricated using ITO coated polyethylene terephthalate (Adafruit, 1309, hereby denoted PET), 8 mm wide carbon tape (Ted Pella, 16073), copper tape with a conductive adhesive (Ted Pella, 16072-1), and 22 AWG copper wires. A 25 mm long strip of carbon tape was adhered to the ITO side of a 25 mm long by 10 mm wide section of PET. The pattern, designed in Asymptote and seen in Fig. 3.3a was cut through the carbon tape and ITO, leaving just the PET support intact. As the ITO has a very low resistance, the main source of resistance in this configuration is the vertical resistance through the carbon tape. Thus the effective series resistance is comprised of the vertical resistance through the carbon tape combined with the transverse resistance through the ITO to the contacts on the exterior. Each end of the structure is contacted by the adhesive copper tape which has negligible resistance relative to the rest of the structure. Wire leads are soldered onto the copper tape for reproducible contact with alligator clips. The electrode structure works as follows. A film would bridge the 100 μm gap between the positive and negative electrodes allowing for current to flow. The interdigitated design increases the length over which this occurs allowing for a detectable current to flow. In this case, the interdigitated design increases the length from 25 mm (width of ITO piece) to 408 mm.

There is a resistance inherent to the electrode structure which was measured by adhering a sheet of ITO, with a known sheet resistance of 50 Ω per square, to the electrode and measuring the resistance [67]. The resistance was measured to be $22.3 \pm 0.6 k\Omega$. As the ITO has such a low sheet resistance, most of the measured resistance was due to the electrode structure. This means that for materials with resistances lower than $22.3 \pm 0.6 k\Omega$, the series resistance of the electrode would dominate and little information about the sample resistance could be obtained. Thus the lower limit of detection was set at $22.3 \pm 0.6 k\Omega$ with the upper limit set at 500 MΩ (the maximum of the multimeter).

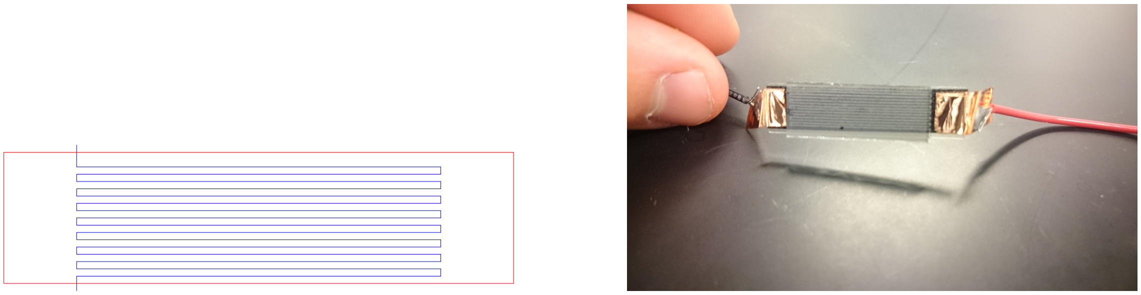

(a) (b)

Figure 3.3: **(a)** Asymptote schematic for IDE structure fabricated using ITO and carbon tape. 25 mm by 10 mm rectangular heterostructures of carbon tape on ITO were cut out using laser settings of 8% power, 10% speed, 1000 ppi and a focus of 0.1 mm along the red trace. Subsequently, the blue trace was cut through the carbon tape and ITO layer, leaving the PET support layer with laser settings of 20% power, 27% speed, 1000 ppi and a focus of 0.1 mm. The electrode spacing is a function of the width of the ablated cut which, for these parameters, is approximately 100 μm. Asymptote code is available in Appendix B.2.4. **(b)** Image of ITO and carbon tape conformal electrode. Copper tape contacted with wires are visible on the exterior. In the centre, interdigitated structures cut through the carbon tape are visible through a MoS_2 film. The conductive ITO layer is on the reverse.

3.3.2 Graphene Electrodes

An alternative electrode structure was developed based on the laser conversion of Kapton into graphene traces. For our purposes, 63.5 μm thick Kapton tape (Mc-

Master Carr 7648A34) was adhered to a glass microscope slide to provide a 25 mm by 25 mm surface for electrode formation. The IDE pattern, designed in Asymptote and seen in Fig. 3.4a was ablated into the tape using the laser settings of 9% power, 10% speed, 1000 pulses-per-inch, and a focus of 5 mm. The interdigitated region formed by this process is approximately 10 mm wide, with a center-to-center spacing of 1.75 mm. Closer traces are possible, however laser precision and the finite trace width limit the spacing. It should be noted that the stepper motor of the laser is quantized in units of 1/72 of an inch, also called a point ($357.2 \mu m$) and all CAD design should be done in points to prevent rounding errors in software which will produce offsets in the traces and has been observed to produce uneven spacing and shorts. To allow connection to electrical structures, a nickel pen (MG Chemicals 841-P, Digikey:473-1188-ND) was used to attached wires (copper 22 AWG) to the terminal edges of the electrodes. These wires could then be contacted with alligator clips or push connectors at negligible contact resistance.

The resistance of the carbon traces was determined by measuring the resistance of 2 cm long traces contacted with approximately 2 mm diameter circular nickel contacts. Three traces prepared using the above protocol had an average resistance of $877\Omega/cm$ with a standard deviation of $\pm 31\Omega/cm$. While this method is not a four point resistance measurement and thus contact resistance is included in the result, it is an accurate representation of the resistance which will be present in the system during data collection. This method allows for the rapid fabrication of contacts which have been observed to behave ohmically when contacted by MoS_2. A long-standing need for ohmic contacts to MoS_2 has been noted by the likes of Liu *et al.* and Chuang *et al.*, noted that graphene satisfied this criterion [61][60]. However, of the few contacts which have been produced to satisfy this criteria, all have relied upon complex microfabrication processes. The contacts produced using the above protocol represent a demonstration of rapidly-prototyped, cost effective ohmic contacts to MoS_2. When trying to drop cast films of MoS_2 onto the surface of the electrodes it was observed that the surface produced was highly hydrophobic. The contact angle of a $50\mu L$ drop of 25/75 IPA/Water in the interdigitated region of the array was observed to be approximately 130 ± 10 degrees which allowed the droplet to remain confined within this region. Using a densely packed interdigitated array and pure water, a contact angle close to 180° was observed and will be the focus of § 4.

3.3.3 Hydrophobically Confined Film Formation

As noted in the previous subsection, the graphene contacts produced through laser ablation are highly hydrophobic. It was subsequently observed that droplets of water could be confined within the hydrophobic regions. Droplet spreading could be controlled to within 5% by adjusting the electrode spacing and droplet volume. It was hypothesized that films could be formed using the hydrophobic contacts to confine a droplet of MoS_2 suspension from which the solvent would subsequently evaporate depositing the MoS_2 on the surface. The full procedure is located in Appendix C however, in short, a film could be formed from $50\mu L$ of MoS_2 in

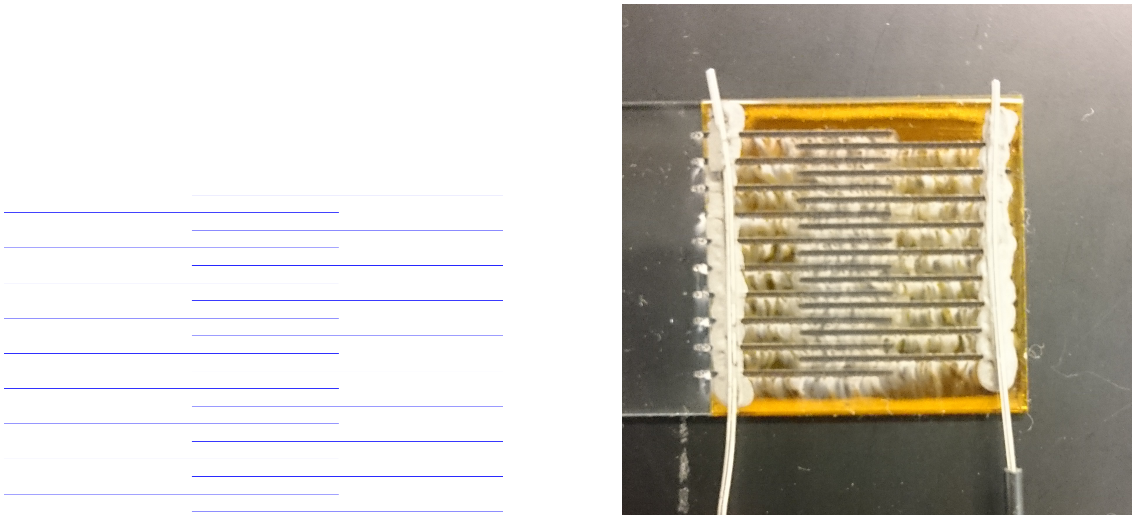
(a) (b)

Figure 3.4: **(a)** Asymptote schematic for interdigitated electrode structure cut into Kapton tape using laser settings of 9% power, 10% speed, 1000 pulses per inch, and a focus of 5 mm. This type of array would be used for film formation using the hydrophobic bubble deflation technique which will be discussed in the next section. Asymptote code is available in Appendix B.2.3. **(b)** Image of the electrode array with interdigitated graphene traces in the middle, contacted with nickel conductive ink on edges and wires for connection to measurement systems.

25 % IPA, 75 % water solvent at any time up to 6 hours after sonication. The same sonication method as discussed in the sample preparation section was followed, however, different settling times were used. It is important to note that settling times were optimized (perhaps incorrectly) for optical and electrical measurements separately. The standard time for extraction for film formation was 15 minutes after sonication as this was observed to form films conductive enough to be measured using either a digital multimeter (DMM) or a lock-in amplifier. While initially overlooked, this settling time likely means that the films were combinations of nanosheets and larger particles. The 50μL of sample was deposited over four interdigitated regions and solvent evaporation occurred over the course of 30 to 60 minutes. The films were reproducibly approximately 7 mm by 10 mm. Initially, the bubble would appear an optically uniform, translucent grey color with, what appeared to be, a homogeneous dispersion of nanosheets throughout the droplet. However, as may be seen in Fig. 3.5a, a film would begin to form on the surface soon after deposition. Starting from nucleation sites at the base, films were observed to grow upwards along the droplets surface much as can be seen in Fig. 3.5a with the centre of the droplet becoming progressively more transparent. Movement of unassembled nanosheets on the surface of the droplet appeared to be driven by currents caused by the Marangoni Effect from evaporating IPA. The film would eventually self-assemble to cover the entire surface of the droplet. As the water evaporated, the self-assembled film was lowered onto the electrode structure. At times a gap in the middle of the film was

observed indicating that insufficient MoS_2 was present in the sample to fully cover the droplet surface. Films were left for a 24 hour period to ensure that all solvent had evaporated before electrical testing.

Macroscopically the resulting films appear highly uniform as can be seen in Fig. 3.5b. Microscopically, variations are clearly visible as can be seen in Fig. 3.6. Also visible in Fig. 3.6 is clear confinement along the edges of the drop with no evidence of spreading past a confined perimeter.

The benefit of this technique is that the film self-assembles onto electrode structures providing easy electrical characterization with highly compliant electrodes. The weakness of this technique is that the electrodes are not optically clear making optical characterization, by techniques such as confocal microscopy, challenging. Additionally, solvent selection was limited to mixtures of water and IPA containing at least 75% water as the hydrophobic confinement properties cannot be leveraged without a water based sample. Lower concentrations of water were tested, however, the resulting droplets were observed to be distended and often breached the confinement of the electrodes resulting in inconsistent film formation.

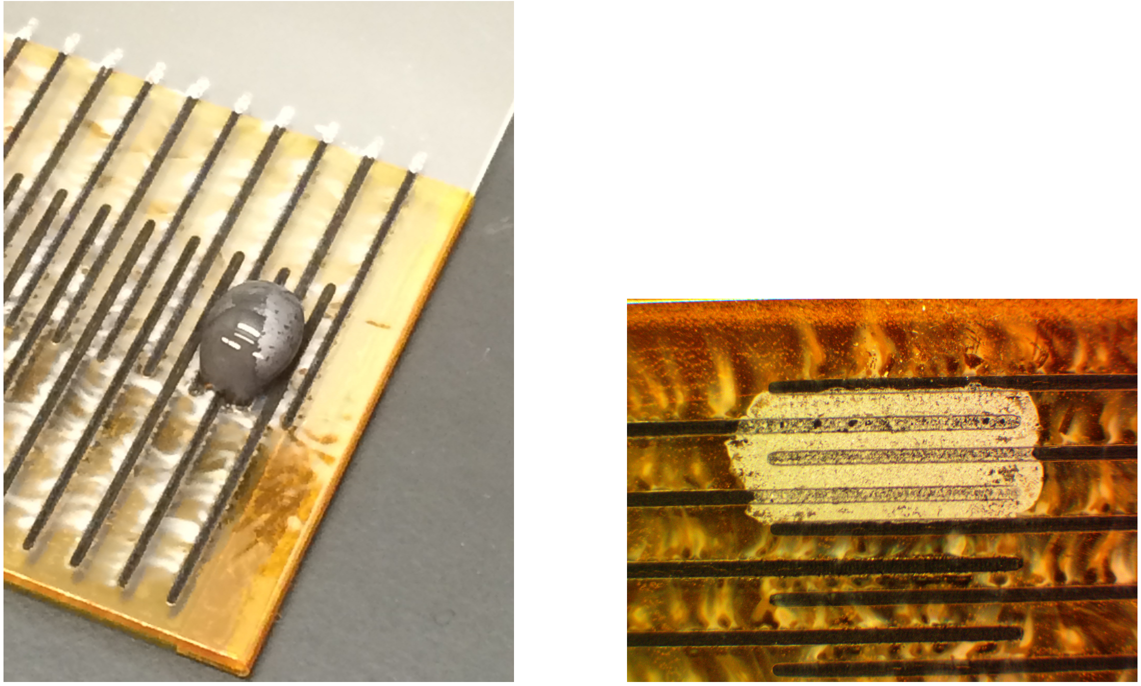

(a) (b)

Figure 3.5: **(a)** Self-Assembly of MoS_2 on the surface of bubble formed on hydrophobic electrode structure. The bubble is $50\mu L$ in volume and covers an area of 7mm by 10 mm ±0.5 mm. **(b)** MoS_2 film prepared from 25/75 IPA/Water using the bubble deflation technique. 50μL of the supernatant was applied to the electrodes 15 minutes after sonication and is likely comprised of both nanosheets and bulk particles. In calculating resistivity, it is assumed that all 5 electrodes are contributing equally. The sample is confined to the interdigitated region by the hydrophobicity of the array.

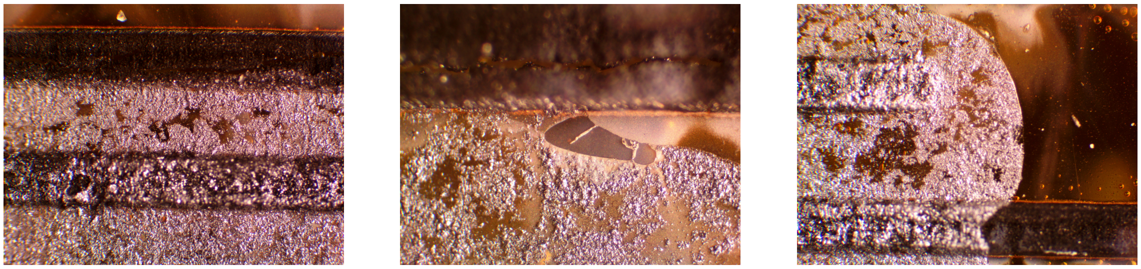

(a) (b) (c)

Figure 3.6: Microscopic images of MoS_2 films taken at 10X magnification with OMAX A35100U Microscope and AmScope Mu900 9 MP microscope camera. Clear confinement along all edges is visible with variations visible within the film. Based upon measurements taken using ImageJ [2], particles approaching 1μm in size were present along with smaller particles, the size of which could not accurately be determined using such methods.

By using this technique with the addition of a trace on the reverse side, it may be possible to fabricate monolithic transistor structures; however, high gate voltages would likely be necessary.

3.3.4 Langmuir-Blodgett Film Assembly

Much as was done by [56], MoS_2 films were formed on the surface of a beaker of water and subsequently transferred onto glass substrates using the Langmuir-Blodgett technique. A setup, seen in Fig. 3.7a was assembled to form the films. A small beaker was placed within a larger beaker to act as a support for the glass microscope slides. The beakers are filled with de-ionized water to a height of approximately 5 cm above the microscope slides. To decrease the amount of MoS_2 needed to form a satisfactorily dense film, a 'corral' was fabricated from laser cut PMMA using the pattern seen in Fig. 3.7b. This corral was floated on the surface of the water and used to confine the nanosheets to one region of the beaker. Samples of MoS_2 could be taken any time up to approximately 6 hours after sonication. As this technique was used primarily for confocal microscopy samples, and not electrical characterization, film conductivity was not the focus as it was in the previous protocol. Consequently, long settling periods were allowed with the technique. The film in Fig. 3.8 was formed at $\tau_3/4$ and the films examined under confocal microscopy in § 3.4.3 were formed at $\tau_3/3$. Thus, these films were more representative of the optical solutions than the films in § 3.3.3. A pipette was used to inject 400μL of MoS_2 supernatant into the corral one drop at a time. The pipette tip was kept approximately 5mm above the water surface and surface disturbances were allowed to disperse before the next drop was injected (injection rate of approximately 1 drop every 5 seconds). While 2H MoS_2 nanosheets are hydrophobic, a solvent concentration of approximately $> 90\%$ water (when IPA is the cosolvent) is necessary for film assembly on the water surface. Higher concentrations of IPA will result in nanosheets entering the liquid subphase rather than floating on the surface. The delay between drop injection combined with the large volume of water in beaker is critical to allow the IPA to diffuse throughout the volume and prevent the local concentration in the film formation region from exceeding the critical limit. Rapid injection of MoS_2 suspension failed to form films and it is hypothesized that the rapid injection resulted in a local IPA concentration which exceeded the critical limit and had a diffusion time constant which was long enough to permit the nanosheets to enter the liquid subphase rather than assemble on the surface. In the future, a smaller drop size (done using a smaller pipette tip or microtubing from a syringe) and/or varying the drop rate may be used to adjust the film formation dynamics. An additional modification would be to use a round corral which may remove the turbulent corner regions of the square corral where layer stacking has previously been observed. After injection of the sample, the film was left for one hour which allowed the nanosheets to assemble in a more uniform structure. This one hour period may have increased the nanosheet concentration of the film as larger particles may have settled out during that time as it § 3.2. The water from the larger beaker was then slowly removed so that the film was lowered onto the slides after which the samples were left in place for 30 minutes to dry before being transferred to an 80°C oven for 2 hours to dry further.

As can be seen in Fig. 3.8, highly uniform films could be formed. Compared to the hydrophobically confined film formation technique, this method has the advantage of using a variety of substrates. Additionally, MoS_2 suspended in different combinations of IPA and water may be used whereas the previous method deteriorated with higher concentrations of IPA due to weaker confinement. Optical characterization of films, such as confocal microscopy would be hindered by opaque graphene electrodes and thus this technique was required to prepare those films.

3.4 Characterization

3.4.1 Absorption Spectroscopy

A Shimadzu UV-1601PC UV-Vis Spectrometer was used for absorption spectroscopy characterization of the MoS_2 samples. Appendix C contains the complete procedure which will be summarized herein. Samples were diluted according to Table 3.1 before being transferred into cuvettes (polystyrene or glass depending upon compatibility) where they were left for 30 minutes before characterization. Solvent only cuvettes (blanks) were used to normalize the spectrum to the solvent absorbance to ensure that all features observed were sample specific. Subsequently, absorption spectra were collected from 300 nm to 900 nm in 1 nm intervals. Documentation for the Shimadzu specifies an uncertainty of 0.002 Abs units for each measurement which agrees with an experimental validation using a blank cuvette and sample-to-sample variations of MoS_2 samples were observed to be approximately 0.01 Abs units. It should be noted that while called absorption spectroscopy, this was truly optical extinction spectroscopy as both absorption and scattering from the MoS_2 particles was present. The resulting spectra were analyzed using Matplotlib and the Scipy analysis package; codes for which are provided in Appendix A.

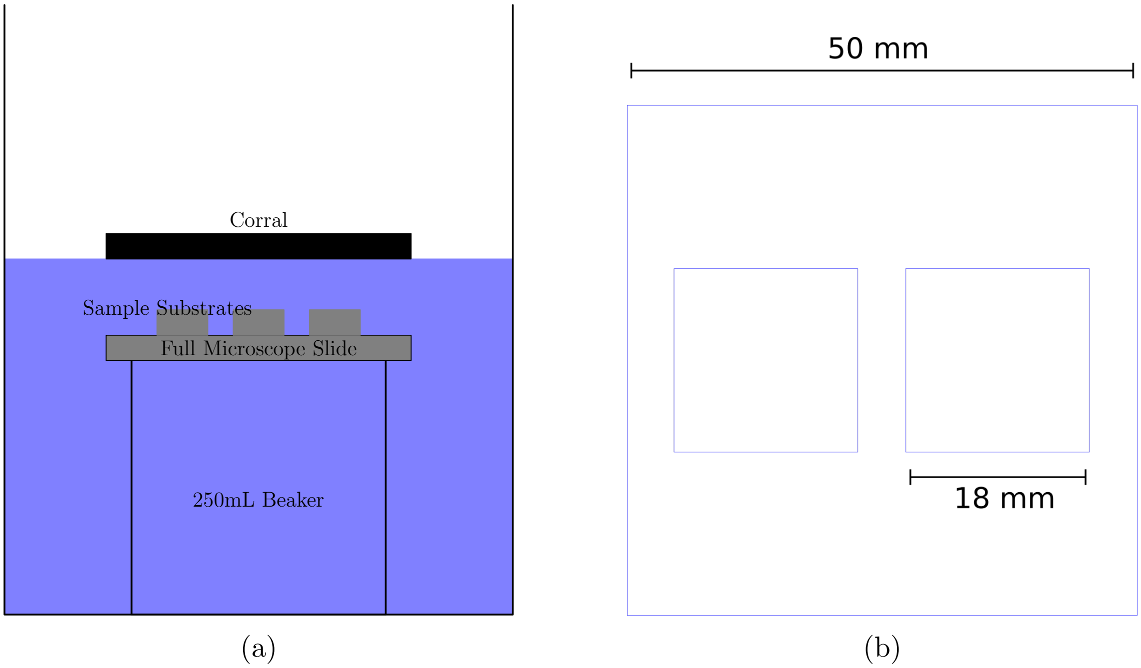

Figure 3.7: **(a)** Diagram of the experimental setup for formation of MoS_2 films using the Langmuir Blodgett technique. A 250 mL beaker is set within a large 1 L beaker. A standard microscope slide is used to bridge the top of the beaker and act as a platform for the small glass sample pieces. The beaker is filled with DI water from the reverse osmosis tap until the small beaker and glass substrates are submerged. A corral made from laser cut 1.5 mm PMMA (Evonik Acrylite FF) is floated on the surface to contain the MoS_2 sheets. The corral may be seen in Fig. 3.7b with Asymptote code in Appendix B. **(b)** Asymptote schematic for corral for Langmuir Blodgett like film formation. Two square regions have been cut from larger frame to contain nanosheets.

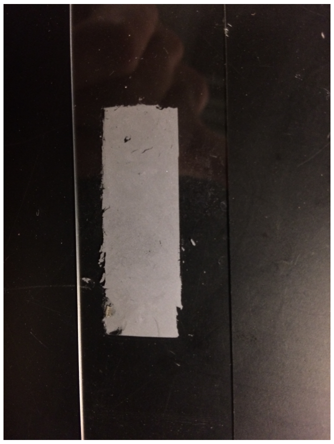

Figure 3.8: A film formed using the Langmuir Blodgett technique at τ_3=1.5hrs after sonication in 25% IPA, 75% water solvent.

Spectra for MoS_2 exfoliated in 25 % IPA, 75 % water, the standard solvent used, are shown in Fig. 3.9 at times from 30 minutes to 8 hours after sonication. When compared with a spectrum from the literature (Table 3.10) many similar features may be observed with a local minima at approximately 320 nm and a global maxima at approximately 450 nm. As was used in [5], all spectra will be normalized to the minimum at 320 nm. In our samples, a much smaller decrease in absorption is visible at longer wavelengths than in [5]. This may be attributed to scattering caused by larger particles remaining in suspension. Based upon the hypothesis that a heterogeneous distribution of particle sizes may be suspended in solution, the samples were allowed to settle for periods up to 8 hours and the spectra were monitored throughout. As can be seen in Fig. 3.9 minimal variation in peak position or amplitude is visible with time, however, absorption at long wavelengths does tend to decrease with time, possibly as larger particles settle and decrease the scattering cross section.

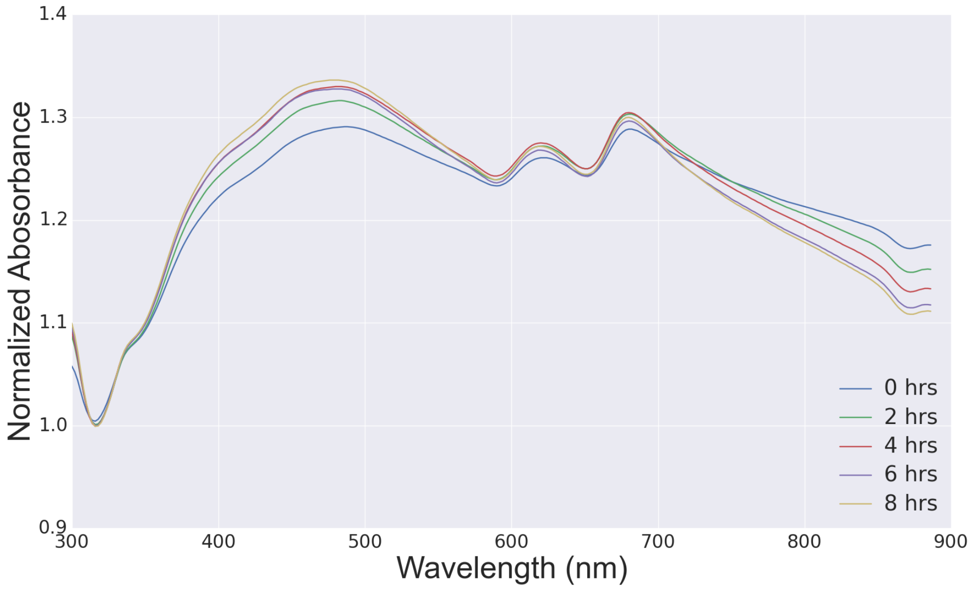

Figure 3.9: Settling time-dependent absorption spectrum of MoS_2 exfoliated in 25% IPA, 75% water. A change in the A peak position of less than 2 nm over the 8 hours was observed, perhaps indicating that the main absorbing species remains in solution for the entire interval. The extinction at longer wavelengths decreases with time which may indicate larger particles are settling from solution, similar to the spectra noted by [3].

An exciton is a quasi-particle formed from a bound electron-hole pair which orbit one another for a period before annihilating. As has been widely reported in the literature ([3] [4] [5]), the formation of certain excitons in MoS_2 correspond to peaks in the absorption spectrum. A broad peak at approximately 450 nm may be attributed to a combination of the C and D excitons [4]. The A and B excitons arise from transitions at the K point of the Brillouin zone and have a wavelength between 600 and 700 nm with the B exciton have slightly greater energy that the A [4]. Decay of these excitons may be observed as photoluminescence and will be discussed in § 3.4.2. Similarly the formation of the X exciton corresponds to an absorption minima between 300 and 350 nm [5] [3].

Based upon the criteria outlined by [4], the peaks in Fig. 3.9 between 600 and 700 nm were assigned to the A and B excitons. As per [4], the higher energy peak was assigned to the B exciton and has the closest agreement (12 nm difference in position). The lower energy peak centered at 680 nm was assigned to the A excition and differs from the reported value by 20 nm. Eda *et al.* noted that the peak positions of these two peaks were redshifted when thicker samples were examined [4]. The presence of thicker nanosheets in suspension may then explain the difference between the experimental and literature values. The C/D peak is centered around 476 nm. While Eda *et al.* reported this peak at 420 nm, Varrla *et al.* showed this peak position shifting up to 500 nm when samples containing large thick nanosheets were examined [4] [5]. This supports the hypothesis of thick nanosheets developed from the A and B exciton data and the assignment of this peak to the C/D exciton. Table 3.10 summarizes the literature and experimentally obtained peak values.

Peak	UV/Vis 1601	Lit	Curve Fit
A	680 nm	660 nm	681 ± 1 nm
B	622 nm	610 nm	623 ± 1 nm
C/D	476 nm	420-500 nm	484 ± 3 nm
X	320 nm	345 nm	320 ± 1 nm

Figure 3.10: Summary of spectral feature peak positions from the literature and determined experimentally with either the UV/Vis 1601 peak finding algorithm or a quadratic curve fit. All experimental values were obtained with solvents of 25% IPA, 75% water. The literature values for A, B, and X peaks are from Eda *et al.*, and the value for the convolved C and D peaks is from Backes *et al.* No uncertainties were reported by either. The UV/Vis 1601 peak finder does not return uncertainties either while the uncertainties in the quadratic fit were determined from the covariance returned by the Levenberg-Marquardt algorithm as detailed in the Scipy curve_fit documentation. Both Eda *et al.* and Varrla *et al.* have demonstrated that the redshifting of the A, B and C/D absorption peaks may be a consequence of thicker nanosheets [4] [5]

Absorption spectra in different solvents were taken at intervals varying from immediately after sonication up to 8 hours after sonication. The absorption spectra of MoS_2 exfoliated in IPA/Water mixtures, chloroform, heptane, acetonitrile, and NMP were all collected and based upon results from conductivity measurements, a 25/75 mixture of IPA and water was selected as a reference standard. The normalized reference spectrum of this solvent can be seen in Fig 3.9 over an 8 hour settling period. Based upon a comparison between the experimentally obtained spectra and those from the literature, similar features were observed for all experimental spectra. This allowed for peak assignments to be performed and are summarized Table 3.10.

As per the Varrla *et al.* absorbance was normalized to the X exciton absorption minima located at approximately 320 nm [3] [5]. In this experimental data, the minima appears at approximately 320 nm whereas, in several reports ([3] [5]), the minima appeared at 345 nm. This shift in minima position could be explained by several of the mechanisms discussed above for the A,B and C/D excitons. Peak identification was done by first identifying the peak value λ_{max} in the measured data. To account for noise, a quadratic curve was fit to the domain $\lambda_{max} \pm \delta$ using the Scipy curve_fit package which utilizes the Levenberg-Marquardt algorithm and the peak was extracted by the quadratic formula. The standard deviation on the peak location was returned by the Levenberg-Marquardt algorithm and was used for the error bars in Fig. 3.13. The value of δ was adjusted based on examination of the residuals to ensure that no diverging trends existed. This adjustment was a consequence of the differing solvent dependent peak shapes which may be a function of nanosheet population statistics in each solvent. The values of δ (in nm) which were used are shown in Table 3.11. It should be noted that while the peak assignments were made based upon similarity in feature shape with literature report values, the experimental peak positions listed in Table 3.10 could differ from the reported values in the same table by 12 to 56 nm. A possible explanation based on nanosheet dimensions will be discussed in the following paragraph. A different explanation could be based around solvatchromic shifts which, as noted by Mao *et al.*, could shift spectral features can be as large as 60 meV resulting in the excitonic peaks agreeing closely with the reported values [68]. Neither [3] nor [4] examined the spectra of nanosheets in water/IPA mixtures. In a study of MoS_2 nanosheets in pure water, A and B peak positions located at 674 and 612 nm respectively were observed [59]. These peak positions agree more closely with the experimental results than those mentions previously. When investigating water/IPA mixtures, [57] observed similar spectra, but with the A peak higher than the B, much as in Fig. 3.9. Based upon these results it can be concluded that there are a diversity of reports on peak positions and factors which may affect them, but the assigned experimental peak positions in this work are close to accepted values, and mechanisms have been proposed for differences.

Fig. 3.12a shows a quadratic fit used to extract the peak position of the A-exciton absorption maximum which, in this case, is 681±1 nm with the uncertainty calculated from the covariance returned by the Levenberg-Marquardt algorithm and detailed in the Scipy curve_ fit documentation. The point-by-point residuals are shown in Fig. 3.12b. A slight divergence at longer wavelengths can be observed, but overall the residuals appear randomly distributed about the mean. Fig. 3.13 shows the time-dependent peak positions extracted from Fig. 3.9 for A,B, and C/D excitons (all exciton peaks extracted in the manner described above) which can be seen to be decreasing with time. Based upon this analysis it may be suggested that due to the different approach used, and even though efforts were taken to settle bulk particles from solution, a heterogeneous suspension existed.

Both Eda and Backes have independently demonstrated the connection between nanosheet thickness and the peak wavelength of the A-exciton absorption peak for MoS_2 on SiO_2 and in suspension respectively [4] [3]. Peak position as a function of thickness may be seen for both in Fig. 3.14. Both curves appear similar in shape with a slight offset of approximately 0.01 eV which can be readily explained by a combination of differing solvents, substrates, and doping effects; all of which have been demonstrated to affect the absorption peak position. Superimposed on this image are the A-exciton absorption peaks from our samples of MoS_2. Varrla *et al.* developed a phenomenological model connecting the width and thickness of nanosheets exfoliated in NMP to the magnitude and peak position of the A and B exciton absorption peaks as can be seen in Eq. 3.2 and Eq. 3.3.

$$L(\mu m) = \frac{3.5Ext_B/Ext_{345nm} - 0.14}{11.5 - Ext_B/Ext_{345}} \tag{3.2}$$

where Ext_x is the absorbance value at either the B exciton peak or 345 nm.

$$N_{layers} = 2.3 \times 10^{36} e^{-54888/\lambda_A} \tag{3.3}$$

Using these equations and the peak positions at 0 hrs in Fig. 3.13 it is possible to approximate the nanosheet length to be approximately 350 nm and the thickness to be 26 layers. It should be noted that Eq. 3.3 is a phenomenological equation dependent on a sensitive exponential which can easily shift the number of layers and is likely highly dependent on the experimental conditions. A demonstration of this is that by changing the peak position assignment by 2 nm (the resolution of the spectrometer), the layer number could vary by 2 -5 layers in the range investigated.

Perhaps the greatest challenge in using absorption spectroscopy to characterize these materials results from the heterogeneous nature of the suspensions. Settling was used in an attempt to remove microscopic particles from the nanosheet suspensions, whereas both [4] and [5] used centrifugation to purify their nanosheet fractions and obtain more homogeneous mixtures. It is likely that based upon the changing absorption spectra seen in Figures 3.9 and 3.13, and complementary analysis techniques (ie. DLS discussed in § 3.4.5) that a heterogeneous dispersion of particles remained in solution even though efforts were taken to allow bulk particles to settle. The optical properties of such heterogeneous solutions are more difficult to characterize as they represent average properties of a diverse ensemble rather than one similar population. This may be an explanation for the presence of hints of monolayer production in the subsequent photoluminescence and confocal microscopy discussions while explaining the differences in absorption spectra from literature reported values.

A standard method for determining the optical band gap of a material is through the use of a Tauc plot [69]. In this method, plots of the form $(\alpha h\nu)^r$ vs. $h\nu$ are formed where α is the absorption coefficient, $r = 2$ for a direct band gap semiconductor, h is Planck's Constant, and ν is the frequency of the light. A clear linear regime should be visible indicating the onset of absorption as for direct band gap materials α is proportional to $\sqrt{h\nu - E_g}$ where E_g is the energy of the band gap. Thus for photon energies less than E_g, the real part of α will equal zero resulting in values for the y-axis of the Tauc plot equal to zero until $h\nu$ equals or exceeds the band gap energy. By fitting this linear region and determining the x-intercept, the energy of

Solvent	δ_A	δ_B	δ_C
Standard (25/75)	12	12	30
NMP	14	12	30
Acetonitrile	10	12	30
Heptane	12	12	30
75/25	12	12	30

Figure 3.11: δ parameters for curve fitting window size. Determined from an examination of trends in residual distribution.

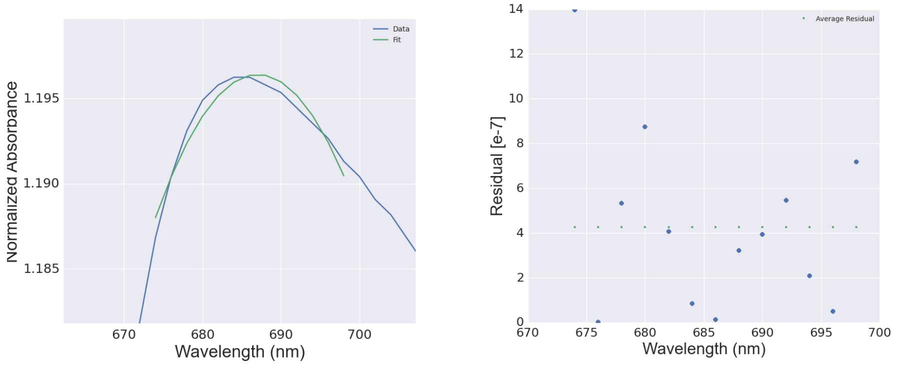

(a) (b)

Figure 3.12: **(a)** Absorption Spectrum for Exfoliated MoS_2 in 25 % IPA, 75% water with Quadratic Fit. **(b)** Residuals from Quadratic Fit as a Function of Wavelength with Peak at 681 nm.

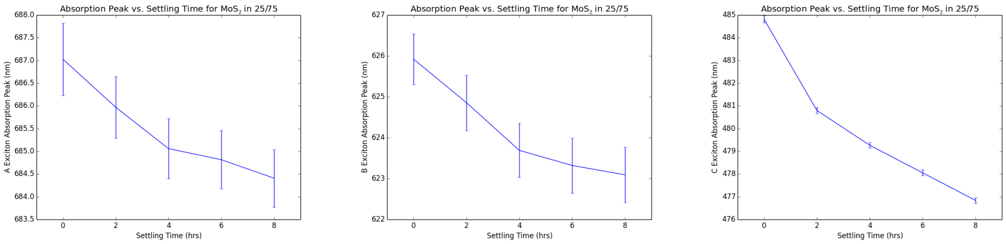

(a) A Exciton (b) B Exciton (c) C/D Exciton

Figure 3.13: Exciton Absorption Peak Position as a Function of Settling Time

optical band gap may be estimated. It should be noted that the exponent r equal to 2 is used based upon the assumption of an allowed direct transition whereas an exponent of 1/2 would be used for an allowed indirect transition. For samples of MoS_2 exfoliated in 25 % IPA, 75 % water, and at 30 minutes after sonication and 8 hours, the optical band gap was calculated to be 1.38 and 1.14 eV respectively as can be seen in Figures 3.16a and 3.16b. This is unexpected as it was thought that larger nanosheets, hence more bulk like in nature, and having smaller bandgaps would settle out of solution earlier. Therefore the opposite trend was anticipated.

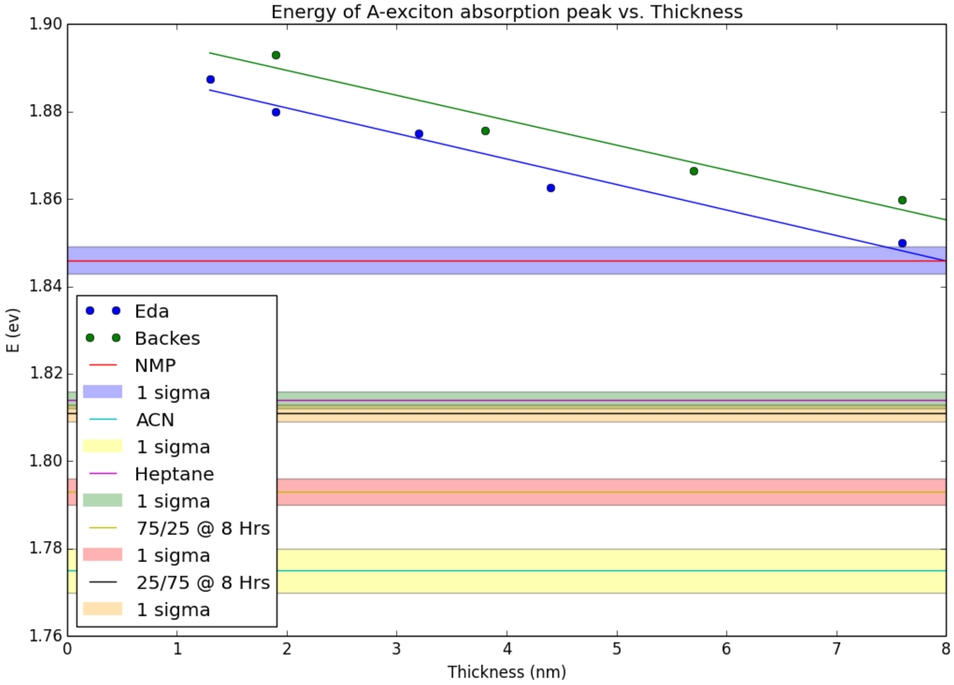

Figure 3.14: Energy of the A exciton absorption peak as a function of thickness. In Eda *et al.* [4] and Varrla *et al.* [5] the peak position of the A exciton is reported as a function of thickness. These are plotted in the blue and green points along with their respective lines of best fit. Experimentally obtained peak positions for nanosheets of unknown thickness in acetonitrile (ACN at $\tau_3/2$), NMP (at $\tau_3/2$), heptane (at $\tau_3/2$), and combinations of IPA and water (at 8 hours) are plotted in bands with their 1 σ uncertainty shaded around them. The objective of this was to observe overlap between the literature values and experimental values, from which an estimate of thickness mass could have been extrapolated. Slight overlap between the spectra of [4] and NMP may be seen around 8 nm thickness with all other solvents much lower. This may indicate that the gentle approach with NMP may be comparable in production rates to the work of others with more aggressive techniques.

For comparison, the Tauc method returned a value of 1.29 eV for the band gap when exfoliated in NMP (Fig. 3.16c). All values calculated using this method were well below the direct band gap of monolayer MoS_2 which is known to be at 1.9 eV. The band gap is known to 1.3 eV in bulk accompanied by a transition from direct to indirect bandgap. Based on this, an exponent of 1/2 was used under the assumption that the material had an indirect band gap. However, in this analysis a negative band gap was calculated, which is obviously non-physical. Although the direct-gap assumption is likely false it provides a realistic estimate of the band gap whereas the indirect assumption does not. Additionally, there exists a precedent for using the direct gap transition for few-layer MoS_2 [70] [71] [72]. It should be noted that due to the low energies and unexpected trend in band gap with time, this is a highly

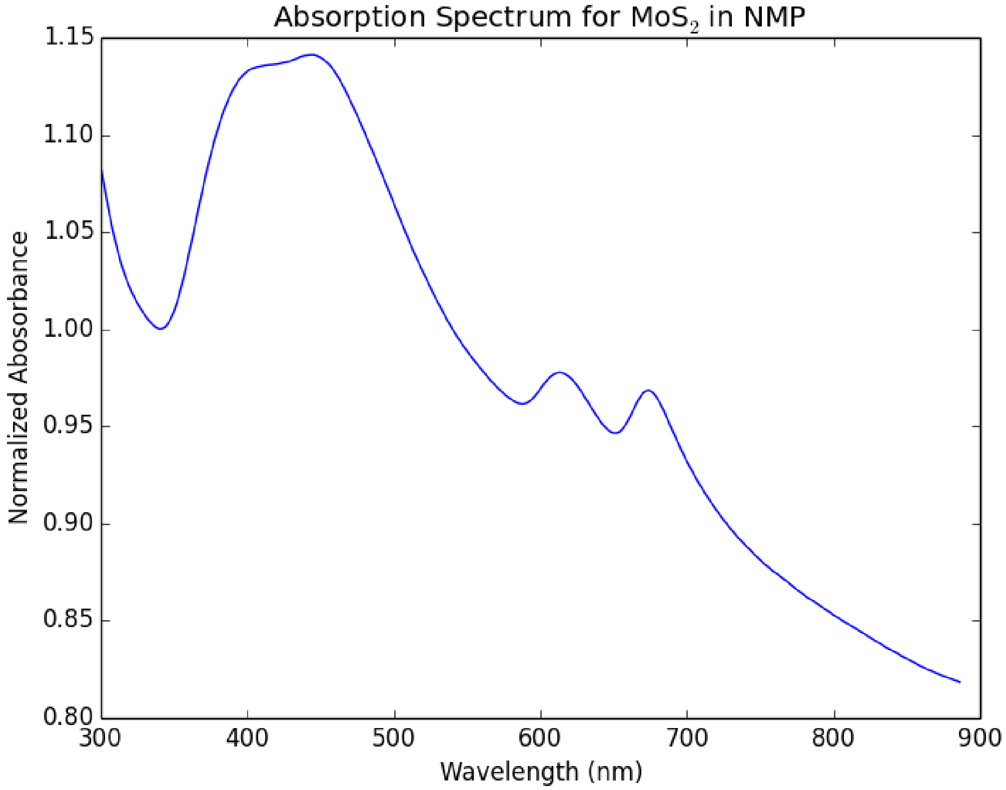

Figure 3.15: In addition to mixtures of IPA and water, MoS_2 was exfoliated in NMP as well. The spectrum seen here is similar in feature shape and peak positions that of [5] who also exfoliated MoS_2 in NMP. The sample was prepared using the above sample preparation protocol with a sonication time of τ_0 (360 seconds) and a settling time of $\tau_3/2$ (4 hours) before data collection. Sonication and settling times are found in Table 3.1.

preliminary study and should be investigated further.

3.4.2 Photoluminescence Spectroscopy

As discussed in § 3.4.1, the absorption of photons can be used to create excited states of bound electron-hole pairs. The recombination of these pairs will emit a photon of an energy equivalent to that of the bound state. For monolayered MoS_2, the bandgap is approximately 1.9 eV which corresponds to the energy of the A exciton [36] [73]. As demonstrated in [36], this effect is strongly quenched in multilayer MoS_2 and thus is an important indicator of the presence of monolayered nanosheets.

In Fig. 3.17 a sample of MoS_2 exfoliated in 25% IPA, 75% water was analyzed using a Shimadzu RF-1501 Spectrofluorophotometer with an excitation wavelength of 512 nm and an emission spectrum scan from 500 nm to 900 nm. As this was one of the first spectra collected, a settling time of 30 minutes was used with a resulting optically clear solution. During subsequent protocol development the settling time

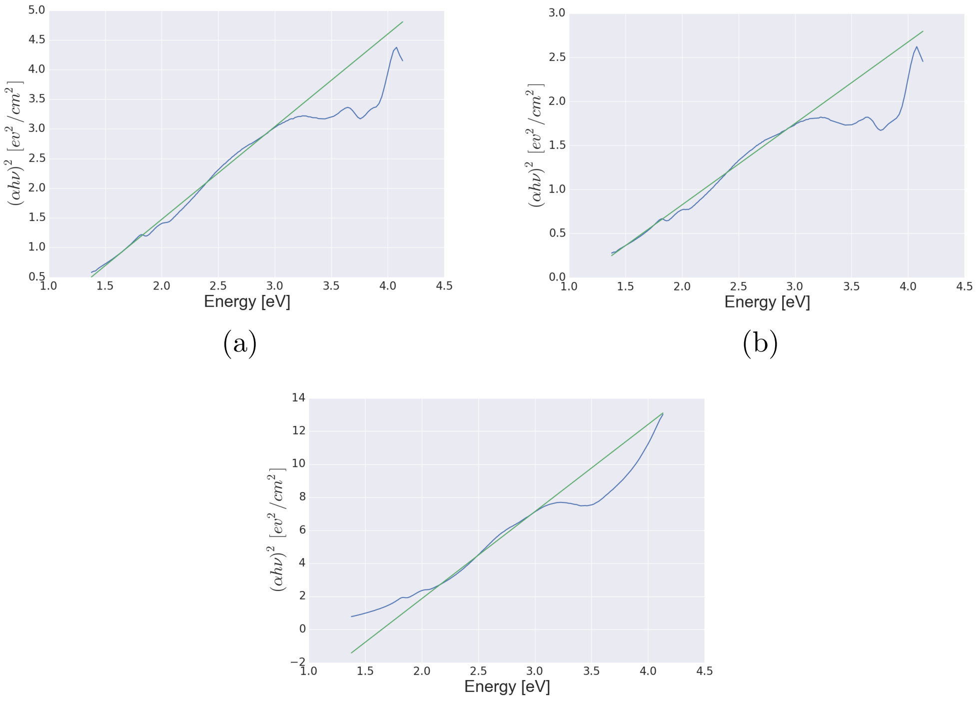

(a)

(b)

(c)

Figure 3.16: **(a)** Tauc plot of MoS_2 exfoliated in 25 % IPA, 75 % water 30 minutes after sonication. Based upon fitting of the linear region, the band gap is estimated to be 1.38 eV. **(b)** Tauc plot of MoS_2 exfoliated in 25 % IPA, 75 % water 8 hours after sonication. Based upon fitting of the linear region, the band gap is estimated to be 1.14 eV. **(c)** Tauc plot of MoS_2 exfoliated in NMP 30 minutes after sonication. Based upon fitting of the linear region, the band gap is estimated to be 1.29 eV.

was increased to $\tau_3/2$ as detailed in § 3.2. The final version of this procedure is in Appendix C. While the specifications of the Shimadzu indicated a beam width of 10 nm, Fig. 3.17 shows a much broader excitation beam which may be a consequence of scattering from the suspended particles. An additional consequence of scattering is the appearance of the shoulder features at 575 and 600 nm. In the literature, the standard method for photoluminescence measurements is to use Raman-like systems to analyze individual nanosheets or films [36]. A distinct peak extending off the shoulder feature is visible at 660 nm in Fig. 3.17 which corresponds to an energy of 1.88 eV. This is similar to the energy reported for the photoluminescence from the A exciton reported by Wu *et al* [74]. The presence of a secondary peak at 740 nm (1.68 eV) is similar to the energy reported for the indirect bandgap recombination present in bilayer and few-layer MoS_2 [74]. No visibly suspended particles were present in either the initial test (which resulted in Fig. 3.17) or the finalized procedure. With the final procedure (settling of $\tau_3/2$), a larger peak near 625 nm was observed and incorrectly interpreted to be photoluminescence.

Scattering of excitation light off the suspended particles proved to be a challenging problem which, in certain scenarios, produced a signal which was incorrectly

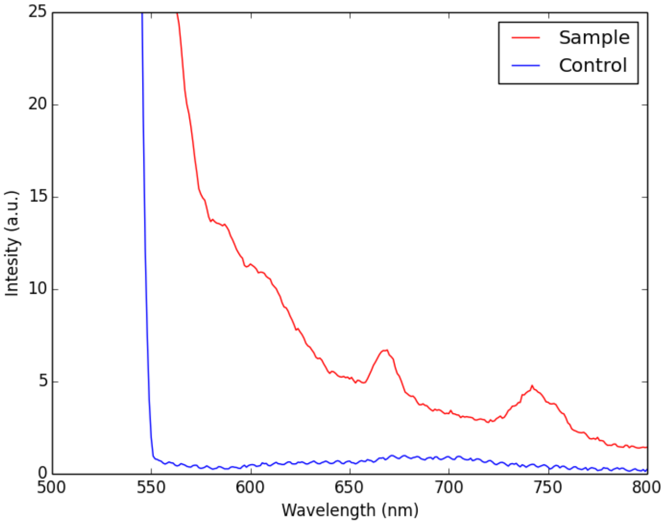

Figure 3.17: Apparent photoluminescence spectrum of MoS_2 nanosheets exfoliated in 25 % IPA, 75 % water. Excitation light of 512 nm was used as the emission was scanned from 500 nm to 900nm. In the solvent only control sample (blue) the excitation beam is seen to clearly cut off at 550 nm. In the MoS_2 sample, broadening of the excitation beam is clearly visible with a tail extending up to the edge of the region (800 nm). Within this tail several peaks may be seen. A distinct peak at 660 nm (1.88 eV) is clearly visible with a secondary peak at 740 nm (1.68 eV). These may indicate the presence of monolayer and few-layer populations. This was one of the first spectra collected and used supernatant extracted 30 minutes after sonication with a resulting optically clear solution. Subsequent protocol develop resulted in the SOP discussed in § 3.2 which had a settling time of $\tau_3/2$.

interpreted to be a unique photoluminescence signal from MoS_2. Fig. 3.18 demonstrates this signal. A scattering peak which progressed from the shoulder feature was interpreted to be the apparent photoluminescence peak of MoS_2. As may be seen in Fig. 3.18 and even more clearly in Fig. 3.19, it can be seen that as the excitation wavelength decreased, the peak wavelength increased. The scattering artifact was identified when similar behaviour was observed in turbid cell suspensions and disappeared when turbidity was removed. Turbidity is a well-known problem in such analyses, and despite allowing visible particles to settle out of solution, it is likely that scattering off suspended particles remained an issue. While very early measurements (such as in Fig. 3.17) may have had small amounts of apparently photoluminescent nanosheets, it is likely that an incorrect optimization of the sample signal in the procedure occurred. In future work, minimizing sample turbidity and scattering should be treated as a primary consideration.

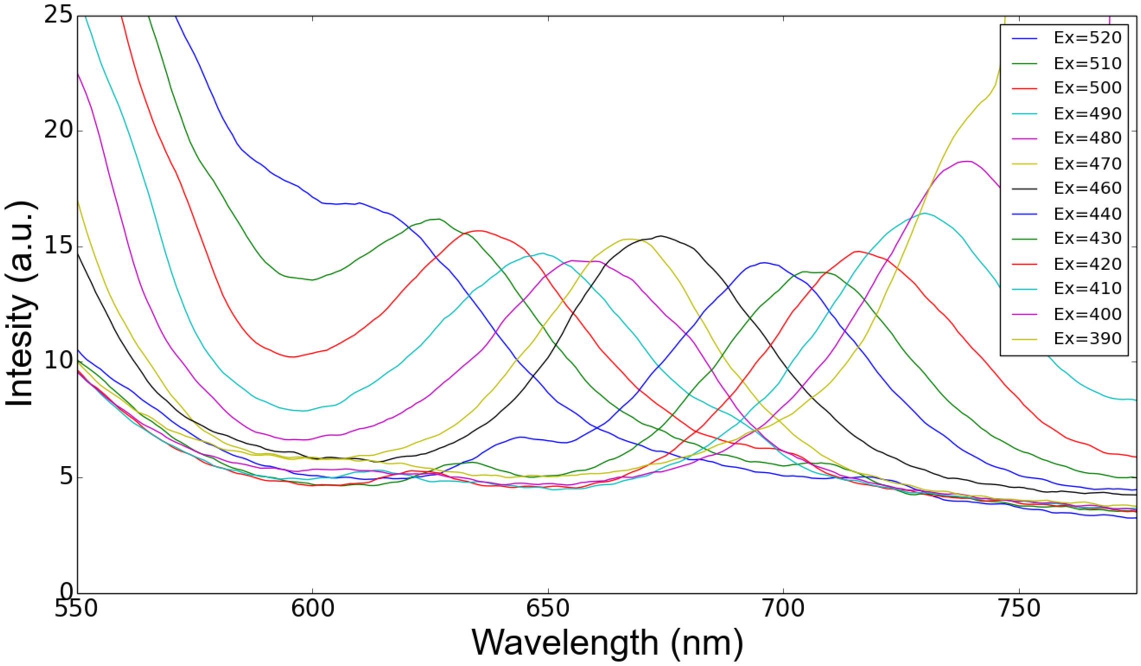

Figure 3.18: Spectrum of MoS_2 in 25% IPA, 75% water solvent between 500 and 800 nm at varying excitation wavelengths. The peak position can be seen redshifting as the excitation wavelength increases. This is an experimental artifact, likely attributed to scattering, that was reproduced when samples of microscope glass with no MoS_2 on their surface were placed in the cuvette holder.

3.4.3 Confocal Microscopy

The photoluminescent properties of MoS_2 films were analyzed in a preliminary manner using a Zeiss LSM 700 Confocal Microscope. This technique differs from the above-described methods in that films rather than suspensions were analyzed in this case. The films were prepared using the Langmuir Blodgett manner using the procedure described in § 3.3 on a microscope glass substrate after a settling time of 2 hours. The resulting films were discontinuous and partially translucent. To seal the films from the microscope oil which is required for confocal microscopy a coverslip was attached to the slide with a clear nail polish. In this discussion the term photoluminescence will be used to denote the bright, fluorescent locations in the images. It should be noted that due to the preliminary nature of this investigation, it is possible that this signal may be attributed to a different phenomenon.

Under microscope operation by Alicia Dubinski, both 405 nm and 488 nm lasers were used to excite the samples. Adjustable long pass and short pass filters were then used to bound the wavelength of the fluorescent region. The wavelength of these filters as controlled by adjusting their value within the Zeiss software. Fig. 3.20 shows images with three different long pass filters at an excitation wavelength of 405 nm with no short pass filter in the optical path. In Fig. 3.20a and Fig. 3.20b,

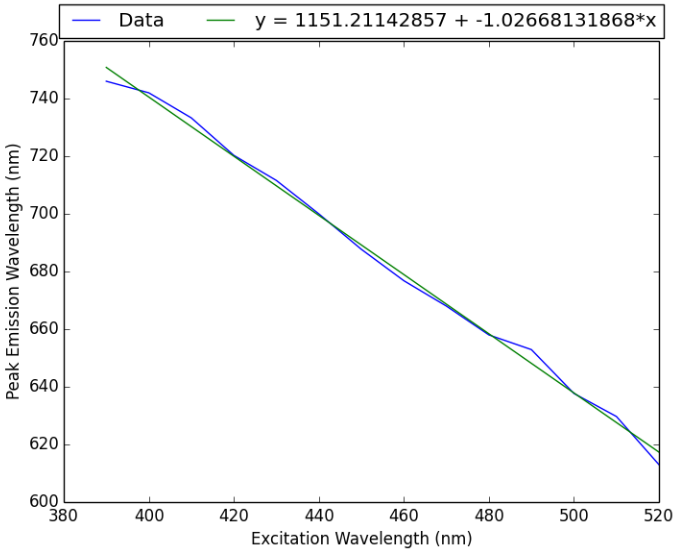

Figure 3.19: Extracted from Fig. 3.18, the wavelength of the peak is plotted on the x-axis with the excitation wavelength on the y-axis. A clear one-to-one linear relationship (slope = -1) is seen.

620 nm and 624 nm long pass filters were used respectively with photoluminescent locations clearly visible. After a 628 nm long pass filter was applied in Fig. 3.20c, no further photoluminescence was visible. The same process was performed with short pass filters (and no long pass filter in the optical path) with no photoluminescence visible when a 620 nm short pass filter was used, but photoluminescence visible when 624 nm and 628 nm short pass filters were used. Based upon this analysis, a photoluminescence peak at 624 ± 4 nm may be estimated which is an extremely narrow region and draws uncertainty to the validity of these results. As well, the peak is approximately 25 nm (0.077 eV) shorter wavelength (higher energy) than reported by [36]; however, many reports exist of mechanisms capable of red or blue shifting the photoluminescence peaks including a preferential excitation of the A^- trion rather than the neutral A exciton as noted by [73]. A high sensitivity scan of the region with an excitation wavelength of 405 nm and no filters is seen in Fig. 3.21. This result is considered preliminary as the photoluminescent peak with a full-width, half-maxima of 4 nm is much narrower than expected. While this result may be photoluminescence, it could also be an artifact from the filters which ended at 630 nm (thus we were operating at the upper end of the range). Additionally, while previous investigations indicated a heterogeneous distribution of nanosheets, a large fraction of the film exhibited photoluminescence. This is unexpected with a heterogeneous distribution of nanosheets. It is hypothesized that perhaps only the thin nanosheets are able to float on the surface of the water, whereas the larger nanosheets enter the liquid subphase; however, this is supposition and requires further investigation. A control sample of non-sonicated MoS_2 adhered to a microscope slide should be used to validate this method in the future.

Preliminary results from confocal microscopy indicate a range of nanosheet sizes and thickness based upon visual observation. Using ImageJ, particle sizes may be estimated to around 500 nm which is similar to the results from § 3.4.5. The large particle in the center is approximately 4 μm across. Highly photoluminescent locations are visible along with less photoluminescent particles. More stringent separation of nanosheets may produce a more uniform distribution of nanosheet sizes and luminosity.

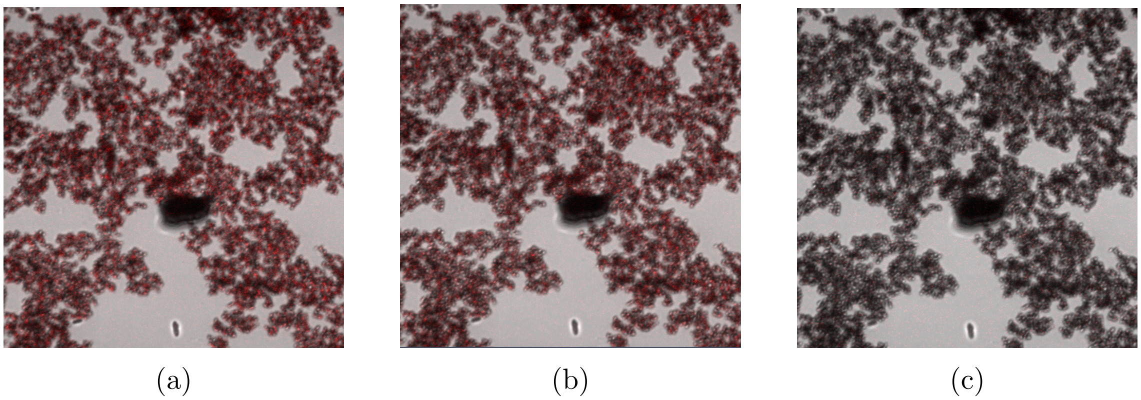
(a) (b) (c)

Figure 3.20: Confocal microscopy images of MoS_2 film formed on glass substrate using Langmuir-Blodgett technique taken with a Zeiss LSM 700 Confocal Microscope at 100X magnification. Laser excitation at 405 nm was used with three different long pass filters: a) 620 nm b) 624 nm c) 628 nm. Bright regions which may indicate photoluminescence can be observed in Panels a) and b), however, no such areas are observed in c). In data not shown here, when 628 nm and 624 nm short pass filters were used photoluminescence was visible and when a 620 nm short pass filter was used, no photoluminescence was visible. This might indicate a photoluminescence peak between 620 and 628 nm. Image preparation was automatically performed using the built-in software.

3.4.4 Conductivity and Photoconductivity

To investigate conductivity, three identical films were prepared using the hydrophobic bubble protocol in § 3.3.3. These samples were observed to have an average mass of 0.0003 g with a standard deviation of 0.0001 g. Substantial error exists in these measurements as they are at the limit of the balance's resolution (0.0001 g). It was assumed that after the 24 hour drying period all solvent has evaporated therefore any mass difference will be attributed to MoS_2. This was verified by weighing the samples at several intervals after the initial 24 hour drying period, and observing no change in mass. Using ImageJ, a general purpose image analysis package ([2]) to analyze images, the average surface area was measured to be $81 \pm 2mm^2$. Using the measured masses and surface areas, along with a density for MoS_2 of 5.06g/cm^3, film thicknesses of $0.73 \pm 0.01\mu m$ were calculated under the assumption that the film is uniformly thick. Using the lock-in amplifier and circuit from Fig. 3.27, the film resistance was determined. As this circuit is a standard voltage divider, the resistance

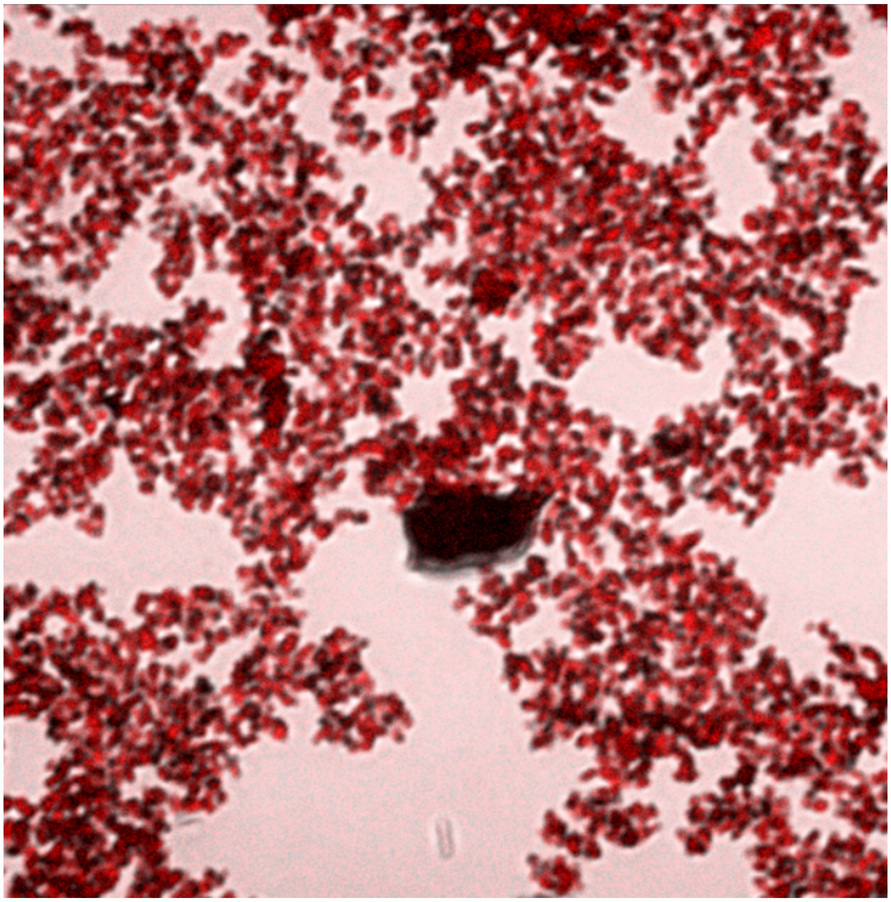

Figure 3.21: High sensitivity scan of MoS_2 film at 405 nm with no filters. Numerous possible photoluminescence locations are visible with a particularly strong location in the upper right.

may be readily calculated and no frequency data was taken in this case. Resistances averaging $24.5 \pm 2M\Omega$ were measured based on 3 samples. As the samples consisted of MoS_2 spanning four interdigitated regions, they were modelled as four resistors in a parallel configuration. Under this model, a resistivity of $477 \pm 4\Omega m$ was calculated. This film preparation protocol is reproducible to ±1% both in film thickness and conductivity. Although further investigation is necessary, this could indicate that the self-assembly of the nanosheets is controlled and reproducible. This resistivity is much lower than that of [56] who reported a value of $20k\Omega m$ which may be a further indicator of larger, more bulk-like particles present in this work. Due to this, the conduction may be more similar to that of bulk MoS_2 rather than nanosheets.

This experiment was extended by using the thermal control of the samples described in § 3.5 which allowed for the current to be measured as a function of temperature. The current displayed an Arrhenius-like behaviour, following the form $I = e^{-E_A/kT}$, with $E_A = 0.16eV$. This is consistent with the existence of a single (dominant) trapping state and given the similarity in activation energies between our E_A and that of Zhu *et al.*, these may be the same traps as what he identi-

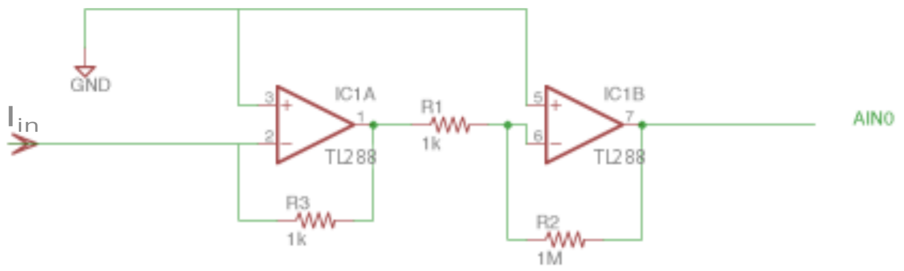

Figure 3.22: Transimpedance amplifier circuit for measurement of current through MoS_2 samples. A two-stage amplifier with a total gain of 10^6 was used. The output was monitored using LabJack U6 microcontroller. Upstream of the sample, a LabJack controlled MIC4422 was used to connect/disconnect a voltage of 10 V to the sample, the other end of which was connected to I_{in}

fies to be Type B traps [45]. Based on the trap constants list by Zhu for Type B traps, we would expect these to contribute signals in the range of 10-100kHz for the temperature range used here.

Using a standard op-amp circuit with a TL288 op amp and 10^6 total gain (two stages of 10^3) assembled on a breadboard in a transimpedance amplifier set up (see Fig. 3.22), the current through the sample was recorded at 200 Hz as a LED was toggled on and off above the sample once per second. The TL288 has a unity-gain bandwidth of 3 MHz. As two stages with 10^3 gain were used and sampling frequency was 200 Hz, the gain-bandwidth product was well below this limit. The analogue input of a LabJack U6 was used to recorded the output of the amplifier. The LabJack was also used to control an LT 3092 current source modulating the current through a 465 nm LED (Kingbright WP710A10QBC/G, Digikey) much as in § 2. An analogue output of the LabJack was also used to control a MIC4422 which switch on and off the voltage applied to the sample. The sampling frequency of 200 Hz is compatible with both the MIC4422 and the gain bandwidth product of the TL288. Between on and off states a change of 2 nA of current was observed as may be seen in Fig. 3.23. The LED power was approximately 120 mW which means that the responsivity may be conservatively calculated to be $1.6^{-8} A/W$ assuming that all LED power was incident upon the sample.

Even though the sample was shielded within a metal box and shielded wiring was used, the results in Fig. 3.23 contain a large amount of noise. When Fourier transformed (not shown here) a clear peak at 60 Hz is visible and the amplitude of the noise is an order of magnitude higher when the power supply is on than when it is off. Additionally, this noise is present when the sample was replaced with a 1 MΩ resistor. It is likely that this noise is due to power supply coupling as the voltage across the sample was directly supplied by a DC lab power supply.

When compared with the report by Cunningham *et al.* of electrical conductivity in films formed from liquid phase exfoliated nanosheets, conductivity values one to two orders of magnitude higher were observed in this work; however, responsivities were 10^4 times lower [56]. This may be attributed to one of several factors including nanosheet thickness and electrode separation. Thinner nanosheets would

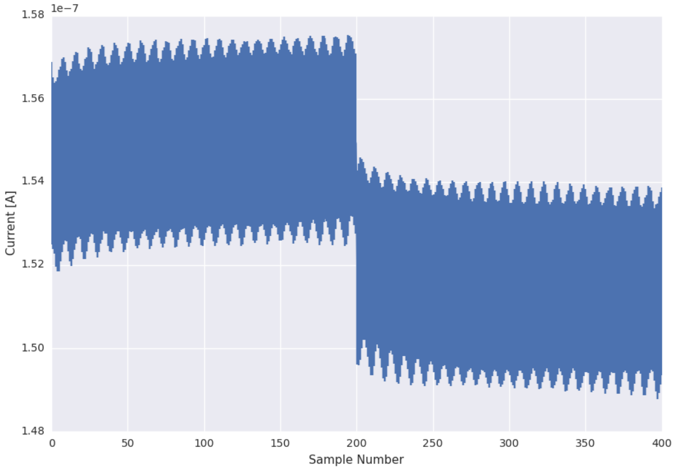

Figure 3.23: Preliminary results of current flow through MoS_2 film sample with 28V applied. From 0 to 200 the LED is illuminating the sample and from 201 to 400 LED is turned off. If both sections are averaged, a change of 2 nA in current is observed between on and off states. This may be used to calculate a responsivity of $1.6^{-8} A/W$.

be expected to demonstrate higher responsivities if still in the thin film regime.

Using the carbon tape ITO electrode structure described in § 3.3 along with an Agilent 1252A Digital Multimeter (DMM) resistance of MoS_2 films prepared by a collaborator (Dr. Michael Pope) using the lithium intercalation exfoliation technique were measured and can be seen in Fig. 3.24. When compared with previous reports, the films prepared by the collaborator have much lower conductivity than the standard reported in the literature. This may be an effect of differing nanosheet properties or electrode characteristics with a difference between intrinsic and percolation resistance due to electrode spacing being one theory. Additionally, these resistances were much higher than those observed in films prepared using the procedure from § 3.3.3, however, upon visual inspection it noted that the collaborator's films were almost transparent whereas our films were opaque. Based on this, it is assumed that the collaborator's films are much thinner than ours which likely explains the variation in resistance. This is supported by [3] who noted that larger and thicker nanosheets had greater optical extinction. The layer number in Fig. 3.24 was determined by the number of depositions which they performed to make the films.

3.4.5 Dynamic Light Scattering

Dynamic light scattering (DLS) was performed on various fractions of the supernatant as a preliminary characterization of the particle size distribution. DLS analyzes the resulting speckle patterns from the scattering of a monochromatic, coherent polarized laser beam off particles in solution [75]. By performing time domain anal-

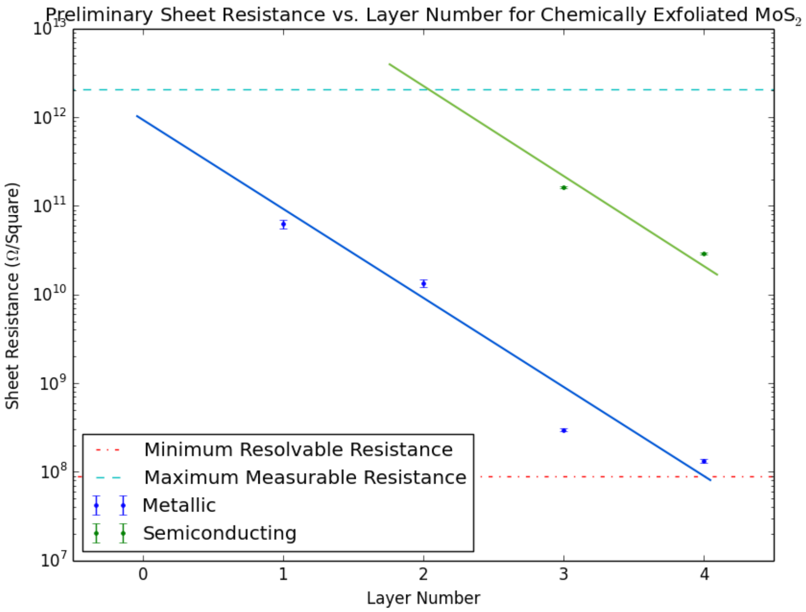

Figure 3.24: Conductivity of metallic (1T) and semiconducting (2H) MoS$_2$ prepared using lithium intercalation technique and deposited using the Langmuir-Blodgett technique onto glass substrates. Contact to the film was made using carbon tape ITO interdigitated electrodes and resistance was measured using an Agilent DMM. The layer number is determined by the number of depositions performed to make the films. Based upon AFM measurements reported by collaborators, each layer is approximately 1.3 nm thick.

ysis, the temporal changes in intensity are related to particle size through a photon autocorrelation function [75]. As Brownian dynamics are the dominant factor in particle motion, the smaller particles will have patterns with greater changes. In this manner the particle size distribution may be characterized. Samples were prepared for analysis using the standard procedure for absorption and photoluminescence analysis after which DLS was performed by Nicholas Lanigan using a Brookhaven 90Plus Particle Size Analyzer using the manufacturer suggested procedure. Two different samples were analyzed with the first being a sample from the black precipitate settled at the bottom of the test tube after 30 minutes of settling (see Fig. 3.2b for layer identification). As may be seen in Fig. 3.25a, a bimodal distribution was observed with one population having an effective hydrodynamic diameter of 100 to 200 nm and the other having an effective diameter of approximately 3 μm. This likely corresponds to a population of small, exfoliated nanosheets accompanied by a population of large, unexfoliated particles. The second sample (Fig. 3.25b) consisted of supernatant after allowing particles to settle for 30 minutes. A bimodal distribution was again observed with one population at just above 100 nm effective diameter and the second population distributed around 700 nm. In § 3.4.1, phenomenological metrics developed by [5] were used to estimate particle diameter using the absorption spectrum after 30 minutes of settling and yielded a diameter estimate of 350 nm which is the same order of magnitude as the DLS results. Allowing for further settling or use of centrifugation may yield a single population of nanosheets.

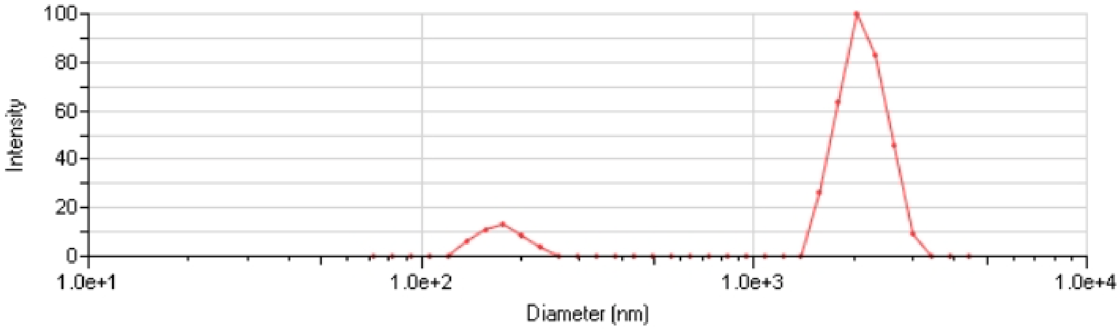

(a)

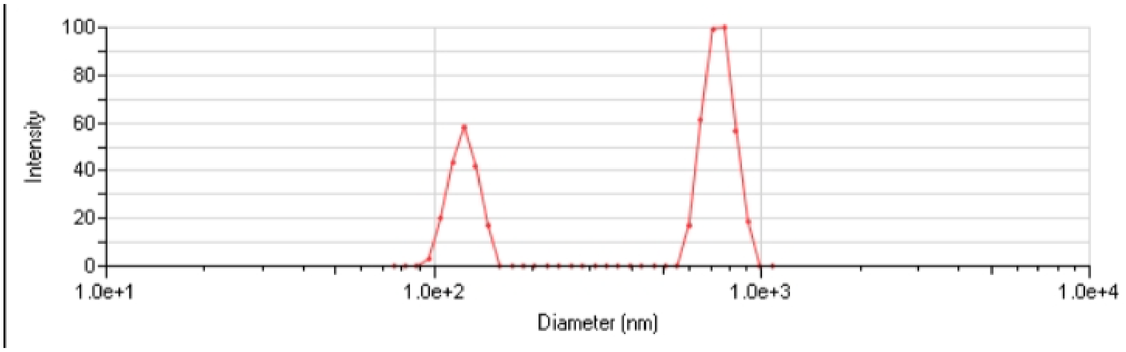

(b)

Figure 3.25: **(a)** DLS results for a black portion of MoS_2 which had settled to the bottom of microfuge tube 30 minutes after sonication. A bimodal distribution may be observed with a small population of partially exfoliated nanosheets with an effective diameter of between 100 and 200 nm. The second, and dominant population is comprised of approximately 3 μ m particles which likely correspond to unexfoliated particles. **(b)** DLS results for supernatant after 30 minutes of settling; extracted from the top fraction of the microfuge tube. A bimodal distribution is also observed in this case however the distributions are more equivalently weighted with one centered at just over 100 nm and the second at approximately 700 nm. Samples were prepared for analysis using the standard developed procedure for absorption and photoluminescence analysis after which DLS was performed by Nicholas Lanigan using a Brookhaven 90Plus Particle Size Analyzer using the manufacturer suggested procedure.

3.5 Deep Level Domain Spectroscopy

The objective of the previously discussed characterization methods was to quantify the effect which processing had on the MoS_2. This processing may introduce defects to the MoS_2 structure which can act as trapping states for electrons [45]. A common method to identify trapping states is with deep level domain spectroscopy (DLDS), one type of which examines the temperature dependence of the frequency components of the current noise in an effort to characterize the trapping states of a material [66]. From this temperature dependence, information such as the trapping cross section and lifetime may be determined. This differs from measurements of current transients which may also be used to gain information on trapping states. A standard implementation of a DLDS systems uses a robust thermal controller to adjust the sample's temperature in conjunction with a high bandwidth transimpedance amplifier to monitor the current noise through the sample. This section discusses the development and validation of the infrastructure necessary for preliminary DLDS-like measurements across a restricted temperature range from room temperature up to approximately 80°C. Preliminary infrastructure was developed to provide thermal control and the measurement of voltage noise through a sample of MoS_2. The plan was to add a simple transimpedance amplifier to convert voltage noise to current noise, allowing the system to perform standard DLDS measurements; however, the discovery of superhydrophobic graphene (focus of Chapters 4 and 5) prevented this from occurring.

Initial development focused on ensuring robust thermal control and accurate use of the lock-in amplifier. The lock-in amplifier used was an Ametek Signal Recovery Model 7270 DSP Lock-In Amplifier, the functionalities of which include: 4 auxiliary 16-bit DACs, 4 auxiliary 1 mV resolution ADCs, and a sampling rate up to 200 kHz depending on the buffer used. Initially, the standard curve buffer of the lock-in amplifier, which has a sampling frequency of up to 1 kHz, was used as it was easier to implement and allowed for quick testing of initial system designs. After initial results were gathered, it was observed that higher frequency sampling was likely required. This was implemented through the fast curve buffer of the lock in which enabled sampling at up to 200 kHz. This chapter will begin with a discussion of the experimental setup for both standard and fast curve buffer implementations. Validation and sample results along with data analysis procedures will then be discussed first for the standard curve buffer followed by the fast.

3.5.1 Setup

The objective of this system is to provide accurate and robust thermal control of the sample while precisely monitoring the electrical characteristics of the sample. A complete SOP is stored on the accompanying USB drive.

Schematics for system assembly are seen in Figures 3.29 and 3.30 with the fully assembled system seen in Fig. 3.31. In short, the system was comprised of an Ocean Optics cuvette holder placed on the bottom of a styrofoam box with two holes for the water hoses. A 6"x6"x1/4" aluminum block was placed on top of the cuvette holder as a spacer layer to keep the Hammond Manufacturing 4,13,12 steel box level and in uniform thermal contact. Depending on whether the standard or fast curve buffer was used, either the circuit in Fig. 3.26 or Fig. 3.27 was assembled on the breadboard then connected to DAC1 and ADC1 using BNC cables. A transimpedance amplifier similar to that in Fig. 3.22, developed by Gordon Hall, was tried in a preliminary manner with this system; however, successful implementation was unachievable on an appropriate time scale.

The LM35 temperature sensor was connected to a LabJack U6 using alligator clips (Fig. 3.28). These circuits feature a voltage divider for determination of sample resistance with a low pass filter designed to short frequency components greater than half the sampling rate, 500 Hz for standard curve buffer and 33 kHz for fast curve buffer, to ground. When calculating the filter cut-off frequency the ADC input resistance (1 MΩ) and capacitance (30 pF) are included in the calculations. Initially, the lock-in was used to monitor the LM35s by connecting them via BNC cables to two of the ADC inputs. However, this was observed to produce oscillations in the reading of the signal channel ADC; the frequency of which would change with temperature. When the LM35s were disconnected from the lock-in, such oscillations disappeared. Therefore, the decision was made to monitor the temperature using the LabJack U6.

The sample holder is shown in Fig. 3.32 and is comprised of an aluminum base with a recessed pocket for samples to be thermally pasted into and an embedded LM35 temperature sensor. An 800 μm thick copper capping layer with a second LM35 is thermally pasted above the sample to prevent convective cooling of the sample and provide a second location for thermal monitoring.

For the standard curve buffer, as seen in Fig. 3.26, a low-pass filter was used to prevent aliasing caused by signal components exceeding the Nyquist frequency of 500 Hz. The voltage before the sample is known from the value to which the DAC is set and the voltage after the sample is recorded using ADC1. The circuit used is shown in Fig. 3.26. The resistance of $R_F = 10k\Omega$ may be neglected as it is orders of magnitude less than the other resistances. The Thevenin equivalent circuit is shown in the middle panel of Fig. 3.26. The sample resistance is the upper arm of the voltage divider with the complex impedance of the bottom arm calculated by Eq. 3.4 with $R1 = 1M\Omega$, $R2 = 1M\Omega$, $C1 = 2nF$, and $C2 = 30pF$.

$$Z = \frac{1}{\frac{1}{R1} + \frac{1}{R2} + j\omega C1 + j\omega C2} \tag{3.4}$$

For $f << f_c$ where $f_c = 1/(RS \times C1)$, Z simplifies as seen in Eq. 3.5.

$$z_T = \frac{1}{1/R1 + 1/R2} \tag{3.5}$$

which simplifies to $500M\Omega$. At higher frequencies, close to f_c, the impedance of C1 dominates and high frequency components are effectively shorted to ground through C1, filtering them out of the signal. In this regime, the system time constant equals $1/f_c = RS \times C1$. The use of a 2nA capacitor and an approximate sample resistance of $1M\Omega$, when multiplied, results in a $\tau = 0.002s$ which equals the system's Nyquist frequency. It should be noted that the sample's resistance will decrease with temperature, causing the time constant τ to decrease. This was not adequately accounted for and should be considered in future developments.

This was a non-standard implementation of DLDS in that voltage noise rather than current noise was monitored. In a standard setup, a transimpedance amplifier, much as in Fig. 3.22, would be included between the sample and the ADC [66]. This design allowed for a preliminary assessment of the presence of traps and a platform for the future implementation of a design including a transimpedance amplifier.

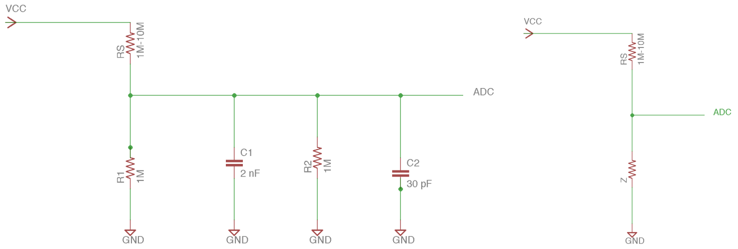

RS = 1-10 MΩ
R1 = 1 MΩ
R2 = 1 MΩ
C1 = 2 nA
C2 = 30 pF

$$Z = \frac{1}{\frac{1}{R1} + \frac{1}{R2} + j\omega C1 + j\omega C2}$$

Figure 3.26: The above circuit is used to measure voltage noise using the standard curve buffer. The low-pass filter has a cut-off frequency of approximately 500Hz which corresponds to the Nyquist frequency of the system. RS is the sample resistance, R1 is the load resistance, R2 is the ADC input resistance, C1 is the filter capacitance, and C2 is the ADC input capacitance. As is further discussed in §4.3, the capacitor acts as a frequency dependent impedance which shorts to ground frequency components greater than the Nyquist frequency.

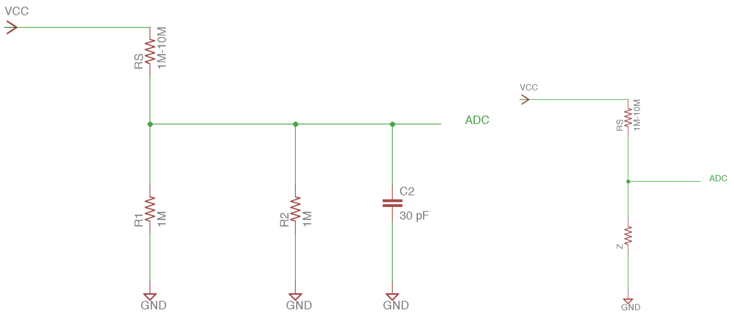

RS = 1-10 MΩ
R1 = 1 MΩ
R2 = 1 MΩ
C2 = 30 pF

$$Z = \frac{1}{\frac{1}{R1} + \frac{1}{R2} + j\omega C2}$$

Figure 3.27: The above circuit is used to measure voltage noise using the fast curve buffer. With no filter capacitor, the cut-off frequency as a result of filtering due to input resistance and capacitance, as calculated using the equation on the right was 33 kHz. This is below the Nyquist frequency and thus will appropriately filter aliased peaks. Unfortunately, there is no way to increase this cut-off using the above circuit and peaks of interest within the range 33 kHz to 100 kHz may be filter as well. RS is the sample resistance, R1 is the load resistance, R2 is the ADC input resistance, and C2 is the ADC input capacitance.

The fully assembled system is seen in Fig. 3.31.

3.5.2 Thermal Profile

The geometry of the system is outlined in Figures 3.29 to 3.32. Heat is supplied through the water flowing through the cuvette holder. The sample holder is heated

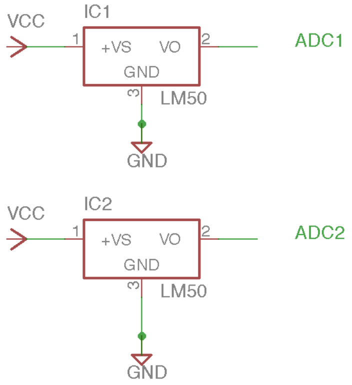

Figure 3.28: The above circuit is used to control the LM35 temperature sensors using the LabJack U6. Initially, the lock-in auxiliary ADCs and DACs were used to control the LM35s, however, they were observed to cause mV level fluctuations in the signal channel ADC; the frequency of which varied with temperature. To prevent any further issues the LM35 control was moved to the LabJack after which all such fluctuations disappeared.

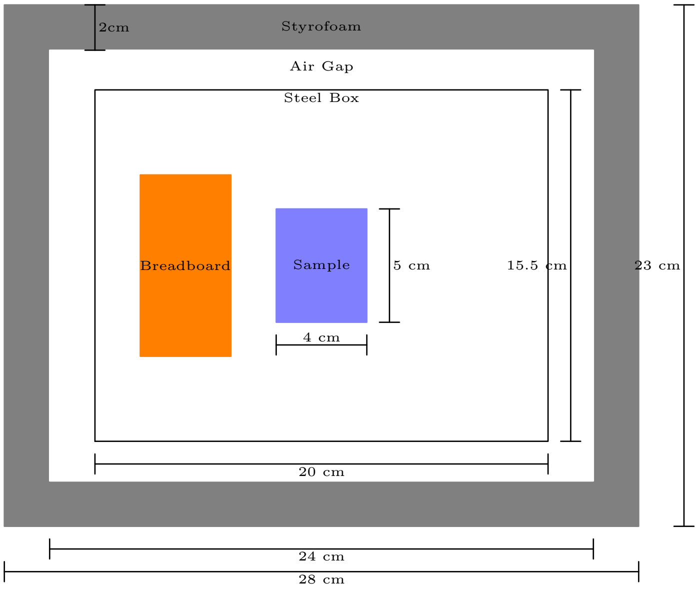

Figure 3.29: Scale drawing of system from above

by conduction through the metallic components encased within the styrofoam box for insulation.

The thermal heating routine will be divided into two stages. First, the water bath will be set to 80°C with the pump on for 2 hours which has been observed to allow the system to reach steady state (steady state is defined to be a temperature change of less than 0.1°C per 5 minutes. Second, the heater and pump will be turned off and the system allowed to slowly cool under no outside influence. The heating and cooling curves produced using this protocol were demonstrated to be reproducible and to have a less than 1°C difference between the top and bottom of

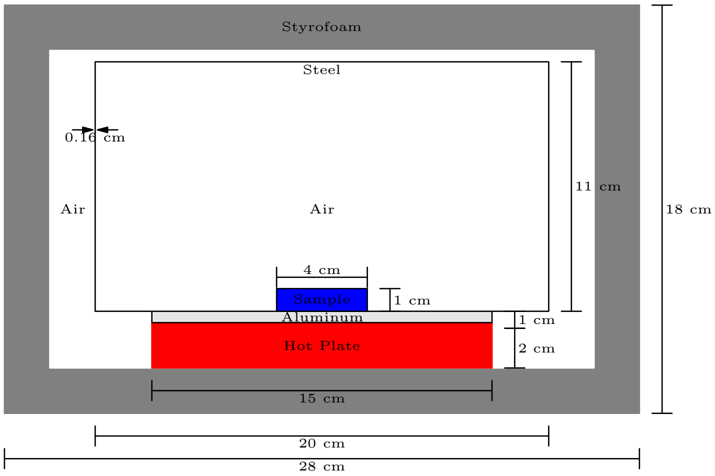

Figure 3.30: Scale drawing of system from side

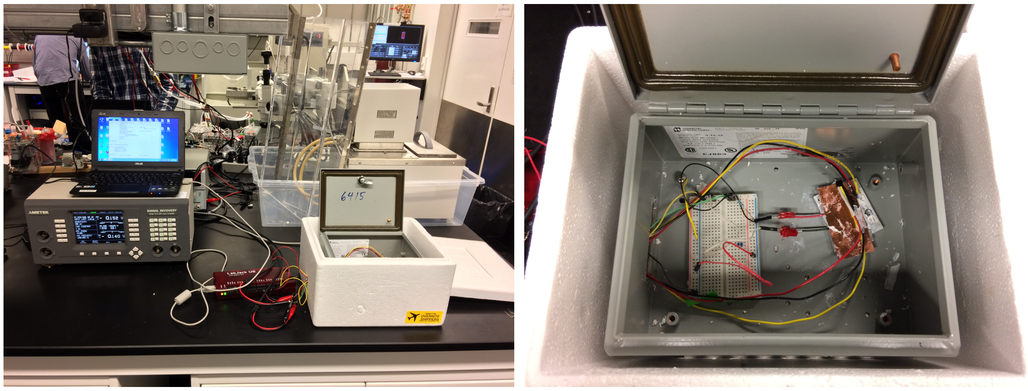

(a)

(b)

Figure 3.31: **(a)** Image of full assembly. On the left of the image, the lock-in amplifier is seen with Netbook resting on top. In the center on the lab bench is the LabJack U6 next to the insulating styrofoam box. With the styrofoam lid removed, the metal shielding box can be seen with the lid open inside. On the right side, behind the styrofoam box, is the water bath sitting inside a large Rubbermaid tub with the plexiglass shield behind. **(b)** Image of the inside of the metal shielding box. On left side of the box, the wire access port can be seen. The breadboard for the circuit is seen at left-center with the sample seen at right-center. The sample is located underneath the copper top layer.

the sample holder at all points in the cooling curve as seen in Fig. 3.33. This implies that no transients are present in the system and is discussed further below.

To analyze the thermal design, let us first assume that the system has already achieved steady state as defined previously and is now in the cooling state. Vertically from the sample is the aluminum sample holder, steel box, aluminum spacer layer, cuvette holder, and then styrofoam box. It is also assumed that good thermal contact exists between all as they are all in intimate contact. It is assumed that the thermal resistance is dominated by that of the styrofoam as it is several orders of magnitude greater than that of any of the metal components. Based upon a thermal resistivity of 30.3 m K/W, thickness of 2 cm and interior surface area of $0.21m^2$, the thermal resistance of the styrofoam can be calculated to be $2.89K/W$. Similarly, the thermal capacitance is assumed to be dominated by the capacitance of the four metallic components which are approximated to be a uniform block of aluminum with specific heat capacity of $0.897J/gK$ and mass of 937 g in contact with negligible thermal resistance to a steel box with a specific heat capacity of 0.446 J/gK and mass of 470g. Based on this the total thermal capacitance is $1060J/K$. The time constant of the system can be approximated by the product of the resistance and capacitance to be $\tau = 3063s$. It was observed that after one hour of cooling the temperature was within 45% of its final value which closely approximates the 36% calculated by truly exponential cooling with time constant calculated above. Within 5 τ the sample had returned to room temperature. The aluminum and copper sample holder possesses a very low thermal resistance and will rapidly equilibrate with the lower thermal conductors enclosing the sample within a thermally uniform box. Thus the sample temperature is dominated by this assembly. It is critical to ensure that no thermal gradient could develop across this assembly. The volume of air above the sample could introduce thermal gradients across the system, however, its effect is minimized by several factors. First, the entire air volume is enclosed within the steel box, and therefore all boundary conditions on the air mass are clamped at temperature T_s (temperature of cuvette holder, aluminum spacer, sample assembly, and steel box; assuming very low thermal resistivity). Second, differential sample cooling could only occur if the rate of thermal losses to the air exceeded the thermal equilibration rate of the copper top with the aluminum body. However, the low resistance in the sample holder combined with its high thermal capacitance results in a fast time constant and rapid equilibration which is reflected by the similarity of the LM35 measurements between the top and bottom.

An internal τ of just the sample holder may be calculated assuming a single uniform thermal capacitance of the aluminum block equal to 1060 J/K and a single uniform thermal resistance of 0.018 K/W. This results in $\tau = 10.4s$. This is equivalent to the time constant of the LM35 (8 seconds in stirred oil bath). The system is approximately symmetric radially, with the only noticeable asymmetry occurring vertically (hoses at the bottom for heating and cooling which will be discussed in next paragraph). Thus any transient variations in temperature should travel vertically through the system along the axis of asymmetry which is the vertical z-axis. The two temperature sensors, with system relevant time constants, vertically separated will allow for detection of such transients (none of which have been observed to date).

The main source of asymmetry in the system and likely cause of any thermal variations are provided by the hoses entering the styrofoam box. The water contained in the hoses has a thermal conductivity 20 times greater than that of the styrofoam, however, the cross-sectional area of the 1cm diameter hoses comprises less than 0.1% of the total surface area of the box. Should the pump 'burp', changing the entire volume of water in hoses (which it wouldn't), and if the water changed was all at room temperature (which it wouldn't be), the maximum amount of energy drawn from the system to heat this water to thermal equilibrium would be 16 J which is negligible when compared to the excess of 50 kJ of energy stored in the system. Finally, the hoses contact the aluminum cuvette holder at the bottom of the box. The sample is located above this, with substantial thermal mass and capacitance between. The large thermal capacitance between the source of perturbations (hoses) and the sample will capacitively dampen any perturbations. Two temperature probes installed above and below the sample would observe any perturbations travelling through the material based on the symmetry considerations discussed in the previous paragraph. Thus when the small surface area, minimal thermal mass, and capacitive dampening is considered, it may be concluded that the hoses will minimally contribute to the formation of a thermal gradient across the sample. The hole through the outside of the box through which the wires pass may be analyzed in a similar manner to the hoses. The hole diameter was kept to a minimum such that approximately 80% of the cross-sectional area of the hole is blocked by the wires which minimizes air currents entering the box. As well, the cross sectional area of the hole is less than 0.05% of the total surface area and can be considered negligible. In the future, improved wiring could be used to minimize both electrical noise and the thermal profile.

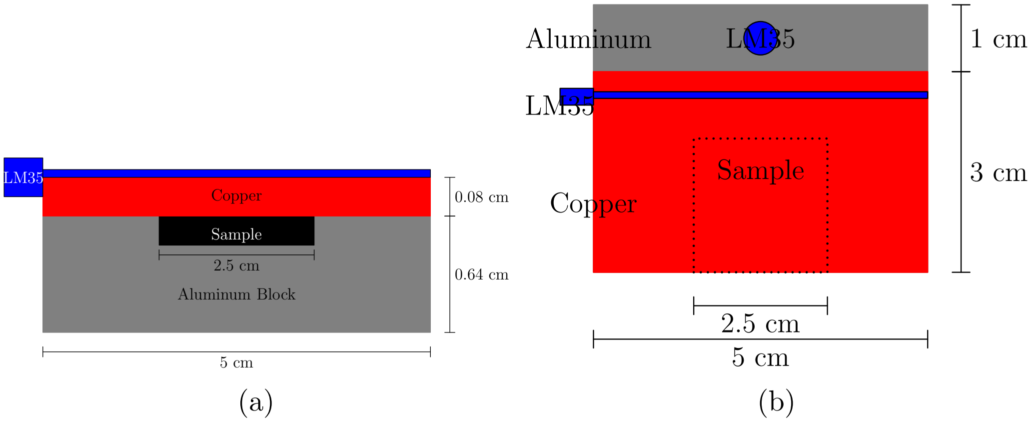

Figure 3.32: **(a)** Side-view of sample holder assembly. **(b)** Top-down view of sample holder

3.5.3 Standard Curve Buffer

Data Collection

The standard curve buffer of the lock-in has the ability to sample the ADCs at a rate of up to 1000 Hz. This buffer was initially used to collect data on the samples and the important design parameters of this system are shown in Table 3.34. A complete operational procedure and Python control codes for the system are detailed in Appendix A. In summary, as may be seen in Fig. 3.26 a potential of 10 V was held across a sample prepared as discussed in § 3.2. The voltage drop across the sample was monitored using an ADC on the lock-in at a frequency up to

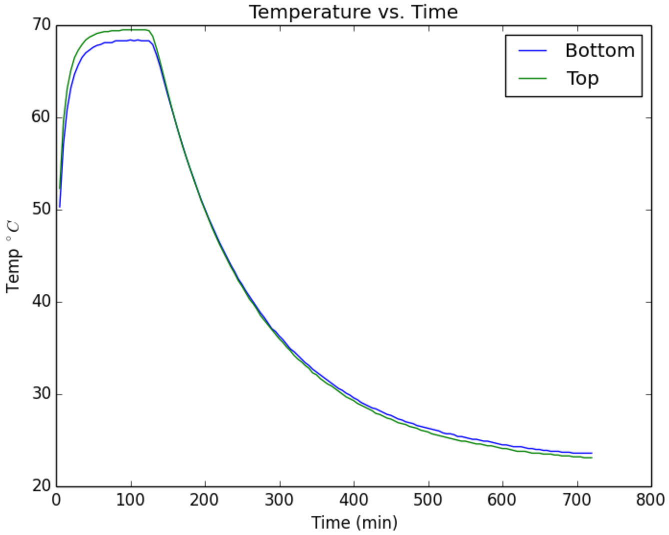

Figure 3.33: Representative Temperature vs. Time Graph for MoS_2 sample. Agreement within 1°C between the top and bottom temperature sensors is observed at times after t=125 mins (5 minutes after cooling begins).

1000 Hz as the sample was cooled from approximately 75° C to room temperature. Data was initially stored in the standard curve buffer before being transferred via standard serial protocol to a connected laptop. Serial communication was used to send commands from the laptop to the lock-in as well.

Setting	Value
Number of Time Points	96
Number of Data Points per Time Point	32768
Frequency	1000Hz
T_{max}	$80°C$
Number of Heating Cycles (5 mins/cycle)	20
Number of Cooling Cycles (5 mins/cycle)	76
Drive Voltage	10V

Figure 3.34: Summary Table of Important Parameters set for Standard Curve Buffer Procedure

Data Analysis

Each data point was collected at a time Δt apart. The sampling frequency is defined as ν, the standard of which is 1000 Hz, and is equal to $1/\Delta t$. Based on the Nyquist-Shannon Theorem for a signal to be reconstructed the sampling frequency must be at least twice the bandwidth of the signal. From this, the Nyquist Frequency, the cutoff frequency for this requirement, is defined to be $\nu/2$. The time period of sampling T is defined to be N (the number of data points collected) divided by ν. The frequency resolution is thus defined as $1/T$. The data was collected in time domain and when Fourier transformed it is transferred to the frequency domain (or k space). Each bin in k space is defined as $\nu_k = k/T$ with k varying from 1 to N. Using this notation the Nyquist Frequency is equivalently defined as $\nu_{NF} = N/(2T)$. The power data collected as a function of time is Fourier transformed and plotted against frequency. Based on the Nyquist-Shannon Theorem only the first $N/2$ data points are plotted and the frequency domain is defined as $[1/T, N/2T]$. The Fourier transform is performed using the Scipy FFT package which returns the discrete Fourier transform. The output of the Fourier transform is convolved with a Hamming window from the Scipy Signal package to reduce high frequency noise which would arise from rectangular windowing. The Hamming window of N points is defined by

$$w(n) = 0.54 - 0.46cos\left(\frac{2\pi n}{N-1}\right); 0 \leq n \leq M-1 \tag{3.6}$$

and a non-symmetric window, necessary for spectral analysis (as the data set began at zero rather than being centered around zero), was used. The Hamming window is shown in Fig. 3.35.

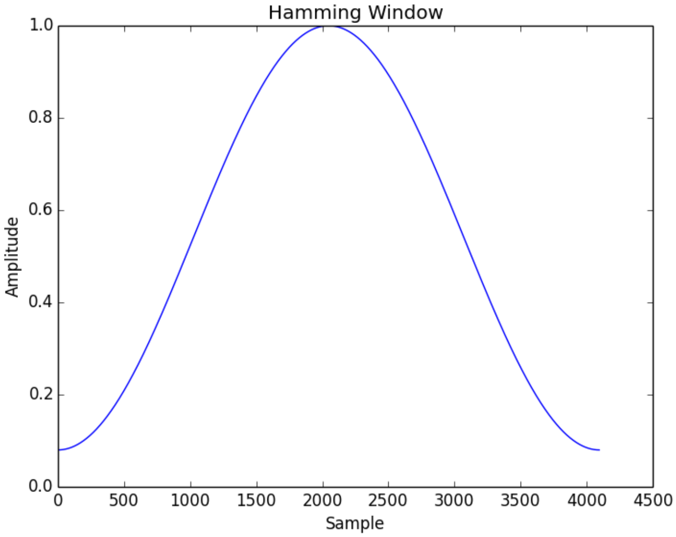

Figure 3.35: 4098 point Hamming window to be convolved with spectral data for Fourier analysis.

This Fourier transform of the power convolved with the windowing function is then plotted vs. frequency using Pyplot. Signal peaks will arise from the movement of electrons into and out of traps at a characteristic frequency which, due to statistical fluctuations, will have a certain frequency spread. The frequency range is from 0 Hz to the Nyquist frequency with a resolution of $1/T$. A constant background was visible in the system and the system's limit of detection (LOD) was determined by taking the mean and standard deviation of the background noise. The 3σ definition of LOD was used, meaning that for a signal peak to be detectable it had to exceed the mean of the background noise by three standard deviations. Using this definition the LOD was determined to be $9 \times 10^{-11} V^2/Hz$. However, due to the wide spread in noise amplitude, multiple noise peaks exceed the LOD. It should be noted that 60 Hz peaks exceed this threshold, however, they possess no discernible width and are temperature invariant. A sample peak will be identified as exceeding the noise reference, having a full-width, half-maximum (FWHM) greater than 5Hz, and translating with temperature changes.

Welch's Method

Welch's method has been used to minimize the amplitude of the fluctuations in the noise of the spectra at the cost of reduced frequency resolution and is a standard analysis method for DLDS [76] [66]. This method involves splitting the data of length N into M segments, overlapping by D points. The overlapping segments are windowed using a Hanning window and the periodogram is calculated by taking the DFT of segments and averaging. This method reduces the variance of the measurements causing the noise in the power spectrum to decrease. Peaks which have no observable width in the isolated method (see Fig. 3.36a) have been broadened to a full-width half-maximum of approximately 15 Hz with Welch's method (see Fig. 3.36b). As can be seen in Fig. 3.36, variance in the noise was reduced by 2 orders of magnitude, however, peak amplitudes were similarly reduced. Using the 3 σ variation from the mean definition, the limit of detection is $5.6 \times 10^{-11} V^2/Hz$ using Welch's method [76]. Identifying sample peaks by width is now more difficult as 60 Hz noise peaks are now broadened. The criteria for a potential signal peak are a full-width, half maximum greater than 15 Hz with an amplitude exceeding the LOD, and a variation in peak position with temperature.

A series of synthetic signals were used to test the system's LOD. An Agilent pulse generator was connected in place of the sample and used to provide sinusoidal voltage signals to the system. Peaks agreeing in frequency to the set value of the pulse generator could easily be seen and were used to validate the system.

Should a set of peaks greater than the LOD be observed that behave consistently and reproducibly, the peaks positions may be plotted on an Arrhenius plot of $ln\left(\frac{T^2}{2\pi f}\right)$ vs. $1/T$. If the trapping states follow the expected behaviour, a linear relationship should be observed with the slope of the line of best fit equalling E_A/k_B.

This system was a preliminary platform for the investigation of trapping states in MoS_2 with the intended implementation of a transimpedance amplifier for current noise measurements. Based upon the trap lifetimes reported by [45], it was hypothesized that detection of such states may have been possible with the frequency range of this system.

Results

Multiple samples were prepared using the sample preparation protocol and were analyzed using this method. Sample age (number of tests), room humidity, and drive voltage were all controlled. At least 10 samples were tested over the course of protocol development with 4 samples tested using the final protocol document herein. Samples were prepared using the hydrophobic bubble film formation protocol defined in § 3.3.3. To remove any possible effects of annealing all samples were tested at least twice. Room humidity was not initially recorded, however for the final 3 samples tested with this protocol, humidity was between 19 % and 47 % at the start of each run. No variation in sample characteristics was observed as a function of room humidity. Under all circumstances, the only peaks visible were 60 Hz harmonics which demonstrated no temperature dependence. Due to the temperature invariance, and more convincingly their presence without a sample (ie a commercial resistor in place of a sample), these peaks are attributed to AC coupling through the power source. In Fig. 3.37 representative power spectra analyzed using Welch's Method are presented. While 60 Hz noise is present, no additional features are visible. These spectra are representative of all runs with the final 4 samples tested. When driven with 10V, voltages of 0.002 V to 0.1 V were recorded by the ADC depending on sample and temperature. Additionally, while not all samples had the same resistance, no samples showed run to run variation in resistance.

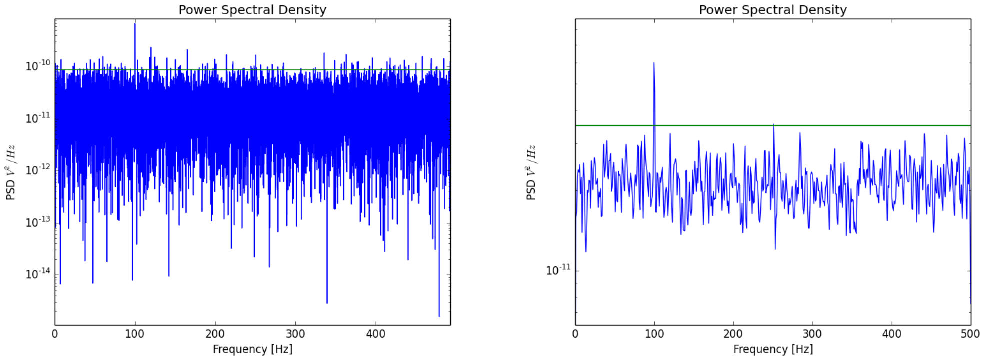

(a) (b)

Figure 3.36: Comparison of FFT vs. Welch's method with 100 Hz, $450\mu V$ P-P synthetic signal supplied by a pulse generator. In **(a)**, which used a single Fourier transform of the data, substantial variation in background noise is apparent with numerous peaks exceeding the limit-of-detection of $9 \times 10^{-11} V^2/Hz$. In **(b)** Welch's method was applied to the same spectrum lowering the fluctuation amplitude of the background noise and decreasing the limit-of-detection to $5.6 \times 10^{-11} V^2/Hz$. In this case it may be seen that only one peak exceeded the LOD which was the 100Hz synthetic signal. The resolution of the lock-in ADC is 1 mV, meaning that the $450\mu V$ pulse should not have been detectable. However, due to fluctuations in signal amplitude, so pulses may have been high enough to trigger the ADC causing the peak seen here.

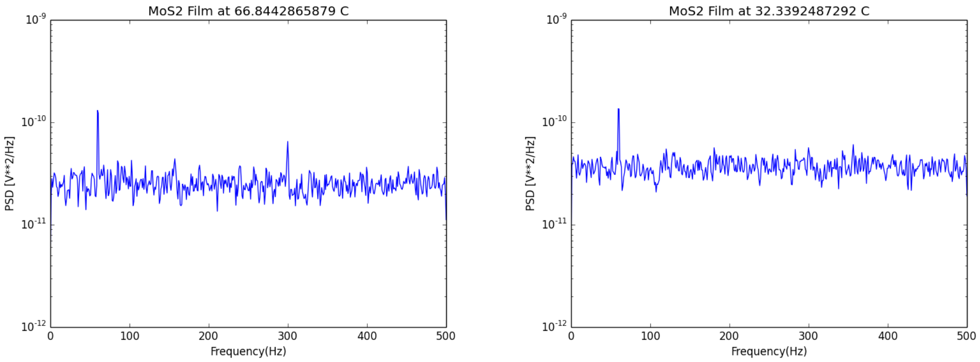

(a) T = 66.8°C

(b) T = 32.3°C

Figure 3.37: Representative power spectra taken during cooling of MoS_2 sample using Welch's Method. A single peak at 60 Hz is visible with white noise across the remainder of the spectrum. The noise of both samples has the same order of magnitude amplitude.

As no signal peaks could be found using the standard curve buffer, and calculations from the experimental results of Zhu *et al.* indicated trapping states would likely possess higher frequencies, the decision was made to transition to use of the fast curve buffer which raised the Nyquist frequency to 100 kHz [45].

3.5.4 Fast Curve Buffer

Data Collection

In the narrow temperature window available with this experimental setup, many trapping states may have characteristics frequencies greater than 500Hz (the Nyquist frequency of the standard curve buffer) as was noted by Zhu *et al* [45]. To investigate these higher frequency states, the fast curve buffer was used. This curve buffer allows for data collection at up to 200 kHz, but turns off all auxiliary inputs except for one ADC. As only one ADC was used in this setup this provided no real limitation. Table 3.38 summarizes the important parameters set for the Fast Curve Buffer Data Collection Procedure.

The maximum number of data points which could be collected was 100 000. As seen in the Fast Curve Buffer Data Collection code in Appendix B, only one ADC is ever added to the curve buffer so up to 100 000 data points may be collected at a given frequency. While this ran smoothly on computers with large amounts of RAM, instabilities existed when run on the lab Netbooks. While the way the code is structured still permitted retrieval of all collected data up to the point of freezing, this still exists as a necessary point of development. In the future, one of the HP Laptops with greater RAM may be substituted to resolve this problem. An alternative means of addressing this issue is by allocating the necessary memory prior to beginning the data sampling which would be a simple modification to the python code. The current operating procedure of collecting a smaller data set of 32

Setting	Value
Number of Time Points	96
Number of Data Points per Time Point	32768
Frequency	200 000Hz
T_{max}	$80°C$
Number of Heating Cycles (5 mins/cycle)	20
Number of Cooling Cycles (5 mins/cycle)	76
Drive Voltage	10V

Figure 3.38: Summary Table of Important Parameters set for Fast Curve Buffer Procedure

768 data points has proved to be stable in all tests.

To utilize this buffer, the circuit had to be modified to the one shown in Fig. 3.27. No additional capacitors are necessary for the system as by the same argument outlined in § 3.5.1, the sample resistance connected with the ADC input capacitance of 30pF will function as a low pass filter with a cut off frequency of 33kHz.

Other than the change in sampling frequency the procedure for utilization of the fast curve buffer remains identical to that of the standard curve buffer.

Data Analysis

The same analysis technique as was used for the Standard Curve Buffer is valid here with the obvious changes to sampling frequency and the number of points collected.

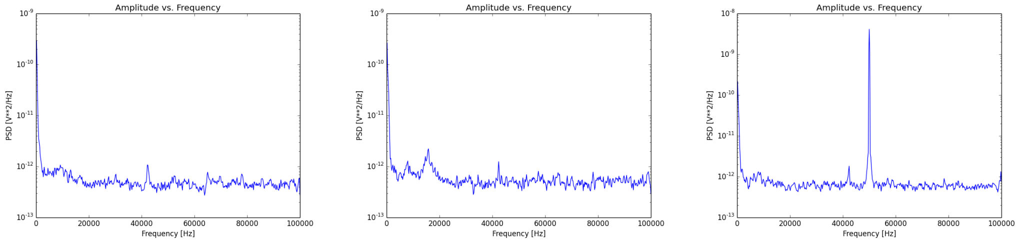

(a) (b) (c)

Figure 3.39: System Validation for Fast Curve Buffer. All spectra were analyzed using Welch's Method. **(a)** Power spectrum of $1M\Omega$ resistor taken at 200kHz sampling rate with $0V$ drive voltage. **(b)** Power spectrum of $1M\Omega$ resistor taken at 200kHz sampling rate with $10V$ drive voltage. **(c)** Power spectrum of $1M\Omega$ resistor taken at 200kHz sampling rate with a $50kHz$, $100mV$ peak-to-peak drive voltage

In Fig. 3.39, representative power spectra calculated using Welch's Method are presented [76]. A constant baseline is clearly observable in all three panels. A small peak is observed at approximately $42kHz$ in all cases. While difficult to investigate this peak may originate internally from the LI as it is present in all cases and is invariant of the sample (ie. present with MoS_2 and commercial resistor). The LOD using Welch's Method of the system, determined using the same method discussed in § 3.5.3, was determined to be $5 \times 10^{-12} V^2/Hz$ which exceeds any anomalous peaks. Further investigation is necessary to determine a source of this peak. As seen in Panel (b) small, transient peaks below 20kHz are present in approximately 50% of the spectra with no clear connection to temperature apparent, and likely originate from the DAC. The sharply increasing power spectral density at low frequencies (less than 1 kHz) is due to the limited sample size of 2^{15} data points and high sampling rate of 200 kHz. Increasing the number of data points collected would reduced this noise, but was observed to cause memory instabilities when the laboratory netbooks were used. When run on a laptop with more memory, no such instabilities were observed. As this was a preliminary study, and the low frequency regime was investigate using the standard curve buffer this issue was not addressed in any manner other than by switching laptops. In the future, adjusting the Python code to allocate memory in advance of beginning collection would likely address this issue.

Results

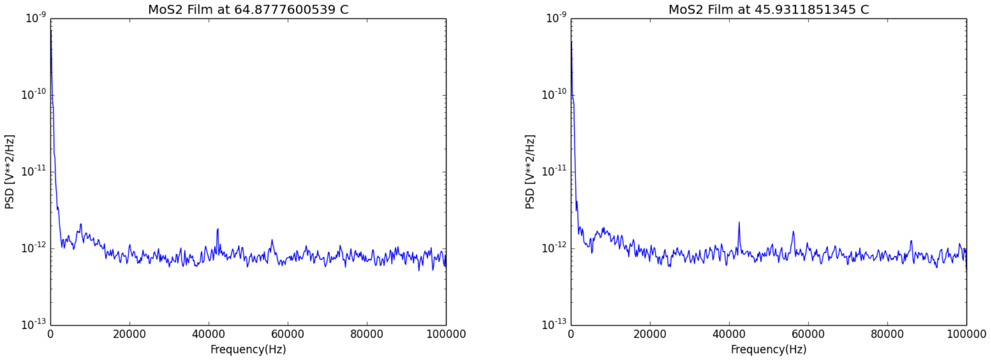

(a) T = 64.8°C (b) T = 45.9°C

Figure 3.40: Representative spectra of MoS_2 sample taken at 200kHz and analyzed using Welch's Method. A baseline consistent with the validation results is seen with the spurious peak at 42kHz. No peaks above the LOD of $5 \times 10^{-12} V^2/Hz$ were observed.

Fig. 3.40 shows representative spectra collected at the 200kHz sampling rate. As seen in the validation , a spurious peak at 42kHz is observed. Several small peaks were additionally observed, however, were temporal in nature and disappeared in subsequent spectra. Investigations at various sampling frequencies above 1kHz were conducted with multiple samples, however, all yielded spectra similar to Fig. 3.40. Three separate samples prepared using the same SOP as for the standard curve buffer (§ 3.3.3 were examined at the 200kHz sampling frequency with all samples tested at least twice. One sample was tested 5 times with no observed changes in electrical properties. The multiple examinations of each sample were designed to test for annealing effects which may be present in the first run. For all runs room humidity was between 21 % and 44 %, but no variation was observed.

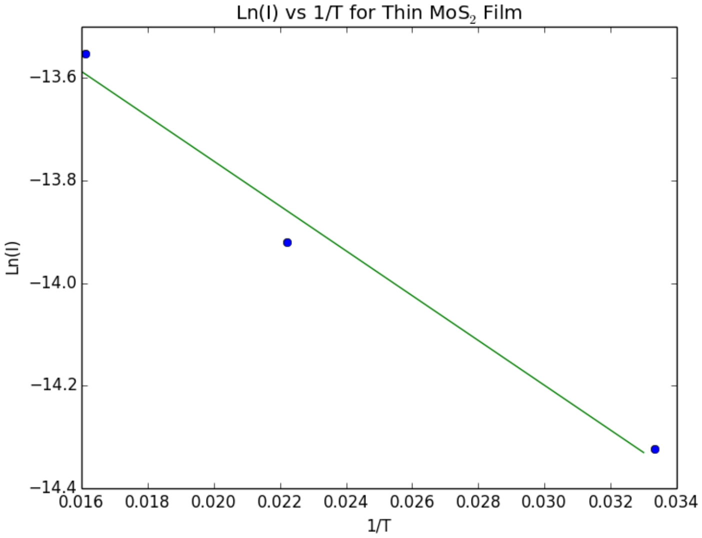

Figure 3.41: Arrhenius plot for $LN(I)$ versus $1/T$. When a linear fit was performed, an activation energy of 0.16 eV was calculated from the slope.

Although no temperature dependent frequency components of the voltage noise signals were seen at frequencies ranging from 0Hz to 100kHz, preliminary sample thermal control and voltage noise monitoring was demonstrated. An activation energy of 0.16 eV was obtained through monitoring current as a function of temperature which agrees with activation energies for mid-gap trapping states from the literature. This Arrhenius plot may be seen in Fig. 3.41. Based upon results from Zhu *et al.*, it is likely that such a trapping state would likely be very close to our upper bandwidth limit. Additionally, it may be below our limit-of-detection as no signal amplification was performed. Future developments with this project should include the use of a transimpedance amplifier which would allow for a more standard implementation and improve the sensitivity of the system (due to amplifier gain rather than unitary gain). A similar amplifier circuit to that seen in Fig. 3.22 inserted after the sample, but before the lock-in in the circuit seen in Fig. 3.26 could add the necessary functionality.

3.6 Conclusion

Rapid prototyping inspired processing and characterization techniques were applied to the preparation of molybdenum disulfide for electronic applications. Substantial infrastructure development was performed in multiple areas; much of which is still being used and developed by others. A reproducible sample preparation protocol was developed along with processes for fabrication of thin films from the products. Additionally, much of the infrastructure necessary for optical characterization in the form of absorption and photoluminescence spectroscopy was completed. An important outcome of this project was the identification of experimental scattering artifacts which could have hindered future progress if not properly identified. While future optimization of these protocols is necessary, they represent a reproducible benchmark to which future results may be compared. Similarly to the optical characterization, substantial infrastructure development was performed for the electrical characterization of MoS_2 films with the assembly and validation of a robust, thermally controlled system capable of performing DLDS with the addition of a transimpedance amplifier circuit. There was insufficient time to complete this investigation along with characterizing the superhydrophobic surfaces discovered while fabricating graphene electrode structures which proved to be of great interest and will the topic of the next two chapters of this thesis. It is hoped that the infrastructure developed herein will act as a starting point for future work and the tools developed will assist in the growth from protocol development to device fabrication and testing.

Chapter 4

Laser Processing of Superhydrophobic Graphene Films

4.1 Introduction

As discussed in Chapter 3, unexpected hydrophobic behaviour was observed on the graphene surface of Kapton which had been chemically modified with the use of a rapid prototyping laser. Upon further investigation, it was discovered that by adjusting the laser power and lattice spacing the surface wettability could be controllably tuned. Under optimal conditions, these rapidly prototyped surfaces are some of the most superhydrophobic ever reported and address the long-standing issues of manufacturability, controllability, and durability.

Due to their excellent self-cleaning and anti-sticking properties, superhydrophobic materials are desirable for applications such as oil/water separation, corrosion resistant coatings, and water repellent fabrics [77]. A material is defined to be superhydrophobic if it has a water contact angle of greater than 150°; roll-off angles of less than 5° and low hysteresis between the advancing and receding contact angles are commonly also observed in such materials [78].

To understand the behaviour of water on a superhydrophobic surface it is first important to understand the models and physics of such systems. A droplet of water on a smooth, flat surface, such as that of unmodified polyimide can be described by Young's Equation (Eq. 4.1) which relates the contact angle to a function of interfacial tensions [79]. The contact angle is defined to be the angle between the substrate surface and a line drawn tangent to the droplet surface, passing through the three-phase interface (see Fig. 4.1).

$$cos\theta = \frac{\gamma_{sv} - \gamma_{sl}}{\gamma_{lv}} \tag{4.1}$$

Young's Equation is seen in Eq. 4.1 where γ_{xy} denotes interfacial tension between the solid(s), liquid(l) and vapour (v) phases. Substrates with a low surface energy will have a higher contact angle as it will be energetically favourable for the water to remain in bulk rather than spread to form an interface with the substrate.

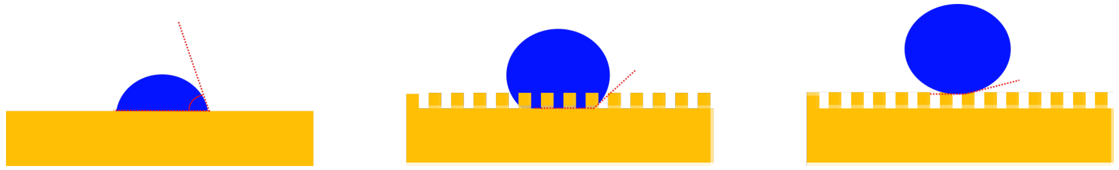

Figure 4.1: Three different wetting states. On the left is a flat surface which is modelled by Young's Equation and may be either hydrophilic or hydrophobic (Eq. 4.1). In the middle is the Wenzel state where water permeates into the spaces between surface roughness and is modelled by Eq. 4.3. On the right is the Cassie-Baxter state where droplets remain suspended above the structures below (Eq. 4.4). The later two states may exhibit superhydrophobicity (contact angles greater than 150°).

While Young's Equation accurately models flat, homogeneous surfaces most superhydrophobic surfaces have a degree of roughness to them, for reasons discussed below, which must be characterized using either the Wenzel or Cassie-Baxter model. The Wenzel state is a micro or nanostructured surface with low surface energy [79]. The roughness increases the surface area by a factor of r seen in Eq. 4.2. In the Wenzel state, the water droplet will surround the microstructures. The Cassie-Baxter state is similar to the Wenzel state in that it is a micro or nanostructured low surface energy surface; however, in this state the water droplet is supported by a cushion of air within the surface and bridges the structures [79]. The differences between these surfaces may be seen in Fig. 4.1.

For calculating the contact angle, the Wenzel and Cassie-Baxter states share a roughness factor defined in Eq. 4.2 [79].

$$r = A_{actual}/A_{planar} \tag{4.2}$$

The Wenzel state is characterized by Eq. 4.3 in which it may be seen that by introducing a surface roughness of r, it will increase the Young's state of the material [79]. This may be seen in Eq. 4.3 where the cosine of the contact angle determined using Young's Equation (Eq. 4.1) is scaled by a factor of r and as r is never negative it will always increase the natural state of the material [79]. For example, if a flat material had a contact angle of θ (determined by Eq. 4.1), and then a surface roughness of r was fabricated into the material, the resulting structure, in the Wenzel state, would have a contact angle determined by Eq. 4.3.

$$cos\theta_w = rcos\theta \tag{4.3}$$

The Cassie-Baxter model is described by Eq. 4.4 where f_1 and f_2 may be determined by projecting the solid and vapour portions respectively onto the surface and determining the fraction associated with each[79].

$$cos\theta_{CB} = rf_1cos\theta - f_2 \tag{4.4}$$

.

In short, surfaces with low surface energies and high degrees of roughness will form the most superhydrophobic surfaces. Thus the objective of designing a superhydrophobic surface requires two factors: appropriate chemistry to minimize the energy of the surface, and fabrication techniques to enhance the surface roughness.

Traditionally, superhydrophobic materials are fabricated in one of two ways: increasing the surface area of inherently low surface energy materials, or fabricating a high surface area material then coating or modifying to lower surface energy[79] [80] [81] [82]. An example of a surface fabricated in the second manner of particular note is a silane coated glass microcone array which had a contact angle of 179°, the highest ever reported [82].

Recently, carbon-based superhydrophobic materials have emerged as a field of promising study with demonstrations of their application to oil-water separation, conductive-transparent films, and self-cleaning applications [83][84][79]. Initial development was focused on using the carbon to create highly textured surfaces. An example of such a surface was an array of vertically aligned carbon nanotubes (VACNT), which when coated with poly(tetrafluoroethylene) had contact angles of up to 170° [85] [86]. The use of activated carbon or graphite as a high surface area skeleton for hydrophobic coatings was demonstrated to produce hybrid materials with contact angles approaching 170° [87]. Contact angle control of graphene surfaces and heterogeneous mixture of graphene and polymers such as PVDF has been demonstrated with contact angles varying from hydrophilic to superhydrophobic [84] [88] [88]. Wang *et al.* demonstrated that laser roughening of graphene oxide surfaces could increase hydrophobicity up to 160°[89]. Control of the wettability of graphene has been demonstrated by varying the substrate onto which it is applied [88]. Recently, a thermally stable superhydrophobic graphene coated sponge capable of repetitive separation of organic solvents from water was reported [90]. Based upon this literature it is clear that graphene is important for the development of novel superhydrophobic materials.

Similarly to carbon-based surfaces, various polymeric superhydrophobic surfaces have been demonstrated. Several examples of superhydrophobic surfaces fabricated from high porosity polymers using such techniques as polymerization with porogenic solvents, electrospinning of fluorinated polyimide, and enhancing the roughness of Kapton films using ArO_2 plasma treatment have been reported [91] [92] [93]. As identified in a recent review, texturing of surfaces through UV, visible, and near-infrared (NIR) laser processing has produced superhydrophobic surfaces [94]. Two beam UV laser interference was used to pattern the surface of graphene oxide films by Wang *et al.* and a similar technique with a visible laser was used by Jin *et al.* to pattern the surface of PDMS [89] [95]. It should be noted that in these instances laser patterning was used to structure the surface of already hydrophobic materials. In a similar experiment Wohl *et al.* used UV laser patterning to fabricate 25 μm pillars into the surface of copoly(imide siloxane) and polyimide [96]. As this processing elicited a structural change and not a chemical, the additional roughness served to enhance the hydrophobicity of the already hydrophobic copoly(imide siloxane) and vice versa for the initially hydrophilic polyimide. Using nano and femto second UV laser pulses Pazokian *et al.* microstructured the surface of polyethersulfone (PES) creating a superhydrophobic surface[97]. While slight chemical modification was observed, the methodology neither allowed for patterning or manufacturability.

In a recent review of the current state of superhydrophobic materials six general limitations of the field were identified: a lack of cost-effective manufacturing strategies, poor long term structural stability, weak durability, little resistance to water vapour, poor resistance to impingement, and a lack of resistance to chemical contaminants, making commercial implementation challenging [78]. In a separate review, Bär *et al.* noted similar fabrication challenges in that many existing methods for the preparation of superhydrophobic surfaces require either harsh conditions or complicated fabrication processes. They identified 8 candidate techniques satisfying the criteria for a facile and potentially manufacturable fabrication; however, reported that none of the techniques exhibited long-term stability of their superhydrophobic properties [98]. From this they concluded the need for fabrication methods for superhydrophobic surfaces which are facile and produce durable surfaces. Based upon these two complementary reviews, it may be concluded that there exists a substantial need for a superhydrophobic surface which may be produced in a manufacturable manner and is robust in a variety of environmental conditions.

Herein we demonstrate the surface modification of Kapton using laser ablation with precise control of contact angles and roll-off angles with values varying from $40° - 171°$ and $0.61° - 180°$ respectively. Lin *et al.* demonstrated the production of porous graphene films in Kapton using laser ablation, however, made no report of hydrophobic behaviour[62]. A contact angle of 171° corresponds to one of the highest ever reported for carbon-based superhydrophobic materials, and the roll-off angle of 0.68° is similarly at the state of the art. Additionally, this material is the first carbon-based superhydrophobic material to exhibit the Moses Effect and was observed to be exceptionally robust in a variety of environments. When compared with a study by Bar *et al.*, it becomes evident that our material exceeds the state-of-the-art for facile, robust superhydrophobic coatings and represents a significant advance in the field. Our process satisfies the criteria for a facile fabrication process and outperforms all of the tested samples in contact angle and roll-off angle measurements.

A paper based on the material in this chapter was submitted to Advanced Functional Materials, but was judged to have insufficient novelty and rejected. However, a paper utilizing a similar methodology was submitted later by a different group and published in Advanced Materials [99]. The paper from the other group functionalized the surface of laser-induced graphene by performing the ablation in a controlled gas atmosphere. They demonstrated contact angle control over a range by varying the atmosphere. When compared with our technique of contact angle control by varying the laser power, there are several key differences. The use of a controlled gas atmosphere decreases the manufacturability of such surfaces and adds extra costs to the process. Additionally, the surfaces produced by [99] did not demonstrate the so-called 'Moses Effect' and had maximum contact angles which were approximately 10° lower than reported herein.

4.2 Materials and Methods

4.2.1 Surface Fabrication

As with the previously discussed graphene electrodes, 63.5 μm thick Kapton HN tape (McMaster Carr, 7648A34) was adhered to a glass microscope slide. Rather than an interdigitated electrode pattern, the 30 W Universal Laser Systems VLS 2.0 CO_2 laser was used to pattern a square grid (ie. array or lattice) of graphene traces into the tapes surface (see Fig. 4.2). As discussed previously, the laser stepper motor is quantized in increments of 1/72”. Due to this quantization, all design was performed in units of 1/72”. The grid spacing was varied from 1/72” to 4/72” while the laser power was varied from 1 % to 6 %. The additional laser parameters of speed, pulses-per-inch (ppi), focus, and quality were held constant at 10 %, 1000, 1.0 mm, and High respectively. These surfaces were viewed through both optical microscopy and scanning electron microscopy (SEM). SEM images were taken by Dilara Yilman by first gold coating the samples then using a Zeiss LEO FESEM 1530 at 5 kV acceleration voltage and using secondary electron detection to collect the images. SEM images of a surface with a grid spacing of 1/72” and powers from 1 % to 5 % are shown in Fig. 4.7.

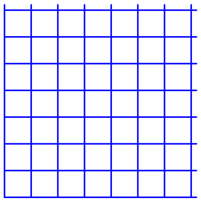

Figure 4.2: Asymptote schematic for square grid pattern ablated into Kapton surface using VLS 2.0 CO_2 laser creating a surface with tunable wettability. Grid spacing was varied from 1/72” to 4/72”. Asymptote code is available in Appendix B.

4.2.2 Contact Angle Measurements

Contact angle measurements were taken using guidelines discussed by [100]. A sessile drop contact angle goniometer as previously used in [101] was used to perform contact angle measurements. 5 μL droplets of de-ionized water (18 MΩ cm) were aliquoted onto the surface to advance or retreat the droplet using a syringe pump (New ERA Pump Systems Inc NE-1010 Syringe Pump). Images were taken in 8-bit greyscale with a Basler SCA 1000 30 fm camera focused at the three phase interface on the circumference of the spherical droplets. The minimum droplet volume of 5 μL was used as it prevented droplet pinning and produced a droplet which was large relative to surface roughness. The syringe was used to advance or retreat the droplet after which the needle was removed before measurement. It was shown that the presence of the needle in the droplet could vary the contact angle by up to 25°.

Contact angles were calculated using one of two algorithms in ImageJ ([2]), which is general purpose image analysis program. The primary algorithm used was the

Dropsnake algorithm (as in [91]) which utilizes a B-spline fit and returns separate contact angles from both sides of the droplet, thus making no assumptions of drop shape or symmetry [102]. It is available as a free package for ImageJ from [102]. To initialize the algorithm, the circumference of the droplet was manually traced with 7 points. Variation in point placement (manual bias) was investigated and found to have no impact on the result. Subsequently, the algorithm was run and the droplet was enclosed within points spaced at 20 pixel intervals with a convergence limit of 0.01°. As a measure of variability, the difference in left and right contact angles was recorded. Unless otherwise stated, all reported contact angles used this method.

As corroboration, the Low-Bond Axisymmetric Drop Shape Analysis (LB-ADSA) algorithm was applied to the data set [103]. It is available as a free package for ImageJ from [103]. This algorithm is standard in many analyses ([78] [88]) and operates by solving the Laplace equation under the assumption of mirror symmetry. To apply this algorithm within ImageJ, the droplet was manually circled within a selection ring. Again the influence of manually selecting the droplet was investigated and found to have no impact. The algorithm was then run with a convergence limit of 0.01° and the results recorded.

Use of the goniometer allowed for accurate measurement of the contact angle, however, it was not practical for monitoring the change in contact angle due to various experimental conditions. In these scenarios, the relative change in contact angle was of greater interest than the absolute value. An in-lab system was developed to perform these measurements comprised of an Andonstar 2.0 MP USB microscope which was vertically aligned to a levelled stage supporting the samples. A 1 mL syringe held vertically by a retort stand was used to advance a droplet of 10-15 μL of DI water on the surface. A halogen lamp was used to illuminate the sample from behind with the camera focused on the three-phase interface of the circumference of the spherical droplets. Measurements were repeated in triplicate and analyzed using ImageJ as above. Contact angles were reproducibly observed to be systematically lower by approximately $3 \pm 1°$ compared to goniometer measurements. This is likely due to inferior lighting and focus at the bottom of the droplet, decreasing the resolution at the contact point.

4.2.3 Rolling Angle Measurements

The rolling angle is defined to be the angle at which a droplet resting on the surface will roll continuously off the surface. The rolling angle was measured using a two-axis micrometre controlled staged. A sample was placed on an initially levelled stage and a 10 μ L droplet was deposited on the surface. One micrometre was used to slowly raise one side of the stage until continuous droplet movement was observed and all trials were repeated in triplicate. In this regime, the uncertainty in rolling angle was ±0.01°. Due to limited micrometre range, for rolling angles greater than 10°, measurements were taken with a protractor under manual sample manipulation with an uncertainty of ±5°.

4.2.4 Durability Testing

As noted in a recent review of superhydrophobic surfaces ([78]), many surfaces suffer from a lack of durability and temporal stability. To test the durability of our samples they were exposed to pressurized water jets, bouncing droplets of water, mineral oil, and the scotch tape test. The so-called 'Moses Effect' ([78]) is the ability of a surface to completely expel water from above it (parting the sea) and is an effective way to measure the temporal stability of a superhydrophobic surface. This effect was investigated with both pure water and saline solutions.

As discussed in § 4.1, superhydrophobic films in the Cassie-Baxter state rely upon a cushion of air existing between the droplet and the surface. Once this cushion has been impinged, superhydrophobic characteristics are frequently lost due to a transition from Cassie-Baxter to Wenzel states as noted Bär *et al* [98]. As a test of resistance to impingement, two 10 mL jets of DI water at approximately 310 kPa were applied at orthogonal incidence to the films from approximately 2 cm above their surface using a syringe (10 mL, BD Luer Lock) which was emptied in approximately 1 second. The pressure was estimated based upon evacuation time of syringe and nozzle diameter using Bernoulli's Equation. The contact angles were recorded before and after exposure using the in-lab Andonstar system. As a further investigation of the surface's resistance to pressurized flow, the bouncing behaviour of droplets incident from 10-15 cm above the surface was recorded at 120 frames/s using an iPhone 5S.

Resistance to contaminants was tested by deposition of 10 μL of mineral oil (Sigma 8042-47-5) onto the sample's surface and allowing the oil to spread through the sample for 5 minutes. Subsequently, the contact angle of a 10 μL water droplet was measured before the sample was placed in a 200 °C oven for 2 hours. After removal, the sample was allowed to cool before the contact angle was measured again. This experiment tested resistance to contaminants, self-cleaning properties, and thermal stability.

Finally, the Scotch tape test was used to quantify the mechanical durability of the superhydrophobic films. A 3/4" wide strip of Scotch Matte Finish Magic Tape (34-8702-0325-3) was adhered to a sample surface and pressed down until clear over the 12.5 mm wide patterned region. Pulling at a 45 ° angle the tape was removed in approximately 0.5 seconds. This process was repeated 5 times with new tape every time after which the contact angle was again measured.

4.2.5 Evaporative Desalination

As discussed in § 4.1, superhydrophobic films have demonstrated promising application to evaporative desalination. As a demonstration of this effect, 50 μL droplets of 35 g/L NaCl solution were deposited on both untreated Kapton and a superhydrophobic processed region. The droplets were allowed to dry and resulting salt deposits were qualitatively analyzed. Contact angles were measured both before and after exposure. This process was repeated for 10 cycles.

4.3 Results

4.3.1 Contact Angle

The most important parameter for a superhydrophobic surface is the contact angle which was observed to vary as a function of both laser power and lattice spacing. This effect is seen in Figures 4.3, 4.4, and 4.5 for lattice spacings of 1/72", 2/72", and 3/72" respectively with numerical values tabulated in Table 4.1. It may be seen that by varying laser power, the surface may be adjusted from more hydrophilic to more hydrophobic than native Kapton whose contact angle was measured to be 73 ± 3°. The most superhydrophobic surface prepared using this method was with 1/72" spacing and 4% laser power which had an average measured contact angle of 171.2° with values as high as 173.8° recorded. When analyzed using the LB-ADSA algorithm, angles averaging 176° were observed. The surfaces could also be made to be more hydrophilic with contact angles as low as 56.64 ± 3.7° measured for 2% power. Surfaces with larger lattice spacing exhibited similar behaviour as may be seen in the weak spacing dependence of Fig. 4.6; however, smaller ranges of contact angles were observed. As well, larger lattice spacing was observed to result in greater contact angle hysteresis.

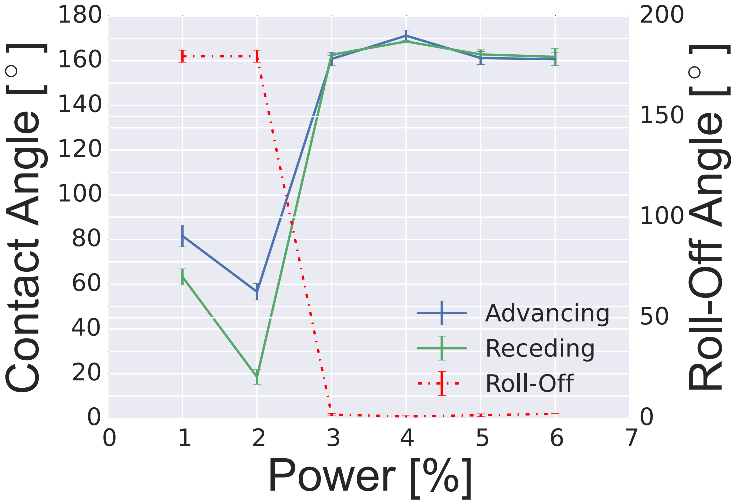

Figure 4.3: In blue and green, advancing and receding contact angles for superhydrophobic patterns with a grid spacing of 1/72" as a function of power are respectively seen. An initial decrease in contact angle may be seen with high hysteresis between advancing and receding. The highest value of 171.2 ± 2.5° is at 4% power. In red, the rolling angle may be seen which follows an inverse relationship to contact angle. Reprinted from "Robust Superhydrophobic Laser-Induced Graphene for Desalination Applications," by Collin M. Tittle, Dilara Yilman, Michael A. Pope, and Christopher J. Backhouse, 2018, *Advanced Materials Technologies, Volume 3,* p. 1700207. Copyright Wiley-VCH Verlag GmbH & Co. KGaA. Reproduced with permission. [6]

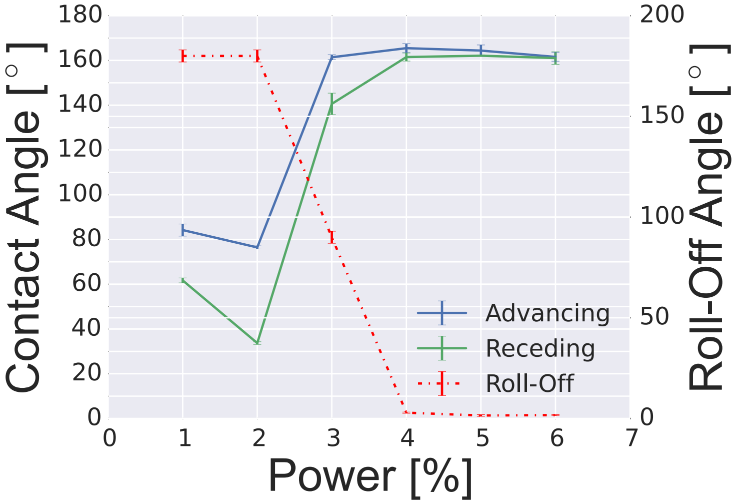

Figure 4.4: In blue and green, advancing and receding contact angles for superhydrophobic patterns with a grid spacing of 2/72” as a function of power are respectively seen. An initial decrease in contact angle may be seen with high hysteresis between advancing and receding. The highest value of $165.48 \pm 2°$is at 4% power. In red, the rolling angle may be seen which follows an inverse relationship to contact angle. Reprinted from ”Robust Superhydrophobic Laser-Induced Graphene for Desalination Applications,” by Collin M. Tittle, Dilara Yilman, Michael A. Pope, and Christopher J. Backhouse, 2018, *Advanced Materials Technologies, Volume 3,* p. 1700207. Copyright Wiley-VCH Verlag GmbH & Co. KGaA. Reproduced with permission. [6]

	Spacing					
	1/72”		2/72”		3/72”	
Power	Advancing (°)	Retreating (°)	Advancing (°)	Retreating (°)	Advancing (°)	Retreating (°)
1	81.63 ± 4.9	63.32 ± 3.6	84.21 ± 2.7	61.71 ± 1.1	90.44 ± 3.4	68.38 ± 9.4
2	56.64 ± 3.7	18.55 ± 3.3	76.45 ± 0.7	33.71 ± 0.6	95.06 ± 4.9	33.21 ± 1.7
3	160.78 ± 3	162.66 ± 0.3	161.41 ± 1.1	140.59 ± 4.8	159.34 ± 2.7	103.17 ± 9.9
4	171.2 ± 2.5	168.61 ± 0.4	165.48 ± 2	161.51 ± 1.8	170.23 ± 1.5	150.45 ± 5.9
5	161.2 ± 2.9	162.83 ± 2.1	164.41 ± 2.5	162.12 ± 0.3	161.57 ± 2.8	162.09 ± 1.1
6	160.65 ± 2.9	161.72 ± 3.8	161.58 ± 1.9	161.05 ± 2.8	161.78 ± 1.9	159.88 ± 3.4

Table 4.1: Table of contact angles as a function of lattice spacing and laser power. Reprinted from ”Robust Superhydrophobic Laser-Induced Graphene for Desalination Applications,” by Collin M. Tittle, Dilara Yilman, Michael A. Pope, and Christopher J. Backhouse, 2018, *Advanced Materials Technologies, Volume 3,* p. 1700207. Copyright Wiley-VCH Verlag GmbH & Co. KGaA. Reproduced with permission. [6]

4.3.2 Rolling Angle

As shown by the red line in Fig. 4.3 and in Table 4.1, for the most superhydrophobic surface (1/72” spaced lattice, 4 % power), the rolling angle was measured to be as low as $0.61 \pm 0.01°$. While the measurement uncertainty was $\pm 0.01°$, the standard

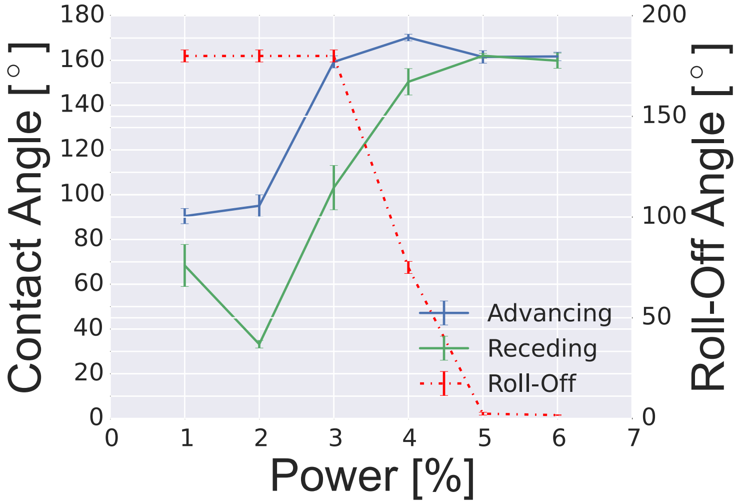

Figure 4.5: In blue and green, advancing and receding contact angles for superhydrophobic patterns with a grid spacing of 3/72” as a function of power are respectively seen. An initial decrease in contact angle may be seen with high hysteresis between advancing and receding. The wider spacing of this grid leads to the formation of intermediate states at 3 % and 4 % power which are characterized by high contact angles, hysteresis, and rolling angles. The highest value of 170.23 ± 1.5° is at 4% power. In red, the rolling angle may be seen which follows an inverse relationship to contact angle. Reprinted from ”Robust Superhydrophobic Laser-Induced Graphene for Desalination Applications,” by Collin M. Tittle, Dilara Yilman, Michael A. Pope, and Christopher J. Backhouse, 2018, *Advanced Materials Technologies, Volume 3,* p. 1700207. Copyright Wiley-VCH Verlag GmbH & Co. KGaA. Reproduced with permission. [6]

deviation of multiple runs was 0.3° which may indicate the presence of surface variability. Intermediate rolling angles of approximately 90° may be seen in Figures 4.4 and 4.5 which is much greater than the rolling angle of unprocessed Kapton tape which was measured to be approximately 30°. Under slightly larger lattice spacing (4/72”, not shown here) samples could be rotated completely upside down with the droplet remaining attached which corresponds to a rolling angle of 180° as may be seen in Fig. 4.9b after which samples could be left inverted until the droplet evaporated. The corresponding adherence force must be at least equal to the force of gravity (490 μN).

4.3.3 Scanning Electron Microscopy

Fig. 4.7 shows SEM images of the surfaces prepared at 1/72” lattice spacing with powers ranging from 1% to 5%. Little surface roughness is visible at low laser powers, but after a threshold of approximately 3% power, significant featuring is clearly visible. As can be seen in Eq. 4.4, additional surface roughness acts to increase the contact angle and images taken at higher magnification (not shown here) indicate

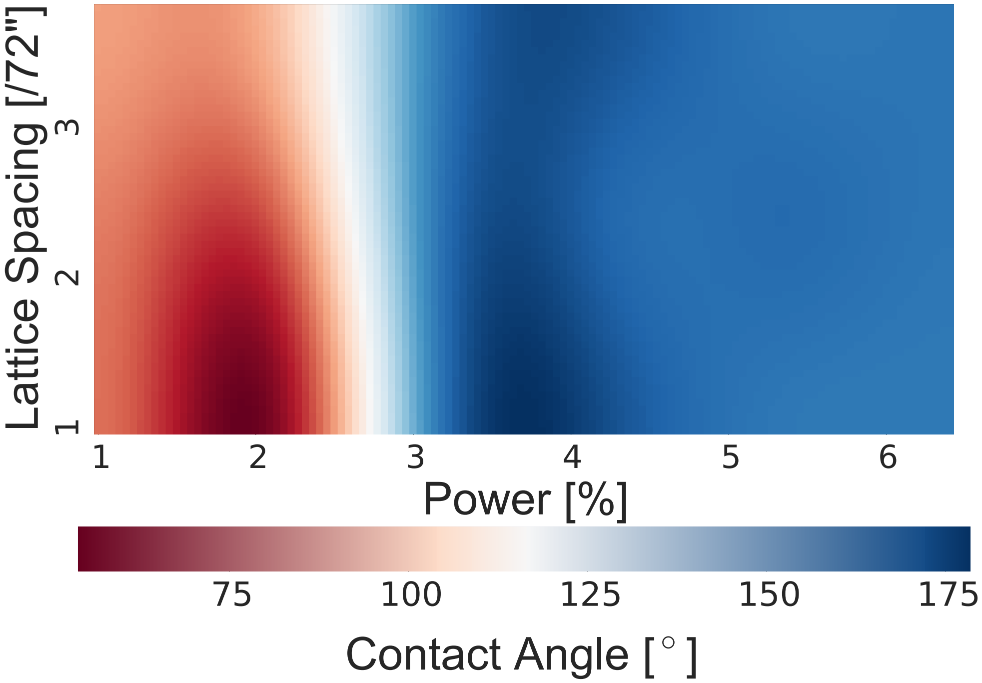

Figure 4.6: Surface plot of contact angle as a function of lattice spacing and power. Weak dependence on lattice spacing is observed with a strong dependence on laser power. Evidence of carbonization (ie. surface appears black) is visible at all power settings greater than or equal to 2%. Electrical conductivity was observed for 4% power, but was not investigated for other power settings. Reprinted from "Robust Superhydrophobic Laser-Induced Graphene for Desalination Applications," by Collin M. Tittle, Dilara Yilman, Michael A. Pope, and Christopher J. Backhouse, 2018, *Advanced Materials Technologies, Volume 3,* p. 1700207. Copyright Wiley-VCH Verlag GmbH & Co. KGaA. Reproduced with permission. [6]

the presence of nanoscale features. Individual traces were observed to be conductive with resistivities of 5 - 15 $k\Omega$/cm, however for clear SEM images, gold coating was used to improve electrical conduction. After samples were prepared as detailed in § 4.2, they were gold coated and SEM images were taken by Dilara Yilman using a Zeiss LEO FESEM 1530 with a 5 kV accelaration voltage and secondary electron detection.

4.3.4 Desalination

The results from the evaporation of 50 μL droplets of 35 g/L NaCl solution on processed and unprocessed surfaces may be seen in Fig. 4.8. On untreated Kapton surfaces, dried salt may be observed to be adhered to the surface indicating surface wetting. While Kapton is resistant to corrosion, similar salt adherence on aluminum or steel surfaces may cause significant damage [78]. Additionally, such adherence

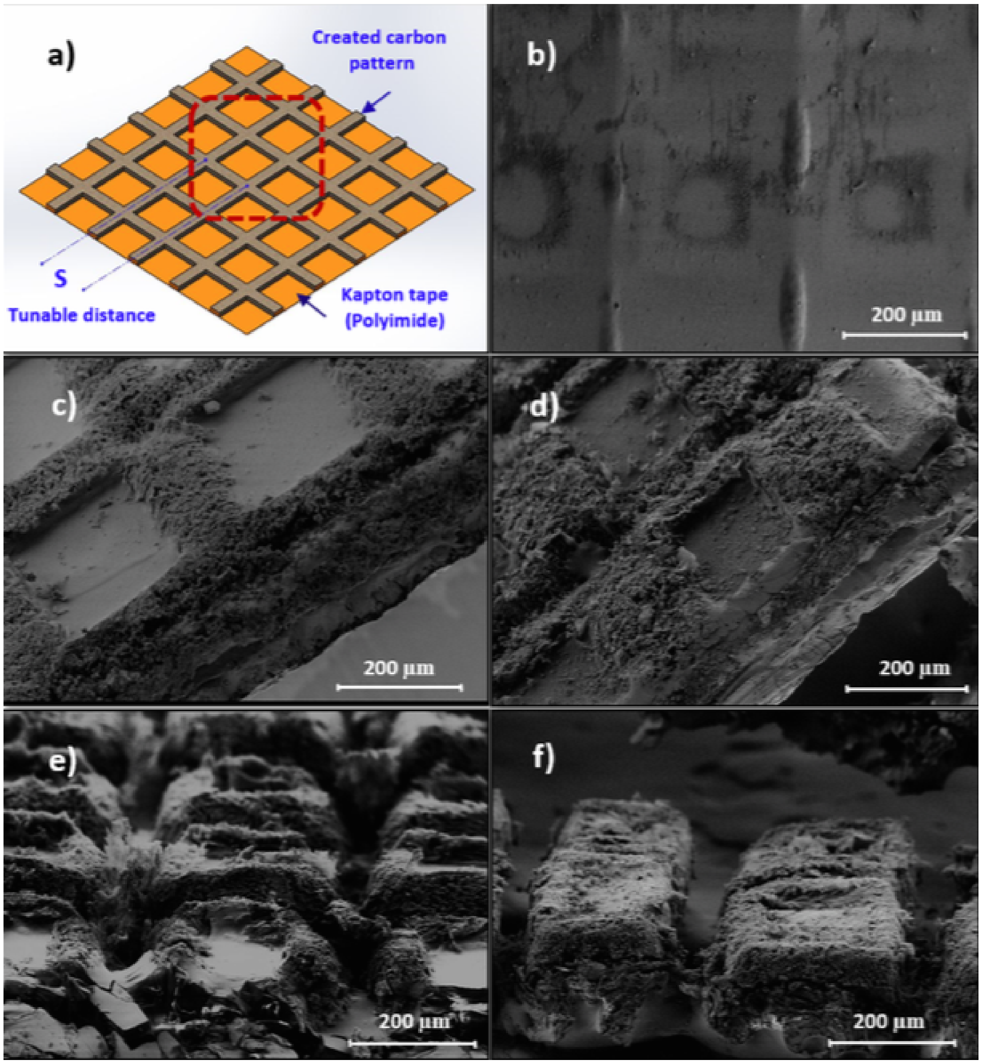

Figure 4.7: Process schematic and SEM images of surface of 1/72" spaced array. Laser powers increase linearly from 1% in Panel b) to 5% in Panel f). At low powers, little carbonization and surface featuring is visible, whereas at higher power significant carbonization and featuring is apparent. Images taken and figure created by Dilara Yilman.Reprinted from "Robust Superhydrophobic Laser-Induced Graphene for Desalination Applications," by Collin M. Tittle, Dilara Yilman, Michael A. Pope, and Christopher J. Backhouse, 2018, *Advanced Materials Technologies, Volume 3,* p. 1700207. Copyright Wiley-VCH Verlag GmbH & Co. KGaA. Reproduced with permission. [6]

makes salt recovery difficult and, over time, significant deposits could develop impairing fluid flow or device function. However, on the superhydrophobic surfaces seen in Fig. 4.8d, all visible salt formed a single crystal which was easily removed by tilting. This indicates little surface wetting and thus the minimal opportunity for corrosion. Additionally, salt recovery is extremely simple with such surfaces. This evaporative process was repeated ten times with no change in contact angle or rolling angle observed. Additionally, after a sample was submerged in saline solution for seven days no change in contact angle was observed. Surface fouling by salt -adhesion of insufficiently superhydrophobic is a known mode of failure [104]. Fig. 4.8d shows an optical microscopy image of a salt crystal formed on the surface of a superhydrophobic array.

4.3.5 Confinement

These surfaces have been demonstrated to be capable of strongly confining water to particular regions. Fig. 4.9a is a representative image from the contact angle goniometer in which highly spherical droplet shape is observed. As was discussed in the section on rolling angles, strong adherence to certain superhydrophobic surfaces has been seen as in Fig. 4.9b where a surface has been rotated through 180° with the droplet maintaining contact. An important demonstration of confinement and patternability is seen in Fig. 4.9c where one region with hydrophilic behaviour is seen on the left within 350μm of a superhydrophobic region on the right. When considered with the previous two characteristics, it is clear that it is possible to create arrays of highly confined droplets, pinned to specific hydrophilic locations with high resistance to shifting. This is crucially important for applications such as multiplexed arrays for biological assays.

As discussed in § 4.2, the Moses Effect demonstrates high levels of superhydrophobicity. Sustained demonstration of this phenomenon corresponds to high levels of surface stability. As may be seen in Fig. 4.10, samples demonstrated the Moses Effect with both pure water and saline solutions repelling up to 5 mm of solution from their surface. Additionally, no collapse of the Moses Effect (which would correspond to a change in hydrophobicity) has been observed with tests exceeding 8 weeks of constant exposure. Not only is this the first demonstration of the Moses Effect with a carbon-based superhydrophobic material, it also addresses the critical mode of failure noted by Bär *et al.* Bär *et al.* sought a durable and facile superhydrophobic surface, and tried various candidate unsuccessfully [98].

4.3.6 Bouncing

The formation of satellite droplets with no residual interaction with the surface is indicative of the most superhydrophobic types of surfaces as little kinetic energy is lost to wetting [105]. A clean rebound of droplets from the superhydrophobic surface can be seen in Fig. 4.11. Droplets were observed to bounce multiple times from the surface before coming to rest. Additionally, multiple smaller droplets were often formed after initial droplet contact with the surface. Observation of

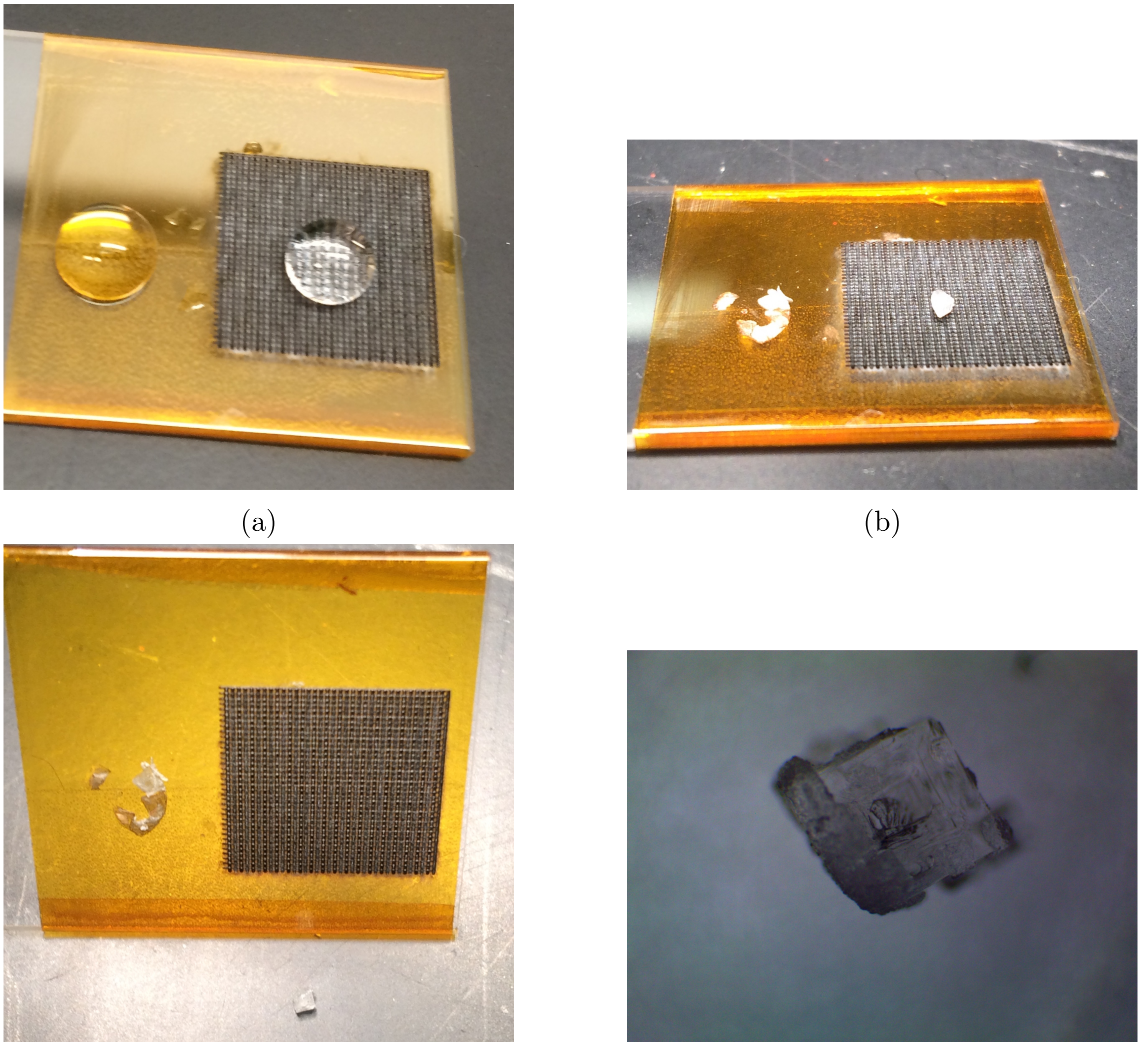

(a) (b)

(c) (d)

Figure 4.8: Demonstration of evaporative desalination of processed and unprocessed Kapton surfaces. **(a)** Two 50 μL droplets of 35 g/L NaCl solution are shown on unprocessed Kapton (left) and superhydrophobic processed Kapton (right). While difficult to see in this image, the right droplet is highly spherical in shape while the left is more distended. **(b)** Two salt deposits were visible after the evaporation of the water. On unprocessed Kapton, salt deposits adhered to the surface are visible. On processed surface, a singular crystal of salt is visible. **(c)** Variation in adherence of salt is demonstrated by inversion of sample. On left, salt is strongly adhered to unprocessed to surface. On right, crystal of salt fell off surface with tilting and is visible on the lab bench. **(d)** Microscopy image at 40 X magnification of salt crystal formed

this bouncing behaviour provides insight into possible applications to anti-icing and fouling resistant coatings using this material.

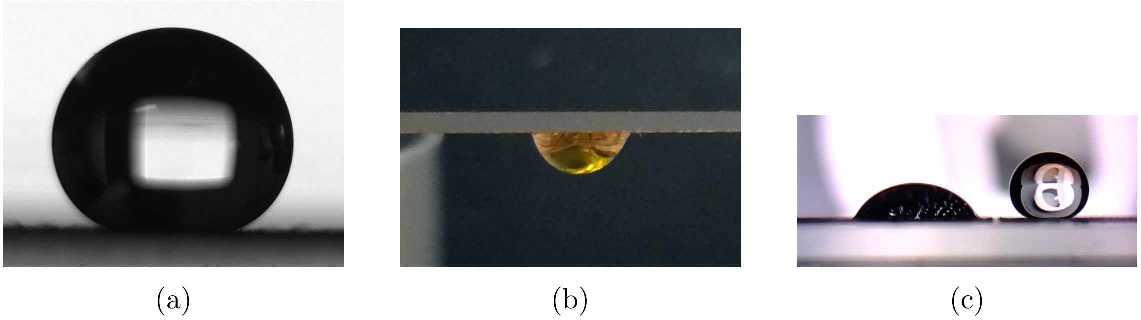
(a) (b) (c)

Figure 4.9: Demonstrations of liquid confinement on surface. **(a)** A 15 μ L droplet confined into a highly spherical shape on the surface of 4% power, 1/72" spaced surface. The measured contact angle for this sample was 171°. **(b)** A 50 μL droplet confined to a superhydrophobic surface after being inverted (corresponding to a roll-off angle of 180°). Droplets would roll off unprocessed Kapton tape at an angle of approximately 30°, but pinning associated with the Wenzel state superhydrophobicity confines this droplet to the surface. **(c)** Hydrophilic (left) and superhydrophobic (right) regions separated by 350 μm from one another indicating the precise surface control possible. Reprinted from "Robust Superhydrophobic Laser-Induced Graphene for Desalination Applications," by Collin M. Tittle, Dilara Yilman, Michael A. Pope, and Christopher J. Backhouse, 2018, *Advanced Materials Technologies, Volume 3,* p. 1700207. Copyright Wiley-VCH Verlag GmbH & Co. KGaA. Reproduced with permission. [6]

4.3.7 Durability

Durability Test	Change in Contact Angle (°)
310 kPa Water Jet	1.8 ± 1.3
Scotch Tape Test	13 ± 4
Oil/ Self Cleaning	2.6 ± 2.8

Table 4.2: Change in contact angle of most superhydrophobic surface after exposure to the durability tests.

As can be seen in Table 4.2, when exposed to the pressurized water jet negligible change in contact angle was observed. Similarly, exposure to oil and subsequent self-cleaning at high temperatures showed little change in hydrophobic behaviour. When the mechanical durability was tested with the Scotch Tape test, an initial decrease in contact angle of 9° to $165 \pm 2°$ was observed. The surface appeared to stabilize subsequently and maintain its superhydrophobic properties with the contact angle after five repetitions measured at $160 \pm 3°$. A grey residue was visible on the scotch tape after all repetitions, but no visible damage to the surface was visible. After the seventh repetition, failure of the adhesive holding the Kapton to the glass slide resulted in large portions being detached by the tape. Remaining portions retained superhydrophobic behaviour; however, contact angle measurement was not possible as droplet would migrate to exposed glass surfaces and disperse.

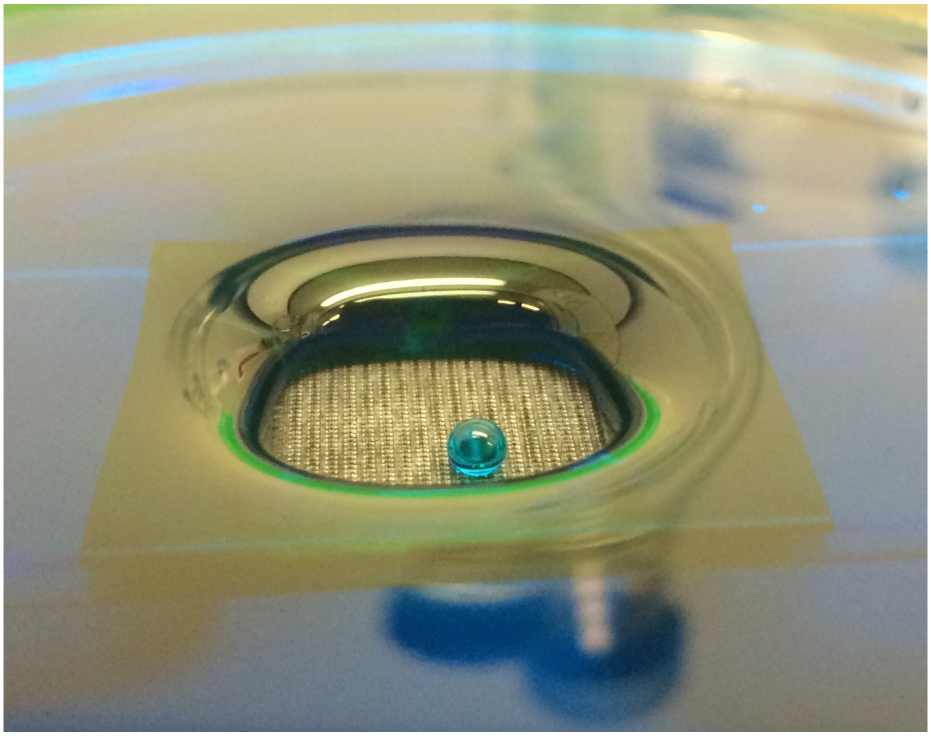

Figure 4.10: The most superhydrophobic surfaces exhibited the Moses Effect where up to 5 mm of water could be repelled from the surface of the sample. No deterioration of the effect has been observed with tests exceeding 8 weeks. This indicates high levels of surface stability. Reprinted from ”Robust Superhydrophobic Laser-Induced Graphene for Desalination Applications,” by Collin M. Tittle, Dilara Yilman, Michael A. Pope, and Christopher J. Backhouse, 2018, *Advanced Materials Technologies, Volume 3,* p. 1700207. Copyright Wiley-VCH Verlag GmbH & Co. KGaA. Reproduced with permission. [6]

4.4 Discussion

As discussed in the introduction, in previous reports of superhydrophobic surfaces utilizing laser processing, the laser was used primarily as a means of structuring the surface rather than to modify the surface chemistry. By utilizing long wavelength IR laser processing to chemically convert polyimide to graphene while simultaneously modifying the surface structure it was possible to fabricate any combination of hydrophilic, hydrophobic, or superhydrophobic patterns. Many reports exist ([106] [88] [90] [84]) as to the structural properties of graphene which might explain the extraordinary durability of these films. While Li *et al.* used a similar wavelength laser to induce graphene and surface morphology they relied on atmospheric control to functionalize the resulting graphene to control the surface energy [99]. It was demonstrated herein that similar surface control and, in fact, even higher contact angles may be obtained by varying the laser power flux incident upon the surface. Our tunable fabrication process led to the formation of three distinct regimes which may be seen in Fig. 4.12. At low laser flux, as can be seen in Fig. 4.7, minimal

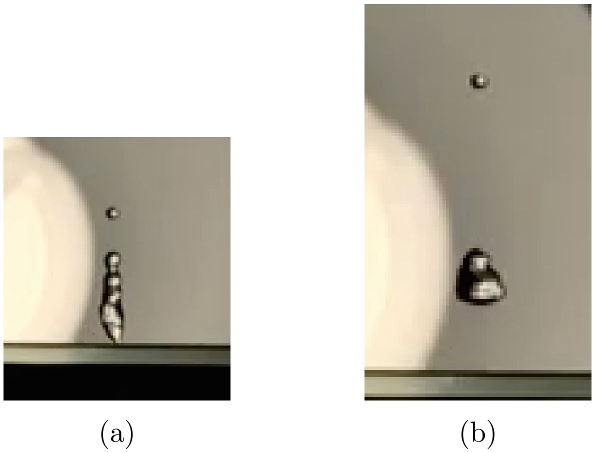

(a) (b)

Figure 4.11: Two images of water droplets bouncing off superhydrophobic surface. 25 mL droplets were released from 10-15 cm above the surface of superhydrophobic samples. Their contact with the surface was recorded at 120 fps using an iPhone 5S. Reprinted from ”Robust Superhydrophobic Laser-Induced Graphene for Desalination Applications,” by Collin M. Tittle, Dilara Yilman, Michael A. Pope, and Christopher J. Backhouse, 2018, *Advanced Materials Technologies, Volume 3,* p. 1700207. Copyright Wiley-VCH Verlag GmbH & Co. KGaA. Reproduced with permission. [6]

carbonization resulted and simple patterning occurred. This resulted in an enhancement of the hydrophilicity of Kapton as expected from theory. In Region I of Fig. 4.12 various settings which produced this region characterized by low contact angles, high contact angle hysteresis, and high rolling angles are shown. An intermediate regime characteristic of a Wenzel-like state was present for certain parameters and is highlighted in Region II of Fig. 4.12. These superhydrophobic surfaces were characterized by high contact angles, moderate contact angle hysteresis, and high rolling angles. It was this intermediate region which demonstrated the ability to confine a droplet to its surface when rotated through 180°. The final region (Region III) has characteristics indicative of a Cassie-Baxter like superhydrophobic surface: high contact angles, low contact angle hysteresis, and low rolling angles.

Prior to this demonstration, only three reports of superhydrophobic materials capable of exhibiting the Moses Effect existed ([82] [81], [80]) with this, to the best of our knowledge, being the first demonstration of the Moses Effect by a carbon-based superhydrophobic surface. As the Moses Effect has not been observed to disappear, with tests exceeding 8 weeks in duration, it served as an excellent demonstration of the temporal stability of the surface. This is important as many reports highlight the lack of temporal stability in superhydrophobic films. An example of this is in [93] where storage conditions could greatly affect the contact angle. Similarly, in a review of facile superhydrophobic surfaces it was observed that all samples tested exhibited a decrease in contact angle over a time scale of hours [98]. This was reported to be an irreversible transition from the Cassie-Baxter state to the Wenzel state. Even after weeks of exposure, low rolling angles and high contact angles indicative of

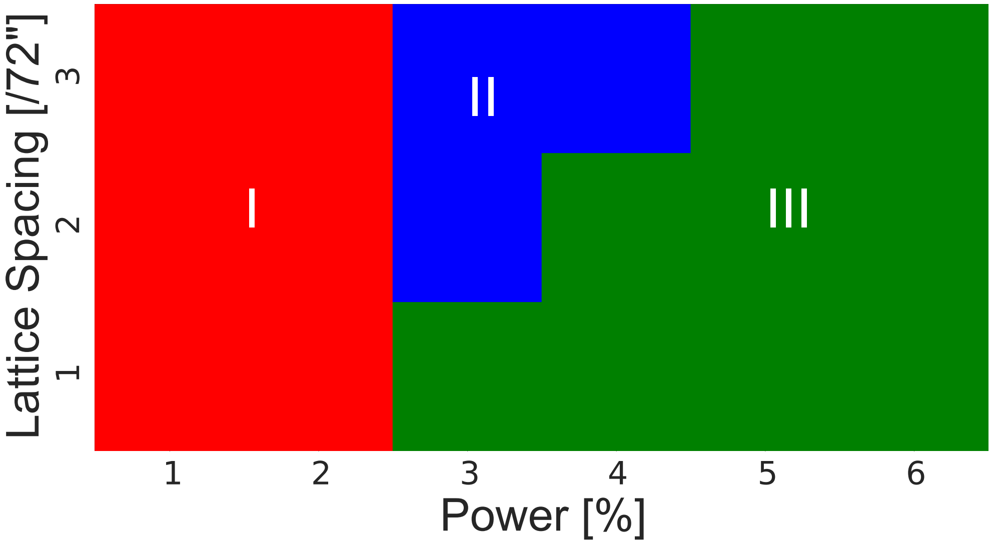

Figure 4.12: Three distinct regimes of behaviour are observed. Zone I is a hydrophilic surface characterized by low contact angles, high contact angle hysteresis, and high rolling angles. Zone II is an intermediate regime characterized by contact angles over 150°, intermediate hysteresis and high rolling angles. Zone III is a purely superhydrophobic regime characterized by contact angles approaching 180°, negligible hysteresis, and rolling angles approaching zero degrees. Reprinted from "Robust Superhydrophobic Laser-Induced Graphene for Desalination Applications," by Collin M. Tittle, Dilara Yilman, Michael A. Pope, and Christopher J. Backhouse, 2018, *Advanced Materials Technologies, Volume 3,* p. 1700207. Copyright Wiley-VCH Verlag GmbH & Co. KGaA. Reproduced with permission. [6]

the Cassie-Baxter state were still observed with our samples. We believe that this temporal stability, combined with its resistance to water vapour over the course of weeks, when combined with the observed chemical, and thermal stability makes this film highly unique. This film additionally has a contact angle higher than any graphene-based surface detailed in the review by Meng *et al.* and all other reports to the best of our knowledge [79].

The importance of facile fabrication techniques was highlighted by Bar *et al.* while challenges associated with fabrication were noted by several reviews [98] [78] [79]. In this regard, CO_2 lasers provide an excellent option balancing the necessary resolution with the ability to rapidly process large areas. It takes approximately 100 seconds to process the 100 mm diameter surfaces used in these tests. Additionally, the use of this technology allows for hybrid surfaces containing regions of varying hydrophobicity (or philicity) in one pattern with the regions independent of surroundings at distances of approximately 350 μm.

4.5 Conclusion

The surfaces discussed above demonstrate tunable wettability produced using a facile fabrication process. The fact that the resulting films are mechanically durable, chemically inert, and temporally stable provides a solution to long-standing challenges in the field. Difficulties in addressing these challenges with previous fabrication methods has stifled the application of superhydrophobic materials to several important problems; one such which has been identified by several reviews is the need for novel superhydrophobic materials in desalination technologies [78] [7]. Therefore the demonstration of desalination assisted by this superhydrophobic material was a natural application and will be the topic of the following chapter.

Chapter 5

Desalination Using Superhydrophobic Graphene Films

5.1 Introduction

There exists a substantial need for water desalination technologies as much of the world's population, especially those in arid, equatorial regions, suffer from a lack of fresh water [107]. This need for fresh water will only grow in the future as the Worldwatch Institute estimates that by the year 2025 more than two-thirds of the world's population will suffer from water shortages [107]. Currently, commercial scale water desalination is done using either reverse osmosis (RO) or multi-stage flash distillation (MSF); technologies which suffer from high energy requirements and modes of failure through corrosion or membrane fouling [108].

Membrane distillation, a technology still in the experimental stage, is a promising alternative as it has the potential to operate in a highly energy efficient manner and with the use of renewable energy sources [109] [7]. For many arid regions, the necessary temperature gradient could be established simply from cold seawater and solar heating; resources these regions likely have in abundance. This technology depends upon the use of a porous, hydrophobic membrane to separate the saline feed solution from the distilled permeate and, as identified by recent reviews, these membranes must be resistant to fouling, possess a long working life, and be manufacturable in a scalable manner [108] [110] [7].

In this work, the rapidly prototyped superhydrophobic surfaces discussed in the previous chapter will be used to form membranes for water desalination using membrane distillation.

5.1.1 Principle

Membrane distillation uses a vapour permeable membrane to separate two solutions. On one side is a hot feed solution of saline water while on the other side is a colder sweep solution or air gap. The thermal gradient across the membrane induces a vapour pressure gradient which drives the transport of water vapour molecules through the semi-permeable membrane.

When compared to other desalination technologies, this method has several advantages. The primary advantage is that it can be done at atmospheric pressure and moderate temperatures (30 to 90 °C) [109] [7]. This reduces both the infrastructure and operational costs when compared to the high energy and pressure technologies like multi-stage flash distillation and reverse osmosis while simultaneously making the technology more conducive for use with renewable energy sources. Specifically, when compared to reverse osmosis, the lower pressures result in more relaxed membrane design requirements and greater resistance to fouling due to larger pore sizes [7]. However, challenges still remain with low mass flux and inadequate membrane lifetime being two of the major issues [111].

5.1.2 Variations

Four main architectures exist for membrane distillation with each having positive and negative attributes. Figure 5.1, taken from [7], shows the four leading configurations for membrane distillation.

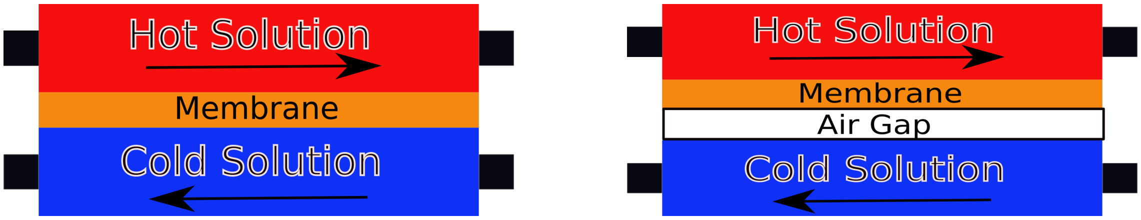

(a) Direct Contact (DCMD) (b) Air Gapped (AGMD)

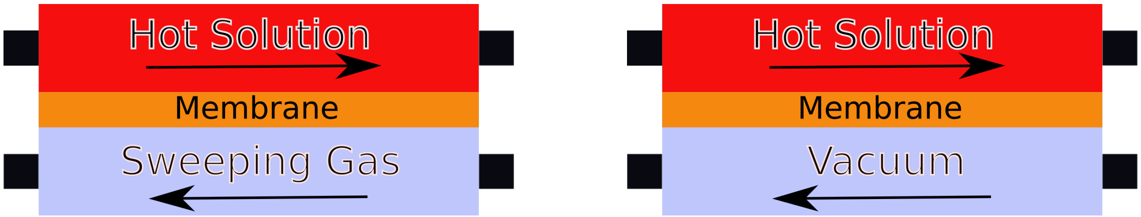

(c) Sweeping Gas (SGMD) (d) Vacuum (VMD)

Figure 5.1: Types of membrane distillation, inspired by figure from [7]. **(a)** DCMD has high permeate fluxes and simple set up, however, suffers from high heat loss. **(b)** AGMD has minimal heat loss, however, suffers from lower fluxes. **(c)** SGMD has better mass flux than AGMD, however, suffers from additional costs and complexity associated with sweep gas and water vapour recovery. **(d)** VMD has the highest mass fluxes, however, suffers from higher risk of membrane wetting and complexity associated with water vapour recovery.

Direct Contact Membrane Distillation

Direct contact membrane distillation (DCMD), seen in Fig. 5.1a uses the hydrophobic membrane to separate a hot, saline feed solution from a colder permeate solution. This method is relatively simple to set up as it only requires two pumps and sources of hot and cold. It also produces fairly high mass fluxes in the range of 10 to 70 kg m^{-2} h^{-1} [7]. Its major drawback is that it suffers from high heat loss due to conduction into the cold permeate solution [109].

Air Gap Membrane Distillation

Air gap membrane distillation (AGMD), seen in Fig. 5.1b, only has the hot feed solution in direct contact with the membrane. On the permeate side of the assembly, an air gap separates the membrane from the cold condenser plate onto which water vapour aggregates before dripping into a collection chamber. The insulating air gap means that AGMD has less heat loss relative to DCMD, however, the mass flux is limited by the diffusion time through air gap [109]. Typical mass fluxes are on the order of 1 to 10 kg m^{-2} h^{-1} [7] .

Sweeping Gas Membrane Distillation

Sweeping gas membrane distillation (SGMD), seen in Fig. 5.1c, is similar to AGMD in that only the hot feed solution is in thermal contact with the membrane. However, in this version, the stagnant air gap of AGMD has been replaced with a flow inert dry gas (usually N_2). As a result of the decreased diffusion time, SGMD has a higher mass flux than AGMD (5 to 20 kg m^{-2} h^{-1}) while maintaining the low heat loss [7]. However, it suffers from the additional costs of both the sweeping gas and a condenser unit to recover the water vapour [109].

Vacuum Membrane Distillation

Vacuum membrane distillation (VMD), seen in Fig. 5.1d, is similar to SGMD in that it removes the diffusion limiting step of AGMD. Because it also increases the pressure differential across the membrane it has an even higher mass flux, usually on the order of 10 to 100 kg m^{-2} h^{-1} [7]. However, VMD suffers from a higher risk of membrane wetting, high energy consumption due to the required vacuum pump, and the additional cost of a condenser unit to recover the water vapour [109].

5.2 State of the Art

Currently, no commercial scale membrane distillation desalination plants are in operation with the industry being dominated by large-scale reverse osmosis plants [107]. These large-scale operations, such as the recently opened Carlsbad Desalination Plant in Carlsbad California, utilize commercially available desalination membranes capable of producing approximately 31 L/m^2-hr of fresh water (Dow Chemical SW30HRLE-440i membrane) under optimal operating conditions. Such large scale reverse osmosis plants use between 4 to 8 kWh of electricity per m^3 of desalinated water with costs between \$ 0.50 to \$ 1.00 USD per m^3. While this technology is effective, it requires high pressures and thus large quantities of energy to force water through the semi-permeable membranes. Additionally, the dominating factors in reverse osmosis membrane lifetime are the required pretreatment and membrane cleaning which add substantial costs to the system [112] [113]. While having high mass fluxes are important, from an industrial perspective the most important variable is the total volume of water which may be desalinated using a single membrane. This total product, denoted as γ, is the product of the mass flux and membrane lifetime and will be used as the primary metric for membrane performance. According to Dow Chemicals, a world leader in reverse osmosis membranes, the total expected lifetime for their membranes is approximately 5 years [112]. Based on this 5-year lifetime, the total product (γ) a typical reverse osmosis membrane could be expected to produce is approximately $1.36 \times 10^6 L/m^2$ assuming ideal membrane operation at all times.

In contrast to reverse osmosis, air-gapped membrane distillation (AGMD) has been noted by many for its high level of energy efficiency and compatibility with sources of renewable energy [7]. While all variations of membrane distillation have superior energy efficiency to reverse osmosis, AGMD is exceptionally efficient due to the insulating air gap which minimizes heat flow and decreases the energy necessary to generate the thermal gradient [7]. This energy efficiency means that the thermal gradient may be readily established using solar or geothermal energy sources; sources which are often present in the regions which need water desalination the most and are not compatible with reverse osmosis [7].

While AGMD appears promising, commercial implementation has been limited by membrane lifetime and mass flux [110] [111]. The leading materials for membrane fabrication, as noted by Alkhudhiri *et al.*, have been PTFE and PVDF due to their hydrophobic properties (contact angles of approximately 110°) and pore forming abilities; however several issues have been noted with such membranes including representative mass fluxes which are, on average, an order of magnitude lower than reverse osmosis membranes [7][114]. A standard reverse osmosis membrane such as those used at the Carlsbad Desalination Plant have an average mass flux of approximately 30 kg m^{-2} hr^{-1} whereas, in a recent review, Alkhudhiri *et al.* found most AGMD membranes to have mass fluxes less than 10 kg m^{-2} hr^{-1} [7] [115]. Additionally, a series of reports have identified a critical lack of membrane longevity with most degrading on a time scale of hours [116] [109] [117]. A consequence of these low mass fluxes and lifetimes is that the γ values (described above as a metric for overall membrane performance and defined to be the total quantity of water desalinated by a membrane) of these membranes are insufficient to compete with reverse osmosis membranes for industrial implementation.

In an effort to improve the mass flux through the membrane, many attempts at surface functionalization and hybrid membrane structures have been investigated for air-gapped membrane distillation, however as many of these reports are still experimental in nature a wide spread in reported mass fluxes was observed in conjunction with inconsistent methods of reporting membrane lifetime [118] [119] [120]. The highest mass flux for an AGMD membrane was reported to be 22.9 kg m^{-2} hr^{-1} by Woo *et al.* who formed electrospun membranes from graphene and polyvinylidene fluoride-co-hexafluoropropylene [119]. While high mass fluxes were reported, membrane wetting did occur in certain cases and only up to 60 hours of operation was investigated. As a representative survey of the field, on April 24, 2017, the 50 most recent papers on Web of Science with keyword search "Air gap membrane distillation" were analyzed. Membranes capable of supporting instantaneous mass fluxes comparable to those of reverse osmosis were reported, however, no γ values exceeding 5000 L/m^2 were observed.

To address the long-standing issues of low mass fluxes and short lifetimes the use of superhydrophobic membranes has been proposed by many, with Alkhudhiri *et al.* going so far as to identify the development of highly hydrophobic membranes as crucial for the technological development of the field [7] [78]. There are two properties in particular which make superhydrophobic membranes appealing. Firstly, because of their enhanced water repelling properties, they are capable of preventing water penetration while possessing larger pore sizes (calculation seen in § 5.3) which improves the mass flux through the membrane. Secondly, as was discussed in Chapter 4, Cassie-Baxter state superhydrophobic membranes possess an air gap which separates the fluid from the membrane's surface. This results in self-cleaning properties and a resistance to membrane fouling, a common mode of failure identified by Duong *et al.* [104].

The demonstration of high contact angles along with long term stability of the so-called 'Moses Effect' in Chapter 4 provides a strong indication of the likely successful implementation of these superhydrophobic films for air-gapped membrane distillation. The highly superhydrophobic nature of these films will allow for larger pore sizes to be permitted and, as will be shown in § 5.3, the large pore size of this design results in an estimated mass flux of 52 L/m^2-hr which is superior to that of even state of the art reverse osmosis membranes. Additionally, in the demonstration of the Moses Effect, membranes were shown to maintain their superhydrophobic properties for a minimum of 8 weeks without any change in behaviour. Using this conservative estimate of 8 weeks for membrane lifetime, the gross product of the membrane may be calculated to be 61 000 L/m^2 which exceeds the state of the art value report by [119] by an order of magnitude. As no change in membrane behaviour has been observed with time, and membrane regeneration after contamination via heat was observed, it is reasonable to expect the membrane lifetime to be much greater; likely on the order of years. With an estimated mass flux and lifetime of 52 L/m^2-hr and 5 years respectively, a reasonable expectation for γ for a laser-induced graphene membrane in an AGMD assembly is $2.28 \times 10^6 L/m^2$; a 66% increase in product relative to state of the art reverse osmosis technology.

5.3 Theory

The basic principle of membrane distillation operation is that the temperature gradient across the hydrophobic membrane establishes a difference in Laplace pressure across the membrane which drives diffusion of water molecules through the membrane while confining the saline, liquid phase to one side of the membrane. The standard assumptions made in this model are that the system is at thermal equilibrium, feed temperature is constant along the membrane interface, the system is

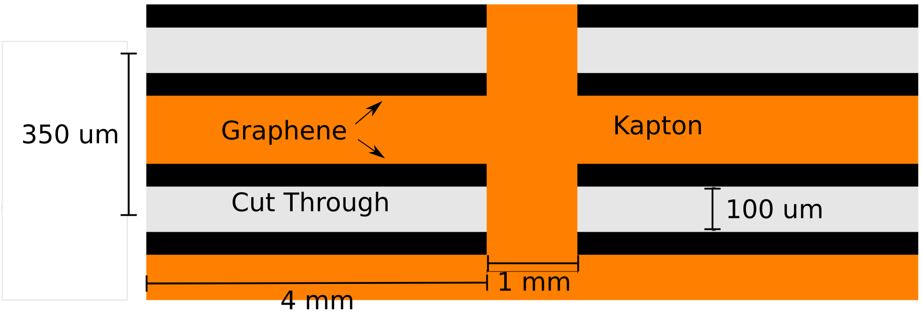

Figure 5.2: Zoomed in view of membrane design (not to scale). Trenches are cut through the Kapton tape allowing for optimal mass transfer while the superhydrophobic graphene regions prevent water from breaking through. The cut-through regions are approximately 100 μm wide with carbonized regions approximately 50 μm wide on either side. The unaffected areas separating the pores are approximately 100 μm wide. Unablated vertical supports with width $L = 1$ mm are spaced 5 mm apart.

closed (no water vapour enters or leaves the system), and infinite sources of hot and cold are available.

The mass flux through a membrane has, as seen in Eq. 5.5, first order dependency on each of the membrane's porosity (ϵ), pore size (r_m), tortuosity (τ), and thickness (δ) making these the most important metrics for membrane characterization. From our work to date it is possible to conclude that our porosity and membrane thickness are slightly worse than the state of the art ($\epsilon = 28.5\%$ versus 70%, and $\delta = 125$ μm versus 75 μm) while our tortuosity and pore size exceed the state of the art ($\tau = 1$ versus 1.2, and $r_m = 100$ μm versus 100 nm) [121]. While all other metrics are within an order of magnitude of one another, r_m improves upon the state of the art by 3 orders of magnitude which results in a world-leading predicted mass flux of 52.7 kg/m^2 hr.

This improvement in pore size will be achieved by using lines cut through the Kapton rather than relying on a porous network as was done in most previous works. This results in optimal geometry for mass transfer and is only possible as a result of the Moses Effect demonstrated by this material. The Asymptote schematics for this may be seen in Fig. 5.3a with a diagram seen in Fig. 5.2. Based upon previous work, it is known that the centre to centre spacing of the trenches is approximately 350 μm with each cut-through region being 100 μm wide with 50 μm carbonized regions on either side.

The porosity (ϵ) or fraction of the membrane which is a void with respect to the total volume may be calculated by observing that 100 μm out of every 350 μm unit is cut-through and thus a void in the polyimide film. This is a conservative estimate as voids also exist within the carbon structure, but will be neglected. Based upon this assumption, 100/350 of the membrane is a void, thus the porosity ϵ is 28.5% with an average pore diameter of 100 μm and a membrane thickness of 125 μm.

Pores are further characterized by their tortuosity τ which is a measure of the pores deviation from an ideal cylindrical case. As these pores are cut straight through, they possess the ideal geometry and thus have a tortuosity of 1.

One of the most important membrane parameters in the liquid entry pressure (LEP) which is the hydraulic pressure the membrane is capable of resisting before water permeation through the membrane. Roughly speaking the LEP increases with increasing porosity and decreasing pore size [121]. The LEP is determined by Equation 5.1 where ΔP is the pressure difference across the membrane, B is the geometric pore coefficient, γ_l is the liquid surface tension, θ is the contact angle, and r_m is the pore radius [7]. The pore coefficient B is related to the pore curvature and is between 0.4 and 0.6 for most systems [121]. Because the pores in this study are throughcut and have a tortuosity of 1, the pore coefficient B is also 1 [121].

$$\Delta P = \frac{-2B\gamma_l cos\theta}{r_m} \tag{5.1}$$

Based upon values of B to be 1, γ_l to be 72 mN/m (that of pure water), θ to be 176°, and r_{max} to be 100μm (from previous measurements), the liquid entry pressure may be estimated to be 1.4kPa, which is well below all water pressures used in this experiment.

5.3.1 Mass Flux

Assuming a steady state thermal gradient across the membrane, infinite sources of hot and cold, and a stagnant air gap inside the membrane it was shown that the mass flux could be given by Eq. 5.2 where J is mass flux, D is the diffusion coefficient, P_{fm} is the vapour pressure of the feed solution at the membrane, and P_{pm} is the vapour pressure of the permeate solution at the membrane [7].

$$J = D(P_{fm} - P_{pm}) \tag{5.2}$$

The partial pressure of water vapour on either side may be determined using the Antoine Equation (Eq. 5.3) [7].

$$P_w = exp\left(23.2964 \times \frac{3818.44}{T - 46.13}\right) \tag{5.3}$$

A correction to the Antoine Equation is necessary for the feed side as the added salt increases the boiling point of water. This correction may be seen in Eq. 5.4 which is an empirical version of Raoult's Law where P_{sw} is the vapour pressure of the seawater and S is the salinity in g/kg [7].

$$\frac{P_w}{P_{sw}} = 1 + 0.57357\left(\frac{S}{1000 - S}\right) \tag{5.4}$$

The diffusion coefficient D is determined by the relevant transport mechanisms. For AGMD, Knudsen diffusion (collisions with pore walls much greater than particle-particle collisions) and molecular diffusion dominate, leading to the form for D seen in Eq. 5.5. In this equation δ is the membrane thickness, R is the universal gas

Parameter	Value
τ	1
ϵ	0.285
δ	127 μm
r_m	100 μm
R	8.314 $kgm^2s^{-2}K^{-1}mol^{-1}$
T_{high}	70°C
T_{low}	20°C
M_w	18 g/mol
P_{air}	101.325 kPa
D_{wa}	0.282 cm^2s^{-1}

Table 5.1: Table of values for approximation of expected mass flux

constant, T is the average temperature, M_w is the molecular weight of water, P_T is the sum of air and water partial pressures in the pores, p_{air} is the partial pressure of air, and D_{wa} is a mass diffusivity constant between water and air [7].

$$D = \left[\frac{2\tau\delta}{3\epsilon r_m}\left(\frac{\pi RT}{8M_w}\right)^{1/2} + \frac{\tau\delta}{\epsilon}\frac{p_{air}}{P_T D_{wa}}\frac{RT}{M_w}\right]^{-1} \tag{5.5}$$

Using the parameters in Table 5.1, estimation of the expected mass flux through the system may be made.

Using the parameters in Table 5.1, the mass flux can be estimated using Equations 5.2 and 5.5 to be 52.7 kg/m^2 hr; which exceeds the state-of-the-art value report by [119]. With an estimated membrane area of 1 cm^2 in the experimental system, the collected mass will be 5.27 g/hr which is well above the limit of detection of the balance.

5.3.2 Heat Transfer

When modelling the heat transfer the following assumptions are used: the system is at steady state with infinite sources of hot and cold available, all cross-sectional areas are equal, edge effects are neglected, and any condensed water forms a film of negligible thickness. Heat transfer from the heat source to feed is given by Eq. 5.6 where h_h is the heat transfer coefficient, T_h is the temperature of the heat source, and T_{fm} is the temperature of the feed solution at the membrane [7].

$$Q_h = h_h(T_h - T_{fm}) \tag{5.6}$$

The heat transfer through the membrane is given by Eq. 5.7 which is comprised of both conductive and mass flux terms [7].

$$Q_m = Q_{con} + Q_v \tag{5.7}$$

The heat transfer associated with conductivity is seen in Eq. 5.8 where k_{air} and k_m are the thermal conductivities of the air and membrane respectively [7].

$$Q_{con} = \frac{\epsilon k_{air} + (1-\epsilon) k_m}{\delta}(T_{fm} - T_{pm}) \tag{5.8}$$

The heat transfer associated with the mass flux is the product of the mass flux and latent heat of vaporization as seen in Eq. 5.9 [7].

$$Q_v = J \Delta H_v \tag{5.9}$$

Through the air gap, heat is again transferred by both conduction through the air (Q_{air}) and mass flux as seen in Eq. 5.10 [7].

$$Q_{ag} = Q_{air} + Q_v \tag{5.10}$$

The heat transfer by conduction through the air is given by Eq. 5.11 where l is the width of the air gap, T_{pm} is the temperature on the permeate side of the membrane, and T_c is the temperature of the cold plate [7].

$$Q_{air} = \frac{k_{air}}{l}(T_{pm} - T_c) \tag{5.11}$$

Finally, the heat transferred into the cold plate is given by Eq. 5.12 where h_c is the transfer coefficient [7].

$$Q_c = h_c(T_{pm} - T_c) \tag{5.12}$$

Each individual quantity may now be sequentially calculated and the total heat flow determined. Using these quantities, the energy requirements of the system may be determined and thermal gradient across the membrane predicted.

5.4 Methods and Materials

5.4.1 Membrane Fabrication and Characterization

For membrane fabrication and subsequent characterization the following procedure will be used. A 3/4" diameter circular hole (as seen in red in Fig. 5.3a) was laser cut into the center of a polystyrene petri dish (100 mm diameter, 10 mm height) with settings of 10% power, 10% speed, 1000 pulses-per-inch (ppi), and a focus of 0.8 mm. An alignment jig made from 1.5 mm thick PMMA consisting of a circular cut out of the same diameter as the outside of the petri dish with a known offset was used to ensure accuracy and is also seen in Fig. 5.3a. Across the hole in the petri dish and on the inside of the dish, a strip of 0.0025" thick, 1" wide Kapton tape (McMaster Carr, 7648A34) was applied, completely sealing the hole as seen in Fig. 5.3b. The adhesive on this tape was previously been observed to be water tight for periods of greater than 24 hours. Using the same alignment jig to ensure accuracy, a 5/8" diameter circular pattern consisting of dashed horizontal lines with supporting unablated regions was cut in the Kapton tape and centred directly above the hole (seen in blue in Fig. 5.3a). A more detailed view of this pattern may be seen in Fig. 5.4. The ablated regions were 1.41 mm long with 0.35 mm wide support strips of unablated Kapton which are necessary to ensure rigidity of the pore structures. This patterning resulted in the formation of an air permeable superhydrophobic surface which acted as a desalination membrane and a survey of representative laser powers was performed.

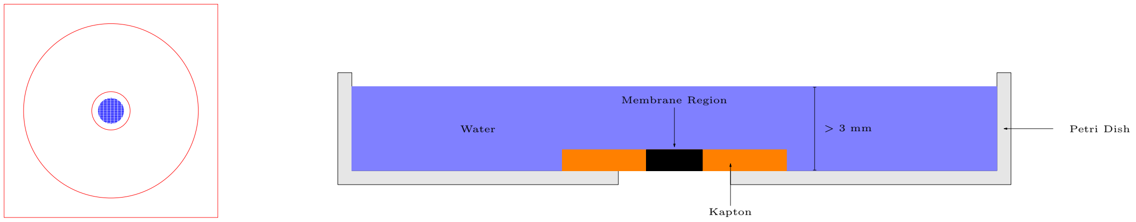

(a) (b)

Figure 5.3: **(a)** Asymptote design of PMMA frame, Petri dish substrate and superhydrophobic membrane. Through cuts will be ablated using laser settings 10% power, 10% speed, 1000 ppi, and 0.8 mm focus along the red lines. Subsequently 0.0025" thick Kapton tape will be adhered to the frame over the hole removed in the center. The line pattern seen in blue will be ablated using settings of 4% power, 5% speed, 1000 pulses-per-inch, and 0.8 mm focus. Although not visible at this scale 1 mm wide unablated vertical Kapton strips every 4 mm are present. The key criteria for membrane functionality is to support at least 3 mm of water for 1 hour without penetration. Asymptote code found in Appendix B. **(b)** Schematic of membrane characterization set up. A hole is cut into a Petri dish which is then covered in Kapton tape (orange). The central region of the Kapton tape is then ablated to form the air permeable membrane (black). Water will be added to the Petri dish up to a height of h. The key criteria for membrane functionality is to support at least 3 mm of water for 1 hour without penetration.

To characterize the membrane, the Petri dish was placed upon supports to raise it off a lab bench. The dish was then filled with water and observed for water penetration. As the initial test of membrane functionality, water was poured into the Petri dish on the edge (away from the membrane area to minimize transients on the membrane) and the height was measured using a ruler after which the Petri dish was capped and observed for at least 1 hour. The criteria for designating a membrane as functional was that it could support at least 3 mm of water for a minimum of 1 hour. Based upon the previous characterization work and knowledge of laser settings, it was expected that a functional membrane would be achieved within the first few iterations. Further optimization of membrane porosity and superhydrophobicity was performed and once the optimal membrane was developed, the upper reservoir was filled with saline solution and the assembly sealed in a container. This was observed to quantifying membrane durability and lifetime. To be competitive with current AGMD membranes, the membrane must maintain water repellency for at least 96 hours (corresponds to an expected γ = 5000 L/m^2). As was observed and

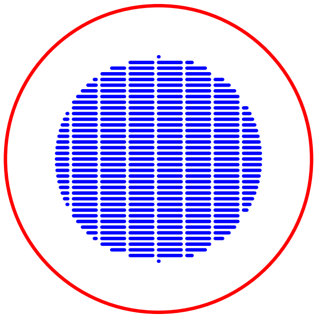

Figure 5.4: Asymptote schematic of membrane pattern. 1.41 mm long traces will be cut (seen in blue) with 0.35 mm wide structural Kapton spacers left in place. The red circle represents the cut out region of the PMMA and thus the area the membrane must span. Asymptote code found in Appendix B.

discussed previously, it is expected that these membranes will demonstrate water repellency for at minimum 8 weeks, and likely on the order of years.

The liquid entry pressure was determined using a gravity head method. A peristaltic pump was used to prime a line running from a beaker to the PMMA enclosure. This enclosure was very similar to that seen in Fig. 5.6 except that the entire enclosure is PMMA and there is only one barbed fitting on the top. The line was connected to the barbed fitting and the beaker elevated until membrane penetration was observed. The height difference was then measured to determine the liquid entry pressure.

5.4.2 Air Gapped Membrane Distillation Assembly

The main structure of the membrane distillation assembly was fabricated from two pieces of 76.2 mm wide by 4.76 mm thick aluminum. The top piece (or hot side) was 203.2 mm long with a 15° bend in the middle. On one end, four, 4.57 mm diameter holes were drilled which allows for a close fit of 8-32 Nylon bolts to pass through. Equally offset from the center of the square made by the four bolt holes, two holes spaced 12.7 mm apart were drilled with a # 45 drill bit and tapped with a 3-56 tap. Into these holes, a 1.58 mm diameter barbed fitting (McMaster Carr 5454K74) was inserted and sealed using a Viton o-ring (McMaster Carr 9464K103). 1.58 mm diameter Tygon tubing (McMaster Carr 6516T11) was used to connect to the barbed fittings for circulation of the hot feed solution.

The second piece of aluminum was 279.4 mm long and divided into three sections. There exists a central 76.2 mm long section flanked by two 101.6 mm long sections. One of the outer sections is bent upwards by 15° relative to the central section, with the other bent 15° downwards. In the upward bent section, four bolt holes, complementary to those in the hot side, were drilled. Equally offset from the center of the square made by the four bolt holes, two holes spaced 12.7 mm apart were drilled, one with a # 45 drill bit and tapped with a 3-56 tap and another with a 1 mm diameter drill bit to act as a vent and prevent vapour locks. The tapped hole was fitted with an identical barbed fitting and o-ring as above and a short length of

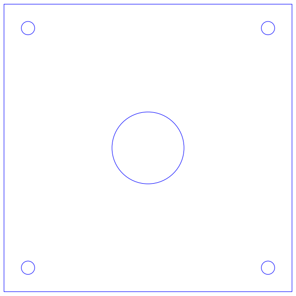

Figure 5.5: Asymptote schematic of 1.5 mm thick PMMA frames. In centre of circular region will be membrane pattern identical to that seen in Fig. 5.3a. Frame will be cut out using laser settings of 20% power, 10% speed, 1000 ppi, and 1.5 mm focus along the blue lines. These frames will contain the o-rings and improve alignment. Asymptote code found in Appendix B.

Tygon tubing was attached leading to the permeate collection tube.

The membrane assembly was placed between the two aluminum plates. It was comprised of three sheets of 76 mm by 76 mm by 1.5 mm thick PMMA (Evonik Acrylite FF). In the centre of these squares a 19.05 mm diameter hole was cut using a Universal Laser Systems VLS 2.0 CO_2 laser (10.6μm, laser settings 20% power, 5% speed, 1000 pulses-per-inch, focus of 1.5 mm). In the center of each hole, a 19.05 mm outer diameter, 15.875 mm inner diameter o-ring was inserted. On the top of the bottom layer of PMMA, a strip of 25 mm wide, Kapton HN tape was placed over the hole. Into this tape, the pattern seen Fig. 5.4 was formed using the laser (settings 4% power, 5% speed, 1000 pulses-per-inch, focus of 1.5 mm). Based upon the results shown in § 5.5 these settings were chosen from the many surveyed. Complementary holes for the bolts to pass through the entire assembly were also cut in the PMMA using above laser settings as seen in Fig. 5.5. The entire apparatus was then assembled as seen in Figures 5.6 and 5.7 using the bolts to compress the o-rings and seal the entire assembly.

On the surface of both sides an LM35 temperature sensor was placed into a small recess with thermal paste and adhered to the surface using commercial electrical tape. These temperature sensors were connected to a LabJack U6 microcontroller and monitored using a Python program (see Appendix). The surface of the hot side was covered in commercial bubble wrap to insulate the surface and improve thermal uniformity.

150 mL of 3.5 % NaCl solution coloured using red food coloring (approximately 1% by volume, Clubhouse Neon) was placed in a beaker on a conventional hot plate. The hot side of the membrane assembly was placed on the same hot plate. A short length of Tygon tubing was run from the beaker to the assembly input. An exit line runs from the hot side back to the beaker through a peristaltic pump. The gravity head of 5 cm allows hot feed solution to flow into the assembly (after priming) after which it is returned via the peristaltic pump. The permeate side is inserted into an ice and water bath to establish the temperature gradient.

Initially, the system is allowed to reach thermal equilibrium before pumping is started. Once the thermal gradient is established, the feed line is primed and pumping commenced at a rate of approximately 2 mL/min. During the 12 hour test, the system was allowed to run constantly with the feed beaker being topped up once per hour and the ice bath replenished at a similar rate. The permeate beaker was removed once per hour and weighed to quantify the mass transfer. After completion, the permeate conductivity was measured using an Oakton PC 700 combination pH/conductivity probe.

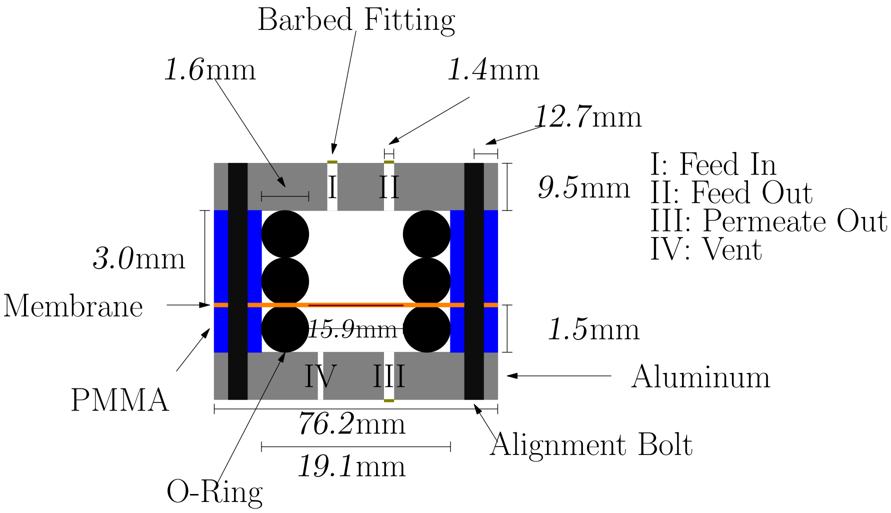

Figure 5.6: Cross section of assembly for membrane distillation. Two aluminum plates comprised the main structure with both containing LM35 temperature sensors recessed into their surfaces. Between these plates, a membrane sandwiched between PMMA frames as seen in Fig. 5.3a was placed. Aligned bolt holes run from top to bottom to support the assembly and prevent rupturing. The top plate was supported on the left edge by a hot plate. This plate had two 3/56" tapped holes with barbed fittings connect to Tygon tubing to pump hot saline solution through the enclosed void below. The bottom plate was placed into an ice bath and contained one barbed fitting to allow condensed water to leave the membrane assembly and collect in Falcon tube below. A vent hole has also been drilled to prevent a vapour lock from forming. Reprinted from "Robust Superhydrophobic Laser-Induced Graphene for Desalination Applications," by Collin M. Tittle, Dilara Yilman, Michael A. Pope, and Christopher J. Backhouse, 2018, *Advanced Materials Technologies, Volume 3,* p. 1700207. Copyright Wiley-VCH Verlag GmbH & Co. KGaA. Reproduced with permission. [6]

Thermal Behaviour

While a more complete model of the heat transfer through the system was discussed in § 5.3, below are simplified calculations modelling the thermal behaviour of the system.

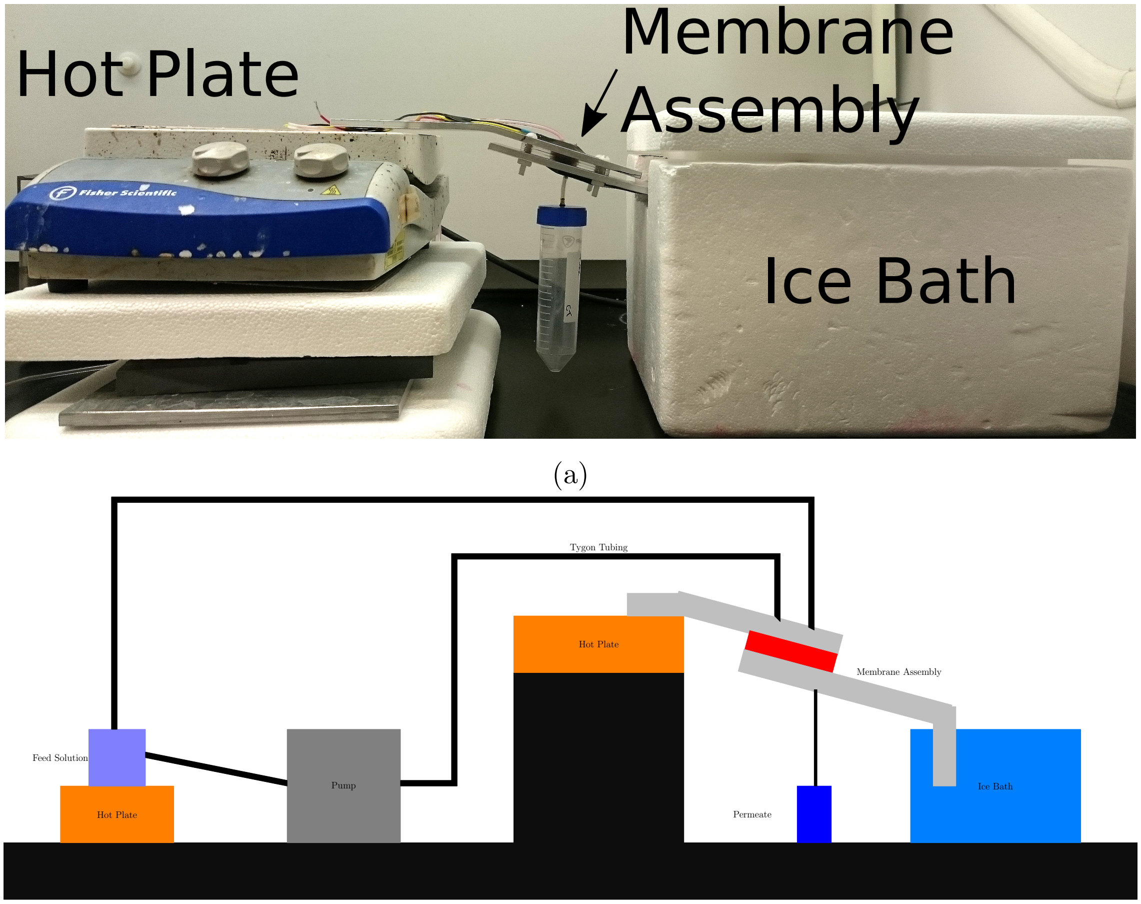

(a)

(b)

Figure 5.7: **(a)** Image of assembly membrane distillation setup. The hot plate, membrane assembly, and ice bath have been highlighted. **(b)** Schematic of experimental assembly for membrane distillation. A sealed beaker on a hot plate contains 3.5% NaCl solution which is heated. Tygon tubes connect the solution to a peristaltic pump which moves the fluid through additional tubing which runs along the surface of the membrane assembly before delivering the solution to distillation chamber. A second Tygon tube returns solution to the beaker. The membrane assembly rests on two points: a hot plate and an ice bath. This establishes the necessary thermal gradient. The aluminum plates will be bent to deliver the necessary slope to the assembly for fluid flow. A third tube transports the permeate solution to a Falcon tube for collection and measurement.Reprinted from ”Robust Superhydrophobic Laser-Induced Graphene for Desalination Applications,” by Collin M. Tittle, Dilara Yilman, Michael A. Pope, and Christopher J. Backhouse, 2018, *Advanced Materials Technologies, Volume 3,* p. 1700207. Copyright Wiley-VCH Verlag GmbH & Co. KGaA. Reproduced with permission. [6]

The time constant for thermal equilibration of this assembly may be calculated using the following assumptions. It is assumed that conductivity in plane within the aluminum will dominate both convective cooling to the air, and thermal conduction through the Viton O-rings. The Viton O-rings have a thermal conductivity three orders of magnitude less than that of the aluminum supporting this assumption. In calculating this value, it is also assumed that no water is in the system and that all thermal energy is entering or leaving the plates by contact with either the hot plate or ice bath. The lack of water assumption is assumed to be valid as there is only 0.48 mL of water within the assembly at one time, resulting in a very small thermal capacitance (2 J/K) which is much lower than the capacitance of the aluminum (approximately 180 J/K). It is also assumed that there are infinite sources of hot and cold available.

The thermal capacitance of an aluminum plate maybe calculated by Eq. 5.13 and the thermal resistance by Eq. 5.14.

$$C_{al} = \rho_{al} c_p V = 2.7 g/cm^3 \times 0.9 J/gK \times (20.3cm \times 7.6cm \times 0.48cm) = 180 J/K \quad (5.13)$$

$$R = \frac{L}{kA_s} = \frac{20.3cm}{2.05 W/cmK \times (7.6cm \times 0.48cm)} = 2.7 K/W \quad (5.14)$$

Using these the thermal time constant may be calculated by Eq. 5.15.

$$\tau = C_{al} R = 180 J/K \times 2.7 K/W = 486 s \quad (5.15)$$

Thus it is seen that within several minutes the system will reach approximate thermal equilibrium.

The water in the tubing will cool between the beaker and the membrane apparatus. However as both ends are held at the same temperature, and minimal tubing length will be used, water temperature should be accurately measured by the LM35 sensors.

Within the membrane assembly the model in Fig. 5.8 may be used.

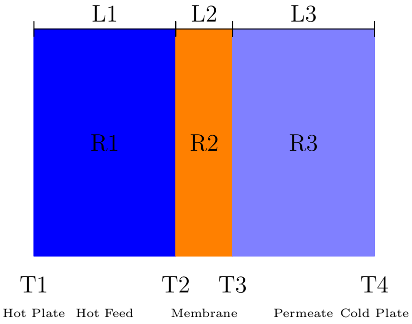

Figure 5.8: Thermal model of system. Assuming steady state, the temperatures T_1, T_2, T_3, T_4 are fixed. R_1 is the resistance attributed to the water, R_2 is the thermal resistance attributed to the membrane (Kapton), R_3 is the thermal resistance attributed to air. $L_{1,2,3}$ is the length of the denoted region. The thermal mass of the hot saline water dominates the system determining the temperature.

The thermal transport through the membrane assembly may be seen in Fig. 5.8 where the left boundary condition is fixed at a hot temperature T_1 and the right boundary condition is fixed at a cooler boundary condition T_2. Thermal transport occurs through the water (R_1), Kapton membrane (R_2) and air (R_3). The high capacitance of the water results in it dominating the system.

Assuming the model seen in Fig. 5.8 and Eq. 5.16, with heat transfer through the air gap dominating, all cross-sectional areas equal, and all temperatures fixed (steady state), the following expression for thermal resistance may be derived.

$$R = R_1 + R_2 + R_3 = \frac{L_1}{k_1 A} + \frac{L_2}{k_2 A} + \frac{L_3}{k_3 A} = 0.0051 K/W + 0.00014 K/W + 0.0625 K/W = 0.06774 K/W \tag{5.16}$$

The values of these variables may be seen in the table below.

Variable	Value
L_1	3.0 mm
L_2	0.064 mm
L_3	1.5 mm
k_1	0.591 W m^{-1} K^{-1}
k_2	0.46 W m^{-1} K^{-1}
k_3	0.024 W m^{-1} K^{-1}

From this AR may be determined to be 0.067 m^2 K / W and the heat flux per unit area through the system determined. Assuming steady state temperatures of 60°C and 10°C (will be measured using LM35 temperature sensors) the following value may be determined

$$q = \frac{T_1 - T_4}{RA} = \frac{50°C}{0.068 m^2 K/W} = 746.2 W/m^2 \tag{5.17}$$

As the q through each section is constant, the temperature of the feed solution at the membrane (T_2) may be determined.

$$T_2 = T_1 - qR_1A = 60°C - 746.2 W/m^2 \frac{3.0 \times 10^{-3} m}{0.591 W m^{-1} K^{-1}} = 56.2°C \tag{5.18}$$

Thus it may be concluded that there is minimal temperature drop across the feed saline solution before the membrane. As the membrane area is approximately $0.0225 m^2$, the necessary power to maintain this gradient is 17 W, which is readily achievable using commercial hot plates.

5.5 Results

5.5.1 Membrane Characterization

The following membrane parameters were tested. It should be noted that the focus was set to 0.8 mm as that was the thickness of the Petri dish, thus the laser was focused on the surface of the tape. When assembled into the distillation apparatus, the focus was changed to 1.5 mm to match the PMMA frame used.

Settings (% Power/ % Speed/ PPI/ Focus(mm)	Width	Length	Superhydrophobic
5/10/1000/0.8	$40\mu m$	$670\mu m$	Yes
6/10/1000/0.8	$60\mu m$	$670\mu m$	Yes
7/10/1000/0.8	$64\mu m$	$670\mu m$	Yes
8/10/1000/0.8	$84\mu m$	$680\mu m$	Yes
9/10/1000/0.8	$117\mu m$	$656\mu m$	Yes
10/10/1000/0.8	$120\mu m$	$720\mu m$	Yes
12/10/1000/1.2	$113\mu m$	$693\mu m$	Yes*
12/15/1000/1.2	$87\mu m$	$670\mu m$	Yes
15/10/1000/1.2	$140\mu m$	$707\mu m$	Yes*
4/5/1000/0.8	$100\mu m$	$700\mu m$	Yes

Figure 5.9: Tested parameters for superhydrophobic membranes. All parameters tested produced membranes capable of supporting at least 10 mm of water pressure. The two settings denoted by an asterisk produced superhydrophobic films with vertical carbon fibers extending from the surface. These fibers and membranes were observed to be highly fragile and were thus determined to be unsuitable. Preliminary studies indicated that power to speed ratios exceeding one produced such fibrous and fragile membranes.

A brief survey of appropriate laser parameters was performed with the results summarized in Table 5.9. It may be observed that many laser parameters demonstrated adequate performance. For further experimentation, the settings of 4% power, 5% speed, 1000 ppi, and 0.8 mm focus was selected. Pictures of this membrane may be seen in Fig. 5.5. It was observed that when the power to speed ratio was less than one (as was standard and used in these membranes), the resulting carbonized structures appeared embedded within the Kapton with no protrusions exceeding 100 μm. When the power to speed ratio exceeded one, vertical carbon fibers were formed with micrometer diameters and extending between 1 and 2 mm from the surface giving it a fuzzy appearance. As these structures were noted to be fragile, and brittle further development was pursued with power to speed ratios less than 1. The liquid entry pressure of this structure was measured using the elevation (gravity head) technique to be 15.7 cm of water which corresponds to an entry pressure of 1.54 kPa which is close in agreement to the experimentally predicted value of 1.02 kPa calculated using Eq. 5.1.

5.5.2 Membrane Distillation

When this membrane was used for membrane distillation in the assembly described in § 5.4, an average mass flux of 10 kg m^{-2} hr^{-1} was observed during a twelve-hour test. This corresponds to between 0.87 g and 1.51 g of distilled water being collected by the system every hour. Significant variance was observed over the course of the test, however no decreasing trend in mass flux was observed. In fact the slope of the line of best fit was positive, indicating that the mass flux was on average increasing

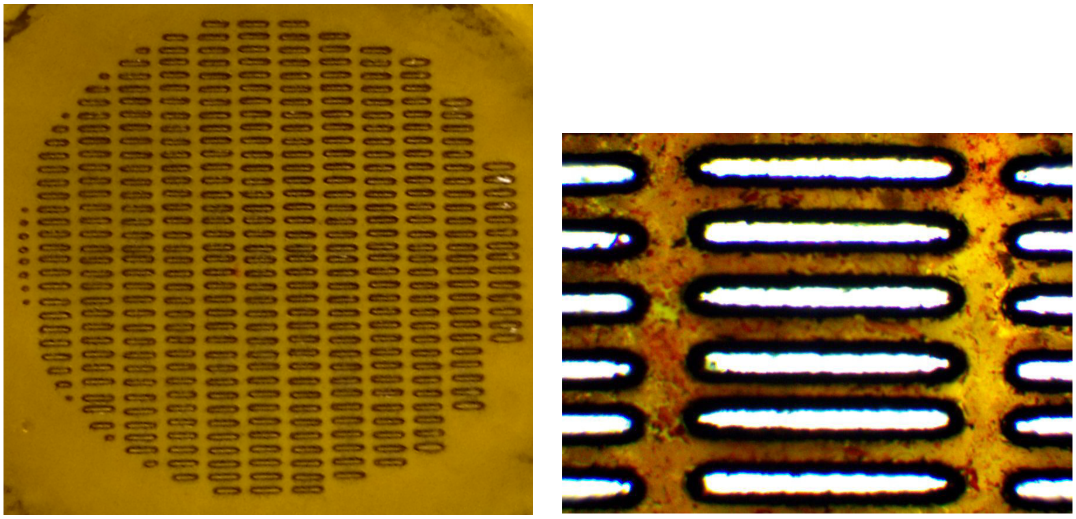

(a) (b)

Figure 5.10: **(a)** Image of a representative membrane **(b)** Image of membrane pores taken at 4X magnification. Reprinted from ”Robust Superhydrophobic Laser-Induced Graphene for Desalination Applications,” by Collin M. Tittle, Dilara Yilman, Michael A. Pope, and Christopher J. Backhouse, 2018, *Advanced Materials Technologies, Volume 3,* p. 1700207. Copyright Wiley-VCH Verlag GmbH & Co. KGaA. Reproduced with permission. [6]

with time, however a poor variance value (0.4) was also calculated. This flux was less than predicted, however, it should be noted that when the porosity was halved, the mass flux remained constant. This may indicate that diffusion within the assembly is dominating and limiting transport rather than membrane characteristics.

Some of this variation may be explained by drops being trapped in the aluminum assembly until they reach a certain volume before they will roll out. In testing, it was observed that the first droplet often did not emerge until after 22 minutes. Assuming a stable mass flux through the membrane, this indicates that a volume of almost 300 μL was in the aluminum chamber before a droplet emerge. A 300 μL uncertainty accounts for most of the variance observed in the data.

Permeate conductivity was measured to be 7.9 μS-cm indicating a high level of water purification. The 3.5% saline solution was measured to have a conductivity of 3.11 mS-cm with the lab de-ionized water tap having a conductivity of 9.8 μS-cm. Due to the small membrane size, insufficient permeate was produced each hour for the conductivity to be measured concurrently with the mass flux. In the future, larger membranes should be used to allow for this. Approximately 5 mL of water is needed for measurement, thus indicating that the membrane area should be increased by a factor of 5.

In addition to the Moses Effect demonstration in Chapter 4 which indicated exceptional membrane stability, several other demonstrations are on-going. A membrane sealing a hole in a Petri dish has confined 10 mm of 3.5% saline solution at room temperature for 60 days. This test is on-going and indicates that this process

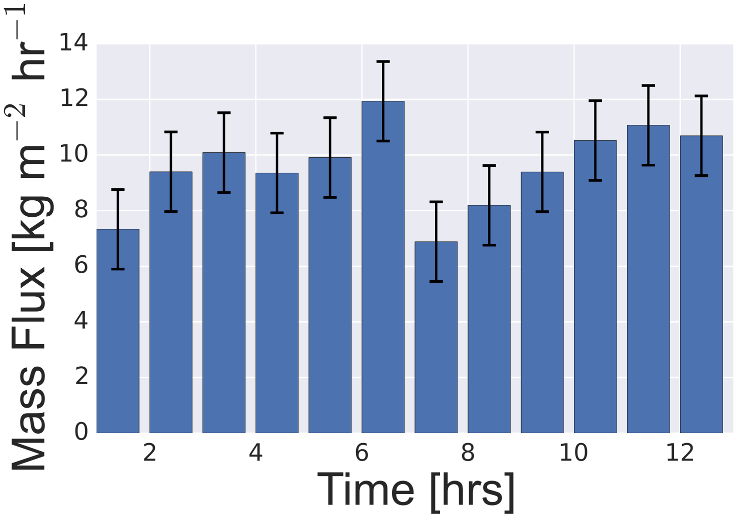

Figure 5.11: Mass flux as a function of time for twelve-hour test of membrane function. Significant variance in the measurements is seen however no trend of decreasing mass flux over the course of the test was observed. This is significant as it is commonly observed with other membrane materials. The conductivity permeate was measured to be $7.9 \pm 0.1 \mu S$ which was less than that of the lab de-ionized water supply and less than the standard for distilled water of 11μS-cm [8]. Reprinted from "Robust Superhydrophobic Laser-Induced Graphene for Desalination Applications," by Collin M. Tittle, Dilara Yilman, Michael A. Pope, and Christopher J. Backhouse, 2018, *Advanced Materials Technologies, Volume 3,* p. 1700207. Copyright Wiley-VCH Verlag GmbH & Co. KGaA. Reproduced with permission. [6]

produces highly stable, superhydrophobic membranes. Additionally, a similar set up repelled 3 mm of 3.5% saline solution when held at 55° C for 14 days with no evidence of failure.

5.6 Discussion

In conclusion, a stable and constant mass flux of 10 ± 1 kg m^{-2} hr^{-1} was observed which is close to the state of the art for air gapped membrane distillation. Additionally, the membrane stability demonstrated by the long-term Moses Effect, room temperature membrane test, and elevated temperature membrane test indicates the membrane's potential to provide long-term performance thus addressing a critical issue currently hampering membrane distillation technologies.

Using the current laser system, a square meter of membrane could be produced in approximately an hour; however, it should be noted that speed was set to only 5% of its maximum value and it is likely that by increasing both the power and speed similar surfaces could be produced an order of magnitude more quickly. Additionally, there exists the possibility of using a more powerful laser and splitting its output into multiple beams. The use of such a multiple head laser would again improve the membrane production linearly with the number of beams. As no controlled atmosphere chambers are required, the only limiting factor for scaling would be the size of the laser table.

In the future, a larger scale pilot system should be developed to further test the membrane. Using such a system would allow for long term testing which would demonstrate the membranes stability in a better manner. Additionally, such a system would likely address some of the flow and thermal issues with the present system which likely were responsible for the mass flux, temperature dependence, and pore size dependencies being weaker than anticipated. A design of such a system is currently being developed and will be supplied to Professor Backhouse when complete.

Such a pilot scale system could also be used to perform membrane distillation of organic compounds from water. In a recent review of membrane separation, the need for membranes in the separation of organic solvents from water was identified [110]. A common mode of failure for these membranes is the rapid degradation of membranes in these solvents. Both graphene and polyimide have been observed to be resistive to compounds such as ethanol and ketones making these membranes possibly applicable for such applications [83] [122]. This process is very important for the chemical manufacturing industry which uses 10-15% of the world's energy supply to separate chemicals and, as has been reported previously, membrane distillation can, in theory, can achieve 100% separation of water from non-volatile solvents [110]. Therefore, the use of such chemically resistant graphene and polyimide superhydrophobic surfaces for chemical separation could provide both another application of the technology and reduce the energy consumption of such processes.

Chapter 6

Summary

The objective of this thesis was to demonstrate the application of rapid prototyped processing of nanomaterials to microfluidics and nanoelectronics.

To develop an understanding of fabrication skills, electrical circuits, and molecular biology procedures an initial portion of this thesis involved the design and fabrication of a microheater capable of providing robust thermal control to microlitre volumes of PCR reagents. The microheaters were fabricated by both milling and laser ablating commercially available polymeric mirror which represents a highly manufacturable alternative to the standard methods of lithographic patterning of thin films of metals such as platinum. Additionally, the long-standing issue of thermal sensor integration identified by Almassian *et al.* was addressed by fabricating a resistive temperature sensor into the heater design and using the thermal coefficient of resistance to measure the temperature. An iterative design approach was used to address several modes of microheater failure and develop a reproducible fabrication protocol for functional microheaters. The robust thermal nature of the sensor was demonstrated with the successful completion of genetic amplification using the polymerase chain reaction.

Similar rapid prototyping technologies were then applied to the processing and characterization of molybdenum disulfide rather than traditionally high cost, low throughput measures such as CVD and lithography which are normally required. Initial protocol development for sample processing, optical characterization, electrode fabrication, and electrical characterization was performed; many of which are still being followed by others. Novel electrode structures formed from graphene induced in polyimide, and carbon/ ITO heterostructures were demonstrated to provide electrical contact to MoS_2 films and preliminary results from the optical measurements indicated some similarities with literature results while helping to identify sources of measurement error. A preliminary system capable of providing robust thermal control and voltage monitoring for DLDS like measurements was validated and documented for future implementation; however, the serendipitous discovery of superhydrophobic behaviour produced during the laser processing of polyimide resulted in a shift of focus.

The wetting behaviour of graphene surfaces produced during laser ablation of polyimide was investigated. It was discovered that by adjusting the laser power, surfaces could be varied from hydrophilic to superhydrophobic with the most superhydrophobic of these surfaces possessing contact angles exceeding 170° and a rolling angle of less than 1°. Additionally, long-term stability and durability was observed which addresses a critical mode of failure in many similar surfaces. These surfaces represent one of the highest contact angles ever for, and the first demonstration of the Moses Effect on, a carbon-based superhydrophobic surface.

The application of these superhydrophobic surfaces as membranes for membrane distillation of saline water was then discussed. The benefits of membrane distillation compared to other methods was highlighted and the technology's need for superhydrophobic membranes identified. Mass flux and thermal calculations were presented to validate the possibility of this application. It was experimentally demonstrated that these membranes could support pores with diameters greater than 100 μm and liquid entry pressure exceeding 1.5 kPa. The rapidly prototyped membranes were then used for membrane distillation where state-of-the-art mass fluxes were achieved and long term stability was demonstrated. Demonstration of high mass flux along with long-term stability has the potential to address two challenges which have been hampering the field.

In conclusion, while applications of rapid prototyping technologies to the fabrication of thin film microheaters and the processing of MoS_2 were demonstrated, the most substantial application occurred in the fabrication of superhydrophobic surfaces. Laser processing was demonstrated to simultaneously induce chemical change while modifying the surface structure of polyimide films, creating some of the most superhydrophobic surfaces ever reported. This methodology was subsequently applied to the rapid prototyping of membranes used in the membrane distillation of salt water. The resulting membranes demonstrated exceptional robustness and long lifetimes addressing a pressing need in the field. With such membranes, air gapped membrane distillation may be able to be developed on a commercial scale, providing an energy efficient alternative to reverse osmosis desalination.

Bibliography

[1] J. Martinez-Quijada, T. Ma, G. H. Hall, M. Reynolds, D. Sloan, S. Caverhill-Godkewitsch, D. M. Glerum, D. Sameoto, D. G. Elliott, and C. J. Backhouse, "Robust thermal control for CMOS-based lab-on-chip systems," *Journal of Micromechanics and Microengineering*, vol. 25, no. 7, p. 075005, 2015.

[2] C. A. Schneider, W. S. Rasband, and K. W. Eliceiri, "NIH Image to ImageJ: 25 years of image analysis," *Nature Methods*, vol. 9, no. 7, pp. 671–675, 2012.

[3] C. Backes, R. J. Smith, N. McEvoy, N. C. Berner, D. McCloskey, H. C. Nerl, A. O'Neill, P. J. King, T. Higgins, D. Hanlon, N. Scheuschner, J. Maultzsch, L. Houben, G. S. Duesberg, J. F. Donegan, V. Nicolosi, and J. N. Coleman, "Edge and confinement effects allow in situ measurement of size and thickness of liquid-exfoliated nanosheets," *Nature Communications*, vol. 5, p. 4576, 2014.

[4] G. Eda, H. Yamaguchi, D. Voiry, T. Fujita, M. Chen, and M. Chhowalla, "Photoluminescence from chemically exfoliated MoS 2," *Nano Letters*, vol. 11, no. 12, pp. 5111–5116, 2011.

[5] E. Varrla, C. Backes, K. R. Paton, A. Harvey, Z. Gholamvand, J. McCauley, and J. N. Coleman, "Large-Scale Production of Size-Controlled MoS2 Nanosheets by Shear Exfoliation," *Chemistry of Materials*, vol. 27, no. 3, pp. 1129–1139, 2015.

[6] C. M. Tittle, D. Yilman, M. A. Pope, and C. J. Backhouse, "Robust superhydrophobic laser-induced graphene for desalination applications," *Advanced Materials Technologies*, vol. 3, no. 2, pp. 1700207–n/a, 2018. 1700207.

[7] A. Alkhudhiri, N. Darwish, and N. Hilal, "Membrane distillation: A comprehensive review," *Desalination*, vol. 287, pp. 2–18, 2012.

[8] Myron L Company, *Application Bulletin: Deionized Water.* `http://www.myronl.com/PDF/application_bulletins/di_ab.pdf`.

[9] A. Jain and K. E. Goodson, "Thermal microdevices for biological and biomedical applications," *Journal of Thermal Biology*, vol. 36, no. 4, pp. 209–218, 2011.

[10] M. A. Burns, B. N. Johnson, S. N. Brahmasandra, K. Handique, J. R. Webster, M. Krishnan, T. S. Sammarco, P. M. Man, D. Jones, D. Heldsinger,

C. H. Mastrangelo, and D. T. Burke, "An Integrated Nanoliter DNA Analysis Device," *Science*, vol. 282, no. 5388, pp. 484–487, 1998.

[11] T. Abe, Y. Segawa, H. Watanabe, T. Yotoriyama, S. Kai, A. Yasuda, N. Shimizu, and N. Tojo, "Point-of-care testing system enabling 30 min detection of influenza genes," *Lab on a Chip*, vol. 11, no. 6, p. 1166, 2011.

[12] D. Han, Y. C. Jang, S. N. Oh, R. Chand, K. T. Lim, K. I. Kim, and Y. S. Kim, "MCU based real-time temperature control system for universal microfluidic PCR chip," *Microsystem Technologies*, vol. 20, no. 3, pp. 471–476, 2014.

[13] N. Thaitrong, P. Liu, T. Briese, W. I. Lipkin, T. N. Chiesl, Y. Higa, and R. A. Mathies, "Integrated Capillary Electrophoresis Microsystem for Multiplex Analysis of Human Respiratory Viruses," *Analytical Chemistry*, vol. 82, no. 24, pp. 10102–10109, 2010.

[14] D. R. Almassian, L. M. Cockrell, and W. M. Nelson, "Portable nucleic acid thermocyclers," *Chemical Society Reviews*, vol. 42, no. 22, p. 8769, 2013.

[15] H. Saha and C. Chaudhuri, "Complementary Metal Oxide Semiconductors Microelectromechanical Systems Integration," *Defence Science Journal*, vol. 59, no. 6, pp. 557–567, 2009.

[16] L. R. Volpatti and A. K. Yetisen, "Commercialization of microfluidic devices," *Trends in Biotechnology*, vol. 32, no. 7, pp. 347–350, 2014.

[17] F. Ahmad and S. A. Hashsham, "Miniaturized nucleic acid amplification systems for rapid and point-of-care diagnostics: A review," *Analytica Chimica Acta*, vol. 733, pp. 1–15, 2012.

[18] G. Wong, I. Wong, K. Chan, Y. Hsieh, and S. Wong, "A Rapid and Low-Cost PCR Thermal Cycler for Low Resource Settings," *PLOS ONE*, vol. 10, no. 7, p. e0131701, 2015.

[19] Python Software Foundation, *Python Language Reference, version 2.7.* `http://www.python.org`.

[20] LibUSB, *libusb-1.0.* `http://libusb.org`.

[21] PyUSB, *PyUSB 1.0.* `https://walac.github.io/pyusb/`.

[22] NumPy Developers, *NumPy.* `http://www.numpy.org`.

[23] J. D. Hunter, "Matplotlib: A 2d graphics environment," *Computing In Science & Engineering*, vol. 9, no. 3, pp. 90–95, 2007.

[24] LabJack Corporation, *Exodriver*, 2015. `https://labjack.com/support/software/installers/exodriver`.

[25] M. S. Alnaes, J. Blechta, J. Hake, A. Johansson, B. Kehlet, A. Logg, C. Richardson, J. Ring, M. E. Rognes, and G. N. Wells, "The FEniCS Project Version 1.5," *Archive of Numerical Software*, vol. 3, no. 100, pp. 9–23, 2015.

[26] K. S. Novoselov, A. K. Geim, S. V. Morozov, D. Jiang, Y. Zhang, S. V. Dubonos, I. V. Grigorieva, and A. A. Firsov, "Electric Field Effect in Atomically Thin Carbon Films," *Science*, vol. 306, no. 5696, pp. 666–669, 2004.

[27] X. Zhang, Z. Lai, C. Tan, and H. Zhang, "Solution-Processed Two-Dimensional MoS2 Nanosheets: Preparation, Hybridization, and Applications," *Angewandte Chemie International Edition*, vol. 55, no. 31, pp. 8816–8838, 2016.

[28] M. Chhowalla, Z. Liu, and H. Zhang, "Two-dimensional transition metal dichalcogenide (TMD) nanosheets," *Chem. Soc. Rev.*, vol. 44, no. 9, pp. 2584–2586, 2015.

[29] B. Radisavljevic and A. Kis, "Mobility engineering and a metalinsulator transition in monolayer MoS2," *Nature Materials*, vol. 12, no. 9, pp. 815–820, 2013.

[30] S. S. Chou, Y.-K. Huang, J. Kim, B. Kaehr, B. M. Foley, P. Lu, C. Dykstra, P. E. Hopkins, C. J. Brinker, J. Huang, and V. P. Dravid, "Controlling the Metal to Semiconductor Transition of MoS2 and WS2 in Solution," *Journal of the American Chemical Society*, vol. 137, no. 5, pp. 1742–1745, 2015.

[31] B. Cho, M. G. Hahm, M. Choi, J. Yoon, A. R. Kim, Y.-J. Lee, S.-G. Park, J.-D. Kwon, C. S. Kim, M. Song, Y. Jeong, K.-s. Nam, S. Lee, T. J. Yoo, C. G. Kang, B. H. Lee, H. C. Ko, P. M. Ajayan, and D.-H. Kim, "Charge transfer based Gas Sensing Using Atomic-layer MoS2," *Scientific Reports*, vol. 5, no. 1, p. 8052, 2015.

[32] J. Li, M. M. Naiini, S. Vaziri, M. C. Lemme, and M. Östling, "Inkjet Printing of MoS2," *Advanced Functional Materials*, vol. 24, no. 41, pp. 6524–6531, 2014.

[33] B. Radisavljevic, A. Radenovic, J. Brivio, V. Giacometti, and A. Kis, "Single-layer MoS2 transistors," *Nature Nanotechnology*, vol. 6, no. 3, pp. 147–150, 2011.

[34] D. Voiry, M. Salehi, R. Silva, T. Fujita, M. Chen, T. Asefa, V. B. Shenoy, G. Eda, and M. Chhowalla, "Conducting MoS2 Nanosheets as Catalysts for Hydrogen Evolution Reaction," *Nano Letters*, vol. 13, no. 12, pp. 6222–6227, 2013.

[35] H.-M. Li, D. Lee, D. Qu, X. Liu, J. Ryu, A. Seabaugh, and W. J. Yoo, "Ultimate thin vertical p-n junction composed of two-dimensional layered molybdenum disulfide.," *Nature communications*, vol. 6, p. 6564, 2015.

[36] K. F. Mak, C. Lee, J. Hone, J. Shan, and T. F. Heinz, “Atomically thin MoS2: A new direct-gap semiconductor,” *Physical Review Letters*, vol. 105, no. 13, pp. 2–5, 2010.

[37] H. Li, J. Wu, Z. Yin, and H. Zhang, “Preparation and Applications of Mechanically Exfoliated Single-Layer and Multilayer MoS2 and WSe2 Nanosheets,” *Account of chemical research*, vol. 47, no. 4, pp. 1067–1075, 2014.

[38] H. Li, X. Qi, J. Wu, Z. Zeng, J. Wei, and H. Zhang, “Investigation of MoS2 and Graphene Nanosheets by Magnetic Force Microscopy,” *ACS Nano*, vol. 7, no. 3, pp. 2842–2849, 2013.

[39] A. Splendiani, L. Sun, Y. Zhang, T. Li, J. Kim, C. Y. Chim, G. Galli, and F. Wang, “Emerging photoluminescence in monolayer MoS2,” *Nano Letters*, vol. 10, no. 4, pp. 1271–1275, 2010.

[40] Z. Yin, H. H. Li, H. H. Li, L. Jiang, Y. Shi, Y. Sun, G. Lu, Q. Zhang, X. Chen, and H. Zhang, “Single-layer MoS2 phototransistors,” *ACS nano*, vol. 6, no. 1, pp. 74–80, 2012.

[41] O. Lopez-Sanchez, D. Lembke, M. Kayci, A. Radenovic, and A. Kis, “Ultrasensitive photodetectors based on monolayer MoS2,” *Nature Nanotechnology*, vol. 8, no. 7, pp. 497–501, 2013.

[42] H. Li, Z. Yin, Q. He, H. Li, X. Huang, G. Lu, D. W. H. Fam, A. I. Y. Tok, Q. Zhang, and H. Zhang, “Fabrication of single- and multilayer MoS2 film-based field-effect transistors for sensing NO at room temperature,” *Small*, vol. 8, no. 1, pp. 63–67, 2012.

[43] M. Xia, B. Li, K. Yin, G. Capellini, G. Niu, Y. Gong, W. Zhou, P. M. Ajayan, and Y.-H. Xie, “Spectroscopic Signatures of AA and AB Stacking of Chemical Vapor Deposited Bilayer MoS2,” *ACS Nano*, vol. 9, no. 12, pp. 12246–12254, 2015.

[44] D. Sharma, M. Amani, A. Motayed, P. B. Shah, a. G. Birdwell, S. Najmaei, P. M. Ajayan, J. Lou, M. Dubey, Q. Li, and A. V. Davydov, “Electrical transport and low-frequency noise in chemical vapor deposited single-layer MoS2 devices.,” *Nanotechnology*, vol. 25, no. 15, p. 155702, 2014.

[45] W. Zhu, T. Low, Y. H. Lee, H. Wang, D. B. Farmer, J. Kong, F. Xia, and P. Avouris, “Electronic transport and device prospects of monolayer molybdenum disulphide grown by chemical vapour deposition,” *Nat Commun*, vol. 5, p. 3087, 2014.

[46] R. Kappera, D. Voiry, S. E. Yalcin, W. Jen, M. Acerce, S. Torrel, B. Branch, S. Lei, W. Chen, S. Najmaei, J. Lou, P. M. Ajayan, G. Gupta, A. D. Mohite, and M. Chhowalla, “Metallic 1T phase source/drain electrodes for field effect transistors from chemical vapor deposited MoS2,” *APL Materials*, vol. 2, p. 092516, sep 2014.

[47] M. Acerce, D. Voiry, and M. Chhowalla, "Metallic 1T phase MoS2 nanosheets as supercapacitor electrode materials," *Nature Nanotechnology*, vol. 10, no. 4, pp. 313–318, 2015.

[48] V. Nicolosi, M. Chhowalla, M. G. Kanatzidis, M. S. Strano, and J. N. Coleman, "Liquid Exfoliation of Layered Materials," *Science*, vol. 340, no. 6139, p. 1226419, 2013.

[49] U. Halim, C. R. Zheng, Y. Chen, Z. Lin, S. Jiang, R. Cheng, Y. Huang, and X. Duan, "A rational design of cosolvent exfoliation of layered materials by directly probing liquid-solid interaction," *Nature Communications*, vol. 4, p. 2213, 2013.

[50] J. N. Coleman, M. Lotya, A. O'Neill, S. D. Bergin, P. J. King, U. Khan, K. Young, A. Gaucher, S. De, R. J. Smith, I. V. Shvets, S. K. Arora, G. Stanton, H.-Y. Kim, K. Lee, G. T. Kim, G. S. Duesberg, T. Hallam, J. J. Boland, J. J. Wang, J. F. Donegan, J. C. Grunlan, G. Moriarty, A. Shmeliov, R. J. Nicholls, J. M. Perkins, E. M. Grieveson, K. Theuwissen, D. W. McComb, P. D. Nellist, and V. Nicolosi, "Two-dimensional nanosheets produced by liquid exfoliation of layered materials.," *Science (New York, N.Y.)*, vol. 331, no. 6017, pp. 568–571, 2011.

[51] K. Lee, H.-Y. Kim, M. Lotya, J. N. Coleman, G.-T. Kim, and G. S. Duesberg, "Electrical Characteristics of Molybdenum Disulfide Flakes Produced by Liquid Exfoliation," *Advanced Materials*, vol. 23, no. 36, pp. 4178–4182, 2011.

[52] A. Gupta, V. Arunachalam, and S. Vasudevan, "Liquid-Phase Exfoliation of MoS2 Nanosheets: The Critical Role of Trace Water," *The Journal of Physical Chemistry Letters*, vol. 7, no. 23, pp. 4884–4890, 2016.

[53] A. Jawaid, D. Nepal, K. Park, M. Jespersen, A. Qualley, P. Mirau, L. F. Drummy, and R. A. Vaia, "Mechanism for Liquid Phase Exfoliation of MoS2," *Chemistry of Materials*, vol. 28, no. 1, pp. 337–348, 2016.

[54] L. Dong, S. Lin, L. Yang, J. Zhang, C. Yang, D. Yang, and H. Lu, "Spontaneous exfoliation and tailoring of MoS2 in mixed solvents," *Chem. Commun.*, vol. 50, no. 100, pp. 15936–15939, 2014.

[55] R. J. Smith, P. J. King, M. Lotya, C. Wirtz, U. Khan, S. De, A. O'Neill, G. S. Duesberg, J. C. Grunlan, G. Moriarty, J. Chen, J. Wang, A. I. Minett, V. Nicolosi, and J. N. Coleman, "Large-scale exfoliation of inorganic layered compounds in aqueous surfactant solutions," *Advanced Materials*, vol. 23, no. 34, pp. 3944–3948, 2011.

[56] G. Cunningham, U. Khan, C. Backes, D. Hanlon, D. McCloskey, J. F. Donegan, and J. N. Coleman, "Photoconductivity of solution-processed MoS2 films," *J. Mater. Chem. C*, vol. 1, no. 41, pp. 6899–6904, 2013.

[57] M. M. Bernal, L. Álvarez, E. Giovanelli, A. Arnáiz, L. Ruiz-González, S. Casado, D. Granados, A. M. Pizarro, A. Castellanos-Gomez, and E. M. Pérez, “Luminescent transition metal dichalcogenide nanosheets through one-step liquid phase exfoliation,” *2D Materials*, vol. 3, no. 3, p. 035014, 2016.

[58] K. G. Zhou, N. N. Mao, H. X. Wang, Y. Peng, and H. L. Zhang, “A mixed-solvent strategy for efficient exfoliation of inorganic graphene analogues,” *Angewandte Chemie - International Edition*, vol. 50, no. 46, pp. 10839–10842, 2011.

[59] V. Forsberg, R. Zhang, J. Backstrom, C. Dahlstrom, B. Andres, M. Norgren, M. Andersson, M. Hummelgard, and H. Olin, “Exfoliated MoS2 in Water without Additives,” *PLOS ONE*, vol. 11, no. 4, p. e0154522, 2016.

[60] H. J. Chuang, B. Chamlagain, M. Koehler, M. M. Perera, J. Yan, D. Mandrus, D. Tománek, and Z. Zhou, “Low-Resistance 2D/2D Ohmic Contacts: A Universal Approach to High-Performance WSe2, MoS2, and MoSe2 Transistors,” *Nano Letters*, vol. 16, no. 3, pp. 1896–1902, 2016.

[61] Y. Liu, H. Wu, H. C. Cheng, S. Yang, E. Zhu, Q. He, M. Ding, D. Li, J. Guo, N. O. Weiss, Y. Huang, and X. Duan, “Toward barrier free contact to molybdenum disulfide using graphene electrodes,” *Nano Letters*, vol. 15, no. 5, pp. 3030–3034, 2015.

[62] J. Lin, Z. Peng, Y. Liu, F. Ruiz-Zepeda, R. Ye, E. L. G. Samuel, M. J. Yacaman, B. I. Yakobson, and J. M. Tour, “Laser-induced porous graphene films from commercial polymers,” *Nature Communications*, vol. 5, no. 5714, pp. 1–8, 2014.

[63] M. Amani, D.-H. Lien, D. Kiriya, J. Xiao, A. Azcatl, J. Noh, S. R. Madhvapathy, R. Addou, S. KC, M. Dubey, K. Cho, R. M. Wallace, S.-C. Lee, J.-H. He, J. W. Ager, X. Zhang, E. Yablonovitch, and A. Javey, “Near-unity photoluminescence quantum yield in MoS2,” *Science*, vol. 350, no. 6264, pp. 1065–1068, 2015.

[64] V. Štengl and J. Henych, “Strongly luminescent monolayered MoS2 prepared by effective ultrasound exfoliation.,” *Nanoscale*, vol. 5, no. 8, pp. 3387–94, 2013.

[65] J. Hong, Z. Hu, M. Probert, K. Li, D. Lv, X. Yang, L. Gu, N. Mao, Q. Feng, L. Xie, J. Zhang, D. Wu, Z. Zhang, C. Jin, W. Ji, X. Zhang, J. Yuan, and Z. Zhang, “Exploring atomic defects in molybdenum disulphide monolayers.,” *Nature communications*, vol. 6, p. 6293, 2015.

[66] C. Backhouse, H. Kato, and L. Young, “Low-frequency oscillations in semi-insulating gaas and inp: deep level domain spectroscopy,” *Canadian Journal of Physics*, vol. 72, no. 9-10, pp. 608–617, 1994.

[67] Adafruit Industries, *ITO (Indium Tin Oxide) Coated PET Plastic - 100 mm x 200 mm.* part number = 1309, `https://www.adafruit.com/product/1309`.

[68] N. Mao, Y. Chen, D. Liu, J. Zhang, and L. Xie, "Solvatochromic effect on the photoluminescence of MoS2 monolayers," *Small*, vol. 9, no. 8, pp. 1312–1315, 2013.

[69] J. Tauc, "Optical properties and electronic structure of amorphous Ge and Si," *Materials Research Bulletin*, vol. 3, no. 1, pp. 37–46, 1968.

[70] A. Winchester, S. Ghosh, S. Feng, A. L. Elias, T. Mallouk, M. Terrones, and S. Talapatra, "Electrochemical characterization of liquid phase exfoliated two-dimensional layers of molybdenum disulfide," *ACS Applied Materials and Interfaces*, vol. 6, no. 3, pp. 2125–2130, 2014.

[71] J. Xiao, M. Long, X. Li, Q. Zhang, H. Xu, and K. S. Chan, "Effects of van der Waals interaction and electric field on the electronic structure of bilayer MoS2," *Journal of Physics: Condensed Matter*, vol. 26, no. 40, p. 405302, 2014.

[72] J. Jiang, S. Xiu, M. Zheng, T. Jia, H. Liu, Y. Zhang, and G. Chen, "Indirectdirect bandgap transition and gap width tuning in bilayer MoS2 superlattices," *Chemical Physics Letters*, vol. 613, pp. 74–79, 2014.

[73] K. F. Mak, K. He, C. Lee, G. H. Lee, J. Hone, and T. F. Heinz, "Tightly bound trions in monolayer MoS2," *Nature Materials*, vol. 12, no. December 2012, pp. 207–211, 2013.

[74] Y.-C. Wu, C.-H. Liu, S.-Y. Chen, F.-Y. Shih, P.-H. Ho, C.-W. Chen, C.-T. Liang, and W.-H. Wang, "Extrinsic Origin of Persistent Photoconductivity in Monolayer MoS2 Field Effect Transistors," *Scientific Reports*, vol. 5, no. November 2014, p. 11472, 2015.

[75] Horiba Scientific, *Dynamic Light Scattering.* `http://www.horiba.com/scientific/products/particle-characterization/technology/dynamic-light-scattering/`.

[76] R. M. Howard, *Principles of Random Signal Analysis and Low Noise Design: the power spectral density and its applications.* Wiley, New York, 2002.

[77] X.-M. Li, D. Reinhoudt, and M. Crego-Calama, "What do we need for a superhydrophobic surface? A review on the recent progress in the preparation of superhydrophobic surfaces.," *Chemical Society reviews*, vol. 36, no. 8, pp. 1350–1368, 2007.

[78] J. T. Simpson, S. R. Hunter, and T. Aytug, "Superhydrophobic materials and coatings: a review," *Reports on Progress in Physics*, vol. 78, no. 8, p. 086501, 2015.

[79] L.-Y. Meng and S.-J. Park, “Superhydrophobic carbon-based materials: a review of synthesis, structure, and applications,” *Carbon letters*, vol. 15, no. 2, pp. 89–104, 2014.

[80] T. Aytug, D. F. Bogorin, P. M. Paranthaman, J. E. Mathis, J. T. Simpson, and D. K. Christen, “Superhydrophobic ceramic coatings enabled by phase-separated nanostructured composite TiO2-Cu2O thin films.,” *Nanotechnology*, vol. 25, no. 24, p. 245601, 2014.

[81] G. Liu, W. S. Y. Wong, N. Nasiri, and A. Tricoli, “Ultraporous superhydrophobic gas-permeable nano-layers by scalable solvent-free one-step self-assembly,” *Nanoscale*, vol. 8, no. 11, pp. 6085–6093, 2016.

[82] B. D’Urso, J. T. Simpson, and M. Kalyanaraman, “Emergence of superhydrophobic behavior on vertically aligned nanocone arrays,” *Applied Physics Letters*, vol. 90, no. 4, pp. 88–91, 2007.

[83] D. D. Nguyen, N.-H. Tai, S.-B. Lee, and W.-S. Kuo, “Superhydrophobic and superoleophilic properties of graphene-based sponges fabricated using a facile dip coating method,” *Energy & Environmental Science*, vol. 5, no. 7, p. 7908, 2012.

[84] Z. Chen, L. Dong, D. Yang, and H. Lu, “Superhydrophobic graphene-based materials: Surface construction and functional applications,” *Advanced Materials*, vol. 25, no. 37, pp. 5352–5359, 2013.

[85] K. K. S. Lau, J. Bico, K. B. K. Teo, M. Chhowalla, G. A. J. Amaratunga, W. I. Milne, G. H. McKinley, and K. K. Gleason, “Superhydrophobic Carbon Nanotube Forests,” *Nano Letters*, vol. 3, no. 12, pp. 1701–1705, 2003.

[86] C.-F. Wang, C.-S. Liao, S.-W. Kuo, and H.-C. Lin, “Tunable wettability of carbon nanotube/poly (-caprolactone) hybrid films,” *Applied Surface Science*, vol. 257, no. 21, pp. 9152–9157, 2011.

[87] I. S. Bayer, V. Caramia, D. Fragouli, F. Spano, R. Cingolani, and a. Athanassiou, “Electrically conductive and high temperature resistant superhydrophobic composite films from colloidal graphite,” *Journal of Materials Chemistry*, vol. 22, no. 5, p. 2057, 2012.

[88] J. Rafiee, M. A. Rafiee, Z. Z. Yu, and N. Koratkar, “Superhydrophobic to superhydrophilic wetting control in graphene films,” *Advanced Materials*, vol. 22, no. 19, pp. 2151–2154, 2010.

[89] J. N. Wang, R. Q. Shao, Y. L. Zhang, L. Guo, H. B. Jiang, D. X. Lu, and H. B. Sun, “Biomimetic graphene surfaces with superhydrophobicity and iridescence,” *Chemistry - An Asian Journal*, vol. 7, no. 2, pp. 301–304, 2012.

[90] H. Zhu, D. Chen, W. An, N. Li, Q. Xu, H. Li, J. He, and J. Lu, "A Robust and Cost-Effective Superhydrophobic Graphene Foam for Efficient Oil and Organic Solvent Recovery," *Small*, vol. 11, no. 39, pp. 5222–5229, 2015.

[91] P. A. Levkin, F. Svec, and J. M. J. Fréchet, "Porous polymer coatings: A versatile approach to superhydrophobic surfaces," *Advanced Functional Materials*, vol. 19, no. 12, pp. 1993–1998, 2009.

[92] G. Gong, J. Wu, J. Liu, N. Sun, Y. Zhao, and L. Jiang, "Bio-inspired adhesive superhydrophobic polyimide mat with high thermal stability," *Journal of Materials Chemistry*, vol. 22, no. 17, p. 8257, 2012.

[93] H. C. Barshilia, A. Ananth, N. Gupta, and C. Anandan, "Superhydrophobic nanostructured Kapton surfaces fabricated through Ar+O2 plasma treatment: Effects of different environments on wetting behaviour," *Applied Surface Science*, vol. 268, pp. 464–471, 2013.

[94] A. T. Abdulhussein, G. K. Kannarpady, A. B. Wright, A. Ghosh, and A. S. Biris, "Current trend in fabrication of complex morphologically tunable superhydrophobic nano scale surfaces," *Applied Surface Science*, vol. 384, pp. 311–332, 2016.

[95] M. Jin, X. Feng, J. Xi, J. Zhai, K. Cho, L. Feng, and L. Jiang, "Superhydrophobic PDMS surface with ultra-low adhesive force," *Macromolecular Rapid Communications*, vol. 26, no. 22, pp. 1805–1809, 2005.

[96] C. J. Wohl, M. A. Belcher, L. Chen, and J. W. Connell, "Laser ablative patterning of copoly(imide siloxane)s generating superhydrophobic surfaces," *Langmuir*, vol. 26, no. 13, pp. 11469–11478, 2010.

[97] H. Pazokian, a. Selimis, J. Barzin, S. Jelvani, M. Mollabashi, C. Fotakis, and E. Stratakis, "Tailoring the wetting properties of polymers from highly hydrophilic to superhydrophobic using UV laser pulses," *Journal of Micromechanics and Microengineering*, vol. 22, no. 3, p. 035001, 2012.

[98] R. M. Bär, S. Widmaier, and P. A. Levkin, "Facile fabrication of robust superhydrophobic surfaces: comparative investigation," *RSC Adv.*, vol. 6, no. 100, pp. 98257–98266, 2016.

[99] Y. Li, D. X. Luong, J. Zhang, Y. R. Tarkunde, C. Kittrell, F. Sargunaraj, Y. Ji, C. J. Arnusch, and J. M. Tour, "Laser-Induced Graphene in Controlled Atmospheres: From Superhydrophilic to Superhydrophobic Surfaces," *Advanced Materials*, vol. 1700496, pp. 1–8, 2017.

[100] J. Drelich, "Guidelines to measurements of reproducible contact angles using a sessile-drop technique," *Surface Innovations*, vol. 1, no. 4, pp. 248–254, 2013.

[101] Z. Pan, H. Shahsavan, W. Zhang, F. K. Yang, and B. Zhao, "Superhydro-oleophobic bio-inspired polydimethylsiloxane micropillared surface via FDTS coating/blending approaches," *Applied Surface Science*, vol. 324, pp. 612–620, 2015.

[102] A. F. Stalder, G. Kulik, D. Sage, L. Barbieri, and P. Hoffmann, "A snake-based approach to accurate determination of both contact points and contact angles," *Colloids and Surfaces A: Physicochemical and Engineering Aspects*, vol. 286, no. 1-3, pp. 92–103, 2006.

[103] A. F. Stalder, T. Melchior, M. Müller, D. Sage, T. Blu, and M. Unser, "Low-bond axisymmetric drop shape analysis for surface tension and contact angle measurements of sessile drops," *Colloids and Surfaces A: Physicochemical and Engineering Aspects*, vol. 364, no. 1-3, pp. 72–81, 2010.

[104] H. C. Duong, M. Duke, S. Gray, P. Cooper, and L. D. Nghiem, "Membrane scaling and prevention techniques during seawater desalination by air gap membrane distillation," *Desalination*, vol. 397, pp. 92–100, 2016.

[105] V. Hisler, H. Jendoubi, C. Hairaye, L. Vonna, V. Le Houérou, F. Mermet, M. Nardin, and H. Haidara, "Tensiometric Characterization of Superhydrophobic Surfaces As Compared to the Sessile and Bouncing Drop Methods," *Langmuir*, vol. 32, no. 31, pp. 7765–7773, 2016.

[106] C. Lee, X. Wei, J. W. Kysar, and J. Hone, "Measurement of the Elastic Properties and Intrinsic Strength of Monolayer Graphene," *Science*, vol. 321, no. 5887, pp. 385–388, 2008.

[107] I. C. Karagiannis and P. G. Soldatos, "Water desalination cost literature: review and assessment," *Desalination*, vol. 223, no. 1-3, pp. 448–456, 2008.

[108] E. Mathioulakis, V. Belessiotis, and E. Delyannis, "Desalination by using alternative energy: Review and state-of-the-art," *Desalination*, vol. 203, no. 1-3, pp. 346–365, 2007.

[109] L. Eykens, T. Reyns, K. De Sitter, C. Dotremont, L. Pinoy, and B. Van der Bruggen, "How to select a membrane distillation configuration? Process conditions and membrane influence unraveled," *Desalination*, vol. 399, pp. 105–115, 2016.

[110] R. P. Lively and D. S. Sholl, "From water to organics in membrane separations," *Nature Materials*, vol. 16, no. 3, pp. 276–279, 2017.

[111] J. Bundschuh, N. Ghaffour, H. Mahmoudi, M. Goosen, S. Mushtaq, and J. Hoinkis, "Low-cost low-enthalpy geothermal heat for freshwater production: Innovative applications using thermal desalination processes," *Renewable and Sustainable Energy Reviews*, vol. 43, pp. 196–206, 2015.

[112] The Dow Chemical Company, *FILMTEC Membranes - Lifetime*, 2015. `https://dowac.custhelp.com/app/answers/detail/a_id/267/~/filmtec-membranes---lifetime`.

[113] American Membrane Technology Association, *Pretreatment for Membrane Processes*, 2007. `https://www.amtaorg.com/wp-content/uploads/12_Pretreatment.pdf`.

[114] J. Xu, Y. B. Singh, G. L. Amy, and N. Ghaffour, "Effect of operating parameters and membrane characteristics on air gap membrane distillation performance for the treatment of highly saline water," *Journal of Membrane Science*, vol. 512, pp. 73–82, 2016.

[115] The Dow Chemical Company, *DOW FILMTEC SW30HRLE-440i*, 2016. `http://msdssearch.dow.com/PublishedLiteratureDOWCOM/dh_097a/0901b8038097abaa.pdf?filepath=liquidseps/pdfs/noreg/609-03001.pdf&fromPage=GetDoc`.

[116] M. M. A. Shirazi, A. Kargari, and M. Tabatabaei, "Evaluation of commercial PTFE membranes in desalination by direct contact membrane distillation," *Chemical Engineering and Processing: Process Intensification*, vol. 76, pp. 16–25, 2014.

[117] Y. C. Woo, L. D. Tijing, W.-G. Shim, J.-S. Choi, S.-H. Kim, T. He, E. Drioli, and H. K. Shon, "Water desalination using graphene-enhanced electrospun nanofiber membrane via air gap membrane distillation," *Journal of Membrane Science*, vol. 520, pp. 99–110, 2016.

[118] Y. C. Woo, Y. Kim, W. G. Shim, L. D. Tijing, M. Yao, L. D. Nghiem, J. S. Choi, S. H. Kim, and H. K. Shon, "Graphene/PVDF flat-sheet membrane for the treatment of RO brine from coal seam gas produced water by air gap membrane distillation," *Journal of Membrane Science*, vol. 513, pp. 74–84, 2016.

[119] Y. C. Woo, L. D. Tijing, M. J. Park, M. Yao, J. S. Choi, S. Lee, S. H. Kim, K. J. An, and H. K. Shon, "Electrospun dual-layer nonwoven membrane for desalination by air gap membrane distillation," *Desalination*, vol. 403, pp. 187–198, 2017.

[120] R. Aryapratama, H. Koo, S. Jeong, and S. Lee, "Performance evaluation of hollow fiber air gap membrane distillation module with multiple cooling channels," *Desalination*, vol. 385, pp. 58–68, 2016.

[121] L. Li and K. K. Sirkar, "Studies in vacuum membrane distillation with flat membranes," *Journal of Membrane Science*, vol. 523, no. April 2016, pp. 225–234, 2017.

[122] Dupont, *Dupont Kapton: Summary of Properties.* `http://www.dupont.com/content/dam/dupont/products-and-services/membranes-and-films/polyimde-films/documents/DEC-Kapton-summary-of-properties.pdf`.

Appendix A

Python Code

Table of Contents

A.1 Chapter 2

A.1.1 Microheater Control Code

This code corresponds with the microheater control code discussed in § 2. This code was written by Dr. Christopher Backhouse and modified by Collin M Tittle.

```
#!/usr/bin/env python
# This is TwoStep.py: combining Labjack, Ocean Optics SW to control the
   heater,
#  read the temperature, LED on at all times (6 mA), and read the spectra.
import os, os.path, re, time, sys, u6, time, usb.core, usb.util,
   multiprocessing, ctypes
import numpy as np
from pylab import *
from PCR_Run_Subroutines import *

""" Connections:
V+/V- : are across the sensor and connected to AI0, 1
HtrHigh and HtrLow are connected to the dual heaters
200 uA and GND are connected to the sensor
A jumper links the two halves of the dual heater.
See p56. """

global TCR_Def;
#TCR_Def = 2.29e-3; # original value for 1.5 mm mirror chips
#TCR_Def = 2.5277e-3; # see p83, for 1.5 mm mirror chips, valid at 25C
#TCR_Def = 2.49e-3; # see p119, for 1.5 mm mirror chip A0, valid at 25C
TCR_Def = 3.1e-3;

# ************************************
# Labjack subroutines
# ************************************

RampTMax = 93.0; # Maximum T for ramping
Rload = 4.617; # was 4.7 but got 96.7 mA when set 95
global Rest0, T0, HomeDir, SpecNum, oo, d, ISetMax, NClip;
#ISetMax = 180.0;  # Max SetCurrent assuming R0=22 Ohms
ISetMax = 240;
def GetADC(Channel=0):
   """Non-differential auto-ranging, calibrated measurement of
      Channel=0"""
   RV, = d.getFeedback( u6.AIN24AR(Channel, ResolutionIndex = 0,
      GainIndex = 0,
     SettlingFactor = 4, Differential = False ) )
   LRV = d.binaryToCalibratedAnalogVoltage(RV['GainIndex'],RV['AIN'])
   return(LRV);
```

```
def GetADC_DAR(Channel=0):
   """Differential auto-ranging, calibrated measurement of Channel=0"""
   RV, = d.getFeedback( u6.AIN24AR(Channel, ResolutionIndex = 0,
       GainIndex = 0,
      SettlingFactor = 4, Differential = True ) )
   LRV = d.binaryToCalibratedAnalogVoltage(RV['GainIndex'],RV['AIN'])
   return(LRV);

def GetADC_D(Channel=0,gain=1):
   """Differential set gain (gain=1), calibrated measurement of
       Channel=0"""
   RV = d.getFeedback( u6.AIN24(Channel, ResolutionIndex = 0, GainIndex =
       gain,
      SettlingFactor = 0, Differential = True ) )
   LRV =
       d.binaryToCalibratedAnalogVoltage(gainIndex=gain,bytesVoltage=RV[0])
   return(LRV);

def GetADC_200(Channel=0,gain=3,settling=4):
   """Differential set gain (gain=1), calibrated measurement of
       Channel=0"""
   RV = d.getFeedback( u6.AIN24(Channel, ResolutionIndex = 0, GainIndex =
       gain,
      SettlingFactor = settling, Differential = True ) )
   LRV =
       d.binaryToCalibratedAnalogVoltage(gainIndex=gain,bytesVoltage=RV[0])
   return(LRV);

def GetADC_200R(C=0,g=3,s=4):
   """Differential set gain (gain=1), calibrated measurement of
       Channel=0"""
   x=0;
   for i in range(1000):
      x = x + GetADC_200(Channel=C,gain=g,settling=s);
   return(x/1000.0);

def SetDAC(Volts):
   """ Calibrated setting of DAC0 to output Volts """
#  Volts /= 1.05 # My estimate! # Bits = (Volts/4.86)*65536
   Bits = (d.calInfo.dac0Slope*Volts) + d.calInfo.dac0Offset
   if Bits < 0: Bits = 0
   d.getFeedback( u6.DAC16( 0, int(Bits)) ) # set DAC0

def SetCurrent0(mA):
   """Set current via DAC0 as per LT3092 data sheet but with R of Rload
       """
   if (mA > 115.0):
      mA = 115.0;
```

```
   if (mA < 0.5):
      mA = 0.5;
   Vset = (mA/100.0)/(10.0/Rload);
   SetDAC(Vset);

def SetCurrent(mA):
   """Set current via DAC0 as per LT3092 data sheet but with R of Rload,
      allow slow increase in IMax if it is consistently too low """
   if (mA < 0.5):
      mA = 0.5;
   Vset = (mA/100.0)/(10.0/Rload);
   d.writeRegister(5000,Vset);

def GetInstrOut():
   """Default: Get voltage drop across sensor ring with AI0 and AI1
       (about 0.01V)"""
#  x = GetADC_DAR(Channel=0); return(abs(x));
   x = GetADC_200R(C=0,g=2); return(abs(x));

def GetVDrop():
   """Get voltage drop across load resistor (of about 5 ohms) with AI2
       and AI3 (about 0.2 V)"""
   x = GetADC_D(Channel=2,gain=1); return(x);

def CTCurrentMeasure():
   #Measure Actual Current
   Vdrop = d.getAIN(3)-d.getAIN(2);
   Iactual = Vdrop/4.617;
   return(Iactual);

# *************************************
# Spectra handling suboutines
# *************************************

def mean(data):
   return sum(data)/float(len(data))

def fmean(data, wavel,startw=550.0, stopw=650.0):
   sumw = 0.0; ii = 0;
   for i in range(len(data)):
      L = wavel[i];
      if (L>startw) and (L<stopw):
         sumw += data[i];
         ii += 1;
   return sumw/float(ii);

def snmean(data, wavel): # See lab book 2015.03.29 p36
   S = (fmean(data, wavel,startw=550.0, stopw=650.0) - fmean(data,
```

```
      wavel,startw=650.0, stopw=750.0))/ \
     fmean(data, wavel,startw=425.0, stopw=500.0);
   return S;

def Record(oo,d):
   d.getFeedback(u6.BitStateWrite(0,0)); time.sleep(1);
   res_off = oo.getSpectrum(); time_off = time.time();
   d.getFeedback(u6.BitStateWrite(0,1)); time.sleep(1);
   res_on = oo.getSpectrum(); time_on = time.time(); time.sleep(1);
   d.getFeedback(u6.BitStateWrite(0,0));
   return(res_off,time_off, res_on, time_on);

def FastRecord():
   global HomeDir, SpecNum;
   #d.getFeedback(u6.BitStateWrite(0,1));
   res_on = oo.getSpectrum();
   #d.getFeedback(u6.BitStateWrite(0,0));
   np.savetxt(("%s/Spectra/Spectrum%1d.txt" % (HomeDir,SpecNum)),res_on);
   SpecNum += 1;

def T_Est(Vio, T0, R0, TCR=TCR_Def):
   """Calculate the estimated T from the voltage across the sensor,
   the room temperature (T0) and its resistance (R0), and the TCR """
   R = Vio/200e-6;
   return( ((T0 - 273.16) + (((R/R0) - 1.0)/TCR) )); # return Tapparent

def IScale(Ttarg, Tmeas, Tassumed,Treached=0):
   """Calculate the estimated scaling for the currents needed when the
      ambient temperature has changed"""
   rv = math.pow( (Ttarg-Tassumed)/(Ttarg-Tmeas), 0.5);
   print("Correcting for ambient temperature variations due to
      Tambient=%5.3f" % Tmeas);
   if (Treached != 0): # correct for power variations due to R changes
      rv = rv*math.pow( (Ttarg-20)/(Treached-20), 0.5);
      print("Correcting for resistance variations that led to previous T
         of %5.3f C" % Treached);
   return(rv); # return Tapparent

# *************************************
# Temperature Controller Routines
# *************************************
#THigh          = 85.0;  # Temperature of high-temperature step
#THigh          = 93.0;  # Temperature of high-temperature step
THigh          = 94.0;  # Temperature of high-temperature step
#THigh          = 97.0;  # Temperature of high-temperature step
#tHighPID       = 30.0;  # Time to control at the high T target (in
   steps!)
tHighPID       = 40.0;  # Time to control at the high T target (in
```

```
    steps!)
tHighinitialheat = 63.0; # Estimated time for first cycle (in steps!)
    (for 2min at 90ish, with 45s to warm)
#IHighhold      = 95.0;  # Estimated current to hold at high T target
#IHighhold      = 100.0;  # Estimated current to hold at high T target
IHighhold      = 240.0;  # Estimated current to hold at high T target
#IHighhold      = 145;  # Estimated current to hold at high T target

#TLow          = 65.0; # Temperature of Low-temperature step
TLow          = 63.0; # Temperature of Low-temperature step
#tLowPID        = 30.0; # Time to control at the Low T target (in steps!)
tLowPID       = 40.0; # Time to control at the Low T target (in steps!)
ILowhold      = 160.0; # Estimated current to hold at Low T target

# Medium is not used here...
TMed          = 72.0; # Temperature of Med-temperature step
IMedpreheat   = 91.0; # Estimated current to preheat with for Med T
    target
tMedpreheat   =  3.0; # Estimated time to preheat with for Med T target
tMedPID       = 10.0; # Time to control at the Med T target
#IMedhold       = 87.0; # Estimated current to hold at Med T target
IMedhold      = 91.0; # Estimated current to hold at Med T target


# Signal = Kp*(e + (Sum(deltat*e)/TimConi) + TimCond*deltae/deltat)
def  PID(timehold=10,tempset=90.0,Ihold=10, TimConi=10, TimCond=10, Kp =
    2.0, Igain=1.0):
   """ PID control algorythm """
   global SpecNum;
   ESum = 0.0;
   CloseEnough = False;
   LastError = tempset - PresentTemp();
   DVec = [];
   #FastRecord();
   for i in range(int(timehold)):
      FastRecord();
      Error = tempset - PresentTemp();
      if (abs(Error) < 0.01):
         CloseEnough = True;
      if (CloseEnough==True):
         ESum = ESum + Error;
      if (TimConi > 0.001):
         Iset = Ihold +\
             Kp*( Error + ((ESum*Igain)/TimConi) +
                 (TimCond*(Error-LastError)));
      else:
         Itest = Ihold + Kp*( Error + (TimCond*(Error-LastError)));
         if Itest <= 220:
```

```
            Iset = Itest;
         else:
            Iset = 220;
         #Iset = Ihold + Kp*( Error + (TimCond*(Error-LastError)));
      x = (time.time(),Iset,tempset,tempset-Error,SpecNum);
      DVec.append(x);
      IactualCT = CTCurrentMeasure(); #returns current from previous set
      print("Time: %5.3f Step: %2d Iset: %2f TSet: %2f Temp: %5.3f Sum:
          %5.3f Der: %5.3f Spec: %d Imeasure: %f" %
         (x[0],i,x[1],x[2],x[3],ESum,Error-LastError,SpecNum,IactualCT));
      LastError = Error;
      SetCurrent(Iset);
   return(DVec);

def RecentRun():
   """ determines whether the program was recently run, and if so, uses
       saved values for Rest0 and T0 """
   try:
      (timelast,LastRest0,LastT0) = np.loadtxt("WarmFile.txt");
   except:
      timelast = 0;
   if ((time.time() - timelast ) > 300.0):
      Vdr0 = GetVDrop(); Vio0 = GetInstrOut(); T0 = d.getTemperature();
      Rest0 = Vio0/200e-6;
      print("Estimating R0 as %5.3f ohms at a temperature of %5.3f" %
          (Rest0,T0))
   else:
      Rest0 = LastRest0;
      T0 = LastT0;
      print("Re-using old values: R0 as %5.3f ohms with a temperature of
          %5.3f" % (Rest0,T0))
   return(Rest0, T0);

def NoteWhenLastRun(r0,t0):
   """ notes when program last ran the heater and saves values for Rest0
       and T0 """
   np.savetxt("WarmFile.txt",(time.time(),r0,t0));

def PresentTemp():
   global Rest0, T0;
   x= T_Est(GetInstrOut(), T0, Rest0);
#  print("Time %5.3f: Temp: %5.3f" % (time.time(),x));
   return(x);

def TsetHigh(initialcycle=False):
   global IScHigh;
   print("TSetHigh");
   if (initialcycle == True):
```

```
    tHigh = int(tHighinitialheat);
  else:
    tHigh = tHighPID;
#timehold=10,tempset=90.0,Ihold=10, TimConi=10, TimCond=10, Kp = 2.0)
  rv=PID(timehold=tHigh,tempset=THigh,Ihold=IHighhold,TimConi=0.0,
     TimCond=3.0, Kp = 4 );
  return(rv);

def TsetLow():
  global IScLow;
  print("TSetLow");
  rv=PID(timehold=tLowPID,tempset=TLow,Ihold=ILowhold,TimConi=0.0,
     TimCond=3.0, Kp = 4 );
  return(rv);

def TsetMed():
  global IScMed,SpecNum;
  print("TSetMed");
  DatVec = [];
  tim_in = tMedpreheat;
  SetCurrent(IMedpreheat*IScMed);
  #DatVec.append((time.time(),IMedpreheat*IScMed,TMed,PresentTemp()));
  for i in range(int(tim_in)):
    FastRecord();
    x = (time.time(),IMedpreheat*IScMed,TMed,PresentTemp(),SpecNum);
    print("Time: %5.3f Step: %2d Iset: %2f TSet: %2f Temp: %5.3f
       Spectrum: %d" %
      (x[0],i,x[1],x[2],x[3]),SpecNum);
    DatVec.append(x);
  rv=PID(timehold=tMedPID,tempset=TMed,Ihold=IMedhold*IScMed, N=5,
     Igain=0.6, Pgain=0.3);
  DatVec.extend(rv);
  return(DatVec);

#
   **************************************************************************
# Main Code
#
   **************************************************************************
SpecNum = 0; mAmin = 0.0;
global IScLow, IScMed,IScHigh;
print("This is TwoStep.py.\nNow setting up instruments.");
if (len(sys.argv)>1):
  MinMCA = float(sys.argv[1]);
else:
  MinMCA = 10.0;
if (MinMCA > 0.01):
  print("Will perform a MCA with a ramp-up time of %5.3f minutes" %
```

```
      MinMCA);
d  = u6.U6(); d.getCalibrationData(); SetCurrent(mAmin);
oo    = USB4000()
try:
   fp = open("RunData/Num_DRunAnalyse.txt","r");
   RunNum = int(fp.readline()); fp.close();
except:
   RunNum = 0;
   #os.mkdir("RunData");
RunNum = RunNum + 1;
print("** Run%d with normal configuration! **" % RunNum);
print("Now creating Data directory.");
HomeDir = ("RunData/DRuns/Run%1d" % RunNum);
TarCom = ("tar cvfz RunData/Arch_Run%1d.tgz RunData/DRuns/Run%1d" %
    (RunNum,RunNum));
os.mkdir(HomeDir);
os.mkdir(HomeDir+'/Spectra');
os.mkdir(HomeDir+'/Figures');
print("Now estimating RT R of ring sensor");
SetCurrent(mAmin); time.sleep(0.1);
(Rest0,T0) = RecentRun();  # Measure R0, T0 is cool enough, otherwise use
    last values
ISetMax *= math.pow(25.0/Rest0,0.5); # Assume Rheater scales similarly,
    need less current for same power (p100)
print("Estimating ISetMax as %5.3f mA" % ISetMax);

print("Estimating current scaling factors as:")
IScHigh = IScale(THigh,T0,292.3,Treached=0);
IScMed  = IScale(TMed,T0,292.3,Treached=0);
IScLow  = IScale(TLow,T0,292.3,Treached=0);
print("Low: %5.3f Medium: %5.3f High: %5.3f" % (IScLow, IScMed,IScHigh))
#if (len(sys.argv)>1):# RtRes = float(sys.argv[1]);
#d.getFeedback(u6.BitDirWrite(0,1)); d.getFeedback(u6.BitDirWrite(1,1));
    d.getFeedback(u6.BitDirWrite(3,1));
#d.getFeedback(u6.BitStateWrite(0,0));
    d.getFeedback(u6.BitStateWrite(1,0));
    d.getFeedback(u6.BitStateWrite(3,0));
scr = raw_input("Initialised.\nPress enter when ready to proceed.");
print("Please dim the lights as needed and check the spectrum.");

print oo.findAllConnectedSpectrometers()
wl    = oo.wlArr;
np.savetxt(("%s/Spectra/wavelengths.txtf" % HomeDir),wl);
oo.setIntegrationTime(1000000)

(res_off,time_off, res_on, time_on) = Record(oo,d);
np.savetxt(("%s/Spectra/AboutToStartNoINoL.txt" % HomeDir),res_off);
np.savetxt(("%s/Spectra/AboutToStartNoIL.txt" % HomeDir),res_on); # Note
```

```
    LED always on now

fp = open(("%s/CalRawDat.txt" % HomeDir),"w");
fp.write("Rest0 and T0: \n %7.5f %7.5f \n" % (Rest0,T0));
fp.write("NoI Off %f %f On %f %f\n" % (time_off, fmean(res_off,wl),
    time_on, fmean(res_on,wl)));
InitFmean = fmean(res_on,wl);

plot( wl/1000, res_on/1000 );
#axis([0.9*amin(wl), 1.1*amax(wl), 0.9*amin(res), 1.5*amax(res) ])
xlabel('Wavelength (um)'); ylabel('Counts/1000'); title('Spectrum')
print("Close window when ready to proceed.");
savefig(("%s/Figures/Initial_NoIL_Results.png" % HomeDir)); show();
scr = raw_input("Press enter when ready to proceed.");

Vdr = GetVDrop(); Vio = GetInstrOut();
(res_off,time_off, res_on, time_on) = Record(oo,d);
np.savetxt(("%s/Spectra/AboutToStartINoL.txt" % HomeDir),res_off);
np.savetxt(("%s/Spectra/AboutToStartIL.txt" % HomeDir),res_on);
fp.write("NoI Off %f %f On %f %f (and Vdr=%f Vio=%f Rest0 =%f )\n" %\
   (time_off, fmean(res_off,wl), time_on,
      fmean(res_on,wl),Vdr,Vio,Rest0));
Tvec = []; Nrec = 0; tstart = time.time();
print("Using the 4-pt measured value of R0 (%f ohms)" % Rest0)
fp.write("Using the 4-pt measured value of R0 (%f ohms)\n" % Rest0)
#fp.write("%7s %7s %7s %7s %7s %7s %7s %7s %7s\n" % (
# "mA", "Vdr", "Vio", "t_off", "t_on", "f_off", "f_on", "sn_off",
    "sn_on"));
fp.close();

#d.getFeedback(u6.BitStateWrite(0,0));
FullDataVec = [];
InitialHeating = True;
#d.getFeedback(u6.BitStateWrite(0,1)); time.sleep(5); # Allow time for
    LED to warm up
"""
for Ncycle in range(40):
   print("Now in cycle %d " % Ncycle);
   rv = TsetHigh(initialcycle=InitialHeating); FullDataVec.extend(rv);
      InitialHeating = False;
   rv = TsetLow(); FullDataVec.extend(rv);
#  rv = TsetMed(); FullDataVec.extend(rv);
"""
if (MinMCA > 0.0):
   print("Now starting cool-down");
   #rv = TsetLow(); FullDataVec.extend(rv);
   print("Now starting ramp-up");
   PseudoPmin=math.pow(ILowhold,2);
```

```
   PseudoPmax=math.pow(IHighhold*1.1,2);
   StepSec = MinMCA*60.0/200;
   if (StepSec<3.0):
      StepSec = 0.0;
   elif (StepSec>30.0):
      StepSec = 30.0;
   else:
      StepSec -= 3.0;
   LTemp = 0.0;
   for Power in range(200):
      PseudoP = PseudoPmin + (Power*(PseudoPmax-PseudoPmin)/200.0);
      Iset = math.pow(PseudoP,0.5);
      SetCurrent(Iset);
      time.sleep(StepSec);
      FastRecord();
      PTemp = PresentTemp();
      if (PTemp>RampTMax) and (LTemp>RampTMax):
         break;
      LTemp = PTemp;
      x = (time.time(),Iset,Power,PTemp,SpecNum);
      print("Time: %5.3f Iset: %2f Pset: %2f Temp: %5.3f Spectrum#: %2d" %
         (x[0],x[1],x[2],x[3],SpecNum));
      FullDataVec.append(x);
   print("Ramp-up complete!");
SetCurrent(mAmin); #d.getFeedback(u6.BitStateWrite(0,0)); # Turn the LED
    off!
NoteWhenLastRun(Rest0,T0);
np.savetxt(("%s/Tvector.txt" % HomeDir),Tvec);
np.savetxt(("%s/Datavector.txt" % HomeDir),FullDataVec);
fp = open("RunData/Num_DRunAnalyse.txt","w"); fp.write(("%d\n" %
    RunNum)); fp.close();
print("Run%d now complete" % RunNum);
#TarCom = ("tar cvfz RunData/Arch_Run%1d.tgz RunData/DRuns/Run%1d" %
    (RunNum,RunNum));
os.system(TarCom);
print("Done:\nPlease power off. (External Power First!)");
tv = [(j[0]-FullDataVec[0][0])/60.0 for j in FullDataVec];
Tv = [j[3] for j in FullDataVec];
plot( tv,Tv);
xlabel('Time (min)'); ylabel('Temperature (C)'); title('Temp Control')
print("Close window when ready to proceed.");
savefig(("%s/Figures/Temp_Results.png" % HomeDir)); show();
```

A.2 Chapter 3

A.2.1 Absorption Spectra of MoS_2 Nanosheets: Plotting and Analysis

This code was written by Collin M Tittle and is designed to be used in conjunction with § C.1.6.

```
import os, os.path, time, sys, u6, time, operator
import numpy as np
from pylab import *
import matplotlib.pyplot as plt
from scipy.interpolate import interp1d
from scipy.optimize import curve_fit
from scipy import stats

c = 2.998e8;  #speed of light
h = 4.135e-15; #Planck's constant

#-------------Functions

def runningMeanFast(x, N): # x=array of data, N = number of data points
    for moving average
    return np.convolve(x, np.ones((N,))/N)[(N-1):]

def func(x,a,b,c): #Fitting Function
   return a*(x-b)**2+c;

def wvtoev(x): #Converts nm to eV
   ev = h*c/(x*1e-9);
   return ev;

#-------------Main Code

#Load Data
data =
    np.loadtxt("/Users/collintittle/Documents/Research/Experiments/MoS2/absorption/mar8/mar
#Find Value at X for normalization
for i in range(len(data)):
   if data[i,0] == 344:
      a = data[i,3];

c = data[:,1]; #Abs values

da = data[:,0]; #wavelength values

index = [296,297,298,299,300]; #remove values set to zero by boxcar
```

```
   algorithm
da = np.delete(da,index); #same as above

c = runningMeanFast(c/a,6); #run boxcar
c = np.delete(c,index);
#Set windows to find max values
amin = 650;
amax = 700;
bmin = 600;
bmax = 640;

#X and Y arrays to fill with window values for A and B peaks
ax = [];
ay = [];
bx = [];
by = [];

#Find windows for fitting
for i in range(len(c)):
   if amin <= da[i] <= amax:
      ay.append(c[i]);
      ax.append(da[i]);
   if bmin <= da[i] <= bmax:
      by.append(c[i]);
      bx.append(da[i]);

maxa = np.amax(ay);
maxb = np.amax(by);


for i in range(len(c)):
   if c[i] == maxa:
      k = da[i];
   if c[i] == maxb and bmin <= da[i] <= bmax:
      kb = da[i];

j = 1;
w = 12;

while j == 1:
   afit = [];
   apeak = [];
   for i in range(len(c)):
      if k-w <= da[i] <= k+w:
         apeak.append(c[i]);
         afit.append(da[i]);
   popt,pcov = curve_fit(func,afit,apeak);
   residuals = apeak-func(afit,*popt);
```

```
   perr = np.sqrt(np.diag(pcov));
   sig = np.std(residuals);
   afres = residuals**2;
   chi = sum((residuals/sig)**2)/(len(afit)-3);
   print chi
   (x,y)=stats.ks_2samp(func(afit,*popt),apeak);
   print x,y
   j=0;
resmean = np.mean(afres);
resmean = resmean*np.ones(len(afit));

j = 1;
w = 12;
while j == 1:
   bfit = [];
   bpeak = [];
   for i in range(len(c)):
      if kb-w <= da[i] <= kb+w:
         bpeak.append(c[i]);
         bfit.append(da[i]);
   poptb,pcovb = curve_fit(func,bfit,bpeak, maxfev = 100000);
   residualb = bpeak-func(bfit, *poptb);
   fresb = residualb**2;
   fresb = [a/b for a,b in zip(fresb,bpeak)];
   fresb = sum(fresb)/(len(bpeak)-3);
   if fresb <= 1e-6:
      w = w+1;
   if fresb > 1e-6:
      j = 0;
print poptb[1],np.sqrt(pcov[1,1]);


plt.plot(da,c,label = 'Data');
plt.plot(afit,func(afit,*popt),label ='Fit');
plt.xlabel("Wavelength (nm)");
plt.ylabel("Normalized Absorbance");
plt.title("Absorbance of 25/75 with Quadratic Fit");
plt.legend();
plt.show();

plt.plot(afit,afres,'o');
plt.plot(afit,resmean,'.',label = 'Average Residual');
plt.xlabel("Wavelength (nm)");
plt.ylabel("Residual");
plt.title("Squared Residual vs. Wavelength for Quadratic Fit");
plt.legend();
plt.show();
```

A.2.2 Standard Curve Buffer Data Collection Code

This code was written by Collin M Tittle and is designed to be used with the SOP for DLDS with the standard curve buffer. This SOP is located on the USB drive given to Dr. Chris Backhouse.

```
#Python Code for Communicating With Ametek Lock-In Amplifier Via PySerial
    and Water Bath Via USB
#Collin M Tittle
#June 21, 2016

import time,u6
import serial
import numpy as np
import string

#----------------Functions

def vtoT(v): #converts voltage from LM35 measured by LI ADC4 to
    temperature in C.
   T = 100*v;
   return T

def readserial1(x):  # function to read Lock-In serial output and
    convert to float
   time.sleep(0.1);
   out = [];
   i=0;
   while i < x:
         out.append(ser1.readline());
         i=i+1;
   data = [float(a[:-2])/1000 for a in out];
   return data

def setLI(a):
   clearbuf(1);
   ser1.write('NC \r\n'); #Clear previous data in curve buffer
   clearbuf(1);
   ser1.write('TADC 3\r\n');  #Trigger Mode for ADC
   clearbuf(1);
   ser1.write('CBD 256\r\n');  #Add ADC1 to curve buffer
   clearbuf(1);
   ser1.write('STR 1000\r\n'); #Time interval between points 1000us -
       minimum for standard curve buffer
   clearbuf(1);
   ser1.write('LEN %s\r\n'%a); #Set length of curve buffer to 32768 data
       points
   clearbuf(1);
```

```
def clearbuf(a):   #Clears serial buffer 1 and waits to allow for
    transport
   ser1.flushInput();
   ser1.flushOutput();
   time.sleep(a);

def clearbuf2(a):  #Clears serial buffer and waits to allow for transport
   ser2.flushInput();
   ser2.flushOutput();
   time.sleep(a);

def Tmeasure(a):
   Vout = u.getAIN(a);   #Gets voltage from AIN of Labjack and converts
      from binary to actual
   Temp = Vout;
   return (Temp);

#Set up Serial Ports

#For Mac/Linux
ser1 = serial.Serial(      #RS232 Connection to Lock In
    port='/dev/cu.usbserial',
    baudrate=38400,
    parity=serial.PARITY_NONE,
    #stopbits=serial.STOPBITS_ONE,
    bytesize=serial.EIGHTBITS,
    timeout = 180,
    xonxoff=True,
    rtscts=False
)

ser2 = serial.Serial(      #Water Bath
   port='/dev/cu.usbserial-AH00138Q',
   baudrate=19200,
)

"""
For Windows Netbook

ser1 = serial.Serial(      #RS232 Connection to Lock In
    port='\\.\COM9',
    baudrate=38400,
    parity=serial.PARITY_NONE,
    #stopbits=serial.STOPBITS_ONE,
    bytesize=serial.EIGHTBITS,
    timeout = 180,
    xonxoff=True,
```

```
    rtscts=False
)

ser2 = serial.Serial(      #Water Bath
   port='\\.\COM8',
   baudrate=19200,
)
"""
#--------------------Main Program
V = 10;       #Drive DAC voltage---set up voltage sweeps later
d = 32768;       #Number of data points to be collected.
a = 20;          #Number of cycles for heating
b = 96;       #Number of cycles total

u=u6.U6(); #initialize U6
u.getCalibrationData();  #calibrate U6

# = np.zeros((b,d)); #create array of zeros to populate with data

clearbuf2(0.1);
ser2.write('SO 1\r\n'); #Turn on Water Bath
clearbuf2(0.1);
clearbuf(1);
k=0;
Ts = [];
Tr1 = [];
Tr2 = [];
t = [];

ser2.write('SS 80\r\n'); #Set water bath to temp
clearbuf2(0.1);

clearbuf(0.1);
setLI(d);                #Set LI settings
clearbuf(2);
ser1.write('DAC. 1 %s \r\n'%V); #Set DAC drive voltage
clearbuf(1);

f = open("nov1_ps1.txt",'w');

while k < a:
      time.sleep(300);
      clearbuf(0.1);
      a1 = Tmeasure(0);
      a2 = Tmeasure(1);
      Tr1.append(vtoT(a1));    #Bottom Temp
      Tr2.append(vtoT(a2));    #Top Temp
      Ts.append(k);         #Data Point
```

```
     t.append(time.time());  #Time
     clearbuf(0.1);
     setLI(d);
     clearbuf(2);
     ser1.write('TD \r\n');  #Take Data
     clearbuf(40);          #Wait to take data
     clearbuf2(0.1);
     ser1.write('DC 8\r\n')  #Get data from ADC 1
     dat1=readserial1(d);
     clearbuf(1);
     for j in range(len(dat1)):
        f.write('%s,'%dat1[j]);
     f.write('\n');
     print k;
     k=k+1;


ser2.write('SO 0\r\n'); #Turn Water Bath off
clearbuf2(0.1);

while k < b:
     time.sleep(300);
     clearbuf(0.1);
     a1 = Tmeasure(0);
     a2 = Tmeasure(1);
     Tr1.append(vtoT(a1));   #Bottom Temp
     Tr2.append(vtoT(a2));   #Top Temp
     Ts.append(k);          #Data Point
     t.append(time.time());  #Time
     clearbuf(0.1);
     setLI(d);
     clearbuf(2);
     ser1.write('TD \r\n');  #Take Data
     clearbuf(40);          #Wait to take data
     clearbuf2(0.1);
     ser1.write('DC 8\r\n')  #Get data from ADC 1
     dat1=readserial1(d);
     clearbuf(1);
     for j in range(len(dat1)):
        f.write('%s,'%dat1[j]);
     f.write('\n');
     print k;
     k=k+1;

clearbuf(1);


tdata = np.zeros((4,len(Ts)));
```

```
for i in range(len(Ts)):
   tdata[0,i] = Ts[i];
   tdata[1,i] = Tr1[i]
   tdata[2,i] = Tr2[i];
   tdata[3,i] = t[i];

f.close();
np.savetxt('nov1_tdata.txt',tdata);  #Save temp data

ser1.close()
ser2.close()
```

A.2.3 Fast Curve Buffer Data Collection Code

This code was written by Collin M Tittle and is designed to be used with the SOP for DLDS with the fast curve buffer. This SOP is located on the USB drive given to Dr. Chris Backhouse.

```
#Python Code for Communicating With Ametek Lock-In Amplifier Via PySerial
    and Water Bath Via USB
#Collin M Tittle
#June 21, 2016

import time,u6
import serial
import numpy as np
import string

#----------------Functions

def vtoT(v):  #converts voltage from LM35 measured by LI ADC4 to
    temperature in C.
   T = 100*v;
   return T

def readserial1(x):   # function to read Lock-In serial output and
    convert to float
   time.sleep(0.1);
   out = [];
   i=0;
   while i < x:
         out.append(ser1.readline());
         i=i+1;
   data = [float(a[:-2])/1000 for a in out];
   return data
```

```
def setLI(a):
   clearbuf(1);
   ser1.write('NC \r\n'); #Clear previous data in curve buffer
   clearbuf(1);
   ser1.write('TADC 2\r\n');  #Trigger Mode for ADC (1- 40kHz, 2- 200kHz,
      3- 1000Hz)
   clearbuf(1);
   ser1.write('CBD 256\r\n');  #Add ADC1 to curve buffer
   clearbuf(1);
   ser1.write('STR 5\r\n'); #Time interval between points in us. 5 us
      corresponds to 200kHz
   clearbuf(1);
   ser1.write('LEN %s\r\n'%a); #Set length of curve buffer
   clearbuf(1);


def clearbuf(a):   #Clears serial buffer 1 and waits to allow for
    transport
   ser1.flushInput();
   ser1.flushOutput();
   time.sleep(a);

def clearbuf2(a):  #Clears serial buffer and waits to allow for transport
   ser2.flushInput();
   ser2.flushOutput();
   time.sleep(a);

def Tmeasure(a):
   Vout = u.getAIN(a);   #Gets voltage from AIN of Labjack and converts
      from binary to actual
   Temp = Vout;
   return (Temp);

#Set up Serial Ports

#For Mac/Linux
ser1 = serial.Serial(      #RS232 Connection to Lock In
    port='/dev/cu.usbserial',
    baudrate=38400,
    parity=serial.PARITY_NONE,
    #stopbits=serial.STOPBITS_ONE,
    bytesize=serial.EIGHTBITS,
    timeout = 180,
    xonxoff=True,
    rtscts=False
)

ser2 = serial.Serial(      #Water Bath
```

```
   port='/dev/cu.usbserial-AH00138Q',
   baudrate=19200,
)
"""
#For Windows Netbook
ser1 = serial.Serial(      #RS232 Connection to Lock In
    port='\\.\COM9',
    baudrate=38400,
    parity=serial.PARITY_NONE,
    #stopbits=serial.STOPBITS_ONE,
    bytesize=serial.EIGHTBITS,
    timeout = 180,
    xonxoff=True,
    rtscts=False
)

ser2 = serial.Serial(      #Water Bath
   port='\\.\COM8',
   baudrate=19200,
)
"""

#--------------------Main Program
V = 10;       #Drive DAC voltage---set up voltage sweeps later
d = 100000;      #Number of data points to be collected.
a = 18;          #Number of cycles for heating
b = 96;       #Number of cycles total

u=u6.U6();    # set up LI
u.getCalibrationData();  #calibrate LI

# = np.zeros((b,d)); #create array of zeros to populate with data

clearbuf2(0.1);
ser2.write('SO 1\r\n'); #Turn on Water Bath
clearbuf2(0.1);
clearbuf(1);
k=0;
Ts = [];
Tr1 = [];
Tr2 = [];
t = [];

ser2.write('SS 80\r\n'); #Set water bath to temp
clearbuf2(0.1);

clearbuf(0.1);
setLI(d);                #Set LI settings
```

```
clearbuf(2);
ser1.write('DAC. 1 %s \r\n'%V); #Set DAC drive voltage
clearbuf(1);

f = open("sept20_ps1.txt",'w');

while k < a:
     time.sleep(300);
     clearbuf(0.1);
     a1 = Tmeasure(0);
     a2 = Tmeasure(1);
     Tr1.append(vtoT(a1));    #Bottom Temp
     Tr2.append(vtoT(a2));    #Top Temp
     Ts.append(k);         #Data Point
     t.append(time.time());   #Time
     clearbuf(0.1);
     setLI(d);
     clearbuf(2);
     ser1.write('TD \r\n');   #Take Data
     clearbuf(2);          #Wait to take data
     clearbuf2(0.1);
     ser1.write('DC 3\r\n')   #Get data from ADC 1
     dat1=readserial1(d);
     clearbuf(1);
     for j in range(len(dat1)):
        f.write('%s,'%dat1[j]);
     f.write('\n');
     print k;
     k=k+1;


ser2.write('SO 0\r\n'); #Turn Water Bath off
clearbuf2(0.1);

while k < b:
     time.sleep(300);
     clearbuf(0.1);
     a1 = Tmeasure(0);
     a2 = Tmeasure(1);
     Tr1.append(vtoT(a1));    #Bottom Temp
     Tr2.append(vtoT(a2));    #Top Temp
     Ts.append(k);         #Data Point
     t.append(time.time());   #Time
     clearbuf(0.1);
     setLI(d);
     clearbuf(2);
     ser1.write('TD \r\n');   #Take Data
     clearbuf(2);          #Wait to take data
```

```
        clearbuf2(0.1);
        ser1.write('DC 3\r\n')  #Get data from ADC 1
        dat1=readserial1(d);
        clearbuf(1);
        for j in range(len(dat1)):
            f.write('%s,'%dat1[j]);
        f.write('\n');
        print k;
        k=k+1;

clearbuf(1);


tdata = np.zeros((4,len(Ts)));

for i in range(len(Ts)):
    tdata[0,i] = Ts[i];
    tdata[1,i] = Tr1[i]
    tdata[2,i] = Tr2[i];
    tdata[3,i] = t[i];

f.close();
np.savetxt('sept20_tdata.txt',tdata);  #Save temp data

ser1.close()
ser2.close()
```

A.2.4 Deep Level Domain Spectroscopy Analysis Code

This code was written by Collin M Tittle and is designed to be used with the SOP for DLDS with either curve buffer. This SOP is located on the USB drive given to Dr. Chris Backhouse. This code extracts the relevant data from the file and performs Welch's Method analysis on the power spectral density. It will save individual spectra for each temperature point.

```
#Python Code for Fourier Analysis of Power Spectrum Data
#Collin Tittle June 23, 2016

import time
import serial
import numpy as np
import matplotlib.pyplot as plt
from scipy.fftpack import fft
import scipy.signal as sig

#-----------------Functions----------------
def Res(x,y,z):
```

```
   R = x*y/z-x;
   return R

def current(x,y,z):
   I = (x-y)/z;
   return I

def power(x,y,z):
   P = (x-y)*z;
   return P

def LSF(x,y):
   N = len(x);
   delta = N*np.sum(np.square(x))-np.square(np.sum(x));
   A =
       (np.sum(np.square(x))*np.sum(y)-np.sum(x)*np.sum(np.dot(x,y)))/delta;
   B = (N*np.sum(np.dot(x,y))-np.sum(x)*np.sum(y))/delta;

   xbar = np.average(x);
   ybar = np.average(y);

   r =
       (np.sum(np.dot((x-xbar),(y-ybar))))/np.sqrt(np.sum(np.square(x-xbar))*np.sum(np.squa
       #correlation coefficient
   return(A,B,r); #returns values of form y=A+B*x and correlation
       coefficient

#----------------------Main Code--------------------------
#n = 16384;
n = 16384;
dt = 0.001;   #Time point separation in [s]


data = np.loadtxt('aug14_ps1.txt'); #Load Data File
data = np.around(data,3);
print data[0,:]
time = np.linspace(0,4.096,4096);
frequency = np.linspace(1/(n*dt),n/(n*dt),n);
print frequency
s = 108;
RL = 5e5;
window = sig.hamming(n,False);

i = 0;

#Declare Dictionaries
V1 = {};
V2 = {};
```

```
I = {};
R = {};
P = {};
T = {};
FFT = {};

#Preliminary Data Set up
while i <= s:
   #V1['%s'%i] = data[3*i,:];  #Fill Drive voltage dictionary
   V1['%s'%i] = np.ones(n);
   V2['%s'%i] = data[3*i+1,:]; #Fill sense voltage dictionary
   T['%s'%i] = data[3*i+2,:];  #Fill temperature dictionary
   i = i+1;

for i in range(s):
   a1 = []; #dummy array 1
   a2 = []; #dummy array 2
   a3 = []; #dummy array 3
   for j in range(n):
      v1 = Res(RL,V1['%s'%i][j],V2['%s'%i][j]);
      a1.append(v1);
      v2 = current(V1['%s'%i][j],V2['%s'%i][j],v1);
      a2.append(v2);
      v3 = power(V1['%s'%i][j],V2['%s'%i][j],v2);
      a3.append(v3);

   R['%s'%i] = a1;    #Fill Resistance Dictionary
   I['%s'%i] = a2;    #Fill Current Dictionary
   P['%s'%i] = a3;    #Fill Power Dictionary
   fs,Pden = sig.welch(V2['%s'%i],1e3);
   FFT['%s'%i] = Pden; #Fill fft dictionary

   plt.semilogy(fs,Pden);
   plt.xlabel('Frequency(Hz)');
   plt.ylabel('PSD [V**2/Hz]');
   a = 100*np.mean(T['%s'%i]);
   plt.title('MoS2 Film at %s C'%a);
   plt.savefig('%s.png'%i);
   plt.close();


Tbar = [];
dT = [];
Rave = [];
dR = [];
for i in range(s):
   Tbar.append(np.mean(T['%s'%i])*100+273);
   dT.append(np.std(T['%s'%i])*100);
```

```
   Rave.append(np.mean(R['%s'%i]));
   dR.append(np.std(R['%s'%i]));

xfit = np.linspace(np.amin(Tbar),np.amax(Tbar));
(A,B,r) = LSF(Tbar,Rave);
yfit = A+B*xfit;

plt.errorbar(Tbar,Rave,xerr=dT,yerr=dR,fmt='bo');
plt.plot(xfit,yfit);
plt.text(np.amin(Tbar)+1,np.amin(Rave)+1,'y = %s + %s x'%(A,B));
plt.xlabel('Temperature (K)');
plt.ylabel('Resistance $\Omega$');
plt.title('Resistance vs. Temperature for 4 Layer, 2H MoS$_{2}$ Film');
plt.show();
```

A.3 Chapter 5

A.3.1 Code to Monitor High and Low Temperatures of MD Assembly

This code was written by Collin M Tittle and is designed to be used with the membrane distillation SOP located on the USB drive given to Dr. Chris Backhouse.

```
#Python Code to Monitor Hot and Cold Temperatures Using Labjack U6
#Collin M Tittle, May 9, 2017

import time,u6
import numpy as np
import sys, select, os
import matplotlib.pyplot as plt

#Functions
def Tmeasure(a):
   Vout = u.getAIN(a);   #Gets voltage from AIN of Labjack and converts
      from binary to actual
   Temp = 100*Vout;
   return (Temp);

def close_event():
    plt.close() #timer calls this function after 3 seconds and closes the
       window


#Main Program
```

```
#This program will automatically update a graph showing the temperature
    data every 30 seconds.
#After pressing Enter to stop program, data will be saved to file.

u=u6.U6();    # set up LI
u.getCalibrationData();  #calibrate LI

Th = [];
Tc = [];
t = [];

t1 = time.clock();


i = 0
while True:
    os.system(’cls’ if os.name == ’nt’ else ’clear’)
    print "I’m doing stuff. Press Enter to stop me!"
    print i
    Th.append(Tmeasure(0));
    Tc.append(Tmeasure(1));
    t.append(time.clock()-t1);
    plt.ion();
    plt.plot(t,Th);
    plt.plot(t,Tc);
    plt.xlabel("Time (s)");
    plt.ylabel("Temperature (C)");
    plt.pause(30);
    if sys.stdin in select.select([sys.stdin], [], [], 0)[0]:
        line = raw_input()
        data = np.zeros((3,len(t)));
        for i in range(len(t)):
         data[0,i] = t[i];
         data[1,i] = Th[i];
         data[2,i] = Tc[i];
        plt.savefig(’temp_may30.png’);
        np.savetxt(’temp_may30.txt’,data);
        break

    i += 1
```

Appendix B

Asymptote Code

Table of Contents

B.1 Chapter 2

B.1.1 Microheater Pattern

The asymptote schematic for the microheater discussed in § 2. This code was written by Dr. Christopher Backhouse.

```
//  this is TrioTraceMM.asy: a program to lay out subtractive
    micromachine designs for the microheater design with dual heater
    traces and
//  an internal sensor trace with 4-pt measurement. In contrast to
    Subtractor.py (now obsolete), this script aims to produce only an eps
//  file with the idea that this can be used to generate documentation, a
    chip via the CO2 laser (via eps and Corel Draw) or a chip via
//  the CNC (via an eps and pstoedit to generate the gcode). Although
    much the same as TrioTrace, TrioTraceMM more clearly allows one to
//  set up for either laser cutting or CNC cutting (sample parameters
    given below) 2015.09.16 CJB
//  laser cutting:
//    s = 0.075; // since laser cut is probably 150 um in width
//  CNC cutting:
//    s = 0.20; // since endmill is about 400 um in diameter
// Note that t and w are the desired trace widths (ie after cutting) in
    the leads and heater ring respectively.
// Shrinking s will automatically shrink the gaps, but Gap Widening
    Factors (GWF) might also be adjusted.
// GWFi : factor for isolation trace: 1.0 for original, 2.0 for fully
    flared
// GWFs1: factor for separation trace angle 1: 1.0 for original, 1.8 for
    fully flared
// GWFs2: factor for separation trace angle 1: 1.0 for original, 1.5 for
    fully flared
// ****************  Additional parameters for milling:
//  See 2015.04.27 p63:
//  Paint side up in jig, align to BL corner and set to (-25,-15)
//  Bring down mill to touch paper and set to Z=0.04mm
//  Mill out electronics, flip over x axis, centre 1/8 mill on (0,0) (see
    p60)
//  G90G99 G83F200R.1Q.1Z-1
//  Newfangled Cut Circle CW
//  Material Al 10 krpm max feed 1500mm
//  custom surface speed 500 ft/min (!)
//  Chip load 0.0318 for 636 mm/min
//  Overrides: Spindle 100 Feed 100 Plunge 10
//  diam 6 depth 1 mm step depth 0.25 groove outside
//settings.outformat="dxf";
unitsize(1mm);
real r2d = 180/pi;
```

```
real d2r = pi/180;
real Width  = 40.0;  //  mm
real Height = 30.0;  //  mm
real Xoff = -25;
real Yoff = -15;
real Xoff2=-10;
real Yoff2=0;
real Zup = 1;
real Zdn = 0;
// Adjustables:
pen bluepen=linewidth(0.15mm)+blue; // set to same as twice s (makes
   lines the same width as actual cuts)
real s = 0.075; //  Size: Radius of mill/ or half-width of laser cut
real t = 0.2;   //  Thickness of feed-in traces
real w = 0.2;   //  Width of lines
real SG = 0.2;  //  Was 0.4 for CNC, try 0.2 for laser
real GWFi = 0.5; // Gap Widening Factor for isolation trace: 1.0 for
   original CNC, 2.0 for fully flared CNC
real GWFs1 = 0.8; // Gap Widening Factor for separation trace angle 1:
   1.0 for original CNC, 1.8 for fully flared CNC
real GWFs2 = 0.5; // Gap Widening Factor for separation trace angle 1:
   1.0 for original CNC, 1.5 for fully flared CNC
real SW = 8.0;  // Number of cut-widths to leave in zig-zag sensor
// End of adjustables
// Calculated
real Ri = 1.56;         //  was 1.7; (see p63), then 1.56
real Rs = Ri + (2*s) + w; // was 2.3, then 2.45, then 2.55
real Ro = Rs + (2*s) + w; // was 3.4; (see p63), then 3.54
//
real Sca = 2.9;
real RhoAl  = 2.7e-8;  // Assumed RhoAl = 2.7e-8 Ohm-m
real At  = 150e-9;  // Assumed Aluminum thickness (m)
pen redpen=linewidth(0.4mm)+red;
//pen bluepen=linewidth((0.015 * 25.4)mm)+blue;
pen greenpen=linewidth(0.2mm)+green;
defaultpen(bluepen);

real DeltaRad(real dy,real Ri=1.7) {
// """Calculate how much shorter the width of the circle is at a given
   height"""
  real thet = asin(dy/Ri);
  real delr = Ri*(1 - abs(cos(thet)));
  return(delr); }

real yht(int i) {
  i = 11-i;
  return (15-(25.4*(0.035 + (i*0.1)))); }
```

```
path sArc(real cx,real cy,real Radius,real Angle1,real Angle2, string
    DoR) {
// """ Draw an arc from Angle1 to Angle2 about location (cx,cy). If pen
    is down then draw from present location to starting point.
//   Whatever the starting status, move PenDown upon starting the arc.
    Returns starting point as a tuple."""
   path rv;
   if (DoR == "CW") { rv = arc((cx,cy),Radius,Angle1,Angle2,CW); }
   else { rv = arc((cx,cy),Radius,Angle1,Angle2,CCW); }
   return(rv); }


   path rv[];
   path Inner; path Outer; path Separation;

//
// Here we go!
//
// draw outline
   draw(shift(Xoff,Yoff)*scale(Width,Height)*unitsquare);
// Divide upper and lower
   draw( (Xoff2-Ro,0) -- (-25,0));
   draw( (Xoff2+Ro,0) -- (Xoff2+Ro,yht(6)) -- (15,yht(6)) );
   draw( (Xoff2+Ro,0) -- (Xoff2+Ro,yht(5)) -- (15,yht(5)) );
//def CutArcs(x0=0,y0=0,To=0,s=0.2,t=0.2,w=0.2):
//
   real Rwide = 5; real Rtotal; real R1; real R2; real ht; real Rless;
       real x0=Xoff2; real y0=Yoff2;
   real To = 0.0;
   //real s=0.2; real t=0.2; real w=0.2;
   real ShallowA; pair InnerArcEnd; pair OuterArcEnd; pair OuterArcStart;
       pair SeparArcEnd;
// *********************************RHS
   To = 0.0;
   // cut inner isolation trace arc
   real Angle1 = To + (-90) + (r2d*(1.0*s/Ri));
// real Angle2 = To + 90 - (r2d*((s+t)/Ri));
   real Angle2 = To + 90 - (r2d*((SG)/Ri));
   path StartInnerR = arc((x0,y0),Ri,Angle1-2,Angle2,CCW);     //
          CTEDIT
   OuterArcStart = (x0 + (Ri*Cos(Angle2)), y0 + (Ri*Sin(Angle2)) +
       (Ro-Ri) );
   // cut outer isolation trace arc
   Angle1 = To + 90 - (r2d*((s+t)/Ro));
   Angle2 = To + (-90) + (r2d*((GWFi*5.0*s)+(2.5*w))/Ro);
//     Angle2 was originally ...r2d*((5*s)+(2.5*w))/Ro), see p63, then
    was ...(r2d*((10*s)+(2.5*w))/Ro)
   path StartOuterR = arc((x0,y0),Ro,Angle1,Angle2+5,CW);
```

```
              // CTEDIT
// ShallowA = (3*(Angle2 + 90)/3.0)-90;
   ShallowA = (2.7*(Angle2 + 90)/3.0)-90;
   InnerArcEnd = (x0+s,y0-(Rwide+2));
   OuterArcEnd = ( x0+((Rwide)*Cos(ShallowA)),y0+((Rwide)*Sin(ShallowA))
      ) ;
   draw (InnerArcEnd -- StartInnerR -- StartOuterR -- OuterArcEnd );
   //  cut separation trace arc
   Angle1 = To + 90 - (r2d*(((GWFs1*3.0*s)+t+w)/Rs));
// Angle1  was originally ...r2d*(((3*s)+t+w)/Rs), see p63, then was
   ...(r2d*(((5.5*s)+t+w)/Rs)); //
   Angle2 = To + (-90) + (r2d*((GWFs2*3.3*s)+w)/Rs);
// Angle2 = was originally ...r2d*((3.3*s)+w)/Rs), see p63, then was
   ...(r2d*((5*s)+w)/Rs); //
   ShallowA = (2*(Angle2 + 90)/3.0)-90;
// write("Separation A2 was ",Angle2);
// write("x was ",x0+((Rwide+Rs)*Cos(ShallowA)));
// write("with cos of ",Cos(ShallowA));
// write("y was ",y0+((Rwide+Rs)*Sin(ShallowA)));
   path SeparationArc = arc((x0,y0),Rs,Angle1,Angle2+3,CW);
   SeparArcEnd =
      (x0+((Rwide+1)*Cos(ShallowA)),y0+((Rwide+1)*Sin(ShallowA)));
   draw (SeparationArc -- SeparArcEnd );
   // cut sensor line in
// draw ((x0,y0+Ri) -- (x0,y0+Rwide+Ri));
// Inner Sensor Traces
   draw((x0-(Ri-s),0) -- (x0+Ri-(3*s),0));
   int np = (int) (0.7*Ri/(w+(2*s)));
   for (int i=1; i<= np; i=i+2) {
     ht = i*(w+(2*s));  Rless = Ri - DeltaRad(ht);
     if (Rless > (15*s)) {
        draw((x0+Rless, ht) -- (x0-Rless+(SW*s), ht));
        draw((x0+Rless,-ht) -- (x0-Rless+(SW*s),-ht)); }
     ht = (i+1)*(w+(2*s));  Rless = Ri - DeltaRad(ht);
     if (Rless > (15*s)) {
        draw((x0+Rless-(SW*s), ht) -- (x0-Rless, ht));
        draw((x0+Rless-(SW*s),-ht) -- (x0-Rless,-ht)); }
   //ht = (2*Sca*s); Rless = Ri - DeltaRad(ht);
   //draw((x0+Rless-(6.5*s),ht) -- (x0-Rless,ht));
   //draw((x0+Rless-(6.5*s),-ht) -- (x0-Rless,-ht));
     }
//  Hook up the RHS
   draw(SeparArcEnd -- (5,yht(3)) -- (15,yht(3)) );
   draw(InnerArcEnd -- (5,yht(2)) -- (15,yht(2)) );
// draw((15,yht(8)) -- (5,yht(8)) --(OuterArcStart+(0,0.9)) --
   (xpart(OuterArcStart),yht(9)-1.0) );
   draw((15,yht(8)) -- (5,yht(8)) --(OuterArcStart+(0,0.9)) );
// draw((15,yht(9)) -- (5,yht(9)) -- (x0,y0+yht(9)) );
```

```
   draw((15,yht(9)) -- (5,yht(9)) -- (xpart(InnerArcEnd),y0+yht(9)) );
// ********************************LHS
   To = 180.0;
   //  cut inner isolation trace arc
   real Angle1 = To + (-90) + (r2d*(s/Ri));
   real Angle2 = To + 90 - (r2d*((s+t)/Ri));
   path StartInnerR = arc((x0,y0),Ri,Angle1,Angle2,CCW);
   OuterArcStart = (x0 + (Ri*Cos(Angle2)), y0 + (Ri*Sin(Angle2)) -
       (Ro-Ri) );
   //  cut outer isolation trace arc
   Angle1 = To + 90 - (r2d*((s+t)/Ro));
   Angle2 = To + (-90) + (r2d*((GWFi*5.0*s)+(2.5*w))/Ro); // was
       r2d*((5*s)+(2.5*w))/Ro), see p63
//     Angle2 was originally ...r2d*((5*s)+(2.5*w))/Ro), see p63, then
    was ...(r2d*((10*s)+(2.5*w))/Ro)
   path StartOuterR = arc((x0,y0),Ro,Angle1,Angle2+7,CW);    //
               CTEDIT
   ShallowA = (3*(Angle2 + 90)/3.0)-90;
   InnerArcEnd = (x0-s,yht(9));
// InnerArcEnd = (x0-s,y0+(Rwide+2));
   OuterArcEnd = ( x0+((Rwide)*Cos(ShallowA)),y0+((Rwide)*Sin(ShallowA))
       ) ;
   draw (InnerArcEnd -- StartInnerR -- StartOuterR -- OuterArcEnd );
   //  cut separation trace arc
   Angle1 = To + 90 - (r2d*(((GWFs1*3.0*s)+t+w)/Rs));
// Angle1  was originally ...r2d*(((3*s)+t+w)/Rs), see p63, then was
    ...(r2d*(((5.5*s)+t+w)/Rs)); //
   Angle2 = To + (-90) + (r2d*((GWFs2*3.3*s)+w)/Rs);
// Angle2 = was originally ...r2d*((3.3*s)+w)/Rs), see p63, then was
    ...(r2d*((5*s)+w)/Rs); //
// ShallowA was flared at (2*(Angle2 - 90)/3.0)+90;
   ShallowA = (1.5*(Angle2 - 90)/3.0)+90;
   path SeparationArc = arc((x0,y0),Rs,Angle1,Angle2+5,CW); //Edit this
       for line in and out  CTEDIT
   SeparArcEnd =
       (x0+((Rwide+1)*Cos(ShallowA)),y0+((Rwide+1)*Sin(ShallowA)));
   draw (SeparationArc -- SeparArcEnd );
//  Hook up the LHS
   draw((15,yht(10)) -- (xpart(SeparArcEnd)-2.0,yht(10))
       --(xpart(SeparArcEnd)-2,ypart(SeparArcEnd)) );
   draw((xpart(SeparArcEnd)+1.2,ypart(SeparArcEnd)+1.5)
       --(xpart(SeparArcEnd)-0.3,ypart(SeparArcEnd)+1.5) );
   draw((SeparArcEnd-(2,0)) --SeparArcEnd );
   draw((15,yht(1)) -- (xpart(OuterArcStart),yht(1))
       --(OuterArcStart-(0,1.0)) );
//
   draw((15,yht(9)) -- (5,yht(9)) -- (xpart(InnerArcEnd),y0+yht(9)) );
```

```
R1 = (Ri + Rs)/2; R2 = (Ro + Rs)/2;
Rtotal = 2*pi*RhoAl/At*( (R1/(Rs-(Ri+s+s))) + (R2/(Ro-(Rs+s+s))) );
//save("TrioTrace.dxf");
write("Estimated total heater resistance in Ohms: ",Rtotal);
```

B.2 Chapter 3

B.2.1 Langmuir Blodgett Corral

The asymptote code for the PMMA corral used to minimize film spread in the Langmuir Blodgett film formation protocol discussed in § 3 and § C. This code was written by Collin M. Tittle

```
unitsize(1mm);
pen bp = rgb(0,0,1)+linewidth(0.001);

draw(scale(50,50)*unitsquare,bp);
draw(shift(4.6,16)*scale(18,18)*unitsquare,bp);
draw(shift(27.3,16)*scale(18,18)*unitsquare,bp);
```

B.2.2 Asymptote Code for Sample Holder

The asymptote code for sample holder within the sonicator used in the sample preparation protocol discussed in § 3 and § C. This code was written by Collin M. Tittle

```
unitsize(1cm);

pen b = linewidth(0.001)+blue;

draw(scale(8,5)*unitcircle,b);
draw(shift(0,0)*scale(0.6)*unitcircle,b);
draw(shift(3.5,0)*scale(0.6)*unitcircle,b);
draw(shift(-3.5,0)*scale(0.6)*unitcircle,b);
draw(shift(0,3.5)*scale(0.6)*unitcircle,b);
draw(shift(0,-3.5)*scale(0.6)*unitcircle,b);
```

B.2.3 Graphene Interdigitated Electrode

The asymptote code for laser-induced graphene IDE structures used for electrical characterization discussed in § 3 and § C. This code was written by Collin M. Tittle and inspired by design discussions with Dr. Christoper Backhouse.

```
//Asy File for traditional interdigitated structure design.
```

```
//unitsize(1.5mm);
unitsize(0.013888888 inch); /// one point

pen redpen = rgb(1,0,0)+linewidth(0.001mm);
pen bluepen = rgb(0,0,1)+linewidth(0.001mm);
defaultpen(bluepen);

real W = 85;
real dH = 5;
real xL = 32;
real xR = 57;
real ymin = 11;
real ymax = 74;



for (real j=ymin;j<=(ymax-dH);j+=(dH)) {
   draw( (0,j)--(xR,j));
   }

for (real j=ymin+(dH/2);j<(ymax-dH);j+=(dH)) {
   draw( (xL,j)--(85,j));
   }
```

B.2.4 ITO Interdigitated Electrode

The asymptote code for the ITO/Carbon IDE structures discussed in § 3 and § C. This code was written by Collin M. Tittle and inspired by design discussions with Dr. Christoper Backhouse.

```
unitsize(1mm);

real dH = 0.5;
real w = 25;
real xmin = 0;
real xmax = xmin+w;
real ymin = 0;
real ymax = 8;
real itl = -5;
real itr = 30;

pen bluepen = rgb(0,0,1)+linewidth(0.001);
pen redpen = rgb(1,0,0)+linewidth(0.001);

path ito = (-5,-0.5)--(30,-0.5)--(30,8.5)--(-5,8.5)--cycle;
```

```
for (real j=ymin; j<=(ymax-dH);j+=(2*dH)) {
   draw( (xmin,j)--(xmax,j),bluepen);
   draw( (xmax,j)--(xmax,j+dH),bluepen);
   }

for (real j=ymin+dH; j<=(ymax-dH);j+=(2*dH)) {
   draw( (xmax,j)--(xmin,j),bluepen);
   draw( (xmin,j)--(xmin,j+dH),bluepen);
   }

draw ((0,0)--(0,-1),bluepen);
draw ((0,8)--(0,9),bluepen);
draw(ito,redpen);
```

B.3 Chapter 4

B.3.1 Superhydrophobic Pattern

This asymptote code forms the superhydrophobic surfaces discussed in § 4 and § C. The lattice spacing may be adjusted by vary dH. This code was written by Collin M Tittle.

```
//Preamble
unitsize(0.013888888 inch);

pen bluepen = rgb(0,0,1)+linewidth(0.001mm);
defaultpen(bluepen);

real x1 = 0;
real x2 = 36;
real y1 = 0;
real y2 = 36;

real dH = 1; //spacing of lattice

real n = y2/dH;

int i = 0;

for (i=0; i< n; i = i+1) {
   draw((x1,y1+i*dH)--(x2,y1+i*dH));
   draw((x1+i*dH,y1)--(x1+i*dH,y2));
   }
```

B.4 Chapter 5

B.4.1 Membrane Characterization (Petri Dish)

This code will cut out both the PMMA alignment frame and hole from the centre of the Petri dish for membrane characterization. Additionally, it will pattern the Kapton tape adhered over the hole to form a porous membrane. This code is relevant to the discussion in § 5. This code was written by Collin M. Tittle.

```
unitsize(0.013888888 inch); /// one point

pen redpen = rgb(1,0,0)+linewidth(0.1mm);
pen bluepen = rgb(0,0,1)+linewidth(0.1mm);
defaultpen(bluepen);

real C = 246/2; ///Petri dish diameter
real H = 301; //Frame width
real S = 54/2; // Membrane hole diameter
real M = 18;  //Patterned region diameter

real a = 6;
real l = 4;
real x = 1;
real k = l+x;

real b;
real c;


draw(shift(-H/2,-H/2)*scale(H)*unitsquare,redpen);
draw(scale(C)*unitcircle,redpen);
draw(scale(S)*unitcircle,redpen);

draw(shift(-H/2-1, -H/2-1)*scale(H+2)*unitsquare, white);


/// Begin Grid
path path_mask=scale(M)*unitcircle;

path hl;
path path_mask=scale(M)*unitcircle;

for (int j = -86; j<86; ++j) {
   for (int i = -36; i<0; ++i) {
      hl = (k*i,j)--(k*i+l,j);
      if (intersectionpoints(path_mask,hl).length!=0) {
      draw(intersectionpoints(path_mask,hl)[0]--(k*i+l,j));
      real c = xpart(intersectionpoints(path_mask,hl)[0]);
```

```
      b = b+((k*i+l)-c);
      }
      }
   }

for (int j = -86; j<86; ++j) {
   for (int i = 0; i<36; ++i) {
      hl = (k*i,j)--(k*i+l,j);
      if (intersectionpoints(path_mask,hl).length!=0) {
      draw((k*i,j)--intersectionpoints(path_mask,hl)[0]);
      real c = xpart(intersectionpoints(path_mask,hl)[0]);
      b = b+(c-k*i);
      }
      }
   }

for (int j = -86; j<86; ++j) {
   for (int i = -36; i<0; ++i) {
      hl = (k*i,j)--(k*i+l,j);
      bool result = ((k*i)**2+(j)**2)<M**2;
      if (result) {
      draw(hl);
      b = b + l;
      }
   }
}

for (int j = -86; j<86; ++j) {
   for (int i = 0; i<36; ++i) {
      hl = (k*i,j)--(k*i+l,j);
      bool result = ((k*i+l)**2+(j)**2)<M**2;
      if (result) {
      draw(hl);
      b = b + l;
      }
   }
}
```

B.4.2 Membrane Distillation Assembly

This code will cut out the PMMA spacing layers and, subsequently, fabricate the membrane pattern into the Kapton tape adhered over the holes as discussed in § 5. This code was written by Collin M. Tittle.

```
unitsize(5mm); /// one point
```

```
pen redpen = rgb(1,0,0)+linewidth(3mm);
pen bluepen = rgb(0,0,1)+linewidth(3mm);
defaultpen(bluepen);

real H = 172; //Frame width
real d = 72;  //offset
real r = 14/2;   //Bolt radius
//real S = 58/2; // Membrane hole diameter big
real S = 54/2; // Membrane hole diameter small
real M = 18;  //Patterned region diameter
real a = 6;
real l = 4;
real x = 1;
real k = l+x;

real b;
real c;

//draw(shift(-H/2,-H/2)*scale(H)*unitsquare,redpen);
draw(scale(S)*unitcircle,redpen);
//draw(shift(-d,-d)*scale(r)*unitcircle,redpen);
//draw(shift(-d,d)*scale(r)*unitcircle,redpen);
//draw(shift(d,-d)*scale(r)*unitcircle,redpen);
//draw(shift(d,d)*scale(r)*unitcircle,redpen);


path hl;
path path_mask=scale(M)*unitcircle;

for (int j = -86; j<86; ++j) {
   for (int i = -36; i<0; ++i) {
      hl = (k*i,j)--(k*i+l,j);
      if (intersectionpoints(path_mask,hl).length!=0) {
      draw(intersectionpoints(path_mask,hl)[0]--(k*i+l,j));
      real c = xpart(intersectionpoints(path_mask,hl)[0]);
      b = b+((k*i+l)-c);
      }
      }
   }

for (int j = -86; j<86; ++j) {
   for (int i = 0; i<36; ++i) {
      hl = (k*i,j)--(k*i+l,j);
      if (intersectionpoints(path_mask,hl).length!=0) {
      draw((k*i,j)--intersectionpoints(path_mask,hl)[0]);
      real c = xpart(intersectionpoints(path_mask,hl)[0]);
      b = b+(c-k*i);
      }
```

```
      }
   }

for (int j = -86; j<86; ++j) {
   for (int i = -36; i<0; ++i) {
      hl = (k*i,j)--(k*i+l,j);
      bool result = ((k*i)**2+(j)**2)<M**2;
      if (result) {
      draw(hl);
      b = b + l;
      }
   }
}

for (int j = -86; j<86; ++j) {
   for (int i = 0; i<36; ++i) {
      hl = (k*i,j)--(k*i+l,j);
      bool result = ((k*i+l)**2+(j)**2)<M**2;
      if (result) {
      draw(hl);
      b = b + l;
      }
   }
}

write(b);  // total length of ablated area in points
```

Appendix C

Procedures

Table of Contents

This section provides select procedures corresponding to sections of the thesis. A complete set of procedures was provided on a USB key attached as it was not feasible to list them all.

C.1 Chapter 3

C.1.1 MoS_2 Sample Preparation Protocol

Protocol

1. The technique described within falls under the class of liquid phase exfoliation, however it differs in several key respects to the traditional implementation. The primary difference between the work done by the Coleman group ([51] [56] [5]) and our methodology was that they used aggressive probe sonication or mechanical shear exfoliation while gentle, short term sonication was used in this work.

2. Using a P1000 add 1mL of desired solvent to a 1.5mL polypropylene microfuge tube (Fisherbrand 05-408-129, stored in Cabinet 27). The solvents are listed below with their source detailed in brackets. The (g) or (p) in brackets denotes whether glass or polystyrene cuvettes should be used for optical characterization; the procedures for which are discussed in separate documents. The polystyrene cuvettes (Fisherbrand Cat. No. 14955125) and Fisherbrand Polyethylene cuvette caps (14-385-999) are located in the Cabinet 26. The glass cuvettes used for the reference samples discussed in point 13 are Hellma OG 6300-10-10 (optical crown glass, 360nm-2500nm) and are stored along with the reference samples, additional glass cuvettes (1X Hellma OG 6300-10-10, 2X Hellma OS 110-10-20), and quartz cuvettes (Hellma QS 100-10-40) in the box label MoS_2 spectroscopy in Cabinet 25. The solvents which have been used are listed below and all are stored in Cabinet 19 (other than water).

   - 100% IPA (p) (Fisher Chemical A416SK-4 Certified ACS Plus)
   - 75% IPA, 25% H_2O (p) (Same IPA as above, MilliQ Water from Glerum Lab)
   - 50% IPA, 50% H_2O (p)
   - **25% IPA, 75% H_2O (p)** Standard Solvent
   - 100% H_2O (p)
   - NMP (g) (Sigma-Aldrich CAS 872-50-4)
   - Acetonitrile (g) (Fisher Chemical A998-4 HPLC Grade)
   - Heptane (g) (Chemistry Stores Reagent Grade Bulk Solvents)

   The standard solvent solution for preparation of reference samples is 25% IPA, 75% H_2O. Solvents which may be tested in the future are: methanol, acetone, diethylether, ethanol, formaldehyde, toluene, SDS in water, and sodium cholate.

3. Fill Magnasonic Digital Ultrasonic Jewelry Cleaner (MGUC500), hereby referred to as the sonicator, with 450mL of reverse-osmosis tap water and place holder in sonicator. Run sonicator for 480 seconds with no samples to reach steady-state power output. The sample holder is an ellipse with 16cm and 10 cm major and minor axis respectively laser cut out of 1.5mm PMMA. Holes to hold microfuge tubes of radius $r = 0.6cm$ are located at (0,0),(3.5,0),(-3.5,0),(0,3.5), and (0,-3.5) with all units in centimetres and the origin set at the centre of the ellipse. The asymptote code is documented in Appendix I.

4. Weigh 0.0125 ± 0.0005 g of MoS_2 using balance Mettler Toledo balance in the Backhouse lab (as of v1.4 this balance is functional) or the Sartorius balance in the Glerum Lab; the following protocol applies to both . Weighing paper is stored in Cabinet 28 and should be used. A brief synopsis of the procedure is below.

    (a) Fold weighing paper into quarters then unfold to create depression in middle of paper to contain sample.

    (b) Place weighing paper onto balance, close doors, and tare

    (c) Slowly add MoS_2 to paper, closing doors between measurements to ensure accuracy. A scoopula should be used to add sample. There is currently one stored on the drying edge above the sink. The MolySlip Moly Power - Technical Grade Molybdenum Disulfide is stored in Cabinet 25. Before and after use, the scoopula should be wiped clean using ethanol. The used Kimwipe should be disposed of in waste disposal bin 4.

    (d) When 0.0125 ± 0.0005g of MoS_2 has been weighed remove sample from balance.

    (e) Clean boat and surrounding apron of any sample which may have spilled.

5. In fume hood, add MoS_2 to solvent in microfuge tube. Vortex for 10 seconds on power level 10 using the vortex in the Backhouse lab on top of microwave to suspend the MoS_2 within the solvent.

6. First unplug sonicator, then empty, refill with 450mL of reverse-osmosis tap water, replace sample holder, and place sample microfuge tube to the centre hole. For 25/75 IPA/Water, sonicate for two cycles of 180 seconds, removing the sample and vortexing for 10 seconds between cycles. Sonication times for other solvents are listed in Table C.1

7. After completion of sonication, unplug the sonicator, empty, and lay parts on a paper towel to dry.

Safety

For safety reasons, any solvent which requires a glass container for exfoliation should only be used when a colleague is close enough (i.e. on the 3rd floor) to provide help

Sonication and Settling Parameters for Solvent Exfoliation of MoS_2					
Solvent	τ_0 (s)	τ_1 (mins)	τ_2 (mins)	τ_3 (hrs)	$V_{abs}(\mu L in mL)$
100% IPA	360*	5	30	8+*	200 in 2.8
75/25 IPA/Water	360*	5	30	8*	200 in 2.8
50/50 IPA/Water	360*	5	30	6*	200 in 2.8
25/75 IPA/Water	360	5	30	6.3 ± 0.4	200 in 2.8
100% Water	540*	2	10	2*	200 in 2.8
Chloroform	720*	1	2	0.3*	500 in 2.5
Heptane	1500*	1	2	0.3*	1000 in 2
Acetonitrile	360*	10	30	6*	200 in 2.8
NMP	360*	20	45	8+*	200 in 2.8

Figure C.1: τ_0 denotes sonication time. τ_1 corresponds to the settling time required for the silver layer to form. τ_2 refers to settling time required for black layer to form. τ_3 refers to the settling half life determined by an exponential fit to the data.. V_{abs} denotes the volume of sample in solvent required for absorption measurements. * denotes estimation rather than experimental determination.

should an accident occur and they have been made aware of the procedure which is currently being performed. Waste bottles should be obtained from Greg Friday at the Environmental Safety Facility (ESF). His recommendation is to take waste materials down once every two weeks. A 1L waste bottle is used for all IPA and water solvent solutions, while separate 500mL bottles should be used for other solvents. The solvent label should indicate the solvent(s) present, including the percentages, and molybdenum disulfide nanoparticles. No abbreviations are to be used on the label. The outside of the bottle should be wiped clean and transported to the ESF in the bottle carrier (stored under the sink) or using a cart. Appropriately labelled waste bottles for water/IPA, NMP, Acetonitrile, and Heptane are currently located in the waste cabinet. When handling the molybdenum disulfide powder, care should be taken to ensure micron scale dust is not disturbed. This is best done by smoothly removing the powder and gently adding to weighing paper. The scoopula should be wiped clean with ethanol and the kimwipe disposed of in waste disposal bin 4. After sonication, the sub-micron nanoparticles should be kept in solution or formed into a film and kept within the fume hood. Disposal should again be into waste disposal bin 4 or sealed in plastic and disposed of in glass waste if the film was formed on glass. If decay of processed films or dust is noticed, work should be stopped and Chris should be notified immediately.

C.1.2 Graphene Electrode Fabrication

1. The film will be formed on the highly hydrophobic surface of graphene electrodes which will be produced using an adaptation of the Tour method [62] which involves laser ablation of Kapton films.

2. This protocol was first developed on October 30, 2015 and has been edited as

of February 28, 2018.

3. An interdigitated electrode (IDE) structure with electrode separation of 1.75mm centre-to-centre is formed with laser power settings of 9% Power, 10% Speed, 1000 PPI, and 5mm focus on 0.0025” Kapton HN tape (McMaster Carr # 7648A34) which is supported by a standard microscope slide (currently Fisherfinest Premium Microscope Slides Plain Cat. No.12-544-1). Laser focus was verified using the focus tool approximately once per week.

4. 3mm of tape is adhered to one side of the slide such that the edge of the tape is aligned with the slides edge. The tape is then wrapped around the slide, with care to prevent air bubble formation, and an overlap of 3mm is left on the opposite edge.

5. Substituting a microscope cover slip for the microscope slide and following the same procedure, electrodes on a thinner substrate allowing better thermal transport is possible.

6. The IDE structure is shown in Fig. C.2 and the Asymptote code is documented in Appendix I. Standard laser operation protocol should be adhered to with the addition of a 2 minute waiting period after the ablation process for removal of carbon particles from the chamber. The IDE has an interdigitated region approximately 1.75mm by 10mm. A change to the Asymptote code is necessary to account for the offset currently present.

7. The resistance of the carbon traces was determined by measuring the resistance of 2 cm long traces contacted with approximately 2mm diameter circular nickel contacts. Three traces prepared using the above protocol had an average resistance of $877\Omega/cm$ with a standard deviation of $\pm 31\Omega/cm$.

8. This method allows for the rapid fabrication of contacts which have been observed to behave ohmically when contacted by MoS_2. A long standing need for ohmic contacts to MoS_2 has been noted by the likes of Liu and Chuang [61][60]. However, of the few contacts which have been produced to satisfy this criteria, all have relied upon complex microfabrication processes. The contacts produced using the above protocol represent the first demonstration of rapidly-prototyped, cost effective ohmic contacts to MoS_2.

9. The surface produced has been observed to be highly hydrophobic. The contact angle of a $50\mu L$ drop of 25/75 IPA/Water in the interdigitated region of the array was observed to be approximately 130 ± 10 degrees. Using a densely packed interdigitated array and pure water, a contact angle close to 180° was observed. The water droplet could be rolled around the surface with no observable loss of mass. Based upon observations, it is inferred that closer array spacing increases the contact angle. No investigation into the hydrophobic ’range of influence’ around the electrodes has been done as all tests have been done with samples spanning at least two electrodes.

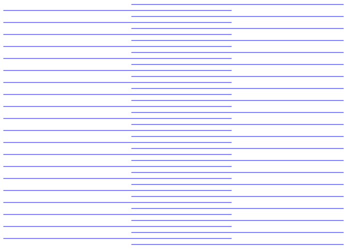

Figure C.2: 2.5cm by 3cm outside dimensions Interdigitated Electrode Structure with a 1.75mm by 10mm interdigitated region. Schematics for IDE fabrication are stored in the Asymptote file Trad.asy which is located in Appendix I and was emailed to Chris Backhouse on August 18, 2016.

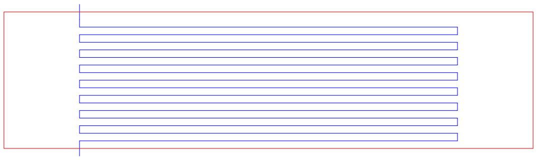

Figure C.3: Asymptote schematic for IDE structure fabricated using ITO and carbon tape. Rectangular heterostructures of carbon tape on ITO of the size of the red box were cut out using laser settings of 8% power, 10% speed, 1000 ppi, and a focus of 0.1 mm. Subsequently the blue trace was cut through the carbon tape and ITO layer leaving the PET support layer with laser settings of 20% power, 27% speed, 1000 ppi, and a focus of 0.1 mm. Asymptote codes is in Appendix B.

C.1.3 Carbon/ ITO Conformal Electrodes

While positive results were observed with graphene electrodes, it was not possible to contact films made on other substrates using these structures. To address this deficiency conformal electrodes made of double sided adhesive carbon tape with an ITO backing were fabricated. This allowed electrodes to be adhered to films made on glass substrates.

Materials

The following materials were used to fabricate the electrodes.

- ITO coated PET (Adafruit, 1309)
- 8 mm wide carbon tape (Ted Pella, 16073)
- Copper tape with conductive adhesive (Ted Pella, 16072-1)
- 22 AWG copper wire

Procedure

1. Place sheet of ITO covered PET in laser. Using laser settings of 8% power, 10% speed, 1000 ppi, and a focus of 0.1 mm cut out the red trace seen in

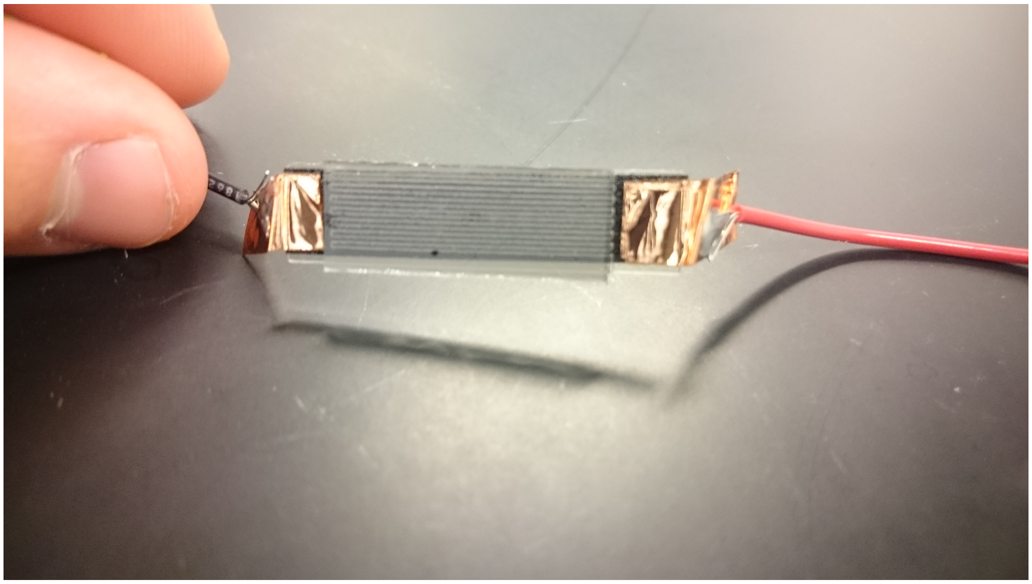

Figure C.4: Image of ITO/ Carbon tape conformal electrode. Copper tape contacted with wires are visible on the exterior. In the centre, interdigitated structures cut through the carbon tape are visible through an MoS_2 films. The conductive ITO layer is on the reverse.

Fig. C.3

2. Using a DMM in resistance mode, identify the ITO side of the PET. Adhere carbon tape to this side covering the entire rectangular coupon.
3. Return ITO/ Carbon heterostructure to laser using the hole in the PET from the first cut as an alignment guide with the carbon tape facing upwards. Using laser settings of 20% power, 27% speed, 1000 ppi, and a focus of 0.1 mm, cut the trace seen in blue through the carbon tape and ITO layer. These laser settings will leave the PET substrate intact.
4. Cut a 2 cm strip of copper tape. Adhere one end of tape to carbon tape on end of structure covering approximately 3 mm of carbon. Fold the remain tape inwards onto itself so that no adhesive is exposed. Repeat on other end using a second piece of copper tape.
5. Issues with reproducibly contacting the copper tape with alligator clips were observed. To address this, 22 AWG wires were soldered to the copper tape and subsequently contacted with alligator clips.
6. A representative image of a finished electrode is seen in Fig. C.4.

C.1.4 Langmuir-Blodgett Film Formation

1. Follow standard sample preparation protocol to prepare MoS_2 sample. A film may be formed from the supernatant at any time up to τ_3 after sonication.

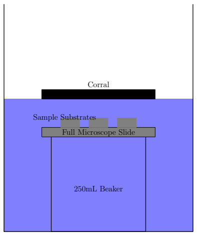

Figure C.5: Diagram of experimental setup for formation of MoS_2 films using a Langmuir Blodget like technique. A 250 mL beaker is set within a large 1 L beaker. A standard microscope slide is used to bridge the top of the beaker and act as a platform for the small glass sample pieces. The beaker is filled with DI water from the reverse osmosis tap until the small beaker and glass substrates are submerged. A corral made from laser cut PMMA is floated on the surface to contain the MoS_2 sheets.

For the standard solvent of 25%IPA/75% Water, this is up to 6 hours after sonication. For the films used for confocal microscopy, settling time was 2 hours.

2. The experimental assembly for film formation is detailed below and shown in Fig. 3.7a.
   (a) Put clean 250mL beaker into centre of clean 1L beaker and fill both with reverse-osmosis tap water until the 250 mL beaker is full and the water level in the 1L beaker is approximately 1 cm above the top of the 250mL beaker.
   (b) Using a carpenters square and glass scribe cut 1cm by 1cm glass squares from microscope slide.
   (c) Wet surface of complete microscope slide with reverse osmosis tap water, then place sample squares on surface. The water will keep the small squares attached to the surface of the slide.
   (d) Place assembled sample slide across the top of the small beaker. It should be fully submerged with approximately 5mm of water above.
   (e) A PMMA corral is used to keep the MoS_2 contained. The current corral is a 2.5" by 1.5" rectangle of PMMA with a 1.5" by 0.5" section cut out from the center. Place this corral in beaker and locate it roughly above the sample.
3. Using a P200, inject 400μL of MoS_2 supernatant into the well one drop at a time. With the current corral size and volumes used, 400μL of sample produces a highly fractured, disperse film (imaged using confocal and showed PL properties). Thicker, uniform films can be formed with greater volumes of sample. Once adequate data has been collected, a table will be compiled. The pipette tip should be kept approximately 5mm above the water surface and surface disturbances should be allowed to disperse before the next drop is

injected. This corresponds to an injection rate of approximately 1 drop every 5 seconds. 2H MoS_2 nanosheets are hydrophobic, however a concentration of 25%IPA is sufficiently high to allow for their suspension in solution with no film formed on the surface. It has been observed that at a solvent concentration of $> 90\%$ water, they will assemble into a film on the water's surface. The delay between drop injection combined with large volume of water in beaker is critical to allow the IPA to diffuse throughout the volume and prevent the local concentration in the film formation region from exceeding the critical limit. Rapid injection of sample failed to form films and it is hypothesized that the rapid injection resulted in a local IPA concentration which exceeded the critical limit and had a diffusion time constant which was long enough to permit the nanosheets to enter the liquid subphase rather than assemble on the surface.

4. In the future, smaller drop size (done using a smaller pipette tip or microtubing from a syringe) and/or varying the drop rate may be used to adjust the film formation dynamics. A round corral may also be used which would remove the turbulent corner regions of the square corral where layer stacking has previously been observed.
5. After injection of the sample allow film to sit for 1 hour. This resting time has been observed to allow the nanosheets to assemble in a more uniform structure. Variation of this assembly time may allow for control of film conductivity in the future.
6. Using a P1000 remove water from beakers, lowering the film onto the glass squares. The corral can be manipulated so that film will come to rest in the desired location without disturbing the film. Continue to remove water until it is several millimetres below the bottom microscope slide
7. After the film has been lowered onto the squares, allow system to sit for 30 minutes and dry.
8. Carefully remove corral and microscope slides. Take corral off of assembly.
9. Keep small samples on large microscope slide and transfer to oven. Hold at 80°C for 2 hours to dry further.
10. Film characterization will be done using a combination of optical, photoluminescence confocal, and scanning electron microscopy in conjunction with conductivity and photoconductivity measurements.

C.1.5 Hydrophobic Film Formation

1. Follow the sample preparation protocol (version 1.6, August 17, 2016) to prepare MoS_2 sample. The standard film sample for characterization is prepared with 25/75 IPA/Water and a settling time of 15 minutes.

2. While the standard sample uses 25% IPA, this technique may be performed using other combinations of IPA/Water provided the concentration of IPA is $\leq 25\%$. This is due to the fact that this technique utilizes a hydrophobic surface to confine the MoS_2 thus high water concentrations are required.

3. The standard settling time after sonication is 15 minutes, however films have been formed at settling times up to τ_3 (for 25/75 IPA τ_3 = 6hrs; τ_3 defined in sample preparation protocol). Films formed at longer settling times were observed to be discontinuous as no conductivity could be measured using an Agilent 1252A DMM (capable of reading up to 500 MΩ at $0.01 M\Omega$ resolution. Film formation at settling times greater than τ_3 have not been investigated.

4. The film will be formed on the highly hydrophobic surface of graphene electrodes which will be produced using an adaptation of the Tour method [62] which involves laser ablation of Kapton films and is documented in the graphene SOP (v1.1, Aug.17, 2016).

5. After formation of the interdigitated electrode structure following the graphene SOP, move to the fume hood for film formation. The electrode structure needs to be placed on a flat surface for film formation.

6. With a P200, extract the top 50μL of supernatant from the sample microfuge tube. When doing so try to avoid disturbing the sides and bottom of the tube as these appear to be the main aggregation points for larger particles which are undesirable. With constant injection rate of approximately 5μL per second, apply 50μL of MoS_2 supernatant to electrode surface in one location. The pipette tip should be kept approximately 5 mm above the surface of the film and directly in the centre of the interdigitated region. Due to the hydrophobicity of the surface the sample will form a bubble on the surface. The injection site should be chosen such that it is between two of the interdigitated electrode structures which will allow for conductivity measurements as the film will eventually bridge the gap. The bubble should cover 4 interdigitated regions where an interdigitated region is defined as the space between positive and negative electrodes, or a region 7mm by 10 mm.

7. Particles will be observed to migrate to the surface of the bubble with nucleation sites located along the bubble-kapton interface. Occasionally, the self-assembled sheets will break from the nucleation sites and migrate around the bubble's surface. Sheet movement is likely assisted by air currents and the Marangoni Effect from evaporating IPA. Over the course of approximately 30 minutes, it will be observed that the inside of the bubble will become increasingly transparent as the particles migrate to the exterior.

8. The solvent can be allowed to evaporate which will deposit the film on the electrode structure.

9. The film is left to dry for 24 hours at which point it is assumed that all solvent has evaporated leaving only MoS_2.

C.1.6 Absorption Spectroscopy

Operation

1. Turn on Shimadzu UV-1601PC UV-Vis Spectrometer in Glerum Lab using power switch on side. As well, turn on computer. The Shimadzu UV-1601PC has a spectral band width of 2 nm, a wavelength accuracy of ±0.5 nm based on on-board wavelength calibration, and a wavelength repeatability of ±0.1 nm. The system also features a photometric accuracy of ±0.002 Abs and a photometric repeatability of ±0.001 Abs (both at 0.5Abs which is close to range which we will be operating in) with a baseline flatness of ±0.001 Abs/h and a noise level of 0.002 Abs. Open UV-Visualizer program on computer and select Connect to initiate communication between the computer and the spectrometer. This process will automatically initiate checks of the system; all of which must pass to continue. The spectrometer should be left for 30 minutes to warm up.

2. Prepare cuvettes as detailed in Sample Preparation One-Pager. Special attention should be paid to volumes of sample and solvent, and required settling times. When 25/75 IPA/Water is used as the solvent the supernatant can be extracted after settling between 30 mins and 6 hrs (τ_2 to τ_3). Two blank cuvettes containing solvent only should be prepared as well. As detailed in the protocol after the sample has been prepared, it should be let sit for 30 minutes to allow for any bulk particles to settle and any air bubbles leave solution.

3. Open new measurement in UV-Visualizer. Select Method from the top toolbar, then select Instrument Parameters tab from the window which opens. Ensure that the Measuring Mode is Absorbance and the Slit Width is 2.0 Fixed. In the same tab, verify that the Light Source Change Wavelength is set to 364 nm (manual recommends 340.8nm, but all measurements have been collected on this setting so far) and the S/R Exchange is Normal. In the Measurement tab, within the same Method window, set the Wavelength Range to Start at 900 nm and End at 300 nm with a Speed of Fast and Interval of 1 nm.

4. Close the Method window and with no cuvettes in the spectrometer select the Baseline button from the bottom menu and wait for process to complete.

5. As disposable polystyrene cuvettes are being used the optical faces should be free of particulates and scratches, however it is good practice to inspect the cuvettes before placing in spectrometer. A dry Kimwipe may be used to remove any drips from the surface or dust. If the surfaces are dirty, an ethanol or IPA soaked KimWipe maybe used to clean the surface which should be dried with another KimWipe before placing in the spectrometer. Scratched cuvettes should be exchanged for defect free cuvettes.

6. After cleaning of the blank cuvettes, place one in each holder with the optical faces (identified by arrow at top of cuvette) parallel to the directional arrow

on holder. After closing the spectrometer, select the AutoZero button on the menu to calibrate the absorbance and remove solvent absorbance from subsequent sample measurements.

7. Remove blank cuvette from front holder. Based on dynamic light scattering (DLS) measurements and observations of the settling behaviour it is hypothesized that the exfoliation process suspends a bimodal population distribution of MoS_2 particles, the larger of which settle out of suspension at a more rapid rate. A potential consequence of this hypothesis is that variations in handling could affect the spectroscopic properties as agitation could resuspend bulk particles. The ideal situation for measurement of this effect would be to baseline and zero the system then collect spectra over a time period without removing the cuvette from the system, however this is not feasible due to the multi-user nature of the equipment and baseline drift which would require the system to be recalibrated. The following handling protocol has been followed to minimize agitation effects.

   (a) As detailed in Sample Preparation SOP, after preparation of sample cuvette, let settle for 30 mins in Backhouse Lab.

   (b) Place cuvettes in styrofoam holder and transport to Glerum Lab in careful manner.

   (c) When wiping cuvette faces and moving to spectrometer do not invert or agitate cuvette.

   (d) If spectra are to be collected at subsequent time points, leave samples in Glerum Lab between points.

   After placing sample in spectrometer select Start to collect data and save output data to personal folder on hard drive as a backup.

8. Select print data display to show table of data. This will open a table containing one column of wavelengths scanned and a second column containing the absorbance values corresponding to each wavelength (in units of Abs). Copy data from table to blank notebook text file. Save this file as a .txt to memory stick. Plot data using Matplotlib or Pyplot. A sample code is shown in Appendix A and a representative absorption spectrum for the standard sample of 25%IPA, 75% Water is shown in Fig. 3.9 which can be compared with the accepted absorption spectrum in [5]. Sample lines from the data file plotted in the representative spectrum are shown below.

```
300.00  0.379
302.00  0.388
304.00  0.397
```

   At 900 nm (the first value read when cuvette is place in spectrometer) the absorbance should be between 0.25 and 0.4 for all solvents.

C.1.7 Photoluminescence Spectroscopy

General Use

1. Turn on Shimadzu using power button on bottom right corner of front panel. Allow the xenon lamp to warm for at least 30 minutes prior to use. The Shimadzu has a beam width of $10nm$ with a wavelength resolution with $1nm$. The spectral sensitivity has a precision of 3 decimal places. The signal to noise ratio of the emission photomultiplier tube at last calibration was 350 for the Raman spectrum of water.

2. Prepare cuvettes with sample as discussed in Sample Preparation Protocol. Specific attention should be paid to concentrations and times detailed in the Table with the standard testing time of $\tau_3/2$. A cuvette containing just solvent should be prepared as well and tested in parallel with the sample.

3. Allow cuvette to sit for time t_s before use. The t_s values are tabulated by solvent and displayed in the sample preparation document.

4. Wipe faces of cuvette with Kimwipe to make as clean as possible. Gloves should be worn when preparing samples, handling cuvettes, and operating Shimadzu.

5. Before opening sample door, ensure that the shutter is closed. If the shutter is closed, the intensity will be highlighted in the top right corner of the display. To close shutter press shutter button on controls.

6. Insert cuvette into spectrometer

7. Enter spectrum menu. Using designated button on keypad enter excitation wavelength sub-menu. The standard excitation wavelength is 514nm. In the results discussed below the excitation wavelength was swept from 533nm down to 390nm.

8. Returned to spectrum menu, press 1 to toggle between EX and EM spectrum type. Set to EM for emission. Press 3 to set the emission scan range. In the subsequent menu set the emission wavelengths to scan from 514nm up to 900nm.

9. Returning to the spectrum menu, press 5 to proceed to INST PARAMS menu and set sensitivity to HIGH.

10. Press 4 to set scan speed, then select FAST.

11. Start recording of spectrum.

12. Save spectrum to the on-board storage using the F2 save function.

13. Connect laptop to output port. The process for establishing a serial connection to a MacOSX system is outlined in this link: `http://plugable.com/2011/07/12/installing-a-usb-serial-adapter-on-mac-os-x`
    ```
    kextstat | grep prolific
    ioreg -c IOSerialBSDClient | grep usb
    screen -L /dev/cu.usbserial
    ```
    This is the only command necessary if different usb serial program is used.

14. In the file menu select the transfer option and select option 12 to transfer to computer.

15. The resulting data file contains a header detailing the experimental parameters and a table containing both wavelength (in nm) and fluorescence intensity (in arbitrary units) data. To store multiple data files leave the computer connected to the Shimadzu. Repeat the saving and transfer protocols detailed above. New spectra will be appended to the end of the screen log file.

16. Disconnect computer from Shimadzu. It is easiest to convert the screen log file to a .txt file for data analysis. This can be done using:
    ```
    cat screenlog.X > crypticfilename.txt
    ```

17. Turn off spectrofluorophotometer

Calibration

The Shimadzu RF-1501 was calibrated to the raman peak of water and the fluorescence spectrum of Rhodamine B. For Rhodamine B, 3mL of 10μM RhB in ethanol was loaded in a cuvette and excited using 510nm light. According to IOM-Berlin the fluorescence emission peak should be at $565nm$ (http://www.iom-berlin.de/pdfs/Farbstofftabelle.pdf). As seen in Fig. C.6, it was measured to be $565 \pm 1nm$. The raman peak of pure water when excited with 350nm light is located at 395nm according to the Shimadzu RF1501 User Manual. This can be verified as an independent measurement, similar to those detailed above, or the built-in Performance Check tool included on the Shimadzu may be used instead. This tool is accessed through the top level menu. It was measured to be $395 \pm 4nm$

C.2 Chapter 4

C.2.1 Contact Angle Measurement

Sample Preparation

1. Samples will be prepared within 2 hours of beginning of testing in triplicate.

2. Between fabrication and testing they will be stored in a petri dish at SATP.

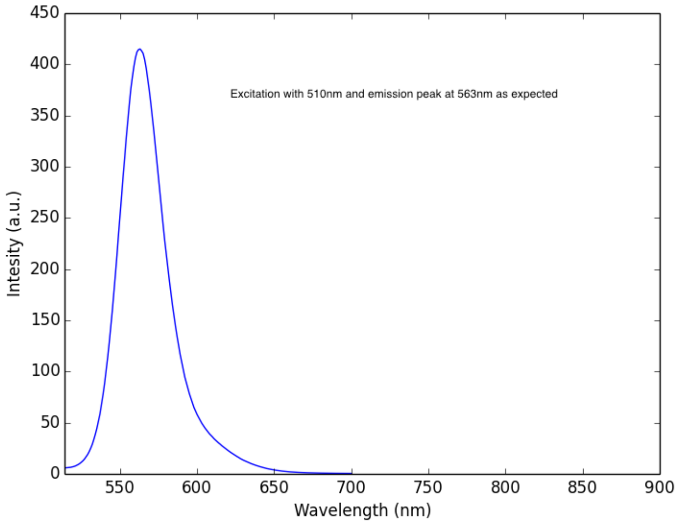

Figure C.6: Fluorescence Spectrum of RhB with 510nm Excitation and Emission Peak at 565nm

3. As has been done for the entirety of this investigation, six samples will be prepared per slide in a line across the top. This is done to ensure consistent ventilation across the sample while ablating and to prevent deposition of ablated material on subsequent samples, potentially changing their properties.

Contact Angle Measurement

1. The sample slide will be placed in the goniometer. The pipette will be aligned above the sample in approximately the middle. Similar position on all samples should be used to provide a similar depth of field and baseline focus in all images.

2. The measurement time will be determined by placing a droplet at least 5mm across on the sample. The contact angle will be monitored for 1 to 3 minutes to observe any dynamic behaviour. The time required for the droplet to reach equilibrium will be called t_{min}. All contact angles subsequently measured will be taken at greater than t_{min} after the droplet has been advanced or retreated.

3. Remove slide from stage and invert to remove water. If surface wetting is observed wait until dry before continuing.

4. Return sample to stage and place droplet on surface with diameter greater than 5mm (may need to be increased if droplet does not terminate) across.

5. Retract pipette tip and wait time t_{min}.

6. Record image for advancing contact angle.

7. Lower pipette tip and add additional water to droplet. Repeat above two steps.

8. At least 3 advancing contact angles should be recorded.

9. To measure receding contact angle, contact droplet with pipette and withdraw liquid. Withdraw liquid until base diameter is observed to recede.

10. Raise pipette tip and wait time t_{min}.

11. Record image for receding contact angle

12. Repeat above 3 steps at least 3 times.

13. For all samples, repeat steps 1-13.